Micromechanical Modelling of Local Failure and Ply Crack Formation in Fiber-Reinforced Plastic Laminates

by

Farzad Sharifpour

A thesis
presented to the University of Waterloo
in fulfillment of the
thesis requirement for the degree of
Doctor of Philosophy
in
Mechanical and Mechatronic Engineering

Waterloo, Ontario, Canada, 2022

Examining Committee Membership

The following served on the Examining Committee of this thesis. The decision of the Examining Committee is by majority vote.

External Examiner:	Stephen Hallett, Ph.D. Professor, University of Bristol
Supervisor:	John Montesano, Ph.D. Associate Professor, University of Waterloo
Internal Member:	Hamid Jahed, Ph.D. Professor, University of Waterloo
Internal Member:	Clifford Butcher, Ph.D. Assistant Professor, University of Waterloo
Internal-External Examiner:	Adil Al-Mayah, Ph.D. Associate Professor, University of Waterloo

Author's Declaration

This thesis consists of material all of which I authored or co-authored: see Statement of Contributions included in the thesis. This is a true copy of the thesis, including any required final revisions, as accepted by my examiners. I understand that my thesis may be made electronically available to the public

Statement of Contributions

I would like to acknowledge my co-authors who contributed to this thesis.

Prof. John Montesano: Supervision, Conceptualization, Funding acquisition, Project administration, Resources, Review and editing, Validation, Investigation.

Prof. Ramesh Talreja: Advisory guidance, Review and editing, Investigation.

Dr. Geng Li: Chapter 4 – Original draft (Sections 4.1 and 4.2), Methodology, Software, Visualization.

Abstract

Establishing an understanding of the multiscale nature of progressive failure in laminated fiber-reinforced plastics is required to develop high fidelity failure prediction models for associated structures. In recent years, virtual testing techniques have been proposed as an alternative to costly experimental characterization campaigns for assessing damage of composite laminates at different length scales. Conventional macroscale and mesoscale models have been widely proposed to predict stiffness/strength degradation of laminated composites. Nevertheless, the presence of manufacturing-induced defects (e.g., micro-voids) and the significance of local phenomena at the microscopic length scale have put into question the fidelity of conventional approaches (e.g., homogenization of internal structures) for predicting the mechanical performance of composite materials. Progressive failure of composite laminates under quasi-static and cyclic loading begins with formation and multiplication of ply (intralaminar) cracks. Physically, ply cracks form due to the linkage of local failures at the microscale, while they can influence the behaviour of the material at larger scales. The overall goal of the thesis is to develop computational micromechanical models to assess the process of ply crack formation in carbon fiber/epoxy [0/90/0] cross-ply laminates, while also integrating with a hierarchical multiscale framework to bridge the micro and mesoscales. At the microscale, the initiation of local failure in epoxies is related to cavitation-induced and pressure-dependent ductile failure. A constitutive model within a finite element framework was developed to capture the onset of local failure in the epoxy matrix, while an isotropic damage model was used to capture the progression of ply cracks. Manufacturing-induced defects (e.g., micro-voids, resin-rich pockets, inter-ply resin-rich zones), and thermal residual stresses that result from cooldown of the manufactured material after curing were represented in the computational models. The effect of the ply constraints on local stress and displacements fields before and after the formation of ply cracks was also investigated by considering the constraining plies within the representative volume elements generated in this study. Micromechanical models with constrained 90° plies subjected to a thermal cooldown followed by a tensile load revealed that the local dilatation energy density in the matrix increased when compared to that in the unconstrained lamina, which promoted brittle cavitation at lower applied strains. Furthermore, the significance of capturing inelastic deformation of the matrix for predicting ply crack formation in cross-ply laminates was revealed. Although the formation of ply cracks was found to be governed by brittle cavitation and crack growth, which is consistent with the outcomes of previous studies, local inelastic deformation of the matrix indirectly influenced crack growth. Dissipation of

energy during the ply crack evolution process was obtained to approximate the corresponding effective energy release rate, and to provide a link between the local response of a laminate and the response at a higher length scale. The outcomes of this study can be incorporated within a multiscale framework to predict damage evolution in laminated composites. For example, a computationally measured strain energy release rate for ply cracking can be used to calibrate mesoscale or macroscale damage prediction models and be utilized within a synergistic damage mechanics multiscale framework to predict stiffness/strength reduction of a laminate.

Acknowledgements

The completion of this thesis would not have been possible without support of numerous individuals and organizations. The credit of this work goes to them. Foremost, I would like to express my deepest gratitude to Prof. John Montesano for providing me with the opportunity to study in the field of composite materials and his continuous encouragement, support, and guidance throughout the completion of this thesis. I wish to extend my gratitude to Prof. Ramesh Talreja for sharing his boundless wisdom and unconditional support during my PhD studies. Henceforward, I respected the alphabetical order to acknowledge the contribution of individuals.

I hereby to acknowledge examining committee members, Prof. Stephen Hallett from the University of Bristol, and Prof. Adil Al-Mayah, Prof. Cliff Butcher, Prof. Hamid Jahed, from University of Waterloo for their valuable feedback and providing insights.

Development of the current material model would not be possible without help of Prof. John Montesano and Prof. Clifford Butcher, who were also my teachers. Additionally, Dr. Zohreh Asaee, Dr. Farinaz Jeyranpourkhameneh, and Dr. Pedram Samadian, who patiently helped me through the development of the material model.

I would like to acknowledge the financial support from Natural Science and Engineering Research Council of Canada (NSERC), Ontario Graduate Scholarships (OGS), and University of Waterloo.

I am thankful for all the motivational and technical support of my friends and colleagues at University of Waterloo. I am grateful of my family for their unconditional love and support throughout my life. Finally, I would like to thank my wife Farinaz for being encouraging, supportive, and understanding in every respect. She is the reason why I could finish this journey.

Dedication

To my parents, my family, and especially my wife Farinaz.

Table Of Contents

List of Figures

List of Tables

Chapter 1

Introduction

1.1 Overview and Motivations

Motivated by lightweighting to economize fuel efficiency and reduce greenhouse gas emissions, industrial sectors, including aerospace, automotive, and marine, have continued to adopt composite materials. The high specific performance and tailorability of fiber-reinforced plastic (FRP) composites have led to their integration into primary load-bearing structures, which has attracted further interest in assessing their long-term durability and damage tolerance characteristics. Fuselage stiffened skin panels, wind turbine blades, and chassis components of automobiles are practical applications of FRP laminates, where the component experiences cyclic loading and progressive failure. For instance, the International Air Transport Association (IATA) has stated that approximately 42% of damage observed in composite structures is related to the mechanical performance of the material (e.g., fatigue failure) [1]. Thus, investigating the complex failure process of corresponding structures is necessary. Despite the fact that further analysis of the structures requires additional effort for the design, the extra cost will be compensated by reducing the enforced maintenance and repair costs (Fig. 1) [2].

Composite structures often comprise a lay-up of several unidirectional (UD) plies in the form of a multidirectional laminate. The damage evolution in FRP laminates under quasi-static or cyclic loading typically follow two sequential stages known as “sub-critical” and “critical.” Sub-critical cracking involves the formation of damage, such as ply cracks, prior to the onset of critical damage modes (i.e., delamination/fiber breakage), where the mechanical properties (i.e., stiffness) of the laminate gradually diminish without the loss of structural integrity. The initiation and evolution of sub-critical cracking is addressed by the field of “damage mechanics” [3]. In this phase, the formation of the first ply crack is followed by the multiplication of ply cracks or increase in ply crack density, and consequently, a reduction in the crack spacing (Fig. 2). Sub-critical ply cracking is followed by unstable growth of critical damage, such as delamination and fiber breakage, leading to laminate failure. The consequence of damage mechanics from a phenomenological perspective is often described by “stiffness degradation” or “strength degradation”, the relevance of which depends on the intended functional requirements of the structure. An aircraft wing and fuselage are typical examples of structures that respectively require a stiffness- and strength-based design approach [3].

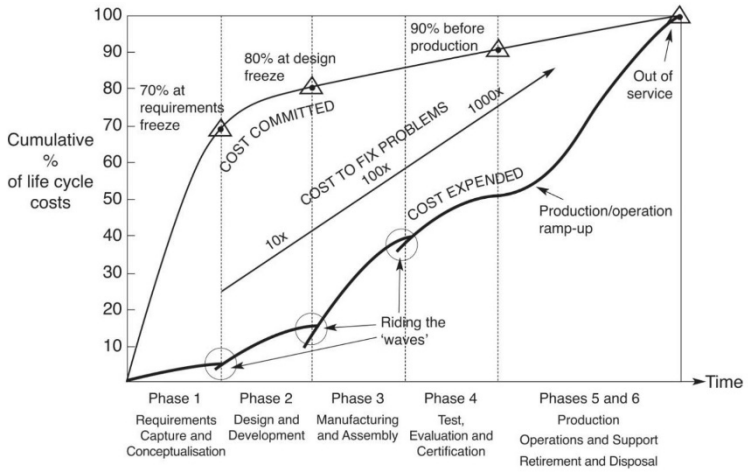

Figure 1. Schematic of an aircraft life cycle cost [2].

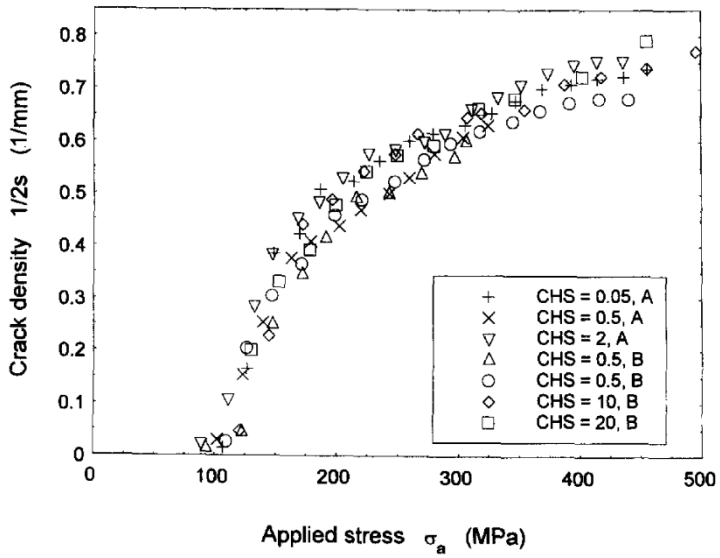

Figure 2. Ply crack density as a function of applied stress for a $[0/90]_s$ glass fiber/epoxy laminate [4].

During the ply crack formation and multiplication process in laminated composites, the interaction of different damage modes occurs at different length scales. According to the empirical microscopic observations, the region close to the fiber-matrix interface is the favourable location for local failure during the early stages of ply crack formation, where high stress concentration causes debonding or matrix cracking [5–11]. Although researchers agree on the presence and source of ductile failure in epoxies [5,6], debonding is related to either decohesion of the fiber-matrix interface [7] or matrix cracking-induced debonding (i.e., dilatation-induced failure) [6, 8–11]. The linkage of matrix microcracks forms full ply cracks that span the ply thickness, which is followed by sub-critical ply

crack multiplication enabled by ply constraints [12]. Figure 3a demonstrates the experimental observation of damage at different length scales and highlights the multiscale nature of failure in FRP laminates. The progression of damage in laminates may become further complicated by the presence of manufacturing-induced defects [13], thermal residual stress, or the interaction of damage modes. Additionally, the laminate stacking sequence, loading multiaxiality, and component geometrical attributes are other factors to be considered in an investigation.

Prediction of progressive failure and long-term durability of laminated composites demands a physical understanding of damage at different scales. Hierarchical multiscale models can capture damage mechanisms at lower length scales and predict the effect of damage on the response of the materials at higher scales [14,15]. This approach often utilizes the concept of a representative volume element by defining the microstructural entities and obtaining the properties at the corresponding scale (i.e., micro or meso). Hierarchical multiscale approaches are more computationally efficient than concurrent approaches and as such they are more widely used [14]. Figure 3b illustrates the framework of a hierarchical multiscale virtual testing approach for damage investigation of laminates.

Progressive failure of laminates involves interactions of damage modes at different length scales, which must be decoupled in a hierarchical multiscale modeling framework. To address the limitation with hierarchical multiscale models, Talreja [15] introduced a physics-based modelling strategy named “synergetic damage mechanics” (SDM) for predicting ply cracking in laminates, where the effect of damage at different scales was distinguished and loosely coupled. Singh and Talreja [16] later improved this model to account for the effect of ply constraints on ply crack multiplication, by determining the crack opening displacement (COD) using computational mesoscale mechanics. Nevertheless, the SDM approach, like other damage-based modeling approaches, often lack robustness as it was revealed in world-wide failure exercise III [17]. Recently, Montesano and Singh [18,19] extended the applicability of the SDM model in predicting material degradation of multidirectional laminates during the sub-critical cracking stage, where the interaction of ply cracks in different plies was captured. Although SDM has shown promising results for damage modelling of composites, incorporating the local phenomena of the material can further extend the capability of the model. Capturing the material microstructure, including manufacturing-induced defects and thermal residual stresses, can improve the calibration of damage parameters at higher length scales.

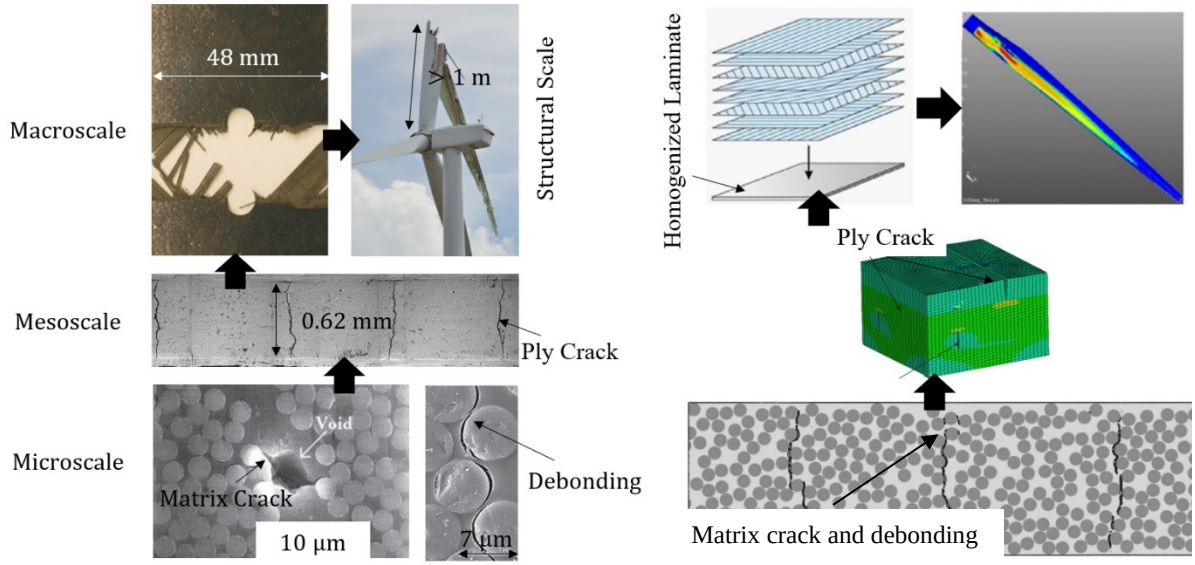

Figure 3. Damage evolution of composites at different length-scales: (a) experimental observation [20–23]; (b) numerical modelling [18,24].

1.2 Thesis Outline

The contents of this thesis are organized in the manuscript-based format and presented in 8 chapters. Chapter 2 presents a background and literature review on the damage mechanics and modelling approaches in FRP composite materials. It has been attempted to minimize the overlap between Chapter 2 and published manuscripts while maintaining the narrative integrity. The objectives and scope of the thesis are outlined in Chapter 3. The subsequent Chapters 4 to 7 include the published or submitted peer-reviewed papers that the candidate authored as the first or co-author and is responsible for developing, data curing, and analyzing the results. Chapters 4 to 7 have been slightly modified for harmonizing the thesis in a broader perspective. Conclusions and recommendations for future directions are provided in Chapter 8. The rest of the thesis comprises three appendices that have been used to present the development of the user-defined material subroutine that is referred to in Chapters 6 and 7. Note, a dedicated list of references has been provided for each chapter in this thesis.

The following published (submitted) peer-reviewed journal papers and book chapter have been used in this thesis:

- J. Montesano, **F. Sharifpour**, Modelling damage evolution in multidirectional laminates: micro to macro, in: W. Van Paepegem (Ed.), Multi-Scale Continuum Mechanics Modelling of

Fibre-Reinforced Polymer Composites, Woodhead Publishing Series in Composites Science and Engineering, 2021: pp. 463–507.

- G. Li, **F. Sharifpour**, A. Bahmani, J. Montesano, A new approach to rapidly generate random periodic representative volume elements for microstructural assessment of high volume fraction composites, Materials and Design 150 (2018) 124–138.
- **F. Sharifpour**, J. Montesano, R. Talreja, Assessing the effects of ply constraints on local stress states in cross-ply laminates containing manufacturing induced defects, Composite Part B: Engineering 199 (2020) 1–13.
- **F. Sharifpour**, J. Montesano, R. Talreja, Micromechanical assessment of local failure mechanisms and early-stage ply crack formation in cross-ply laminates, Composite Science and Technology (Under Review).
- **F. Sharifpour**, J. Montesano, Micromechanical simulation of ply crack formation in cross-ply laminates under quasi-static tensile loading, Composite Part A: Applied Science and Manufacturing (To be submitted in January 2022)

References

[1] IATA, Conclusions of the IATA Questionnaire on Composite Structure Maintenance, in: Montreal Canada IATA, 1991.

[2] G.D. Padfield, So You Want to Be an Engineer?: A Guide to a Wonderful, Mysterious Profession, Second Ed., Gareth D. Padfield, 2015.

[3] R. Talreja, C.V. Singh, Damage and Failure of Composite Materials, Cambridge University Press, 2012.

[4] J. Tong, F.J. Guild, S.L. Ogin, P.A. Smith, On matrix crack growth in quasi-isotropic laminates-I. Experimental investigation, Composite Science and Technology 57 (1997) 1527–1535.

[5] A.R. Melro, P.P. Camanho, F.M.A. Pires, S.T. Pinho, Micromechanical analysis of polymer composites reinforced by unidirectional fibres : Part II – Micromechanical analyses, International Journal of Solids and Structures 50 (2013) 1906–1915.

[6] L.E. Asp, L.A. Berglund, R. Talreja, A criterion for crack initiation in glassy polymers subjected to a composite-like stress state, Composite Science and Technology 56 (1996) 1291–1301.

[7] A.R. Melro, P.P. Camanho, F.M.A. Pires, S.T. Pinho, Micromechanical analysis of polymer composites reinforced by unidirectional fibres : Part I – Constitutive modelling, International Journal of Solids and Structures 50 (2013) 1897–1905.

[8] L.E. Asp, L.A. Berglund, P. Gudmundson, Effects of a composite-like stress state on the fracture of epoxies, Composite Science and Technology 53 (1995) 27–37.

[9] L.E. Asp, L.A. Berglund, R. Talreja, Prediction of matrix-initiated transverse failure in polymer composites, Composite Science and Technology 56 (1996) 1089–1097.

[10] L.E. Asp, L.A. Berglund, R. Talreja, Effects of fibre and interphase on matrix initiated transverse failure in polymer composites, Composite Science and Technology 56 (1996) 657–

665.

[11] F. París, M.L. Velasco, E. Correa, Modelling fibre–matrix interface debonding and matrix cracking in composite laminates, in: W. Van Paepegem (Ed.), Multi-Scale Continuum Mechanics Modelling of Fibre-Reinforced Polymer Composites, Woodhead Publishing Series in Composites Science and Engineering, 2021: pp. 243–274.

[12] J. Aveston, G.A. Cooper, A. Kelly, Single and multiple fracture: The properties of fiber composites. Conference Proceedings, National Physical Laboratory, Guildford, U.K., 1971: pp. 15–26. IPC Science and Technology Press, Ltd. Teddington, U.K.

[13] R. Talreja, Modelling defect severity for failure analysis of composites, in: W. Van Paepegem (Ed.), Multi-Scale Continuum Mechanics Modelling of Fibre-Reinforced Polymer Composites, Woodhead Publishing Series in Composites Science and Engineering, 2021: pp. 275–306.

[14] J. Montesano, F. Sharifpour, Modelling damage evolution in multidirectional laminates: micro to macro, in: W. Van Paepegem (Ed.), Multi-Scale Continuum Mechanics Modelling of Fibre-Reinforced Polymer Composites, Woodhead Publishing Series in Composites Science and Engineering, 2021: pp. 463–507.

[15] R. Talreja, A synergistic damage mechanics approach to durability of composite materials systems, in: Progress in Durability Analysis of Composite Systems, Eds. A. Cardon, H. Fukuda, K. Reifsnider, A.A. Balkema (Rotterdam), 1996: pp. 117–129.

[16] C.V. Singh, R. Talreja, Analysis of multiple off-axis ply cracks in composite laminates, International Journal of Solids and Structures 45 (2008) 4574–4589.

[17] A.S. Kaddour, M.J. Hinton, P.A. Smith, S. Li, A comparison between the predictive capability of matrix cracking, damage and failure criteria for fibre reinforced composite laminates: Part A of the third world-wide failure exercise, Journal of Composite Materials 47 (2013) 2749–2779.

[18] J. Montesano, C.V. Singh, A synergistic damage mechanics based multiscale model for composite laminates subjected to multiaxial strains, Mechanics of Materials 83 (2015) 72–89.

[19] J. Montesano, C.V. Singh, Predicting evolution of ply cracks in composite laminates subjected to biaxial loading, Composites Part B: Engineering 75 (2015) 264–273.

[20] C.A. Wood, W.L. Bradley, Determination of the effect of seawater on the interfacial strength of an interlayer E-glass/ graphite/epoxy composite by in situ observation of transverse cracking in an environmental SEM, Composite Science and Technology 57 (1997) 1033–1043.

[21] V.S. Romanov, S. V. Lomov, I. Verpoest, L. Gorbatikh, Modelling evidence of stress concentration mitigation at the micro-scale in polymer composites by the addition of carbon nanotubes, Carbon N. Y. 82 (2015) 184–194.

[22] D.T.G. Katerelos, J. Varna, C. Galiotis, Energy criterion for modelling damage evolution in cross-ply composite laminates, Composite Science and Technology 68 (2008) 2318–2324.

[23] P.P. Camanho, P. Maimí, C.G. Dávila, Prediction of size effects in notched laminates using continuum damage mechanics, Composite Science and Technology 67 (2007) 2715–2727.

[24] A. Arteiro, G. Catalanotti, A.R. Melro, P. Linde, P.P. Camanho, Micro-mechanical analysis of the in-situ effect in polymer composite laminates, Composite Structures 116 (2014) 827–840.

Chapter 2

Background and Literature Review

2.1 Mechanics of Unidirectional Composites

Unidirectional (UD) fiber-reinforced plastic (FRP) composites typically consist of two distinct phases, including aligned continuous fibers (e.g., glass, carbon, and aramid) and a polymeric matrix (i.e., thermoset or thermoplastic). The former constituent controls the strength and stiffness of a composite, while the latter bounds the constituents and transfers load to the fibers via fiber-matrix interfaces. Owing to their microstructure, UD composites exhibit high strength and stiffness in the longitudinal direction and reduced mechanical properties along the transverse direction. The reduced performance of UD composites in the transverse direction can be remedied by combining perpendicular or off-axis UD FRP plies in the form of multidirectional laminates (Fig. 4).

The existence of manufacturing-induced defects can significantly influence the mechanical behaviour of FRP composite materials, where the fabrication process is often dictated by the matrix type and the geometry of the structure. Common processes for fabricating laminated composites include hot pressing, autoclave-based curing, resin infusion processes such as resin transfer molding (RTM) or vacuum-assisted RTM, and liquid compression molding (LCM). Each process has certain characteristics that may lead to formation of defects depending on the chosen processing parameters, which may manifest at different length scales. Typically, thermosetting polymers have been preferred over thermoplastics for structural applications due to their molecular stability and the availability of several processing methods. Thermosets achieve their improved thermomechanical properties by a high degree of cross-linking during curing, which gives isotropic properties to the polymer due to its (amorphous) structure. Notwithstanding, thermoplastics have attracted attention for their relatively quicker processing and finding an answer for recycling composite materials.

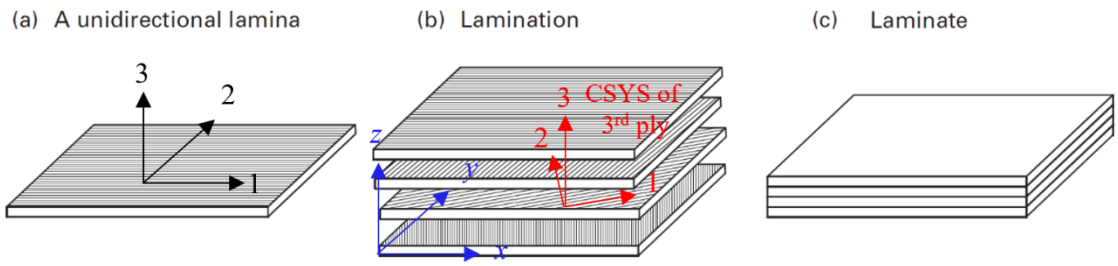

Figure 4. Schematic process of lamination in unidirectional fiber-reinforced plastics [3].

By treating laminated composite materials as continuum bodies, the effective properties can be determined from the properties of the constituents, the material microstructure, and laminate stacking sequence. In this section, the fundamental aspects of UD composite laminates are briefly reviewed, where further details can be found in [1,2]. The elastic constitutive relations of an anisotropic material are defined as:

$$\sigma_{ij} = C_{ijkl}\varepsilon_{kl} \tag{2-1}$$

where σ_{ij}, ε_{ij}, and C_{ijkl} are Cauchy stress, linear (small deformation) strain, and fourth-order stiffness tensors, respectively. Although nine independent constants are required to define the stiffness tensor of orthogonal materials, only five constants are needed for a typical UD ply (e.g., carbon/glass FRP) that are transversely isotropic (see Fig. 4). Elastic constitutive relations for the represented UD lamina in Fig. 4 with isotropic behaviour in 23–plane can be expressed in reduced Voigt notation as:

$$\begin{Bmatrix}\sigma_1\\ \sigma_2\\ \sigma_3\\ \sigma_4\\ \sigma_5\\ \sigma_6\end{Bmatrix} = \begin{bmatrix} \frac{1-\nu_{23}\nu_{32}}{E_2^2\Delta} & \frac{\nu_{21}(1+\nu_{23})}{E_2^2\Delta} & \frac{\nu_{21}(1+\nu_{32})}{E_2^2\Delta} & 0 & 0 & 0 \\ & \frac{1-\nu_{12}\nu_{21}}{E_1E_2\Delta} & \frac{\nu_{32}+\nu_{12}\nu_{21}}{E_1E_2\Delta} & 0 & 0 & 0 \\ & & \frac{1-\nu_{12}\nu_{21}}{E_1E_2\Delta} & 0 & 0 & 0 \\ & & & G_{23} & 0 & 0 \\ & \textit{Sym.} & & & G_{12} & 0 \\ & & & & & G_{12} \end{bmatrix} \begin{Bmatrix}\varepsilon_1\\ \varepsilon_2\\ \varepsilon_3\\ \varepsilon_4\\ \varepsilon_5\\ \varepsilon_6\end{Bmatrix} \tag{2-2}$$

where

$$\Delta = \frac{\left(1-\nu_{23}\nu_{32}-2\nu_{12}\nu_{21}\left(1+\nu_{32}\right)\right)}{E_1E_2^2} \tag{2-3}$$

Here, 1, 2, and 3 respectively refer to the fiber direction, in-plane transverse direction, and out-of-plane transverse in the local coordinate system (see Fig. 4). Also, *E*, *G*, and *v* represent Young's modulus, shear modulus, and Poisson's ratio in the corresponding direction, respectively.

Mechanical properties of UD plies can be related to constituents' properties by using analytical and semi-empirical micromechanics models. Since the accuracy of proposed models depends on the selected material system, the reader is referred to [4] in-depth derivation of expressions. Assuming a one-dimensional stress state for the constituents, the rule of mixture expression for longitudinal modulus, E_1, is defined by:

$$E_1 = E_f V_f + E_m V_m \tag{2-4}$$

and as a result of overall contraction in 2–direction, the major Poisson's ratio is defined as:

$$\nu_{12} = \nu_{12,f} V_f + \nu_m V_m \tag{2-5}$$

Here, V represent volume fraction and subscripts f and m denote the corresponding properties for the fiber and matrix. Minor Poisson's ratio can be obtained by using the reciprocal relationship (i.e., $\nu_{12} = \nu_{21} E_1/E_2$). Semi-empirical relation by Halpin and Tsai [5] and Halpin and Kardos [6] are proposed for other in-plane properties as:

$$\frac{p}{p_m} = \frac{1 + \xi \eta V_f}{1 - \eta V_f} \tag{2-6}$$

$$\eta = \frac{\left(p_f / p_m\right) - 1}{\left(p_f / p_m\right) + \xi} \tag{2-7}$$

Here p indicates E_2 or G_{12}, and p_f and p_m are the corresponding moduli for fiber and matrix. Also, ξ is the fitting parameter that needs to be determined by experimental data. Finally, out-of-plane properties can be obtained by using the Chamis micromechanical model [7] and elasticity relation as:

$$G_{23} = \frac{G_m}{1 - \sqrt{V_f}\left(1 - G_m / G_{23,f}\right)} \tag{2-8}$$

$$\nu_{23} = \frac{E_{22}}{2G_{23}} - 1 \tag{2-9}$$

2.2 Damage in FRP Composite Materials

Damage in composite materials refers to an irreversible change under applied thermomechanical loading that is connected with energy dissipation. The intralaminar cracking, local interlaminar (delamination) cracks, and fiber-matrix debonding crack are examples of damage in composites at different length scales (Fig. 5). In general, failure of FRP laminates and associated structures comprises complex evolving damage processes that are dependent on many parameters, including the component geometry, loading conditions (e.g., quasi-static, dynamic, cyclic), ambient environment (e.g., temperature, humidity, UV exposure), material composition (i.e., laminate stacking sequence, ply orientation and thickness, ply properties, constituent properties, fiber volume fraction, fiber architecture), as well as the interaction between the constituents (i.e., fiber-matrix interface) [8]. Although the contribution of some factors has been addressed, understanding the mechanics of damage

in composite materials is an ongoing topic. In the following Sections, various cracking processes of UD FRP composite materials are introduced, which are collectively referred to as “damage mechanisms.”

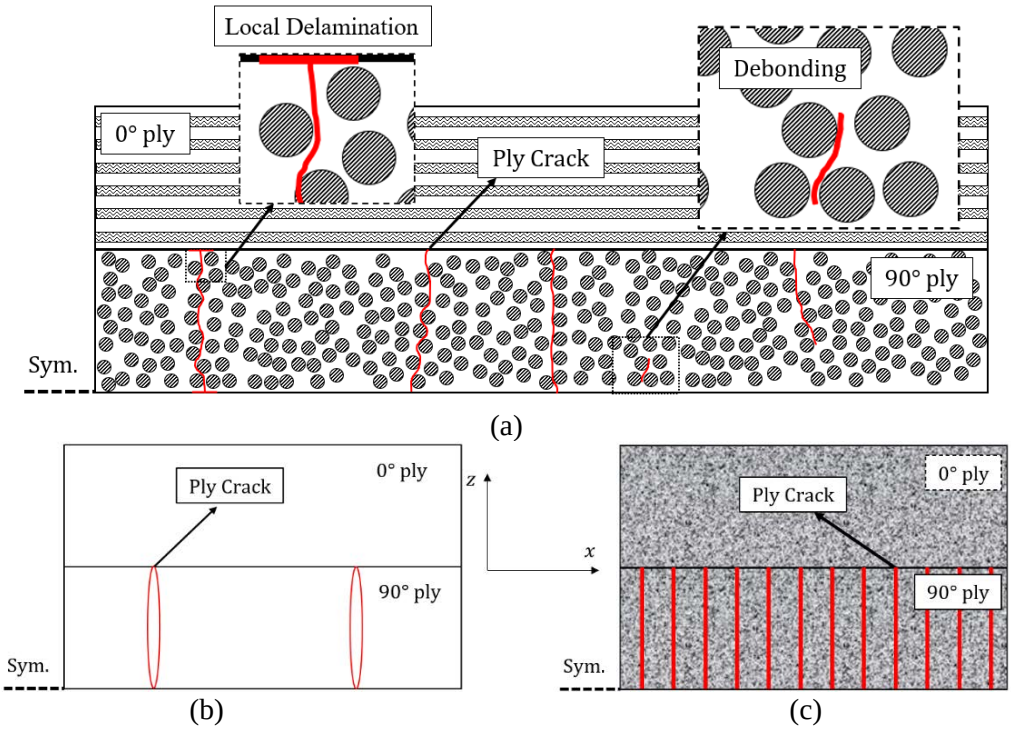

Figure 5. Schematic representation of damage in a cross-ply laminate at: (a) microscale; (b) mesoscale; (c) macroscale.

2.2.1 Damage modes

Damage in composite laminate subjected to tensile loading typically begins with the formation of ply cracks in the off-axis plies. These cracks often originate in the areas that contain manufacturing-induced defects (e.g., voids, fiber cluster and resin-rich zones, or fiber/matrix imperfect bonding) and quickly span the thickness and width, known as tunnelling, of the layer. Subsequently, irregular distribution of ply cracks during the multiplication stage gradually diminishes with decreasing crack spacing, while the laminate stiffness degrades with the formation of each ply crack. Afterwards, the ply cracks reach a “saturation point”, where there is no available space for the formation of an extra crack due to the inability of constraining plies to support enforced stresses by creation of a new ply crack. The termination of ply crack formation, also known as “characteristic damage state” (CDS), is followed by the formation of local delamination at the tip of existing cracks. Finally, the connection of these

delamination cracks causes the creation of large-scale delamination cracks and subsequently fiber breakage, where the material loses its integrity. Figure 6 illustrates a schematic evolution of damage in a cross-ply laminate.

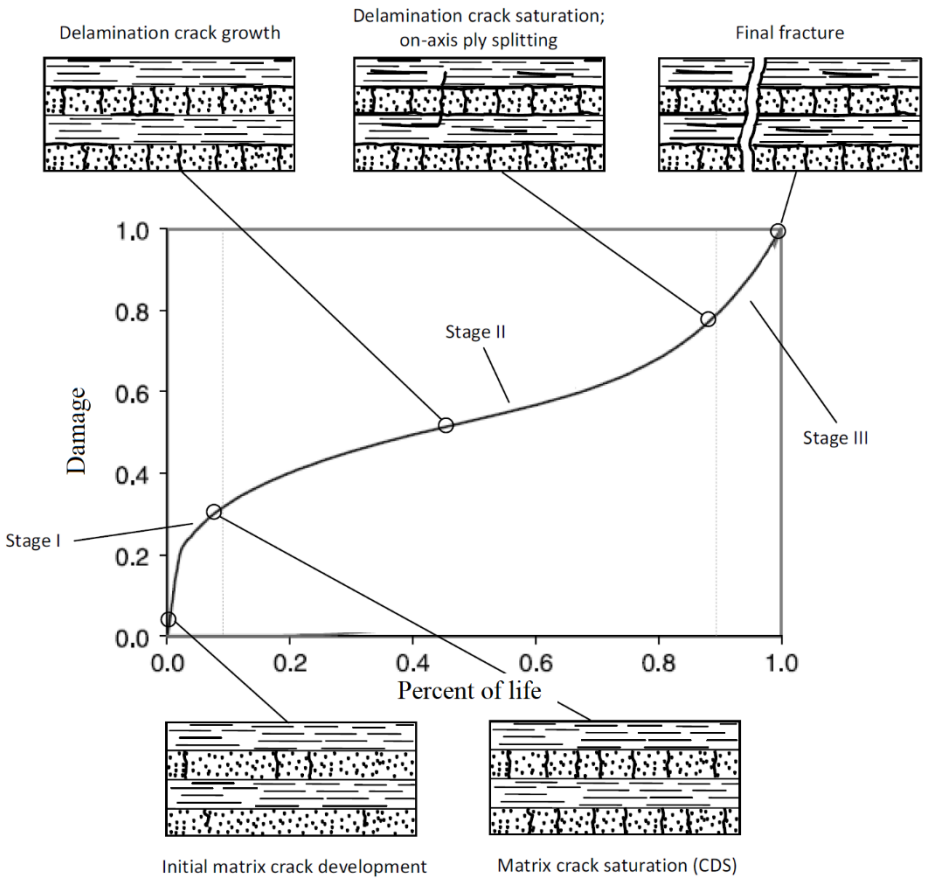

Figure 6. Schematic damage evolution of a cross-ply laminate [9].

In damage mechanics of composites, the formation of crack before the CDS is referred to as “sub-critical cracking,” and the unstable crack initiation after this point is deemed “critical cracking.” The sub-critical stage follows three phases of crack initiation, multiplication, and a gradual increase in crack density until the saturation point. Understanding sub-critical cracking is crucial for structures subjected to cyclic loads for two important reasons. First, ply cracks can provoke the initiation of critical cracks due to the interaction of off-axis cracks, local delamination cracks, and stress redistribution to the main load-bearing plies. Second, sub-critical cracking results in a progressive degradation of laminates which can impact the intended function of the structure [10].

For the case when longitudinal compression stresses are dominant, the fibers in a lamina would tend to locally buckle once the matrix is no longer able to resist this deformation. Local shear stresses in the matrix tend to drive in-phase microbuckling while yielding of the matrix leads to the formation of a kink-band. The kink-band formation consists of fiber breakages along two inclined planes and possibly localized matrix cracking (see Fig. 7). It should be noted that the constraining plies also influence kink-band formation in a 0° lamina, as well as the ensuing local delamination cracks that may form subsequent to the kink-band, as shown in Fig. 7. If longitudinal tensile stresses are dominant, larger clusters of fiber breakages accompanied by local matrix cracks will form within the lamina, while the constraining plies may restrict immediate laminate failure. Typically, kink-band formation and fiber breakage clusters in the primary load-bearing plies lead to complete laminate failure and, as such, are classified as critical damage modes.

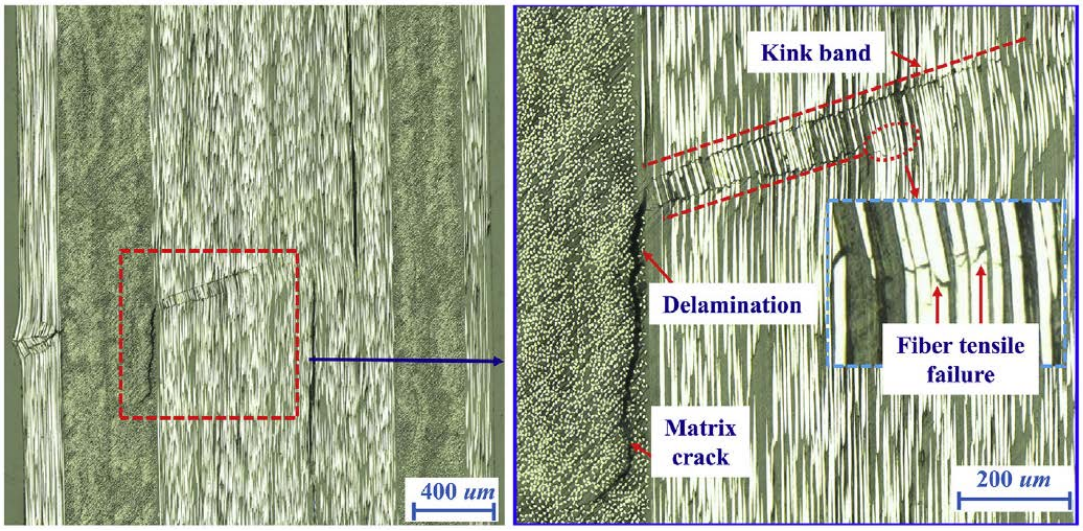

Figure 7. Kink-band formation for a constrained 0° lamina in a cross-ply laminate subjected to compressive stresses along the lamina fiber axis, with ensuing delamination [11].

2.2.2 Multiscale nature of damage formation

Damage mechanisms and progressive failure of composite materials inherently occur at multiple length scales (Fig. 5), where the linkage of failure at lower scales results in damage formation at higher scales. Fundamentally, the onset of damage in laminated composites can be associated with the internal local stress fields and can be further influenced by the existence of manufacturing-induced defects as well as geometrical features in the structure. For the assessment of damage evolution in FRP laminates, cracks are investigated from the scale of fiber and matrix material constituents up to the laminate and are

typically categorized in three length scales: micro, meso, and macro. The following subsections provide a brief overview of the different damage mechanisms observed in FRP laminates at each length scale and the evolution of these mechanisms under specific loading conditions of interest.

2.2.2.1 Microscale

Microscale damage or microdamage refers to the development of cracks in the constituents (i.e., fiber breakage or localized matrix cracking) or at the fiber-matrix interface (i.e., interfacial debonding). It is well established that these cracks interact to form complex localized fracture processes at the microscale, where fiber-matrix interfacial debonding cracks often become prevalent. Fiber-matrix debonds may originate from internal manufacturing-induced defects, including regions with poor fiber/resin wettability or at voids in the vicinity of fibers, the severity of which is process-dependent [12]. Additionally, debonding may initiate due to weak fiber-matrix bonding, which is strongly dependent on the fiber sizing. The generation of thermal stresses during cooldown after processing may be the cause of debond formation. However, provided that a strong bond exists between the fiber and matrix and that there are no manufacturing defects, debonds result from thermomechanical loading.

If the dominant stress field within a lamina is perpendicular to the fiber axes, debonds may form as a result of high local stress concentrations at the fiber-matrix interface. In this scenario, matrix cracks may also stem from debonds following a period of debond crack growth around a fiber (see Fig. 8a). The initiation of a matrix crack may precede a debond, either near a fiber or from a defect such as voids, causing a debond to form subsequently (see Fig. 8b).

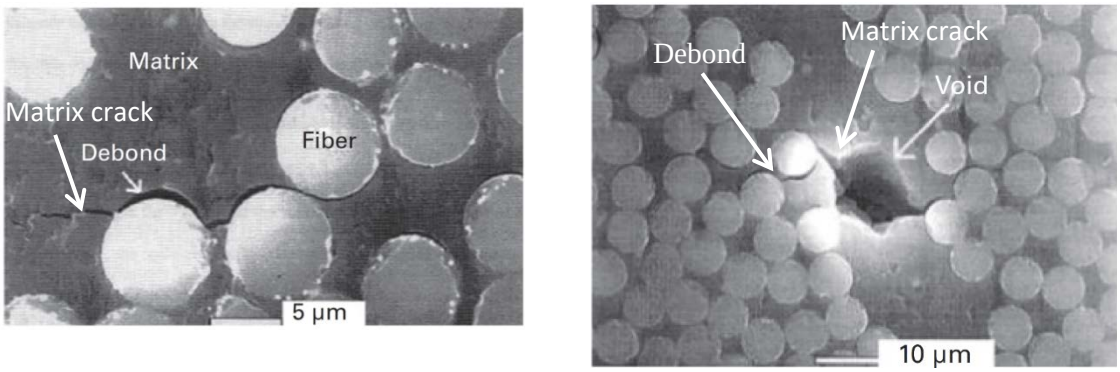

(a) (b)

Figure 8. Matrix crack initiation in a fiber-reinforced composite stemming from: (a) fiber-matrix interface debond; (b) void [26].

2.2.2.2 Mesoscale

From the perspective of a laminate, damage observed at the mesoscale is concerned with intralaminar damage, which consists of a coalescence of microscopic cracks (e.g., local matrix cracks, fiber-matrix debonds) leading to a ply crack spanning the lamina thickness. Ply cracks are the most widely studied damage mechanisms in laminates due to their notable influence on laminate mechanical property degradation, particularly for cyclic loading [13–25]. Ply cracks form under quasi-static, cyclic or thermal loading if transverse stresses are dominant since the lamina is weakest along the transverse direction. Ply cracks develop by the coalescence or linking of fiber-matrix debonds and localized matrix cracks (see Fig. 9a). This rapid microcrack linking process eventually leads to fully developed ply cracks spanning the thickness of the lamina (see Fig. 9b), where the adjacent constraining laminae act as crack arresting sites. Under quasi-static loading, ply cracks tend to propagate or tunnel rapidly along the lamina fiber axis (see Fig. 9c), while under cyclic loading, crack tunnelling is a more gradual process [27]. The constraining effect from adjacent lamina typically promotes the multiplication of ply cracks within a lamina as loading progresses [28]. Initially, multiplying ply cracks form independently from one another within the lamina, initiating an increase in the crack density or proportionally a decrease in crack spacing with a corresponding reduction in the laminate stiffness. As the ply crack spacing further decreases, the growth rate of crack density gradually diminishes due to the interaction of local stress fields of neighbour cracks which is known as “crack shielding” [28,29], as shown in Fig. 9d, until a ply crack saturation point is reached [13]. Ply crack multiplication can be further influenced by the existence of ply cracks in adjacent constraining layers, resulting in interlaminar ply crack interactions [30].

2.2.2.3 Macroscale

Damage at the macroscale is concerned with interlaminar cracking (i.e., delamination) and ultimately failure of the laminate. Although critical delamination cracks propagate “between” laminae, they are considered here as macroscale damage modes since they typically cause laminate failure. Delamination cracks initiate as a result of sufficiently large interlaminar stress fields and often stem from other intralaminar damage modes, including ply cracks (see Fig. 9) or local kink-band formation (see Fig. 7). The existence of a delamination crack effectively reduces the local constraining effect between the adjacent lamina, which tends to encourage critical intralaminar damage modes such as large fiber cluster breakages to occur sooner. Once the main load-bearing laminae exhibit critical intralaminar damage, this ultimately leads to complete laminate failure (and possibly catastrophic failure of a

component or structure). The resulting laminate failure surfaces are typically complex and comprised of multiple damage mechanisms, which depends on the type and direction of local stresses. Figure 10 reveals that in a cross-ply laminate, a delamination crack can span from the tip of a 90° ply crack, subsequently leading to fiber breakage in the adjacent lamina near the ply crack.

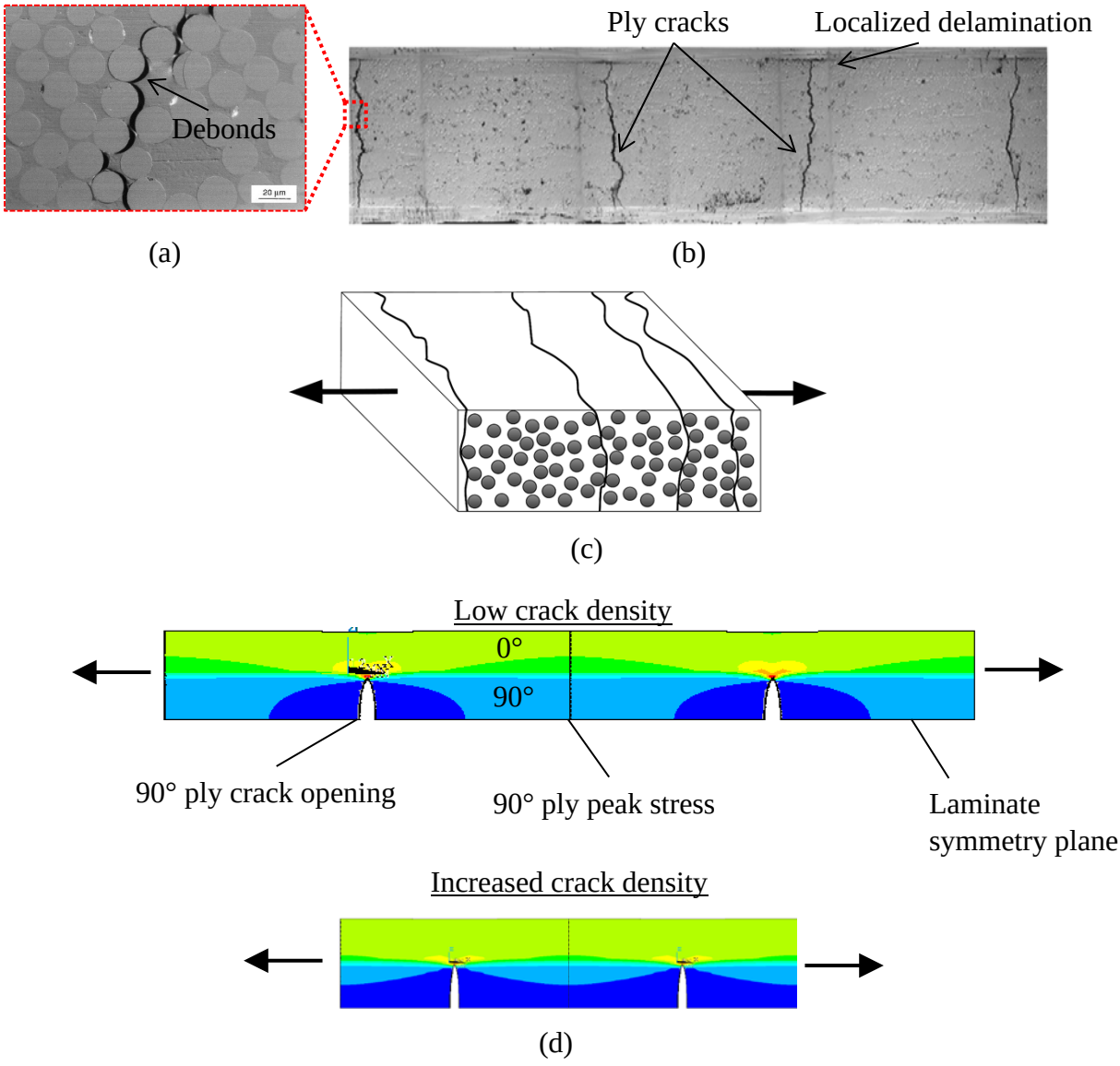

Figure 9. Sub-critical ply crack formation in the 90° lamina of a cross-ply laminate under tensile stress: (a) local coalescence of fiber-matrix debonds and localized matrix cracks [31]; (b) development of multiple ply cracks [32]; (c) schematic representation of multiple ply cracks in a constrained UD ply tunnelling along the fiber axis; (d) stress contours around interacting ply cracks (crack shielding effect).

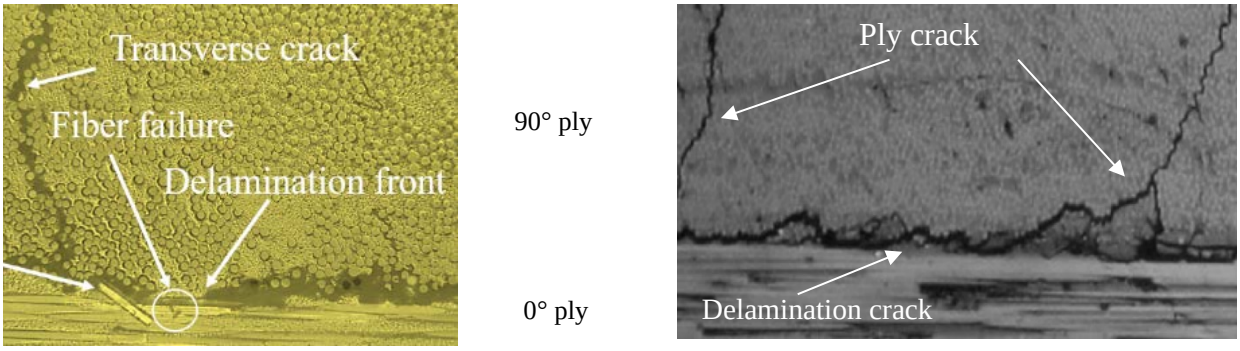

(a) (b)

Figure 10. Interaction of damage modes for cross-ply laminates subjected to uniaxial tensile loading: (a) fiber-reinforced thermoplastic- and (b) fiber-reinforced thermoset [3].

2.2.3 Ply constraining effect

Damage mechanisms at all length scales in a laminate are impacted by ply constraints, particularly ply crack formation. The effect of ply constraints sources from the difference between the surface displacement of a ply crack embedded in a laminate compared to an unconstrained UD ply. In other words, the neighbouring plies provoke a constraining effect which plays an important role in determining the effective properties of the cracked laminate while it may restrict immediate laminate failure. Experimental [33] and numerical [28,34] investigations demonstrated the evident impact of ply constraining effects on the crack multiplication. Fundamentally, the constraining effect may be observed during the formation of individual ply cracks that can provide an insight into the multiscale nature of damage in composite laminates.

2.2.4 Manufacturing-induced defects

The processing of composite materials is always combined with the presence of manufacturing-induced defects, while its severity depends on controlling the processing constraints. These defects can originate from the processing itself (e.g., cure shrinkage, consolidation, and resin bleeding) [35], suboptimal control of the manufacturing process (e.g., minor ply misalignment) [36], structural features (e.g., tapers), or machining after curing [37,38]. For instance, minor deviation from the expected orientation or prepreg thickness in a laminate may provoke the stiffness/strength degradation of the laminate due to a weaker performance of constraining plies. The challenge of safe design cannot be solely addressed by a conservative design that potentially introduce unpredictability to the final product. This imposed overdesign opposes the primary benefits of composite materials that prevent using traditional methods of structural design using homogenized internal structure. Hence, it is essential to comprehend the

correlation between material response and the internal structure of composites that requires the characterization of manufacturing-induced defects.

2.3 Damage Mode-Based Failure Criteria

Preliminary efforts to predict the failure of composite laminates were established based on the formation of the first observed intralaminar damage mode [39]. Hashin [40,41] and Puck and Schürmann [42,43] were the pioneer groups who separated matrix- and fiber-dominated failure modes based on the loading (i.e., tension, compression, shear). Accordingly, different 2D models were proposed to offer improved accuracy. Hinton, Soden, Kaddour, and colleagues [39,44–46] invited several groups to benchmark their models with experimental tests as the first world-wide failure exercise (WWFE-I). In the first exercise, the phenomenological-based model by Puck and Schürmann [42,43] was found as the most comprehensive model. However, the proposed models in WWFE-I were unable to account for triaxial failure under 3D stress and progressive damage of laminates [47]. Accordingly, the fidelity of failure criteria under the 3D stress state was assessed as the WWFE-II [44,45] to extend the capability of the theories from 2D to 3D stress states. This issue is commonly induced in the thick composite materials (e.g., pressure vessels and rotor blades). In this exercise, presented physical-based criteria [48–51] were chosen as reliable models in different loading conditions. Developed models also considered the nonlinear material response, which is originated from the behaviour of the epoxy.

WWFE-III [46] was undertaken to evaluate the ability of damage models to accurately predict the progressive nature of failure (e.g., sub-critical cracking, delamination, material degradation) [52–55]. Although the capability of damage-based models and finite element (FE) were highlighted in capturing damage initiation, progression, and ultimate failure, the limited robustness of the models for different laminate stacking sequences and loading conditions was highlighted. The shortcomings of models were related to the over-simplification or neglecting factors such as size effect, thermal residual stress, material nonlinearity [46]. Furthermore, the restricted application of the experimentally calibrated damage parameters for certain cases was identified. In Section 2.4 – 2.6 that follow, reported works focused on modelling damage of laminates at each relevant length scale are discussed.

2.4 Macro-Damage Mechanics

2.4.1 Continuum damage mechanics

The concept of continuum damage mechanics (CDM) is credited to the pioneering work of Kachanov [56,57], where the formation of voids in metals subjected to creep loading was captured and the associated mechanical property degradation was predicted. Kachanov assumed that a material containing diffuse micro-damage can be represented as an effectively homogeneous material with reduced mechanical properties. A scalar damage parameter φ was defined to describe the loss of the material's integrity where $\varphi = 1$ and $\varphi = 0$ indicate the pristine and failure states, respectively. The damage variable was later redefined by Robotnov [58] as $\omega = 1 - \varphi$ to represent discontinuity as a function of net area reduction (see Fig. 11):

$$\omega = \frac{S_D}{S} = \frac{S - S^*}{S} \tag{2-10}$$

where S_D and S denote the damaged and undamaged cross-sectional area. Additionally, S_D can be defined as the net area of the damaged surface that excludes the discontinuities area (i.e., S^*). Accordingly, Robotnov introduced a new definition for the creep strain rate as:

$$\frac{d\varepsilon}{dt} = B\left(\frac{\sigma}{1-\omega}\right)^n \tag{2-11}$$

where B and n are material constants. Equation (2–11) solved the singularity issue at the failure point from Kachanov's model. Accordingly, the quantity in parenthesis from Eq. (2–11) is defined as the effective stress and denoted by $\tilde{\sigma}$. Thus, Hooke's law can be expressed as:

$$\sigma = \widetilde{E}\varepsilon, \qquad \widetilde{\sigma} = E\varepsilon \tag{2-12}$$

where ε and $\tilde{E}$ are the strain and effective Young's modulus. Thus, the damage parameter can be defined as:

$$\widetilde{\sigma} = \frac{\sigma}{1-\omega} = \frac{E}{\widetilde{E}}\sigma \rightarrow \omega = 1 - \frac{\widetilde{E}}{E} \tag{2-13}$$

This notion was later modified based on the strain equivalence principle [59,60]. There, second-order damage tensor was defined to characterize a brittle creep damage [61] and capture crack orientation [62]. Finally, a three-dimensional damage model led to a fourth-order tensor was introduced by Chaboche [63–65] to characterize the three-dimensional damage case. Further details of CDM theory are found in [66].

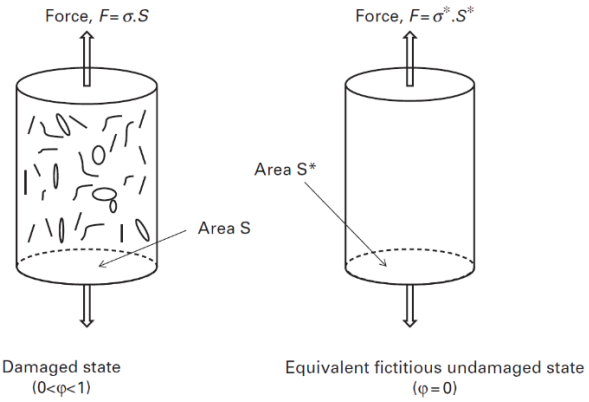

Figure 11. Schematic illustration of the effective stress concept for isotropic damage under uniaxial loading [3].

2.4.2 Continuum damage mechanics of composite materials

In Section 2.4.1, it was shown that CDM was developed based on the influence of damage entities on the net area, where the damage parameter is essentially a scalar. Therefore, CDM cannot distinguish from the influence of different entities on failure in the same plane; thus, this approach is unable to capture anisotropic damage effects. This is an important consideration in composite materials, where dissimilar damage entities with an identical net area may result in different mechanical responses. To alleviate the limitation of CDM and effectively apply the same concepts to composite materials, Laveveze [67] proposed CDM theory of laminate composites. To address the ply cracking in laminated composites, Talreja [17,68–71] proposed an alternative, where second-order damage tensors were defined to represent damage in a homogenized ply. Based on the proposed model, the representative volume element (RVE) size must be large to provide a consistent average response. Figure 12 illustrates the procedure of homogenization for a heterogeneous material, including damage entities. Here, $\vec{n}$ and $\vec{a}$ represent the orientation and influence information of a damage entity (i.e., induced perturbation caused by the presence of that point on the surface) [72]. Accordingly, damage tensor is defined by separating damage modes as:

$$D_{ij}^{(\alpha)} = \frac{1}{V}\sum_{k(\alpha)}\left(\int_S a_i n_j dS\right)_{k(\alpha)} \tag{2-14}$$

where α = 1, 2, …, n denotes the considered damage mode, and $k(\alpha)$ represents the number of entities of the corresponding damage mode.

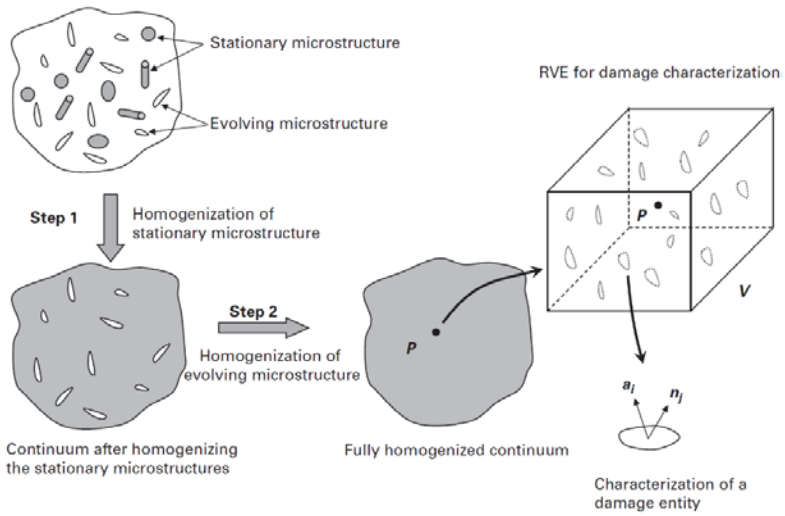

Figure 12. Homogenization of a continuum body with heterogeneous stationary structure and evolving damage entities [3].

Assuming symmetric crack surface separation, Talreja [17] proposed a new definition for the damage tensor by neglecting the tangential effect part of the influence vector as:

$$D_{ij}^{(\alpha)} = \frac{1}{V}\sum_{k(\alpha)}\left(\int_S a n_i n_j dS\right)_{k(\alpha)} \tag{2-15}$$

In other words, Talreja assumed that the driving force for ply crack multiplication is dominated by crack opening displacement (COD), i.e., Mode I. This model was further developed by Singh [73] to capture the effect of crack sliding displacement (CSD), i.e., Mode II. It was shown that neglecting CSD in the multiplication of ply cracks does not cause a significant error.

Singh and Talreja [74] developed a constitutive model that incorporated the second-order damage tensor for representing the stiffness degradation of a laminate using a thermodynamics framework. Accordingly, the components of the extensional stiffness matrix of the laminate shown in Fig. 13 was proposed as:

$$C_{ij} = \begin{bmatrix} \frac{E_x^0}{1-\nu_{xy}^0\nu_{yx}^0} & \frac{\nu_{xy}^0 E_x^0}{1-\nu_{xy}^0\nu_{yx}^0} & 0 \\ & \frac{E_y^0}{1-\nu_{xy}^0\nu_{yx}^0} & 0 \\ Sym. & & G_{xy}^0 \end{bmatrix} + \frac{\kappa t_c^2}{st}\begin{bmatrix} 2a_1 & a_4 & 0 \\ & a_2 & 0 \\ Sym. & & 2a_3 \end{bmatrix} \tag{2-16}$$

where ^{0} indicates the effective elastic properties of the pristine laminate, and κ is the ply constraints parameter. t_c, t, and s are geometrical attributes shown in Fig. 13. Here, C_{ij} is defined as the laminate's extensional stiffness matrix, [A]. Moreover, a_i are phenomenological material constants that need to be determined based on the properties of damaged laminate as:

$$a_1 = \frac{st}{\kappa t_c^2}\left[\frac{E_x}{1-\nu_{xy}\nu_{yx}} - \frac{E_x^0}{1-\nu_{xy}^0\nu_{yx}^0}\right], \qquad a_2 = \frac{st}{\kappa t_c^2}\left[\frac{E_y}{1-\nu_{xy}\nu_{yx}} - \frac{E_y^0}{1-\nu_{xy}^0\nu_{yx}^0}\right]$$
$$a_3 = \frac{st}{\kappa t_c^2}\left[G_{xy} - G_{xy}^0\right], \qquad a_4 = \frac{st}{\kappa t_c^2}\left[\frac{\nu_{xy}E_x}{1-\nu_{xy}\nu_{yx}} - \frac{\nu_{xy}^0E_x^0}{1-\nu_{xy}^0\nu_{yx}^0}\right] \tag{2-17}$$

The developed model only analyses symmetric and balanced laminates loaded in-plane; however, the model can be extended for other cases. The ply constraint parameter, κ, is the only unspecified parameter in this method that depends on the COD and crack density. This parameter can be obtained by comparing the laminate with a reference model to characterize the cracks displacement while capturing the effect of constraining parameters. It is indicated that the ply constraint parameter can be calculated using a computational method instead of experimental calibration. This procedure is discussed in Section 2.8.

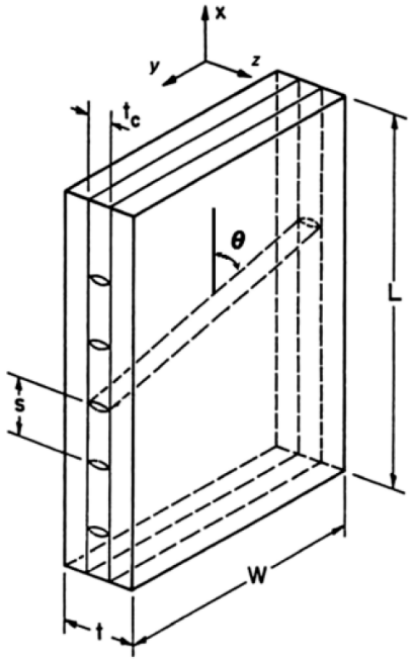

Figure 13. A representative volume element illustrating intralaminar cracking in a general off-axis ply of a FRP laminate [3].

2.5 Meso-Damage Mechanics

The effect of damage accumulation on the mechanical response of a continuum solid (i.e., laminate stiffness) at the ply level has been mainly investigated by meso-damage mechanics (MSDM). This approach concerns investigating damage at the scale of crack formation (i.e., ply crack), where the laminate plies are treated as effectively homogeneous. For composite materials, MSDM approaches are concerned with the multiplication of damage by incorporating micromechanics to find a solution for the local displacement and stress fields around ply cracks.

2.5.1 Shear lag models

Aveston, Cooper, and Kelly (ACK) [75] were the first to investigate the primary mechanism of crack multiplication by focusing on the transfer of shear stress between a small group of constituents. ACK found that constituents redistribute the applied stress in the multiplication process, which results in a nonlinear response. In spite of the novelty of the approach, the method was recognized as inadequate due to the excessive number of simplifying assumptions. The method was the foundation for shear lag models that was later improved by Garret, Bailey, and Parvizi [76–78] and Manders et al. [79] by adopting Cox [80] method for modelling ply cracking. Some of the simplifying assumptions in shear lag models are (Fig. 14):

1. The mutual interaction of cracks due to the shielding effect of cracks is disregarded.
2. Local stress concentration near cracks is neglected. Therefore, the axial stress assumed constant over the transverse ply thickness after cracking.
3. Under the axial shear stress, the shear stress is related to vertical displacement of the ply while the horizontal displacement is neglected. This violates linear elasticity relationship for shear stress.

Later, Highsmith and Reifsnider [13] argued the significance of local stresses near the plies interface, where the shear deformation is restricted to a thin resin-rich region. Based on their experimental observation, ply crack extends to this region that is less stiff than the central part of the transverse ply. Accordingly, the shear lag model was updated [13,81] by assuming that the shear stresses develop in the resin-rich region. This model was extended in different ways to considering the effect of crack interaction, accounting for the progressive shear in the transverse ply and the 2D shear lag model. Nairn and Hu [82] found the stress in the 0° and 90° ply for a general form of shear lag models based on the

preliminary model by Garret and Bailey [78]. However, complicated models, including more adjustable parameters, often lead to less persuasive results, which can be related to the one-dimensional nature of the shear lag models [3]. A comprehensive review of the advantages and disadvantages of the developed shear lag models has been presented in [83–85]. The modified versions of shear lag model have been developed in [86–88].

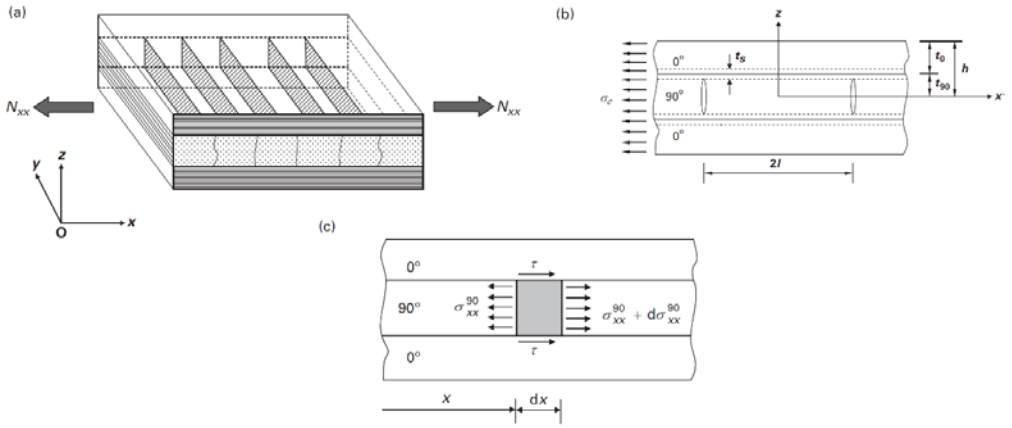

Figure 14. Construction of a unit cell for stress analysis of a cracked cross-ply laminate: (a) cracked laminate in tension; (b) equivalent 2D unit cell; (c) stress acting on an element of 90° ply [3].

2.5.2 Variational models

The variational models were initially introduced to determine perturbation stress/displacement fields around ply cracks in a cross-ply $[0/90]_s$ laminate [18]. Hashin [18] introduced a 2D stress analysis for the RVE in Fig. 15 by employing the principle of minimum complementary energy on cracked cross-ply laminates. Hashin's method was later modified for capturing the effect of thermal residual stress on the crack initiation in a cross-ply laminate [14,89] that had been stated as an important factor in the initiation of ply cracking [90]. Nairn [14] indicated that energy-based models conclude promising results for FRPs. However, a constant stress variation across the thickness limited the applications of the method to uniaxial loading. Varna and Berglund [89,91,92] introduced a new model to extend the application of the variational method by relaxing the constant axial stress field assumption. Kuriakose and Talreja [93] performed another study to analyze the capability of this method for a cross-ply laminate under bending moments. The most recent enhancement of the variational approach to accurately predict the exact or average stress/displacement triaxial, in-plane shear, and out-of-plane shear stress was conducted by Hajikazemi et al. [94–97]. Despite the variational methods obtained

promising results in different cases, models need to be redefined for new cases that limit the applicability of the method.

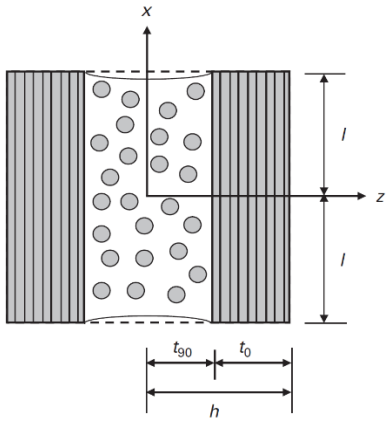

Figure 15. Representative unit cell for a cracked cross-ply laminate [3].

2.5.3 COD-based models

Crack opening displacement-based models have been developed to formulate the effect of crack opening and sliding displacements on the overall response of laminates. Gudmundson and colleagues [98–101] proposed a model to determine the influence of the crack surface displacement of an individual crack on the elastic response (i.e., stiffness degradation) and resultant strain (Fig. 16). Despite the fact that the stiffness of the cracked laminate was obtained by the homogenization procedure, determination of the calibrating parameters is a limiting factor in this method. In fact, heterogeneity of the laminates and ply constraining effects is an obstacle for finding a closed-form solution. Lundmark and Varna [102–105] developed a similar homogenization method that utilizes the finite element method (FEM) to capture the crack surface displacements. Thus, the average stress-strain response (i.e., stiffness degradation) of the laminate (ply) can be obtained, and the simplifying assumptions required in Gudmundson's model are reduced. The application of COD-based models has been further extended for capturing the effect of the residual stresses and thermal expansion coefficients [106–108].

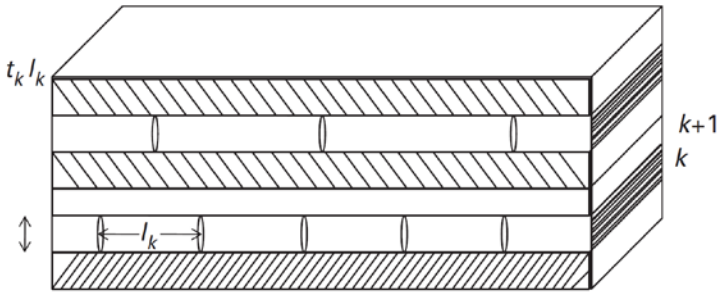

Figure 16. Schematic illustration of a 3D laminate containing off-axis cracks [3].

2.5.4 Limitation with MSDM models

In the previous subsections, MSDM models that are applicable for predicting ply crack evolution and the corresponding effect on laminates stiffness degradation were introduced. Some methods were deemed promising for capturing the local stress fields close to the ply cracks and predicting laminate stiffness degradation. However, the difficulty in developing a robust analytical model for general cases (e.g., a multidirectional laminate with arbitrary stacking sequence under multiaxial loading) is a limitation for this approach. Furthermore, MSDM merely considers one aspect of damage behaviour (i.e., crack multiplication), while other perspectives of damage (e.g., ply crack formation, inter- and intralaminar crack interaction) are disregarded. Damage analysis of cracked laminates, even in a simple lay-up, is intrinsically a highly complex task.

Laminates with unidirectional plies are commonly analyzed based on the presumption that plies are anisotropic and effectively homogenous. Nevertheless, damage formation (e.g., ply crack, local delamination) induces notable local stress gradients, requiring a 3D stress analysis. Mesoscale damage models are developed based on simplifying assumptions to capture the degradation of laminates during the multiplication of cracks. Ply cracks can be irregularly spaced, angled, not fully grown, while cracks can interact with other cracks (e.g., neighbouring crack, local delamination, fiber fracture). Thus, MSDM is deemed inadequate for modelling the crack multiplication as well as damage evolution in the presence of off-axis layers. Stress analysis may be further complicated by the presence of manufacturing-induced defects (e.g., void, nonuniform fiber spatial dispersion, fiber misalignment). Some common crack types in a laminate are demonstrated in Fig. 17 and Fig. 18.

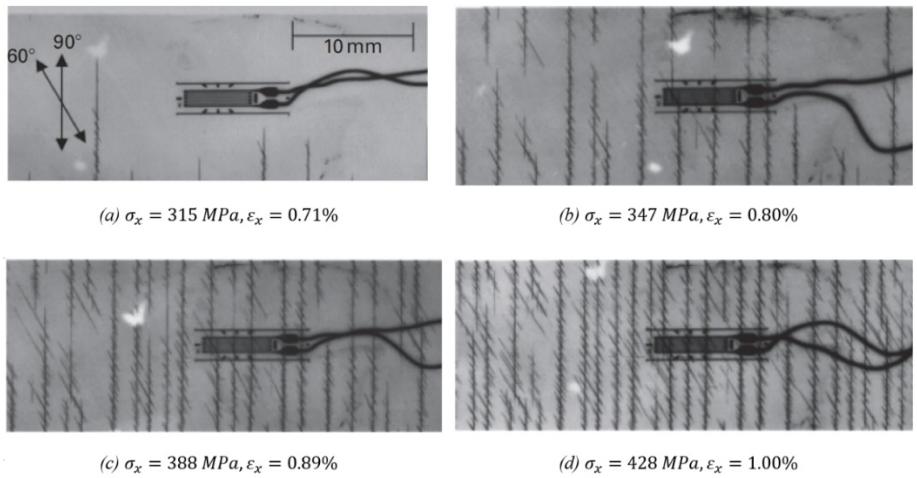

Figure 17. Consecutive matrix cracking behavior in contiguous plies in a $[0/60_2/90]_s$ laminate [109].

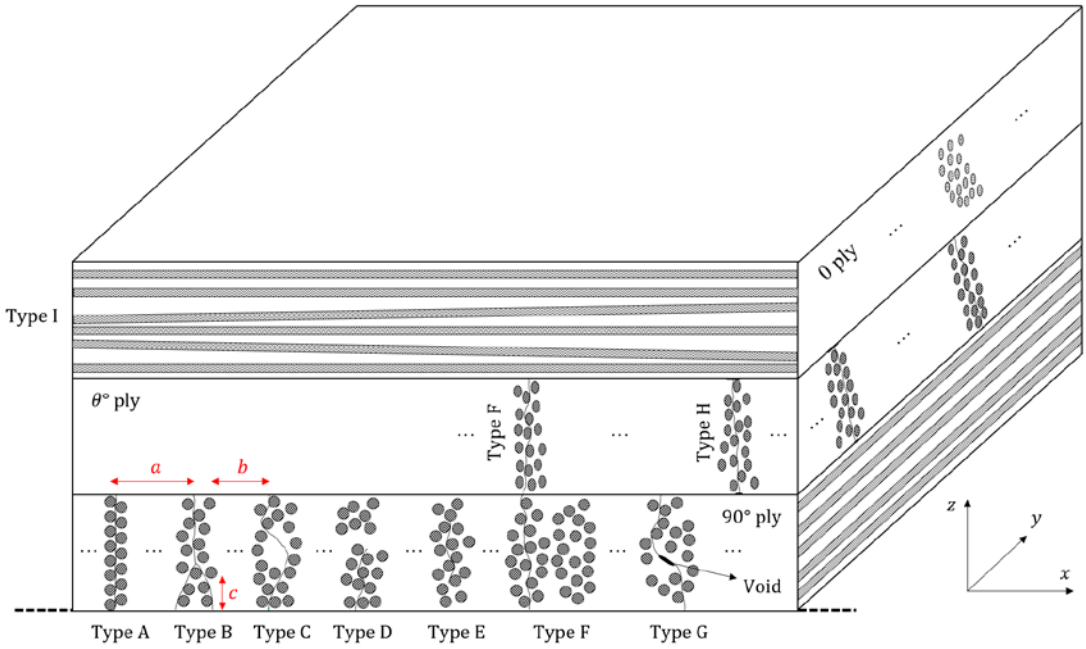

Figure 18. Schematic illustration of crack types in a $[0/\theta/90]_s$ laminate; Type A: ideal ply crack; Type B: branched crack; Type C: oblique crack; Type D: partial crack at ply surface; Type E: partial crack at center; Type F: interaction of cracks in different plies; Type G: void; Type H: interaction of damage modes (local delamination); Type I: fiber misalignment.

2.6 Micro-Damage Mechanics

Micro-damage mechanics aims to physically predict the onset of local failure at the fiber scale. The formation of ply cracks originates from the linkage of local failure of the matrix at the microscale. Local

failure manifests in the form of matrix failure (i.e., ductile failure or cavitation), fiber-matrix interfacial failure (i.e., debonding), and manufacturing-induced failure (e.g., void) [34,38,50,51,110–137]. Figure 19 illustrates a schematic representation of local failure that may or may not lead to the same form of a microcrack. Nevertheless, each local failure scenario requires different amounts of energy to be triggered, resulting in a dissimilar stress state during and after the formation of the crack. Hence, it is essential to properly account for the initiation of local failure to realize the formation of ply cracks, while experimental testing setup at the associated scale is required to capture the behaviour of the epoxy [138,139]. Note that local failure can be further influenced by the effect of ply constraints, thermal stress, and fiber spatial dispersion. In the following subsections, relevant models used to predict local failure and the formation of ply cracks are discussed.

2.6.1 Matrix failure

The formation of failure events in epoxies relates to nucleation (i.e., ductile failure) or dilatation-induced cavitation. Asp et al. [110–113] proposed the onset of the cavitation under triaxial stress states as a function of critical dilatational energy. Performing an experimental test, known as the poker-chip [138], a criterion was introduced for the onset of cavitation when dilatation energy density reaches its critical value (i.e., $U_{dil} = U_{dil}^{cr}$). Asp et al. [110] reported the critical dilatation of epoxies in the range of 0.13–0.20 MPa. Later, Pinho et al. [50,51] confirmed that brittle failure occurs before any substantial inelastic deformation. Cavitation-induced failure has been used to analyze the onset of local failure in epoxies [110–117].

Initial efforts in modelling the ductile failure of polymers were developed based on the incompressible behaviour of metals. However, the pressure-dependent behaviour of polymers was found essential for determining the stress states of epoxies during plastic deformations [124]. Although conventional pressure-dependent theories (e.g., Drucker-Prager) were found appropriate for analyzing ply cracking due to ease of use [117], complex stress state of material during matrix cracking suggest other material models are required. Furthermore, laminates subjected to multiaxial loading experience a higher degree of local shear stresses which requires an improved prediction of the matrix local behaviour. failure Details of local matrix failure is discussed in Chapter 6 and Chapter 7.

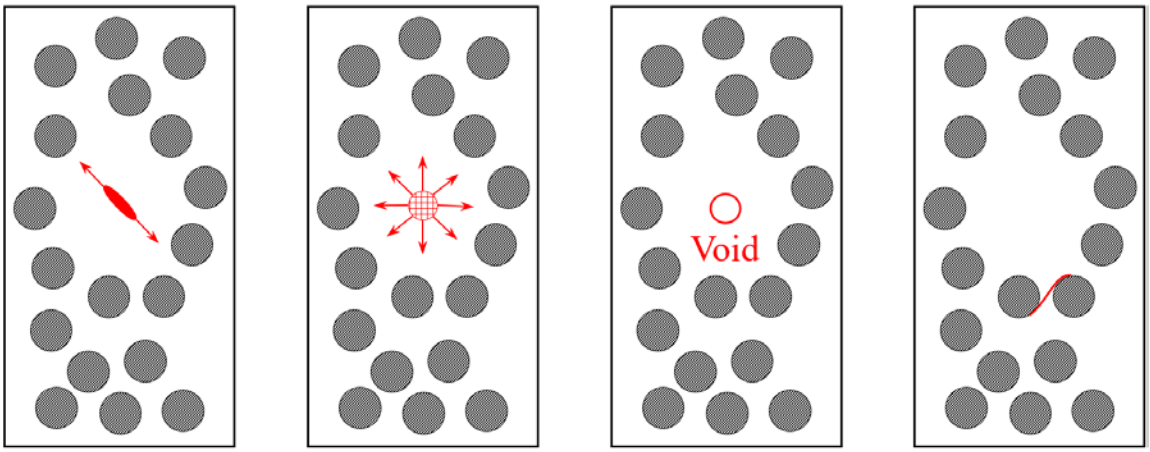

Figure 19. Schematic demonstration of matrix failure in different scenarios: (a) ductile failure, (b) cavitation, (c) void, (d) debonding.

2.6.2 Interfacial failure

According to the empirical observations, (the area close to) the fiber-matrix interfaces were witnessed as the favourable failure location due to a high stress concentration [122]. Several studies were performed to predict the debond crack initiation at the interface based on the fracture toughness [118–123] or cohesive zone modelling [125–131]. Notwithstanding, the existence of the cohesive zone is not evidenced due to the presence of the produced median layer between fibers and the matrix interfaces during fiber sizing. In other words, debonding is viewed as the consequence of matrix crack evolution [122]. Furthermore, it is challenging to calibrate the cohesive behaviour of a fiber-matrix interface through physical tests that is essential to define the traction-separation law parameters for a cohesive zone model [131]. Also, the constraining effects on the matrix imposed by the fibers vary with changing inter-fiber spacing, which would cause a deviation in the fiber-matrix interface cohesive parameters.

2.6.3 Manufacturing-induced defects

The unavoidable presence of manufacturing-induced defects (e.g., voids, nonuniform fiber spatial dispersion, fiber misalignment) is a factor to be considered in the damage evolution of laminates. Nevertheless, adequate modelling of composite materials requires information on processing (e.g., thermal mismatch, chemical shrinkage) and material characterization (i.e., defects) that is a daunting task. Several studies have been performed to characterize voids in composite materials [132], while the contribution of voids on the transverse failure initiation has been rarely investigated [133]. Hamidi et

al. [134] experimentally observed the majority of defects in a transverse layer present in a format of (micro- or macro-) voids. Hence, the local stress state in the vicinity of the void area can be significantly affected, which can cause an expedition or delay in the initiation of the matrix cracking. Correspondingly, Chowdhury et al. [135] investigated the effect of local voids on the initiation and growth of damage by performing a computational study on the microstructure level. These observations imply the potential influence of voids on the intensity of the constraining effect in transverse plies. Recently, Ghayoor et al. [136] investigated the effect of an inconsistent fiber dispersion that results in the resin-rich, and fiber clustered zones. The study clearly showed that nonuniform fiber spatial dispersion directly influences the mechanical response of the composite (i.e., failure and stiffness). Moreover, fiber distancing stated as a decisive factor for the initiation of failure [136,137].

2.7 Multiscale Damage Models

Progressive failure in composite materials is inherently a multiscale process, and the behaviour of the material at a smaller length scale impacts the response at higher scales. Therefore, multiscale modelling of FRP laminates is essential task to predict failure of laminates; however, considering models at different scales is challenging. In general, two multiscale damage modelling strategies have been proposed for FRP composites: hierarchical and concurrent. Hierarchical multiscale approaches often entail bottom-up linking of length scales, where relevant information is passed from lower to higher length scales. The hierarchical approach uses an intuitive multiscale representation of FRP laminates beginning with discrete fiber-matrix representation at the microscale to an effectively homogeneous representation at the macro or continuum scale. The obtained deformation response and corresponding damage state at a particular length scale are averaged over the volume of the RVE to portray the effectively homogenized medium and used as input for a higher length scale, thus “bridging” the scales in a decoupled fashion (i.e., no coupling between scales). Figure 20 illustrates the strategy of a typical uncoupled hierarchical multiscale approach. In this approach, analytical or computational micromechanical models are typically used in conjunction with homogenization theories by utilizing the volume-averaged stresses and strains in the defined RVE. The hierarchical approach was widely used for developing multiscale models to address damage in composite materials [140–150]. Although bottom-up approaches are generally used, utilizing a top-down approach is also viable [151–153].

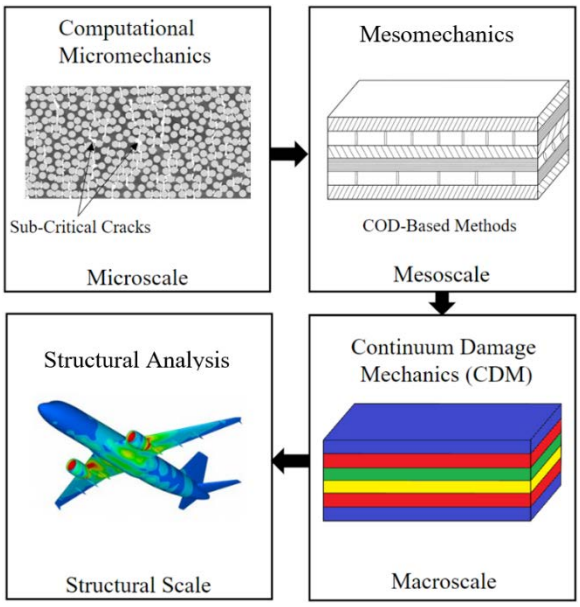

Figure 20. Schematic of a hierarchical bottom-up multiscale modeling approach.

Concurrent multiscale approaches also distinguish between the length scales relevant for damage evolution and analyze each in a fully coupled solution process. Instead of a top-down or bottom-up linking process, the damage state and material response at each length scale are considered simultaneously, while information is passed between length scales actively during the solution process [154]. Although concurrent approaches can improve the fidelity of damage evolution predictions due to their fully coupled nature, their complexity results in a computationally intensive analysis that is often not feasible. Therefore, locally probed regions at specific length scales are required to maintain reasonable computational efficiency; however, these are often limiting since the bulk material response may not be accurately captured. This approach has been employed by Ghosh et al. [140,141] for modelling damage evolution of composites.

Despite the fact that accurate prediction of damage evolution in thermo-mechanically loaded FRP laminates requires a fully coupled analysis due to the complex failure processes, a compromise must be made to adopt a multiscale modelling framework accuracy and computational efficiency. As a result, hierarchical approaches have been more widely employed since they are computationally less costly, while the upsurge of computational mechanics in recent years has further motivated the use of hierarchical multiscale approaches due to increased flexibility compared to analytical models. Talreja [155] indicated that utilizing a hierarchical approach may lead to physically adequate results for some cases, suggesting that the localized material architecture at any length scale can describe the behaviour

of the material at a higher scale. Hence, understanding the local stress fields and the initiation of damage at the microscale such as fiber-matrix debonding, branching of debonding cracks, or local matrix cracking becomes vital for assessing the performance of laminates with multiple ply cracks.

Several complexities are often confronted when conducting damage assessment using hierarchical approaches, despite the fact that they are perceived as being straightforward to implement. First, damage modes may evolve within more than one relevant length scale with the hierarchy of damage shifting. For example, sub-critical ply cracks locally initiate as debonds at the microscale where the fiber diameter is the relevant length scale, then fully forming through the lamina where its thickness becomes the relevant length scale. A hierarchical approach cannot address this point since the damage is represented as an uncoupled entity between different length scales. Furthermore, the multiplicity of a specific damage mode and the simultaneous evolution of different damage modes such as sub-critical ply cracks in multiple laminae are strongly dependent on the constraining effects from the adjacent lamina, where both intralaminar and interlaminar crack interactions occur. Again, the interaction of ply cracks at different length scales poses a problem for hierarchical approaches. In addition, the simultaneous occurrence of both intralaminar ply cracks and interlaminar damage (e.g., delamination) and their interactions would pose additional challenges for hierarchical approaches. Fundamentally, the occurrence of these phenomena discards the use of the averaging scheme for bridging micro-meso or meso-macro scales.

2.8 Multiscale Damage Modelling of Ply Cracking

Based on the preceding discussion, the three relevant length scales for FRP laminates generally include the micro, meso and macroscales. Nonetheless, a simple account for the hierarchy of length scales may not accurately represent the realistic multiscale damage evolution scenario in FRP laminates. Moreover, failure of laminates is a complex process involving a combination of different damage modes that are not necessarily occurring at fixed length scales, which also involves interactions between these damage modes within and across different length scales as well as multiplication of these damage modes. Therefore, a complete account of damage evolution in a simulation model must also consider these complex interactions as well as the coupling of information from one length scale to the next in a coherent fashion.

2.8.1 Representative volume element

One of the primary considerations for a multiscale modelling strategy is to define an appropriate representative volume element (RVE) for each relevant length scale. The size of an RVE should be appropriate for the length scale of interest and can in part be governed by the corresponding material geometric features (e.g., fiber size and architecture, lamina thickness and stacking sequence, etc.), allowing for an accurate representation of the material architecture. However, when the evolution of damage is of concern, the length scales in which the damage modes (e.g., fiber-matrix debonding, ply cracking, delamination) evolve as well as the characteristics of the damage modes (i.e., size, distribution and orientation) must be considered when defining the relevant length scales and the appropriate RVE size. Generally, an RVE for a given length scale must be large enough to observe the effects of "events" occurring at smaller dimensions (e.g., an RVE must include multiple damage entities). Regarding assessing sub-critical ply cracking in laminates, an RVE for microscopic assessment should typically include multiple fibers and the matrix in order to capture local damage modes such as fiber-matrix debonding and matrix cracking as well as the interactions between the neighbouring fibers (Fig. 21). Moreover, the size of an RVE for mesoscale assessment is governed by the laminae thicknesses and stacking sequence as well as the degree of ply cracking and the space between these cracks. At the macro or continuum scale, although ply cracks are not explicitly represented since the laminate is treated as an effectively homogeneous material, the RVE must be large enough to capture the distribution or density of ply cracking and their influence on the laminate response through internal variables.

2.8.2 Synergistic damage mechanics (SDM)

To overcome the inherent limitations of hierarchical approaches, while also maintaining computational efficiency, a new multiscale approach known as synergistic damage mechanics (SDM) was introduced [55]. In this approach, CDM and MSDM are coupled to predict sub-critical ply crack evolution in laminates, and the associated interaction between damage modes is considered in a closely (not fully) coupled multiscale modelling approach. The material microstructure (i.e., fibers and matrix) and sub-critical damage modes are respectively treated as stationary and evolving microstructures whereby a two-step homogenization is performed (Fig. 12) instead of single-step homogenization in conventional CDM approaches. The constraint parameter, κ, was initially related to COD within an experimental framework [156,157] to calibrate the CDM model. Utilizing the virtual crack closure technique (VCCT), Joffe et al. [158,159] measured the critical energy release rate (i.e., G_c) for the formation of a

new ply crack. Singh & Talreja [160] later used this method to find the constraint parameter for ply cracking within a computational framework. The overall strategy of SDM is illustrated in Fig. 22.

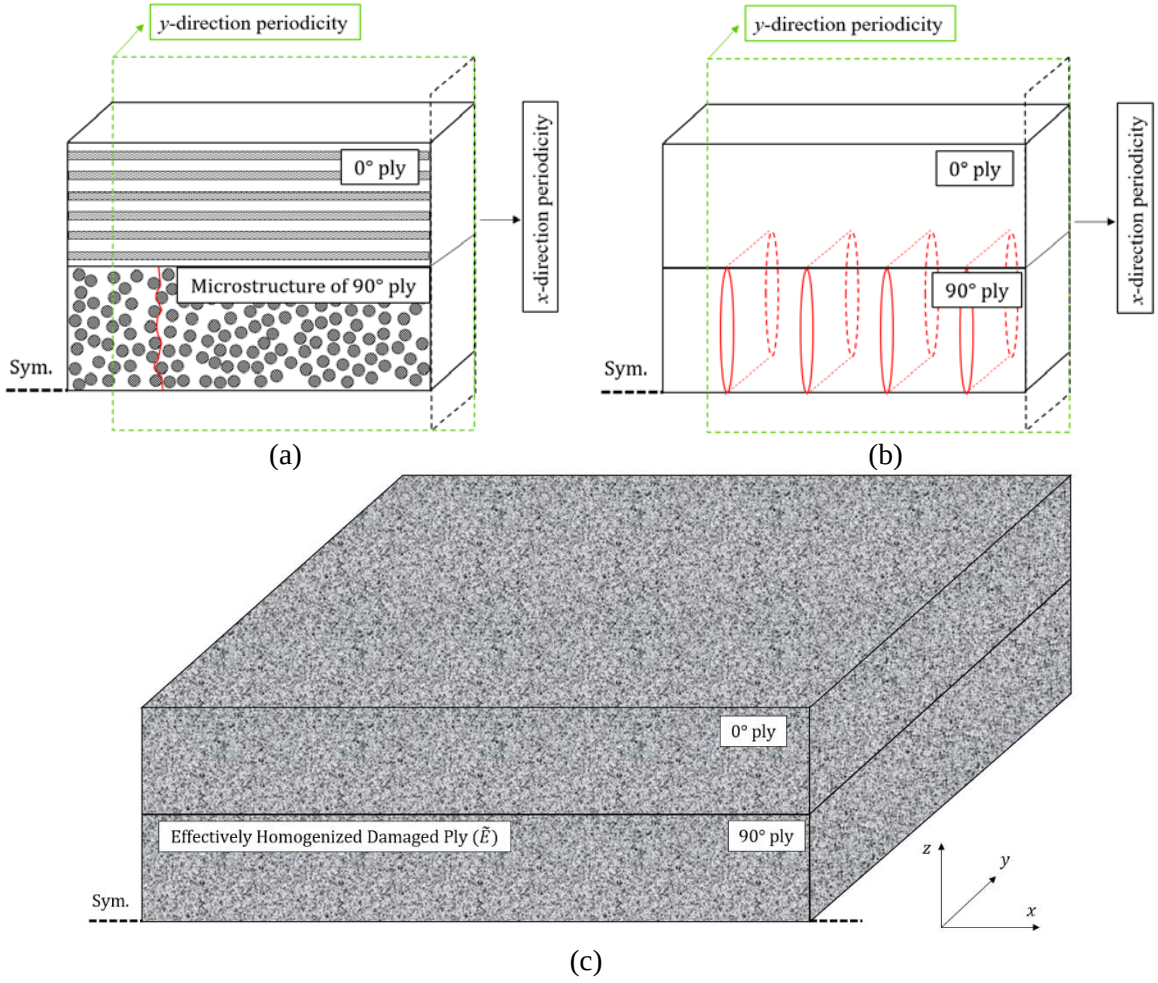

Figure 21. Schematic of RVE of a cross-ply laminate including ply cracks at: (a) microscale; (b) mesoscale; (c) macroscale.

The multiscale framework provides an efficient means to bridge the influence of ply cracking at the mesoscale with the laminate deformation response at the macroscale through damage influence parameters, where the interaction between damage entities and modes as well as ply constraining effects are also considered. Singh and Talreja [160–160] extended this multiscale approach to predict simultaneous damage evolution in multiple plies of multidirectional laminates. Experimental observation validated the capability of the SDM approach [46]. Montesano and Singh [28,29,162] further extended this multiscale approach by accounting for in-plane multiaxial stress states where intralaminar and interlaminar crack interactions were considered. Montesano and Singh [30] later

integrated this approach within a commercial finite element (FE) software package to predict sub-critical damage evolution in a composite wind turbine blade.

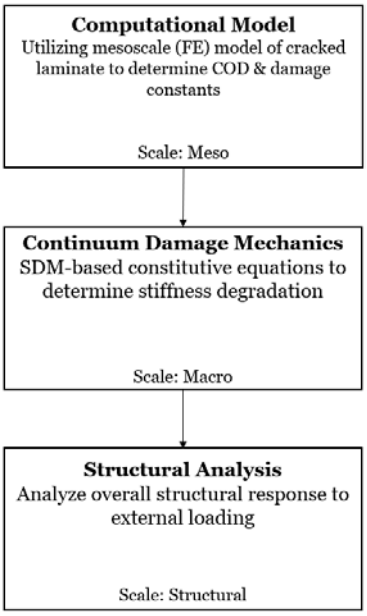

Figure 22. Flowchart showing the multiscale synergistic methodology for analyzing damage behavior of laminates.

References

[1] J.N. Reddy, Mechanics of Laminated Composite Plates and Shells, 2nd ed., CRC Press, 2004.

[2] A.K. Kaw, Mechanics of Composite Materials, 2nd ed., Taylor & Francis Group, LLC, 2005.

[3] R. Talreja, C.V. Singh, Damage and Failure of Composite Materials, Cambridge University Press, 2012.

[4] M.W. Hyer, S.R. White, Stress Analysis of Fiber-reinforced Composite Materials, DEStech Publications, Lancaster, Pennsylvania, 2009.

[5] J.C. Halpin, S.W. Tsai, Environmental Factors Estimation in Composite Materials Design, US Airforce Technical Report, AFML TR. (1967) 67–423.

[6] J.C. Halpin, J.L. Kardos, Halpin–Tsai equations – review, Polymer Engineering & Science 16 (1976) 344–352.

[7] C.C. Chamis, Mechanics of Composite Materials: Past, Present, and Future, Journal of Composites, Technology and Research ASTM 11 (1989) 3–14.

[8] J. Reinoso, A. Blázquez, F. París, Damage simulations in composite structures in the presence of stress gradients, in: R. Talreja (Ed.), Modeling Damage, Fatigue Failure of Composite Materials, Woodhead Publishing, 2016: pp. 391–424.

[9] J. Montesano, Fatigue damage characterization of braided and woven fiber reinforced polymer

matrix composites at room and elevated temperatures, Ryerson University, 2012.

[10] M. Quaresimin, P.A. Carraro, On the investigation of the biaxial fatigue behaviour of unidirectional composites, Composite Part B: Engineering 54 (2013) 200–208.

[11] Q. Sun, G. Zhou, H. Guo, Z. Meng, Z. Chen, H. Liu, H. Kang, X. Su, Failure mechanisms of cross-ply carbon fiber reinforced polymer laminates under longitudinal compression with experimental and computational analyses, Composite Part B: Engineering 167 (2019) 147–160.

[12] M.W. Nielsen, Prediction of process induced shape distortions and residual stresses in large - With application to Wind Turbine Blades, Technical University of Denmark, DTU, 2013.

[13] A.L. Highsmith, K.L. Reifsnider, Stiffness-Reduction Mechanisms in Composite Laminates, in: K.L. Reifsnider (Ed.), Damage in Composite Materials: Basic Mechanisms, Accumulation, Tolerance, and Characterization, ASTM International, West Conshohocken, PA, 1982.

[14] J.A. Nairn, The strain energy release rate of composite microcracking: A variational approach, Journal of Composite Materials 23 (1989) 1106–1129.

[15] J.A. Nairn, S. Hu, The formation and effect of outer-ply microcracks in cross-ply laminates: A variational approach, Engineering Fracture Mechanics 41 (1992) 203–221.

[16] S. Liu, J.A. Nairn, The formation and propagation of matrix microcracks in cross-ply laminates during static loading, Journal of Reinforced Plastics and Composites 11 (1992) 158–178.

[17] R. Talreja, A continuum-mechanics characterization of damage in composite materials, Proceedings of the Royal Society A: Mathematical, Physical and Engineering Sciences 399 (1985) 195–216.

[18] Z. Hashin, Analysis of cracked laminates: a variational approach, Mechanics of Materials 4 (1985) 121–136.

[19] G.J. Dvorak, N. Laws, M. Hejazi, Analysis of progressive matrix cracking in composite laminates i. thermoelastic properties of a ply with cracks, Journal of Composite Materials 19 (1985) 216–234.

[20] D.H. Allen, C.E. Harris, S.E. Groves, A thermomechanical constitutive theory for elastic composites with distributed damage—II. Application to matrix cracking in laminated composites, International Journal of Solids and Structures 23 (1987) 1319–1338.

[21] D.H. Allen, C.E. Harris, S.E. Groves, A thermomechanical constitutive theory for elastic composites with distributed damage—I. Theoretical development, International Journal of Solids and Structures 23 (1987) 1301–1318.

[22] P. Ladeveze, E. LeDantec, Damage modelling of the elementary ply for laminated composites, Composites Science and Technology 43 (1992) 257–267.

[23] J. Zhang, J. Fan, C. Soutis, Analysis of multiple matrix cracking in $[\pm\theta_m/90_n]_s$ composite laminates. Part 1: In-plane stiffness properties, Composites 23 (1992) 291–298.

[24] M. Quaresimin, P.A. Carraro, Damage initiation and evolution in glass/epoxy tubes subjected to combined tension–torsion fatigue loading, International Journal of Fatigue 63 (2014) 25–35.

[25] J.A. Nairn, Matrix Microcracking in Composites, in: R. Talreja, J.A.E. Manson (Eds.), Comprehensive Composite Materials, Elsevier Science & Technology, Amsterdam, Netherlands, 2000: pp. 403–432.

[26] C.A. Wood, W.L. Bradley, Determination of the effect of seawater on the interfacial strength of an interlayer E-glass/ graphite/epoxy composite by in situ observation of transverse cracking in an environmental SEM, Composites Science and Technology 57 (1997) 1033–1043.

[27] A.S.J. Suiker, N.A. Fleck, Modelling of fatigue crack tunneling and delamination in layered composites, Composites Part A: Applied Science and Manufacturing 37 (2006) 1722–1733.

[28] J. Montesano, C.V. Singh, A synergistic damage mechanics based multiscale model for composite laminates subjected to multiaxial strains, Mechanics of Materials 83 (2015) 72–89.

[29] J. Montesano, C.V. Singh, Predicting evolution of ply cracks in composite laminates subjected to biaxial loading, Composite Part B: Engineering 75 (2015) 264–273.

[30] J. Montesano, C.V. Singh, Critical stiffness damage envelopes for multidirectional laminated structures under multiaxial loading conditions, Materials and Design 91 (2016) 218–229.

[31] E.K. Gamstedt, B.A. Sjögren, Micromechanisms in tension compression fatigue of composite laminates containing transverse plies, Composites Science and Technology 59 (1999) 167–178.

[32] D.T.G. Katerelos, J. Varna, C. Galiotis, Energy criterion for modelling damage evolution in cross-ply composite laminates, 68 (2008) 2318–2324.

[33] H. Saito, H. Takeuchi, I. Kimpara, Experimental evaluation of the damage growth restraining in 90° layer of thin-ply CFRP cross-ply laminates, Advanced Composite Materials 21 (2012) 57–66.

[34] A. Arteiro, G. Catalanotti, A.R. Melro, P. Linde, P.P. Camanho, Micro-mechanical analysis of the in-situ effect in polymer composite laminates, Composite Structures 116 (2014) 827–840.

[35] J.P.H. Belnoue, O.J. Nixon-Pearson, A.J. Thompson, D.S. Ivanov, K.D. Potter, S.R. Hallett, Consolidation-driven defect generation in thick composite parts, Journal of Manufacturing Science and Technology ASME 140 (2018).

[36] M.Y. Matveev, J.P.H. Belnoue, O.J. Nixon-Pearson, D.S. Ivanov, A.C. Long, S.R. Hallett, I.A. Jones, A numerical study of variability in the manufacturing process of thick composite parts, Composite Structures 208 (2019) 23–32.

[37] B. El Said, S.R. Hallett, Multiscale modelling of laminated composite structures with defects and features, in: W. Van Paepegem (Ed.), Multi-Scale Continuum Mechanics Modelling of Fibre-Reinforced Polymer Composites, Woodhead Publishing Series in Composites Science and Engineering, 2021: pp. 637–668.

[38] R. Talreja, Modelling defect severity for failure analysis of composites, in: W. Van Paepegem (Ed.), Multi-Scale Continuum Mechanics Modelling of Fibre-Reinforced Polymer Composites, Woodhead Publishing Series in Composites Science and Engineering, 2021: pp. 275–306.

[39] M.J. Hinton, A.S. Kaddour, P.D. Soden, Failure criteria in fibre reinforced polymer composites: The world-wide failure exercise, Elsevier, 2004.

[40] Z. Hashin, Failure criteria for unidirectional fibre composites, Journal of Applied Mechanics 47 (1980) 329–334.

[41] Z. Hashin, Fatigue Failure Criteria for Unidirectional Fiber Composites, Journal of Applied Mechanics 48 (1981) 846–852.

[42] A. Puck, H. Schürmann, Failure analysis of FRP laminates by means of physically based

phenomenological models, Composites Science and Technology 58 (1998) 1045–1067.

[43] A. Puck, H. Schürmann, Failure analysis of FRP laminates by means of physically based phenomenological models, Composites Science and Technology 62 (2002) 1633–1662.

[44] A.S. Kaddour, M.J. Hinton, Benchmarking of triaxial failure criteria for composite laminates : Comparison between models of 'Part (A)' of 'WWFE-II,' Journal of Composite Materials 46 (2012) 2595–2634.

[45] A.S. Kaddour, M.J. Hinton, Maturity of 3D failure criteria for fibre-reinforced composites: Comparison between theories and experiments: Part B of WWFE-II, Journal of Composite Materials (2013).

[46] A.S. Kaddour, M.J. Hinton, P.A. Smith, S. Li, A comparison between the predictive capability of matrix cracking, damage and failure criteria for fibre reinforced composite laminates: Part A of the third world-wide failure exercise, Journal of Composite Materials 47 (2013) 2749–2779.

[47] P. Robinson, E. Greenhalgh, S.T. Pinho, Failure mechanisms in polymer matrix composites: : A criteria, testing and industrial applications, Woodhead Publishing, 2012.

[48] R.G. Cuntze, A. Freund, The predictive capability of failure mode concept-based strength criteria for multidirectional laminates, Composites Science and Technology 64 (2004) 343–377.

[49] R.G. Cuntze, Comparison between experimental and theoretical results using Cuntze's "failure mode concept"' model for composites under triaxial loadings — Part B of the second world-wide failure exercise, Journal of Composite Materials 47 (2012) 893–924.

[50] S. T. Pinho, C. G. Dávila, P. P. Camanho, L. Iannucci, and P. Robinson, Failure models and criteria for FRP under in-plane or three-dimensional stress states including shear non-linearity, NASA/TM-2005-213530 (Langley Research Center Hampton), 2005.

[51] S.T. Pinho, G.M. Vyas, P. Robinson, Material and structural response of polymer-matrix fibre-reinforced composites: Part B, Journal of Composite Materials 47 (2013) 679–696.

[52] N. Carrere, F. Laurin, J.F. Maire, Micromechanical-based hybrid mesoscopic three-dimensional approach for non-linear progressive failure analysis of composite structures – Part B : Comparison with experimental data, Journal of Composite Materials 47 (2012) 743–762.

[53] N. Carrere, F. Laurin, J.F. Maire, Micromechanical-based hybrid mesoscopic 3D approach for non-linear progressive failure analysis of composite structures, Journal of Composite Materials 46 (2012) 2389–2415.

[54] C.V. Singh, R. Talreja, A synergistic damage mechanics approach to mechanical response of composite laminates with ply cracks, Journal of Composite Materials 47 (2012) 2475–2501.

[55] R. Talreja, A synergistic damage mechanics approach to durability of composite materials systems, in: Progress in Durability Analysis of Composite Systems, Eds. A. Cardon, H. Fukuda, K. Reifsnider, A.A. Balkema (Rotterdam), 1996: pp. 117–129.

[56] L.M. Kachanov, Rupture time under creep conditions, International Journal of Fracture 97 (1999) 11–18.

[57] L.M. Kachanov, On the creep rupture time, Izv Akad Nauk SSR, Otd Tekhn Nauk. 8 (1958) 26–31.

[58] Y.N. Robotnov, Creep Problems in Structural Members, North-Holland, Amesterdam, 1969.

[59] J. Lemaitre, R. Desmorat, Engineering Damage Mechanics, Springer, Berlin Heidelberg New York Library, 2005.

[60] J. Lemaitre, A continous damage mechanics model of ductile fracture, Journal of Engineering Matreials and Technology 107 (1985) 83–89.

[61] J. Lemaitre, J.L. Chaboche, Aspect phenomenologique de la rupture par endommagement, J. Mec. Appiquee. 2 (1978) 317–365.

[62] S. Murakami, N. Ohno, In Creep in Structures, in: A.R.S. Ponter, D.R. Hayhurst (Eds.), A Contin. Theory Creep Creep Damage, Springer-Verlag, Berlin, Germany, 1981: pp. 422–444.

[63] J.L. Chaboche, Anisotropic creep damage in the framework of continuum damage mechanics, Nuclear Engineering and Design 79 (1984) 309–319.

[64] J.L. Chaboche, Continuum damage mechanics: part I – general concepts, Journal of Applied Mechanics 55 (1988) 59–64.

[65] J.L. Chaboche, Continuum damage mechanics: part II – damage growth, crack initiation, and crack growth, Journal of Applied Mechanics 55 (1988) 65–72.

[66] S. Murakami, Continuum Damage Mechanics, Springer, Dordrecht Heidelberg London New York, 2012.

[67] P. Ladevèze, A damage computational method for composite structures, Computers & Structures 44 (1992) 79–87.

[68] R. Talreja, Internal variable damage mechanics of composite materials, in: J.P. Boehler (Ed.), Yielding, Damage, Fail. Anisotropic Solids, Mechanical Engineering Publication, London, 1990: pp. 509–533.

[69] R. Talreja, Damage mechanics of composite materials based on thermodynamics with internal variables, in: A. Cardon, G. Verchery (Eds.), Durability of polymer based composite systems for structural applications, Elsevier Ltd, London, 1991: pp. 65–79.

[70] R. Talreja, Continuum modeling of damage in ceramic matrix composites, Mechanics of Materials 12 (1991) 165–180.

[71] R. Talreja, In Damage Mechanics of Composite Materials, Elsevier Ltd, Amesterdam, 1994.

[72] A.A. Vakulenko, L.M. Kachanov, Continual theory of a medium with cracks, Izv AN SSSR, Mekhanika Tverd. Tela (Mech Solids). 6 (1971) 159.

[73] C.V. Singh, A higher order synergistic damage model for prediction of stiffness changes due to ply cracking in composite laminates, Computers, Materials and Continua 34 (2013) 227–249.

[74] C.V. Singh, R. Talreja, Analysis of multiple off-axis ply cracks in composite laminates, International Journal of Solids and Structures 45 (2008) 4574–4589.

[75] J. Aveston, G.A. Cooper, A. Kelly, Single and multiple fracture: The properties of fiber composites. Conference Proceedings, National Physical Laboratory, Guildford, U.K., 1971: pp. 15–26. IPC Science and Technology Press, Ltd. Teddington, U.K.

[76] K.W. Garrett, J.E. Bailey, Multiple transverse fracture in 90° cross-ply laminates of a glass fibre-reinforced polyester, Journal of Materials Science 12 (1977) 157–168.

[77] A. Parvizi, K.W. Garrett, J.E. Bailey, Constrained cracking in glass fiber-reinforced epoxy cross

ply laminates, Journal of Materials Science 13 (1978) 195–201.

[78] A. Parvizi, J.E. Bailey, On multiple transverse cracking in glass fibre epoxy cross-ply laminates, Journal of Materials Science 13 (1978) 2131–2136.

[79] P.W. Manders, T.W. Chou, F.R. Jones, J.W. Rock, Statistical analysis of multiple fracture in 0°/90°/0° glass fibre/epoxy resin laminates, Journal of Materials Science 18 (1983) 2876–2889.

[80] H.L. Cox, The elasticity and strength of paper and other fibrous materials, British Journal of Applied Physics 3 (1952) 72–79.

[81] H. Fukunga, T.W. Chou, P.W.M. Peters, K. Schulte, Probabilistic failure strength analysis of graphite/epoxy cross-ply laminates, Journal of Composite Materials 18 (1984) 339–356.

[82] J.A. Nairn, S. Hu, Micromechanics of damage: A case study of matrix micro cracking, in: R. Talreja (Ed.), Damage Mechanics of Composite Materials, Elsevier Ltd, Amesterdam, 1994: pp. 187–243.

[83] J. Berthelot, Transverse cracking and delamination in cross-ply glass-fiber and carbon-fiber reinforced plastic laminates : Static and fatigue loading, Applied Mechanics Review 56 (2003) 111–147.

[84] J.A. Nairn, J.A., On the use of shear-lag methods for analysis of stress transfer in unidirectional composites, Mechanics of Materials 26 (1997) 63-80.

[85] L.N. McCartney, Predicting properties of undamaged and damaged carbon fibre reinforced composites. In: P.W.R. Beaumont, C. Soutis, A. Hodzic (Eds.), The Structural Integrity of Carbon Fiber Composites: Fifty Years of Progress and Achievement of the Science, Development, and Applications. Springer International Publishing, 2017: pp. 425-467.

[86] T. Yokozeki, T. Aoki, Overall thermoelastic properties of symmetric laminates containing obliquely crossed matrix cracks, Composites Science and Technology 65 (2005) 1647-1654.

[87] P.A. Carraro, M. Quaresimin, A stiffness degradation model for cracked multidirectional laminates with cracks in multiple layers, International Journal of Solids and Structures 58 (2015) 34-51.

[88] E.J. Barbero, F.A. Cosso, F.A. Campo, Benchmark solution for degradation of elastic properties due to transverse matrix cracking in laminated composites, Composite Structures 98 (2013) 242-252.

[89] J. Varna, L.A. Berglund, Multiple transverse cracking and stiffness reduction in cross-ply laminates, Journal of Composites Technology and Research 13 (1991) 97–106.

[90] J.E. Bailey, P.T. Curtis, A. Parvizi, On the transverse cracking and longitudinal splitting behavior of glass and carbon-fiber reinforced epoxy cross-ply laminates and the effect of Poisson and thermally generated strain, Proceedings of the Royal Society A: Mathematical, Physical and Engineering Sciences 366 (1979) 599–623.

[91] J. Varna, L.A. Berglund, Two-dimensional transverse cracking in $[0_m/90_n]_s$ cross-ply laminates, European Journal of Mechanics 12 (1993) 699–723.

[92] J. Varna, L.A. Berglund, Thermoelastic properties of composite laminates with transverse cracks, Journal of Composites Technology and Research 16 (1994) 77–87.

[93] S. Kuriakose, R. Talreja, Variational solutions to stresses in cracked cross-ply laminates under

bending, International Journal of Solids and Structures 41 (2004) 2331–2347.

[94] M. Hajikazemi, L.N. McCartney, W. Van Paepegem, M.H. Sadr, Theory of variational stress transfer in general symmetric composite laminates containing nonuniformly spaced ply cracks, Composites Part A: Applied Science and Manufacturing 107 (2018) 374-386.

[95] M. Hajikazemi, W. Van Paepegem, A variational model for free-edge interlaminar stress analysis in general symmetric and thin-ply composite laminates, Composite Structures 184 (2018) 443-451.

[96] M. Hajikazemi, W. Van Paepegem, Variational analysis of free-edge stress and displacement fields in general un-symmetric and thin-ply laminates under in-plane, bending and thermal loading, Composites Part A: Applied Science and Manufacturing 113 (2018) 220-232.

[97] M. Hajikazemi, D. Garoz, W. Van Paepegem, Model to accurately predict out-of-plane shear stiffness reduction in general cracked laminates, Composites Science and Technology 179 (2019) 88-96.

[98] S. Östlund, P. Gudmundsont, Numerical analysis of matrix-crack-induced delaminations in [±55°] GFRP laminates, Composites Engineering 2 (1992) 161–175.

[99] E. Adolfsson, P. Gudmundson, Matrix crack initiation and progression in composite laminates subjected to bending and extension, International Journal of Solids and Structures 36 (1999) 3131–3169.

[100] P. Gudmundsont, W. Zang, An analytic model for thermoelastic properties of composite laminates containing transverse matrix cracks, International Journal of Solids and Structures 30 (1993) 3211–3231.

[101] P. Gudmundson, S. Östlund, First order analysis of stiffness reduction due to matrix cracking, Journal of Composite Materials 26 (1992) 1009–1030.

[102] P. Lundmark, Damage mechanics analysis of inelastic behaviour of fiber composites, Ph.D. thesis, Lulea University of Technology, 2005.

[103] P. Lundmark, J. Varna, Crack face sliding effect on stiffness of laminates with ply cracks, Composites Science and Technology 66 (2006) 1444–1454.

[104] J. Varna, Physical interpretation of parameters in synergistic continuum damage mechanics model for laminates, Composites Science and Technology 68 (2008) 2592–2600.

[105] P. Lundmark, J. Varna, Constitutive relationships for laminates with ply cracks in in-plane loading, International Journal of Damage Mechanics 14 (2005) 235–259.

[106] P. Lundmark, J. Varna, Stiffness reduction in laminates at high intralaminar crack density: effect of crack interaction, International Journal of Damage Mechanics 20 (2009) 279-297.

[107] M.S. Loukil, J. Varna, Z. Ayadi, Engineering expressions for thermo-elastic constants of laminates with high density of transverse cracks, Composites Part A: Applied Science and Manufacturing 48 (2013) 37-46.

[108] M.S. Loukil, J. Varna, Crack face sliding displacement (CSD) as an input in exact GLOB-LOC expressions for in-plane elastic constants of symmetric damaged laminates, International Journal of Damage Mechanics 29 (2020) 547-569.

[109] T. Yokozeki, T. Aoki, T. Ishikawa, Consecutive matrix cracking in contiguous plies of

composite laminates, International Journal of Solids and Structures 42 (2005) 2785–2802.

[110] L.E. Asp, L.A. Berglund, R. Talreja, A criterion for crack initiation in glassy polymers subjected to a composite-like stress state, Composites Science and Technology 56 (1996) 1291–1301.

[111] L.E. Asp, L.A. Berglund, P. Gudmundson, Effects of a composite-like stress state on the fracture of epoxies, Composites Science and Technology 53 (1995) 27–37.

[112] L.E. Asp, L.A. Berglund, R. Talreja, Effects of fibre and interphase on matrix initiated transverse failure in polymer composites, Composites Science and Technology 56 (1996) 657–665.

[113] L.E. Asp, L.A. Berglund, R. Talreja, Prediction of matrix-initiated transverse failure in polymer composites, Composites Science and Technology 56 (1996) 1089–1097.

[114] S.A. Elnekhaily, R. Talreja, Damage initiation in unidirectional fiber composites with different degrees of nonuniform fiber distribution, Composites Science and Technology 155 (2018) 22–32.

[115] S.A. Elnekhaily, R. Talreja, Effect of axial shear and transverse tension on early failure events in unidirectional polymer matrix composites, Composites Part A: Applied Science and Manufacturing 119 (2019) 275–282.

[116] A. Sudhir, R. Talreja, Simulation of manufacturing induced fiber clustering and matrix voids and their effect on transverse crack formation in unidirectional composites, Composites Part A: Applied Science and Manufacturing 127 (2019) 105620.

[117] E. Marklund, L.E. Asp, R. Olsson, Transverse strength of unidirectional non-crimp fabric composites: Multiscale modelling, Composite Part B: Engineering 65 (2014) 47–56.

[118] L. Zhuang, R. Talreja, J. Varna, Transverse crack formation in unidirectional composites by linking of fibre/matrix debond cracks, Composites Part A: Applied Science and Manufacturing 107 (2018) 294–303.

[119] T. Okabe, H. Imamura, Y. Sato, R. Higuchi, J. Koyanagi, R. Talreja, Experimental and numerical studies of initial cracking in CFRP cross-ply laminates, Composites Part A: Applied Science and Manufacturing 68 (2015) 81–89.

[120] Y. Kumagai, S. Onodera, M. Salviato, T. Okabe, Multiscale analysis and experimental validation of crack initiation in quasi-isotropic laminates, International Journal of Solids and Structures 193–194 (2020) 172–191.

[121] P.A. Carraro, M. Quaresimin, Modelling fibre–matrix debonding under biaxial loading, Composites Part A: Applied Science and Manufacturing 61 (2014) 33–42.

[122] F. París, M.L. Velasco, E. Correa, Modelling fibre–matrix interface debonding and matrix cracking in composite laminates, in: W. Van Paepegem (Ed.), Multi-Scale Continuum Mechanics Modelling of Fibre-Reinforced Polymer Composites, Woodhead Publishing Series in Composites Science and Engineering, 2021: pp. 243–274.

[123] F. Paris, M.L. Velasco, E. Correa, Micromechanical study on the influence of scale effect in the first stage of damage in composites, Composites Science and Technology 160 (2018) 1-8.

[124] M. Herraez, D. Mora, F. Naya, C.S. Lopes, C. Gonzalez, J. LLorca, Transverse cracking of cross ply laminates: a computational micro mechanics perspective, Composites Science and Technology 110 (2015) 196-204.

[125] A.R. Melro, P.P. Camanho, F.M.A. Pires, S.T. Pinho, Micromechanical analysis of polymer composites reinforced by unidirectional fibres : Part I – Constitutive modelling, International Journal of Solids and Structures 50 (2013) 1897–1905.

[126] S. Ghosh, Y. Ling, B. Majumdar, R. Kim, Interfacial debonding analysis in multiple fiber reinforced composites, Mechanics of Materials 32 (2000) 561–591.

[127] P.A. Carraro, M. Quaresimin, Modelling fibre-matrix debonding under biaxial loading, Composites Part A: Applied Science and Manufacturing 61 (2014) 33–42.

[128] P.P. Camanho, A. Arteiro, A.R. Melro, G. Catalanotti, M. Vogler, Three-dimensional invariant-based failure criteria for fibre-reinforced composites, International Journal of Solids and Structures 55 (2015) 92–107.

[129] H. Saito, H. Takeuchi, I. Kimpara, A study of crack suppression mechanism of thin-ply carbon-fiber-reinforced polymer laminate with mesoscopic numerical simulation, Journal of Composite Materials 48 (2014) 2085–2096.

[130] A.R. Melro, P.P. Camanho, F.M.A. Pires, S.T. Pinho, Micromechanical analysis of polymer composites reinforced by unidirectional fibres : Part II – Micromechanical analyses, International Journal of Solids and Structures 50 (2013) 1906–1915.

[131] S. Zhandarov, E. Mäder, Characterization of fiber/matrix interface strength: Applicability of different tests, approaches and parameters, Composites Science and Technology 65 (2005) 149–160.

[132] D. Zhang, D. Heider, J.W. Gillespie, Determination of void statistics and statistical representative volume elements in carbon fiber-reinforced thermoplastic prepregs, Journal of Thermoplastic Composite Materials 30 (2017) 1103–1119.

[133] J. Varna, R. Joffe, L.A. Berglund, T.S. Lundström, Effect of voids on failure mechanisms in RTM laminates, Composites Science and Technology 53 (1995) 241–249.

[134] Y.K. Hamidi, L. Aktas, M.C. Altan, Formation of microscopic voids in resin transfer molded composites, Journal of Engineering Materials and Technology 126 (2004) 420.

[135] K.A. Chowdhury, R. Talreja, A.A. Benzerga, Effects of Manufacturing-Induced Voids on Local Failure in Polymer-Based Composites, Journal of Engineering Materials and Technology 130 (2008) 021010-1-021010–9.

[136] H. Ghayoor, C.C. Marsden, S. V Hoa, A.R. Melro, Numerical analysis of resin-rich areas and their effects on failure initiation of composites, Composites Part A: Applied Science and Manufacturing 117 (2019) 125–133.

[137] L. Zhuang, A. Pupurs, J. Varna, R. Talreja, Z. Ayadi, Effects of inter-fiber spacing on fiber-matrix debond crack growth in unidirectional composites under transverse loading, Composites Part A: Applied Science and Manufacturing 109 (2018) 463–471.

[138] G.H. Lindsey, R.A. Schapery, S.M.L. Williams, A.R. Zak, The triaxial tension failure of viscoelastic materials, Pasadena, California, 1963.

[139] B. Fiedler, M. Hojo, S. Ochiai, K. Schulte, M. Ando, Failure behavior of an epoxy matrix under different kinds of static loading, Composites Science and Technology 61 (2001) 1615–1624.

[140] S. Ghosh, P. Raghavan, Multiscale model for damage analysis in fiber reinforced composites with interfacial debonding materials, International Journal for Multiscale Computational

Engineering 2 (2004) 621–645.

[141] S. Ghosh, J. Bai, P. Raghavan, Concurrent multi-level model for damage evolution in microstructurally debonding composites, Mechanics of Materials 39 (2007) 241–266.

[142] P. Raghavan, S. Ghosh, A continuum damage mechanics model for unidirectional composites undergoing interfacial debonding, Mechanics of Materials 37 (2005) 955–979.

[143] D.H. Allen, Homogenization principles and their application to continuum damage mechanics, Composites Science and Technology 61 (2001) 2223–2230.

[144] P. Raghavan, S. Li, S. Ghosh, Two scale response and damage modeling of composite materials, Finite Elements in Analysis and Design 40 (2004) 1619–1640.

[145] F. Lene, Damage constitutive relations for composite materials, Engineering Fracture Mechanics 25 (1986) 713–728.

[146] F. Devries, H. Dumontet, G. Duvaut, F. Lene, Homogenization and damage for composite structures, International Journal for Numerical Methods in Engineering 27 (1989) 285–298.

[147] J. Fish, Q. Yu, K. Shek, Computational damage mechanics for composite materials based on mathematical homogenization, International Journal for Numerical Methods in Engineering 45 (1999) 1657–1679.

[148] F. Costanzo, J.G. Boyd, D.H. Allen, Micromechanics and homogenization of inelastic composite materials with growing cracks, Journal of the Mechanics and Physics of Solids 44 (1996) 333–370.

[149] D.H. Allen, C. Yoon, Homogenization techniques for thermoviscoelastic solids containing cracks, International Journal of Solids and Structures 35 (1998) 4035–4053.

[150] A. Arteiro, G. Catalanotti, J. Reinoso, P. Linde, P.P. Camanho, Simulation of the Mechanical Response of Thin-Ply Composites: From Computational Micro-Mechanics to Structural Analysis, Archives of Computational Methods in Engineering 26 (2019) 1445–1487.

[151] B. Cox, Q. Yang, In quest of virtual tests for structural composites, Science 314 (2006) 1102–1107.

[152] Q.D. Yang, B.N. Cox, X.J. Fang, Z.Q. Zhou, Virtual testing for advanced aerospace composites: Advances and future needs, Journal of Engineering Materials and Technology Transaction of the ASME 133 (2011) 1–6.

[153] T. Belytschko, J.-H. Song, Coarse-graining of multiscale crack propagation, International Journal for Numerical Methods in Engineering 81 (2010) 537–563.

[154] S. Ghosh, Adaptive Concurrent Multilevel Model for Multiscale Analysis of Composite Materials Including Damage, in: Y.W. Kwon, D.H. Allen, R. Talreja (Eds.), Multiscale Modeling and Simulation of Composite Materials and Structures, Springer, New York, 2008: pp. 83–163.

[155] R. Talreja, Multi-scale modeling in damage mechanics of composite materials, Journal of Materials Science 41 (2006) 6800–6812.

[156] J. Varna, N. V Akshantala, R. Talreja, Crack opening displacement and the associated response of laminateswith varying constraints, International Journal of Damage Mechanics 8 (1999) 174–193.

[157] J. Varna, R. Joffe, N. V. Akshantala, R. Talreja, Damage in composite laminates with off-axis plies, Composites Science and Technology 59 (1999) 2139–2147.

[158] R. Joffe, N. V Akshantala, J. Varna, COD-based simulation of transverse cracking and stiffness reduction in $[S/90_n]_s$ laminates, Composites Science and Technology 61 (2001) 565–637.

[159] J. Varna, R. Joffe, R. Talreja, A synergistic damage mechanics analysis of transverse cracking in $[0/90_4]_s$ laminates, Composites Science and Technology 61 (2001) 657–665.

[160] C.V. Singh, R. Talreja, Analysis of multiple off-axis ply cracks in composite laminates, International Journal of Solids and Structures 45 (2008) 4574–4589.

[161] C.V. Singh, R. Talreja, A synergistic damage mechanics approach for composite laminates with matrix cracks in multiple orientations, Mechanics of Materials 41 (2009) 954–968.

[162] C.V. Singh, R. Talreja, Evolution of ply cracks in multidirectional composite laminates, International Journal of Solids and Structures 47 (2010) 1338–1349.

[163] J. Montesano, H. Chu, C.V. Singh, Development of a physics-based multi-scale progressive damage model for assessing the durability of wind turbine blades, Composite Structures 141 (2016) 50–62.

Chapter 3

Objectives

3.1 Research Objectives

The overall goal of the thesis is to develop advanced computational micromechanical models to study the onset of local failure and formation of ply cracks in carbon fiber/epoxy laminates. The micromechanical models are also used to determine the effective energy release rate (ERR) associated with ply crack formation, which will be integrated within a hierarchical multiscale framework to bridge the micro and mesoscales [1]. A constitutive model within a finite element (FE) framework is developed to capture the onset of local failure in the epoxy matrix, while an isotropic damage model is used to capture the progression of matrix microcracks. Manufacturing-induced defects (e.g., voids, resin-rich pockets, inter-ply resin-rich zones) and thermal residual stress are represented in the computational models. The effect of the ply constraints on local stress and displacements fields before and after the formation of ply cracks is also investigated by considering the constraining plies within the generated representative volume elements (RVE) in this study. Dissipation of energy during the evolution of ply cracks is obtained to approximate the associated ERR. The objectives of this research are:

1. Generate periodic RVEs with nonuniform fiber spatial dispersion for a micromechanical assessment.
2. Develop micromechanical FE models with manufacturing-induced defects to study the influence of ply constraints on local energy (stress) states in the 90° ply of [0/90/0] cross-ply laminates.
3. Investigate the onset of local failure and the corresponding mechanisms in the 90° ply of [0/90/0] cross-ply laminates using micromechanical FE models.
4. Develop a scheme to simulate ply crack formation and evolution in [0/90/0] cross-ply laminates using micromechanical FE models.

3.2 Research Scope

3.2.1 Task 1: A new approach to generate periodic representative volume elements with nonuniform fiber spatial dispersion for the micromechanical assessment of composites [2]

An algorithm based on event-driven molecular dynamics theory is developed to rapidly generate periodic RVEs with nonuniform fiber spatial dispersion for FRP composites. To evaluate the reliability of the generated RVEs, FE analysis is conducted to calculate the volume averaged elastic constants.

Isotropic characteristics of the RVEs are predicted, and correlations with experimental data from the literature are provided. The proposed algorithm is used as a tool for generating 2D/3D RVEs that are required for micromechanical assessments in the following objectives.

3.2.2 Task 2: Assessing the effects of ply constraints on local stress states in cross-ply laminates containing manufacturing-induced defects [3]

Computational micromechanics is employed to assess the influence of the ply constraints on the early stages of 90° ply crack formation in a [0/90/0] cross-ply laminate under tensile loading. Manufacturing-induced defects, including nonuniform fiber spatial distribution, microvoids and microcracks, are explicitly simulated. Local distortion and dilatation energy density in the matrix, associated with local yielding and brittle cavitation, are assessed within unconstrained and constrained 90° plies. The effects of ply constraints are compared when pre- existing microvoids or microcracks are present, as well as different regions of the ply (i.e., fiber clusters, resin-rich zones, plies interface). Additional parametric studies are conducted to investigate the effect of the constrained and adjacent ply thicknesses, ply interface resin-rich layer thickness, and post-cure thermal cooldown on the degree of constraining. The study provides an improved understanding of the early stages of ply crack formation in constrained plies, which is important for predicting local failure in laminates.

3.2.3 Task 3: Micromechanical assessment of local failure mechanisms and early-stage ply crack formation in cross-ply laminates [4]

Three-dimensional computational micromechanical models are developed to study the local failure mechanisms and early-stage ply crack formation of a carbon fiber/epoxy [0/90/0] cross-ply laminate under tensile loading. Pressure-dependent inelastic deformation of the epoxy is captured by a user-defined material (VUMAT) model, where brittle cavitation and ductile failure are defined as the local failure mechanisms. Manufacturing induced defects, including nonuniform fiber spatial dispersion and resin pockets, are represented in the 90° ply. The effects of ply constraints on the local distortional and dilatational energy densities in the matrix are evaluated. Brittle cavitation is found to be the first and dominating failure mechanism, while local inelastic deformation indirectly influences the number and location of cavitation sites. Inelastic deformation is deemed necessary for predicting the linkage of the microcracks that are induced by brittle cavitation. The study provides important insight into the early-stage formation of ply cracks, which is essential for analyzing the subsequent ply crack formation.

3.2.4 Task 4: Micromechanical simulation of ply crack formation in cross-ply laminates under quasi-static tensile loading [5]

A modified VUMAT model is developed within an explicit FE framework to simulate ply crack propagation in [0/90/0] cross-ply laminates, while an isotropic damage model is used to capture the post-peak behaviour of the epoxy matrix. The capability of the FE model is separately verified in predicting crack propagation and full ply crack failure strain. Representative volume elements with different thicknesses are generated to extend the study, where the constituents are explicitly simulated in the 90° ply. It is indicated the first ply crack formation delays in laminates with a thinner 90° ply compared to an unconstrained 90° ply, but the failure is expedited after a certain thickness. Furthermore, the effect of the thermal residual stress, the ply constraints, and fiber volume fraction on the formation of ultimate ply crack are investigated. The reasons for the incapability of mesoscale models in presenting a comprehensive estimation are discussed. Bridging micro-mesoscale modelling within a multiscale framework is proposed as a remedy.

References

[1] J. Montesano, F. Sharifpour, Modelling damage evolution in multidirectional laminates: micro to macro, in: W. Van Paepegem (Ed.), Multi-Scale Continuum Mechanics Modelling of Fibre-Reinforced Polymer Composites, Woodhead Publishing Series in Composites Science and Engineering, 2021: pp. 463–507.

[2] G. Li, F. Sharifpour, A. Bahmani, J. Montesano, A new approach to rapidly generate random periodic representative volume elements for microstructural assessment of high volume fraction composites, Materials & Design 150 (2018) 124–138.

[3] F. Sharifpour, J. Montesano, R. Talreja, Assessing the effects of ply constraints on local stress states in cross-ply laminates containing manufacturing induced defects, Composites Part B: Engineering 199 (2020) 1–13.

[4] F. Sharifpour, J. Montesano, R. Talreja, Micromechanical assessment of local failure mechanisms and early-stage ply crack formation in cross-ply laminates, Composite Science and Technology (Under Review).

[5] F. Sharifpour, J. Montesano, Micromechanical simulation of ply crack formation in cross-ply laminates under quasi-static tensile loading, Composite Part A (To be submitted in January 2022)

Chapter 4

A new approach to rapidly generate random periodic representative volume elements for microstructural assessment of high volume fraction composites

(Published manuscript, Materials and Design 150 (2018) 124-138)

4.1 Introduction

The widespread use of fibrous composite materials is a direct result of their high specific strength and stiffness and the ability to tailor their mechanical and thermal properties. Prior to designing a specific material system and optimizing corresponding structural components, the effective properties of composites can be evaluated through so-called computational experiments using a representative volume element (RVE) [1–7]. In this context, an RVE is an accurate depiction of the material's microstructure that is used to evaluate its effective macroscopic properties, thereby minimizing the requirement for experimental testing during the early stages of design. An advantage with RVEs and related computational assessments is that the anisotropy of the composite material system can be directly tailored, and accurate microstructural assessments can be realized.

Similar to an RVE, a periodic unit cell (PUC) model can also be used to evaluate properties of composite materials. PUCs have simplified structured patterns for the reinforcement phase and often adopt symmetric boundary conditions [8–10]. In practice, however, composite microstructures are rarely structured, thus PUC models may not be suitable for assessing their 3D mechanical properties [11–13]. In addition, the evolution of microstructural parameters for materials involving plasticity or evolving microscopic damage are often not of a structured nature, thus PUC methods may not be suitable for these problems since the implication that all regions of the material are damaged simultaneously is not realistic.

Oh and Jin [14,15] found that RVEs of unidirectional fiber-reinforced composites with nonuniform fiber spatial dispersion, especially for high fiber volume fractions (HFVFs), resulted in variations in strain at fiber/matrix interfaces [14] and thermal residual stresses [15]. Gusev et al. [16] also found that the nonuniform microstructural fiber dispersion of a unidirectional glass/epoxy composite had significant influence on the transverse elastic properties. Recently, Ghayoor et al. [17] found that local stress values were more variable in nonuniform microstructures when compared to periodic microstructures, and more likely to cause a disturbance of the load and stress distribution in the composite. Thus, to accurately assess the 3D mechanical properties and microstructural parameters of

unidirectional fiber-reinforced composites with high volume fractions, including predicting localized damage progression, it is important to generate realistic RVEs with nonuniform fiber spatial dispersions.

Several research efforts have been devoted to generating RVEs for unidirectional fiber-reinforced composite materials using random distribution algorithms (RDAs). The classical approach of RDAs is the so-called hard-core model (HCM), which assesses the position of newly generated random fibers to avoid overlaps [18,19]. Due to the jamming limit with HCM algorithms, close packing [20], stirring, [21,22], random sequential expansion (RSE) [23], and random sequential absorption (RSA) [24–26], algorithms have also been studied. Nonetheless, generating RVEs with higher fiber volume fractions in reasonable computational times remains challenging with these algorithms [27]. To overcome this limitation the nearest neighbour algorithm (NNA) [28] and modified NNA (MNNA) [29] were proposed, where random RVEs were generated with comparatively short computational times using nearest neighbour distribution functions. Recently, the elastic collision algorithm (ECA) was also proposed to generate RVEs with nonuniform fiber spatial dispersions [30]. After defining an initial fiber unit velocity for all fibers along a random direction, fibers displaced under an elastic collision law. However, the disturbance time interval is difficult to adjust for different volume fractions making the ECA impractical.

A new efficient method for generating RVEs for HFVF composites utilizes the principles of molecular dynamics (MD) which involves tracking inter-particle interactions [31], and has been successfully applied to generate 2D RVEs of rigid disks with high volume fractions [32,33]. One of the limitations with time-driven MD (TDMD) or random walking algorithms (RWA) is that they require small time-steps and integration of the equations of motion [34]. Donev et al. [35] presented a more rapid event-driven molecular dynamics (EDMD) algorithm which is suitable for high volume fractions without compromising accuracy. EDMD approaches schedule the sequence of the events that are predicted to occur in the future based on the present particle trajectories [36]. However, these algorithms can be difficult to implement, and the degree of nonuniformity for the resulting RVEs was not assessed in the reported studies. Recent work by Catalanotti [37] has developed a new algorithm aimed to generate RVEs and is among the first to do so for RVEs of composite materials containing HFVFs.

Although the above numerical approaches have made significant contributions toward generating practical RVEs for composite materials, accurate and efficient generation of nonuniformly distributed RVEs for composites with HFVFs remains a challenge. In this study, a simple and efficient algorithm was developed to generate RVEs for unidirectional composites with high fiber volume fractions. The

developed algorithm is based on EDMD theory and utilizes the open-source DynamO software [38] to randomly generate fiber coordinates for RVEs with specified volume fraction in a few minutes or several seconds. The goal of this study was to generate RVEs with nonuniform fiber spatial dispersions. A subsequent aim was to use the generated RVEs for developing finite element micromechanical models using custom scripts in the commercial software Abaqus. The mechanical properties of the composite materials studied were determined, with the goal of providing additional validation for the developed RVE generation algorithm. Unidirectional fiber-reinforced composites with high volume fractions were studied in order to showcase the versatility of the developed algorithm, and its ability to overcome the different challenges when generating RVEs for distinct materials. It should be noted that although the study also focused on particulate composites, only the results pertaining to unidirectional fiber-reinforced composites are presented in this Chapter since these results are directly related to the thesis.

4.2 Development of EDMD-based algorithm for RVE geometry generation

4.2.1 Event-driven molecular dynamics overview

In recent years, MD simulations based on time-stepping algorithms have been broadly used for simulating the mobility of molecules or atoms for various material systems. For particular cases, including the present study, capturing the key features of interactions between particles is required. Thus, the EDMD approach is more suitable for simulating discrete interaction potentials, with the ability to provide quantitative predictions [39,40]. Figure 23 illustrates the conceptual difference with respect to interacting particles between conventional time-stepping MD and EDMD methods.

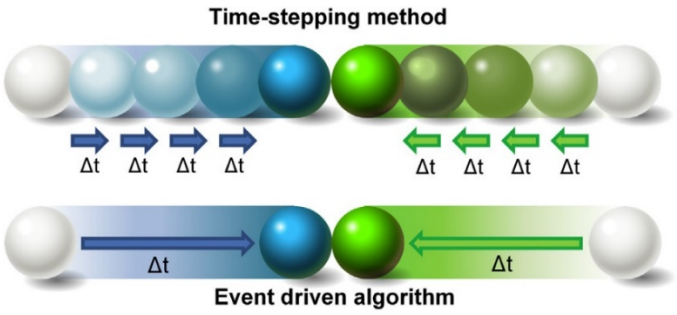

Figure 23. Schematic of time-stepping method and event-driven algorithm.

4.2.2 Generation of periodic RVEs with nonuniform fiber spatial dispersions

In this study, the EDMD open-source software DynamO was used within a customized algorithm to generate periodic RVEs with nonuniform distributions for unidirectional fiber-reinforced composites. Within DynamO, each particle is initially assigned a random velocity vector and an event table is automatically generated which defines all potential collisions between particles in the RVE space (see Refs. [39,40] for full details). Thus, a realistic random particle distribution is effectively guaranteed for all particle regions, with a significantly reduced computational time. Figure 24 represents the algorithm flowchart for the generation of random RVE microstructures. Two cases were considered: (i) a 2D arrangement of circular fibers representing the cross-section of a continuous unidirectional fiber-reinforced composite; (ii) a 3D arrangement of spherical particles representing a particulate reinforced composite. However, only the former is discussed in this Chapter. The detailed 4-step procedure outlined in Fig. 24 is described subsequently.

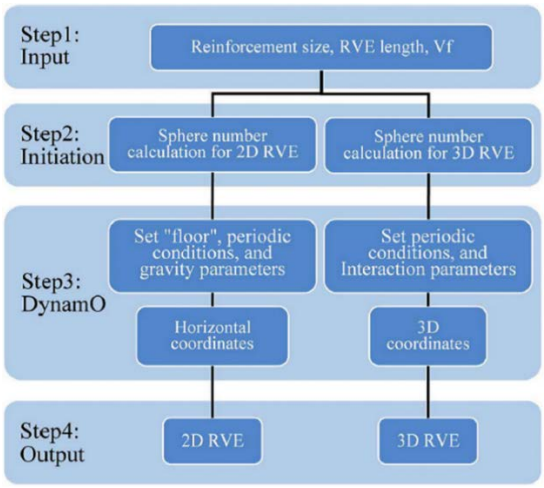

Figure 24. Algorithm flowchart for random RVE generation.

The first step in using the algorithm involved preparing the input for the procedure, including the RVE size and reinforcement dimensions which can be constant or vary randomly depending on the script code (see Fig. 24). For unidirectional continuous fiber-reinforced composites the 2D cross-section perpendicular to the fibers defined the simulation space. During the subsequent step the simulation was initialized using the input values, which included defining the number of fibers, collision times or events, and the initial position of the fibers [39,40].

The third step required performing necessary operations within DynamO to generate the particle output coordinate files. For generation of 2D periodic RVEs, the concept of gravity was used. First, the constant radius spheres were packed in a 3D simulation space, then the spheres were released and allowed to drop to a 2D plane or "floor" (see Fig. 25). The boundary constraints of the simulation floor along the in-plane directions were configured to generate the desired periodic RVE geometry. In order to control the periodic particle distribution along one direction, a "wall" type constraint was used to define the boundary of the simulation space. Figure 25 illustrates periodic constraints applied along the *x*–direction where particles can transfer randomly within the floor plane from one side to the other and particles can only cross the boundaries perpendicular to the *x*–direction. For generating RVEs with periodic geometry along both *x*– and *y*–directions, the wall constraints were not required such that particles were allowed to freely cross all boundaries. The total number of events were adjusted to control the total computational time, where for a personal computer with 3.4 GHz processor and 16 GB RAM, 100,000 events required approximately 10s on average to converge.

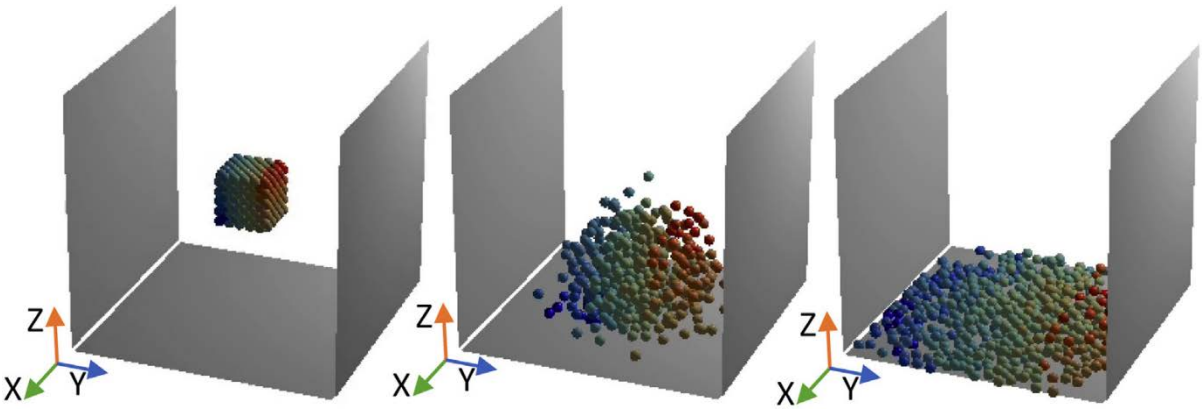

Figure 25. RVE generation procedure for 2D randomly distributed fibers with *x*–direction periodic geometry.

The final step (see Fig. 25) involved transforming the particle coordinates from the generated output file in step 3 to the commercial finite element software Abaqus and adjusting the RVE geometry to generate the proper periodic geometric model for subsequent finite element analysis. For high volume fraction simulations, there are more opportunities for particles to be in contact during RVE generation, however, in reality a small gap between fibers always exists due to very low but tangible particle crimp [22]. At the same time, contact between particles will lead to very small elements in FEA, which also causes unnecessary computational time or failure of convergence during analysis. Consequently, the

minimum distance between particles in the developed algorithm was limited to 0.25% of the particle diameter. Furthermore, Python scripts were used to generate the solid model of the 2D RVEs and to ensure that periodic geometries were maintained, where two examples with single direction periodic boundaries are shown in Fig. 26 (one with constant diameter fibers and the other with variable diameter fibers).

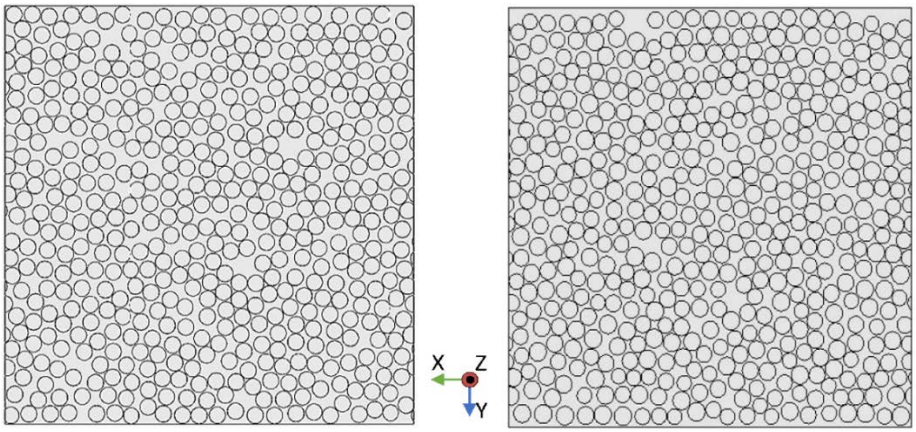

(a) (b)

Figure 26. Examples of generated 2D RVEs with nonuniform fiber spatial dispersions having periodic geometry along *x*–direction and V_f = 0.62, (a) constant diameter; (b) variable diameter.

4.3 Mechanical property assessment of generated RVEs

A high-fidelity assessment of the mechanical properties of composites was the main motivation for developing an algorithm to randomly generate realistic RVEs with nonuniformly distributed reinforcements. Accordingly, the degree of RVE nonuniformity, and thus the reliability of the developed EDMD-based algorithm, can be examined further by evaluating mechanical properties for both unidirectional fiber-reinforced and particulate-reinforced composites. For this purpose, the commercial FEA software Abaqus was utilized, and the predicted values of the engineering constants along different material directions were compared for a unidirectional fiber-reinforced composite material.

4.3.1 Material description

The unidirectional continuous E-glass fiber-reinforced Epikote 828/NMA/BDMA (100:60:1) epoxy material system assessed by Tong et al. [41] was considered in this study. The constituent isotropic elastic properties were determined by approximating typical values for E-glass fibers and epoxy resins found in the literature [42,43]. The resulting constituent property values were E_{1f} = 72 GPa, E_{1m} = 3.35

GPa, v_{12f} = 0.21, v_{12f} = 0.35 and were used for analysis of the glass fiber/epoxy composite. RVEs with various volume fractions were analyzed in this study.

4.3.2 Numerical micromechanical finite element analysis

It was assumed that the unidirectional glass fiber-reinforced/epoxy composites undergo a linear elastic plane strain deformation when loaded in tension along the transverse fiber directions, thus the generated 2D RVEs were considered for obtaining the transverse elastic response of the composite. The square shaped RVEs had lengths of 500 μm and nonuniformly distributed fibers with initially constant diameter of D_f = 20 μm. Three-node linear plane strain elements (i.e., CPE3) were used to mesh each RVE, and it was assumed that the fibers and matrix are perfectly bonded. In order to evaluate the composite transverse modulus E_{22} and the Poisson ratio v_{23}, a horizontal strain of 0.5% was applied to the RVEs, while for evaluation of E_{33} and v_{32} a vertical strain of 0.5% was applied to the RVEs (see Fig. 27). Volume averaging techniques [42] were used to evaluate the elastic constants. For the 2D model area averaging is equivalent to volume averaging since the reinforcement fibers are continuous. Furthermore, assuming a linear elastic response the volume averaged modulus can be written in terms of volume averaged stress and the corresponding volume averaged strain, while the corresponding Poisson's ratio is evaluated as follows:

$$E_{kk} = \frac{\sum_{i=1}^{n} \sigma_{kk}^{i} A^{i}}{\sum_{i=1}^{n} \varepsilon_{kk}^{i} A^{i}}, \qquad \nu_{jk} = \frac{\sum_{i=1}^{n} \varepsilon_{kk}^{i} A^{i}}{\sum_{i=1}^{n} \varepsilon_{jj}^{i} A^{i}} \tag{4-1}$$

where n indicates the total number of elements in the RVE mesh, σ_{kk}^{i} and ε_{kk}^{i} respectively denote the normal stress and strain components for element i, and A^i is the area of element i.

Resultant normal stress distributions for a 2D RVE with 62% fiber volume fraction for both loading cases are depicted in Fig. 27, which illustrates that stress concentrations located at the fiber/matrix interfaces were aligned with the loading direction as expected. Also, the magnitude of the local normal stresses greatly depends on the distance between fibers, where maximum normal stresses resulted in regions with higher fiber concentrations. Using Eq. (4-1) and E_{22} as a metric, a mesh sensitivity analysis was performed with the 62% fiber volume fraction RVE to determine the appropriate element size for all RVEs analyzed. Figure 28 demonstrates the effect of mesh size on E_{22}, which indicates that an element size lower than 30 μm^2 leads to a convergence of the results. For this study, an element size of 30 μm^2 was utilized for all 2D RVEs.

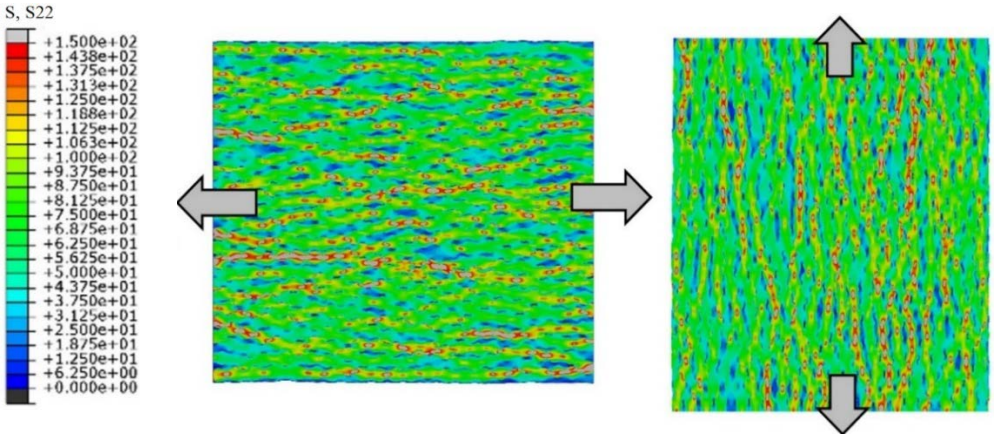

(a) Horizontal loading (b) Vertical loading

Figure 27. Normal stress distribution along loading directions for 2D RVEs with V_f = 0.62, (a) horizontal loading, and (b) vertical loading.

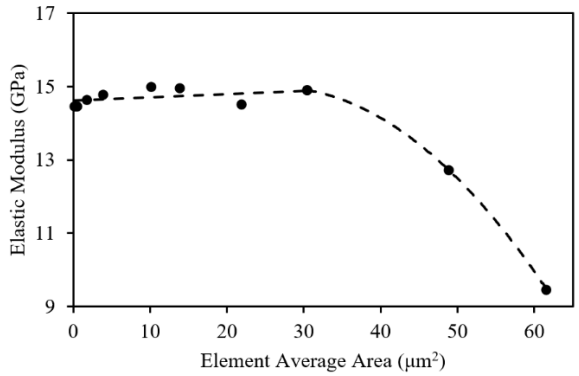

Figure 28. Effect of mesh size on transverse Young's modulus for 2D RVE with V_f = 0.62.

Table 1 presents the evaluated elastic constants for the RVE with V_f = 0.62 as well as the experimental data for the material with the same V_f. The predicted Young's moduli correlate better with the experimental data [43] in comparison to the Halpin-Tsai predictions [44], while the evaluated Poisson's ratios correlate well with experimental data for both cases. Furthermore, unidirectional fiber-reinforced composites typically exhibit transversely isotropic behaviour in accordance with Eq. (4-2), thus the consistency of the elastic properties in both transverse directions of the RVE can be used to assess the degree of nonuniformity of the fibers and provide another form of validation for the RVE generation algorithm.

$$E_{22} = E_{33},\ \nu_{23} = \nu_{32},\ \frac{\nu_{32}}{E_{33}} = \frac{\nu_{23}}{E_{22}} \tag{4-2}$$

Table 1. Evaluated and experimental elastic constants for randomly distributed 2D RVE with $V_f = 0.62$.

	E_{22} (GPa)	E_{33} (GPa)	ν_{23}	ν_{32}
FEA	14.452	14.324	0.344	0.338
Halpin-Tsai	15.18	–	0.33	–
Experimental [41]	13	–	0.3	–
Error 1[a] (%)	4.79	5.64	7.5	5.62
Error 2[b] (%)	11.16	10.18	14.7	12.67

[a] Comparing FEA result with Halpin-Tsai formula
[b] Comparing FEA result with experimental data

As can be inferred from Table 1, the relations defined by Eq. (4-2) held for the RVE analyzed. These results highlight that the fibers have been ideally distributed in the RVE in both transverse directions, suggesting that the EDMD-based algorithm can generate practical RVEs.

To further demonstrate the capability of the algorithm to generate RVEs with nonuniform fiber distributions, five different RVEs with the same V_f = 62% were assessed. The evaluated volume averaged transverse modulus for these RVEs is presented in Table 2, demonstrating consistency in the obtained results and stability of the EDMD-based algorithm. Additional FEA was conducted for a number of similar RVEs with a wide range of fiber volume fractions (i.e., V_f = 0.30, 0.40, 0.50, 0.62). The corresponding mechanical properties are shown in Table 3 along with predictions obtained using Halpin-Tsai expressions. These results reveal that the algorithm can randomly generate practical nonuniformly distributed RVEs since predicted E_{22} and E_{33} values for a specific fiber volume fraction are similar in magnitude, which was the main focus of the study. These results also highlight that the developed algorithm can generate consistent randomly distributed RVEs over a wide range of fiber volume fractions. It should be noted that the predicted moduli have a notable discrepancy in comparison with those predicted using the Halpin-Tsai relation, which assumes a certain structured arrangement of fibers (i.e., not randomly distributed). A similar range of discrepancy was also reported by Pathan et al. [45].

Table 2. Evaluated transverse elastic modulus for randomly distributed 2D RVEs with $V_f = 0.62$ and different random geometries.

	Model 1	Model 2	Model 3	Model 4	Model 5
E_{22} (GPa)	14.45	14.38	14.14	14.64	14.98
Error 1[a] (%)	0.46	0.95	2.6	0.84	3.18

[a] Results were compared with the average of these five models

Table 3. Evaluated elastic constants for randomly distributed 2D RVEs with different V_f.

V_f (%)	E_{22} (GPa)	E_{33} (GPa)	ν_{23}	ν_{32}	$\frac{E_{22}}{E_{33}}$	$\frac{\nu_{23}}{\nu_{32}}$	$\frac{E_{22}\nu_{32}}{E_{33}\nu_{23}}$
	FEM / Ref. [44]						
30 (case 1)	6.10 / 6.91	6.00 / 6.91	0.500 / 0.46	0.493 / 0.46	1.017	1.009	1.008
40 (case 2)	7.57 / 8.74	7.52 / 8.74	0.471 / 0.42	0.468 / 0.42	1.006	1.007	0.999
50 (case 3)	9.70 / 11.12	9.67 / 11.12	0.424 / 0.37	0.420 / 0.37	1.003	1.010	0.994
62 (case 4)	14.45 / 15.18	14.32 / 15.18	0.344 / 0.32	0.338 / 0.32	1.008	1.018	0.991
Error (%)	E_{22} (GPa)	E_{33} (GPa)	ν_{23}	ν_{32}	$\frac{E_{22}}{E_{33}}$	$\frac{\nu_{23}}{\nu_{32}}$	$\frac{E_{22}\nu_{32}}{E_{33}\nu_{23}}$
	FEM / Ref. [44]						
Case 1	11.8	13.3	8.3	7.3	1.72	0.93	0.78
Case 2	13.4	14.0	12.2	11.4	0.64	0.68	0.04
Case 3	12.72	13.01	14.60	13.51	0.33	0.95	0.62
Case 4	4.8	5.6	7.5	5.6	0.89	1.78	0.87

In order to enhance the consistency of the FE model with real UD composites and further validate the RVE generation algorithm, additional simulations were performed on the RVEs with variable diameter fibers for two high fiber volume fractions (i.e., V_f = 0.50, 0.62). In this set of simulations, the variable fiber diameter was defined in the range of $0.9D_f \leq D_{f\,(variable)} \leq 1.1D_f$. The calculated volume averaged transverse modulus for these models were compared to the constant diameter RVE models presented in Table 1 (Fig. 29). It is clear that the consequence of inequality of fiber size can alter the elastic constant up to 10% for the E-glass/epoxy material considered in this study. It is worth noting that same volume fraction was obtained using two distinct fiber distributions.

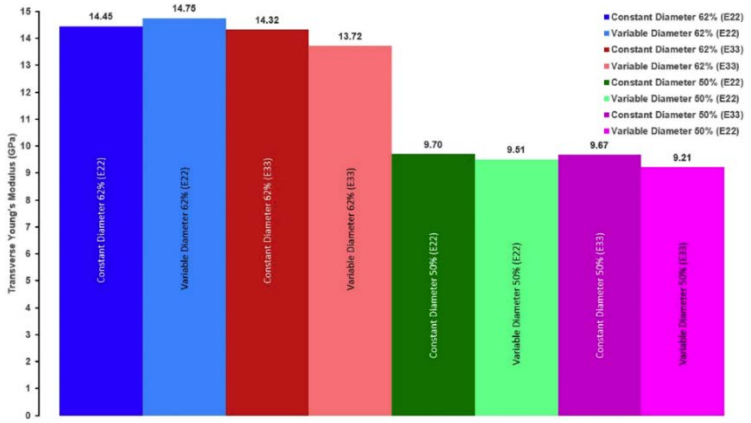

Figure 29. A comparison of volume averaged transverse elastic modulus for RVEs with constant diameter and variable diameter fibers, for a glass fiber/epoxy UD composite with V_f = 0.50 and 0.62.

4.4 Conclusions

An effective and versatile algorithm based on event-driven molecular dynamics theory was developed for rapidly generating random representative volume elements (RVEs) with nonuniformly distributed fibers with either constant or variable diameters. The computational requirement to generate all the RVEs in this study was no more than 20 seconds on a stand-alone personal computer. Finite element analysis was performed on the generated RVEs to provide a form of validation for the developed algorithm. The volume averaged elastic constants for the unidirectional fiber-reinforced composites were equivalent in both transverse directions for all considered volume fractions. Thus, the expected transversely isotropic response was confirmed which indicated that the nonuniform dispersion of fibers in the randomly generated RVEs was indeed representative of the actual material. Additionally, the obtained volume averaged elastic properties from RVEs with the same fiber volume fractions and different generated fiber spatial dispersions were repeatable within 5% of the mean values.

The validated results presented provide confidence in the ability of the developed algorithm to rapidly generate realistic RVEs with high reinforcement volume fractions for unidirectional fiber-reinforced composite materials. In practice, the algorithm can be used as a design tool to accurately evaluate and tailor the mechanical properties of distinct material systems for a specific structural application, and for accurate microstructural assessment including predictions of microscopic crack progression which requires RVEs with realistic nonuniformly dispersed reinforcements. The developed algorithm was used to generate RVEs for subsequent studies described in Chapters 5-7.

References

[1] Z.Q. Wang, X.Q. Wang, J.F. Zhang, W.Y. Liang, L.M. Zhou, Automatic generation of random distribution of fibers in long-fiber-reinforced composites and mesomechanical simulation, Materials and Design 32 (2011) 885–891.

[2] F. Naya, C. Gonzalez, C.S. Lopes, S.V. Veen, F. Pons, Computational micromechanics of the transverse and shear behavior of unidirectional fiber reinforced polymers including environmental effects, Composites Part A: Applied Science and Manufacturing 92 (2017) 146–157.

[3] X.Q. Wang, J.F. Zhang, Z.Q. Wang, S. Zhou, X.Y. Sun, Effects of interphase properties in unidirectional fiber reinforced composite materials, Materials and Design 32 (2011) 3486–3492.

[4] M.J. Mahmoodi, M.M. Aghdam, M. Shakeri, Micromechanical modeling of interface damage of metal matrix composites subjected to off-axis loading, Materials and Design 31 (2010) 829–836.

[5] S. Kirtania, D. Chakraborty, Multi-scale modeling of carbon nanotube reinforced composites

with a fiber break, Materials and Design 35 (2012) 498–504.

[6] D.W. Sohn, Periodic mesh generation and homogenization of inclusion-reinforced composites using an element-carving technique with local mesh refinement, Composite Structures 192 (2018) 153–164.

[7] J. Montesano, B. McCleave, C.V. Singh, Prediction of ply crack evolution and stiffness degradation in multidirectional symmetric laminates under multiaxial stress states, Composites Part B: Engineering 133 (2018) 53–67.

[8] S. Li, A. Wongsto, Unit cells for micromechanical analyses of particle-reinforced composites, Mechanics of Materials 36 (2004) 543–572.

[9] A. Wongsto, S. Li, Micromechanical FE analysis of UD fiber-reinforced composites with fibers distributed at random over the transverse crosssection, Composites Part A: Applied Science and Manufacturing 36(2005) 1246–66.

[10] S. Li, Boundary conditions for unit cells from periodic microstructures and their implications, Composite Science & Technology 68(2008) 1962–1974.

[11] S. Krop, H.E.H. Meijer, L.C.A. Breemen, Multi-mode modeling of global and local deformation, and failure, in particle filled epoxy systems, Composites Part A: Applied Science and Manufacturing 88(2016) 1–9.

[12] S.A. Meguid, G. Shagai, R. Paskaramoorthy, On the local elastic–plastic behaviour of the interface in titanium/silicon carbide composites, Composites Part A: Applied Science and Manufacturing 33(2002) 1629–1640.

[13] S. Kammoun, I. Doghn, L. Adam, G. Robert, L. Delannay, First pseudo-grain failure model for inelastic composites with misaligned short fibers, Composites Part A: Applied Science and Manufacturing 42 (2011) 1892–1902.

[14] J.H. Oh, K.K. Jin, S.K. Ha, Interfacial strain distribution of a unidirectional composite with randomly distributed fibers under transverse loading, Journal of Composite Materials 40 (2005) 759–778.

[15] K.K. Jin, J.H. Oh, S.K. Ha, Effect of fiber arrangement on residual thermal stress distributions in a unidirectional composite, Journal of Composite Materials 41 (2007) 591–611.

[16] A.A. Gusev, P.J. Hine, I.M. Ward, Fiber packing and elastic properties of a transversely random unidirectional glass/epoxy composite, Composite Science & Technology 60(2000) 535–541.

[17] H. Ghayoor, S.V. Hoa, C.C. Marsden, A micromechanical study of stress concentrations in composites, Composites Part B: Engineering 132 (2018) 115–124.

[18] S. Yang, A. Tewari, A.M. Gokhale, Modeling of non-uniform spatial arrangement of fibers in a ceramic matrix composite, Acta Materialia 45 (1997) 3059–3069.

[19] H. Qing, Automatic generation of 2D micromechanical finite element model of silicon–carbide/aluminum metal matrix composites: Effects of the boundary conditions, Materials and Design 44 (2013) 446-453.

[20] W.S. Jodrey, E.M. Tory, Computer simulation of close random packing of equal spheres, Physical Review A 32 (1985) 2347–2351.

[21] A.R. Melro, P.P. Camanho, S.T. Pinho, Generation of random distribution of fibers in long-fiber reinforced composites, Composite Science & Technology 68 (2008) 2092–2102.

[22] V.S. Romanov, S. Lomov, Y. Swolfs, S. Orlova, L. Gorbatikh, I. Verpoest, Statistical analysis

of real and simulated fiber arrangements in unidirectional composites, Composite Science & Technology 87 (2013) 126–134.

[23] L. Yang, Y. Yan, Z.G. Ran, Y.J. Liu, A new method for generating random fiber distributions for fiber reinforced composites, Composite Science & Technology 76 (2013) 14–20.

[24] K.P. Babu, P.M. Mohite, Upadhyay, Development of an RVE and its stiffness predictions based on mathematical homogenization theory for short fiber composites, International Journal of Solids and Structures 130-131 (2018) 80-104.

[25] H. Liu, D. Zeng, Y. Li, L. Jiang, Development of RVE-embedded solid elements model for predicting effective elastic constants of discontinuous fiber reinforced composites, Mechanics of Materials 93 (2016) 109-123.

[26] Y. Pan, L. Iorga, A.A. Pelegro, Numercial generation of random chopped fiber composite RVE and its elastic properties, Composite Science & Technology 68 (2008) 2792-2798.

[27] V.A. Buryachenko, N.J. Pagano, R.Y. Kim, J.E. Spowart, Quantitative description and numerical simulation of random microstructures of composites and their effective elastic moduli, International Journal of Solids and Structures 40 (2003) 47–72.

[28] T.J. Vaughan, C.T. McCarthy, A combined experimental-numerical approach for generating statistically equivalent fiber distributions for high strength laminated composite materials, Composite Science & Technology 70 (2010) 291–297.

[29] W.Z. Wang, Y.H. Dai, C. Zhang, X.S. Gao, M.Y. Zhao, Micromechanical modeling of fiber-reinforced composites with statistically equivalent random fiber distribution, Materials 9 (2016) 1–14.

[30] T.T. Zhang, Y. Yan, A comparison between random model and periodic model for fiber-reinforced composites based on a new method for generating fiber distributions, Polymer Composites 38 (2017) 77–86.

[31] B.J. Alder, T.E. Wainwright, Studies in molecular dynamics. I. general method, The Journal of Chemical Physics 31 (1959) 459–466.

[32] B.D. Lubachevsky, F.H. Stillinger, Geometric properties of random disk packings, Journal of Statistical Physics 60 (1990) 561–583.

[33] E. Ghossein, M. Levesque, A comprehensive validation of analytical homogenization models: The case of ellipsoidal particles reinforced composites, Mechanics of Materials 75 (2014) 135–150.

[34] Z.H. Zhang, X.G. Song, Y. Liu, D. Wu, C.M. Song, Three-dimensional mesoscale modelling of concrete composites by using random walking algorithm, Composite Science & Technology 149 (2017) 235–245.

[35] A. Donev, S. Torquato, F.H. Stillinger, R. Connelly, Jamming in hard sphere and disk packings, Journal of Applied Physics 95 (2004) 989–999.

[36] R. Sain, Numerical simulation of pore-scale heterogeneity and its effects on elastic, electrical and transport properties, Stanford University, 2010.

[37] G. Canalotti, On the generation of RVE-based models of composites reinforced with long fibers or spherical particles, Composite Structures 138 (2016) 84-95.

[38] DynamO. http://dynamomd.org/, 2017 (accessed 13 November 2017).

[39] M.N. Bannerman, R. Sargant, L. Lue, DynamO: A free O(N) general event-driven simulator.

Journal of Computational Chemistry 32 (2011) 3329–3338.

[40] S. Strobl, M.N. Bannerman, T. Poeschel, Stable algorithm for event detection in event-driven particle dynamics: logical states, Computational Particle Mechanics 3 (2016) 383–388.

[41] J. Tong, F.J. Guild, S.L. Ogin, P.A. Smith, On matrix crack growth in quasi-isotropic laminates-I. experimental investigation, Composite Science & Technology 57 (1997) 1527–1535.

[42] D. Trias, J. Costa, J.A.Mayugo, J.E. Hurtado, Random models versus periodic models for fiber reinforced composites, Computational Materials Science 38 (2006) 316–324.

[43] Soden P, Hinton M, Kaddour A, Lamina properties lay-up configurations and loading conditions for a range of fiber-reinforced composites laminates, Composite Science & Technology 58 (1998) 1225–1254.

[44] J.C. Halpin, J.L. Kardos, The Halpin-Tsai Equations: A Review, Polymer Enginering & Science 16 (1976) 344–352.

[45] M.V. Pathan, V.L. Tagarielli, S. Patsias, P.M. Baiz-Villafranca, A new algorithm to generate representative volume elements of composites with cylindrical or spherical fillers, Composites Part B: Engineering 110 (2017) 267–278.

Chapter 5

Assessing the effects of ply constraints on local stress states in cross-ply laminates containing manufacturing-induced defects

(Published manuscript, Composite Part B: Engineering 199 (2020) 108227)

5.1 Introduction

Widespread applications of high-performance fiber-reinforced plastic (FRP) composite materials in different industrial sectors have attracted much attention on the assessment of their long-term durability and inherent damage tolerance characteristics. Particularly, their complex progressive failure processes have been extensively investigated [1]. At the ply level, damage evolution in mechanically loaded FRP laminates typically begins with a "sub-critical" stage of crack formation in the transverse or off-axis plies. Sub-critical damage refers to the formation and multiplication of intralaminar ply cracks which span through the ply thickness and propagate along the fiber direction, a process described as tunneling. Multiplication of ply cracks can occur due to the constraining effect imposed by the adjacent plies on the cracking plies in the laminate [2]. This sub-critical stage is often followed by the growth of "critical" damage mechanisms (e.g., delamination, fiber breakage, and fiber micro-buckling) which can lead to catastrophic laminate failure [3]. For composite laminates under cyclic loading, the early stages involve the growth and multiplication of sub-critical ply cracks which may cause substantial degradation of stiffness without loss of material integrity. Hence, it is necessary to clarify the inherent progressive failure processes of laminated composites to adequately predict their service life.

Although an improved understanding of progressive damage evolution in laminated composites has been gained, predicting this response remains challenging due to the complex multiscale nature of failure. Numerous mechanisms-based [4–11] and continuum damage mechanics-based [2,12–15] models have been developed to address the overall degradation of FRP laminates stemming from the accumulation of fully grown ply cracks. The prediction models developed in these studies all considered the effect of ply constraints on ply crack multiplication in laminates. This important characteristic was attributed to the so-called in-situ "strength" of plies, where the ply thickness was found to be a key factor [16–20]. Nevertheless, these studies reported the presence of the constraining effect in laminates only when full-thickness ply cracks were formed, not accounting for the changes in the local stress fields that could influence the earlier stages of the individual ply crack formation (i.e.,

fiber/matrix debonding and matrix micro-cracking). The current study is focused on this missing aspect, which is addressed by an energy-based approach that utilizes independently obtained material values rather than derived constants such as the in-situ strength.

During the last two decades the formation of intralaminar ply cracks (i.e., growth of fiber/matrix debonds and local matrix cracks) was extensively investigated [21–44] where two approaches to capturing local failure have been considered. Asp et al. [21–24] initially proposed the concept of critical dilatation energy density as an indicator of brittle cavitation in epoxies. Many studies subsequently adopted the concept of dilatation-induced brittle cavitation to predict fiber/matrix debonding in investigating the early stages of intralaminar ply cracking [25–30]. These studies found that brittle cavitation-induced cracking was the first failure event close to the fiber/matrix interface within the matrix. Nonetheless, it remains possible that the resin-rich pockets within the transverse layers may experience significant local inelastic deformation once the cavitated brittle ply cracks grow. Using a distinct approach, Melro et al. [31] proposed a comprehensive plasticity model with a pressure-dependent yield criteria to estimate the inelastic response of polymers. This approach was later used to develop micromechanical finite element (FE) models for predicting transverse ply cracking in constrained plies [32,33]. The importance of including the inelastic matrix behaviour for predicting ply cracking was also discussed in the study by Marklund et al. [30] and Saito et al. [34].

The focus of many computational micromechanics studies has been on the influence of manufacturing induced defects and their severity on the early stages of ply crack formation in laminates. Elnekhaily and Talreja [27,28] were the first to consider the degree of fiber spatial nonuniformity on the local failure based on the critical values of dilatation and distortion energy densities. In their simulation of the fiber distributions, the statistics reflecting the inter-fiber distance was found to be the governing parameter in controlling the applied strain at which local cavitation occurs. In the study by Zhuang et al. [35], who analyzed the growth and coalescence of the debond cracks, the inter-fiber distance was found to be a decisive parameter. Sudhir and Talreja [29] and Ghayoor et al. [36] investigated the effect of fiber spatial non-uniformity on the initiation of failure due to the presence of resin-rich and fiber cluster zones. The presence of these zones was found to be important in initiation and progression of ply cracking. Through an experimental investigation of the manufacturing-induced defects in laminates, Hamidi et al. [37] observed that voids in resin transfer molded composites form the majority of defects. This observation suggests that it is important to study how the local stress states in the vicinity of voids might affect the initiation of ply cracking. In another study, Zhang et al. [38] conducted an experimental investigation on the microstructure of fiber-reinforced thermoplastic

prepreg laminates to characterize and statistically quantify the distribution of manufacturing-induced voids. They developed a statistical distribution function to describe the shape and distribution of voids that would be useful for representing the presence of voids in a representative volume element (RVE). Chowdhury et al. [39] and Sudhir and Talreja [29] investigated the effect of local voids on the initiation and growth of damage. Both these studies used the dilatational energy-based criterion to study fiber/matrix debonding induced by brittle cavitation. The importance of fiber/matrix debonding in the ply cracking process has been shown by several experimental studies [25,40,41]. The interfacial debonding process has been studied by fracture mechanics approaches, e.g., by [35,42]. Cohesive zone models have also been utilized for this purpose [32–34,43,44], which require parameters that are difficult to calibrate experimentally and are often "tuned" for a specific application [41].

There has been notable progress in the development of computational micromechanical models for predicting the early stages of ply cracking process for unconstrained unidirectional plies. It is, however, to be expected that the presence of the constraining plies in a laminate will affect this process. The present study is therefore aimed at clarifying this effect. For this purpose, a computational micromechanical framework was employed here to investigate the significance of the constraining effect on the initiation of local failure in the 90° ply of a [0/90/0] cross-ply laminate containing manufacturing-induced defects. Following the previous studies of the early failure events in the unconstrained unidirectional composite, the energy-based approach to the initiation of these events in the 90° ply was taken. The manufacturing-induced defects included in the 90° ply are nonuniform fiber spatial dispersion and matrix microvoids. Parametric studies were performed to assess the influence of different factors on the degree of ply constraining, including the microvoid size, ply interface resin-rich layer thickness and thermal residual stresses.

5.2 Computational model development

5.2.1 Micromechanical representation

A computational model was developed for a carbon fiber/epoxy material system. The corresponding representative volume element (RVE) for a [0/90/0] cross-ply laminate contained a thin 90° lamina, comprising of explicitly modelled fibers and matrix phases, with homogenized adjacent 0° layers. Figure 30 illustrates the schematic of the 2D RVE of the laminate where b, t, and w are the thickness of the transverse 90° ply, the thickness of the homogenized adjacent 0° layers and the width of the RVE, respectively. In the study, 80 μm and 175 μm thicknesses were assigned to the 90° and 0° plies, respectively. The fiber volume fraction of the 90° ply was set to V_f = 56%, which is representative of

laminates comprised of unidirectional prepreg tapes that are consolidated by hot pressing or in an autoclave. A constant fiber diameter D_f = 5.2 μm was also assigned. Perfect bonding was assumed for the interfaces between layers while the thickness of the pure resin-rich layer between two plies was zero. Similarly, in the 90° ply the fiber/matrix interfaces were regarded as perfectly bonded to represent the case of a strong interfacial bond. It should be noted that for the case where the fiber/matrix interfacial bonding is weak an alternative modeling approach to represent the interface may be required; however, this is beyond the scope of this study.

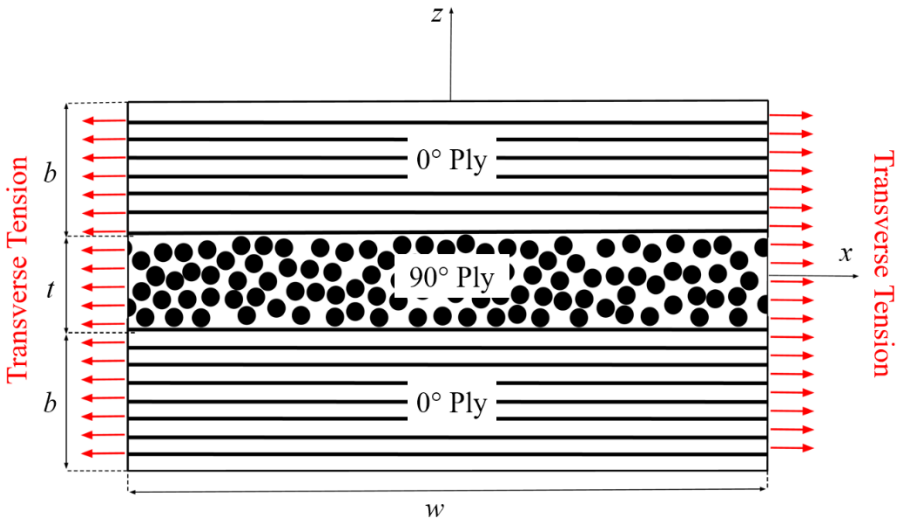

Figure 30. Schematic representation of the 2D RVE with 1D periodicity of the transverse layer in the *x*–direction.

Fibers in the 90° ply were treated as transversely isotropic and linear-elastic, while the assumed pressure-dependent inelastic behaviour of the isotropic matrix phase was captured by employing the Drucker-Prager inner cone in Abaqus [45]. The used yield criterion was an extended version of the conventional Drucker-Prager, as described by Yu et al. [46]. Table 4 shows the utilized properties for the carbon fibers and epoxy matrix in the computational model. It is worth noting that the inelastic behaviour of the epoxy was modelled based on the experimental results reported by Fiedler et al. [47] and Guild et al. [48], which were later outlined by Melro et al. [44]. The effective transversely isotropic linear-elastic properties assigned to the 0° plies were taken from experimental data reported in Refs. [49–51].

Table 4. Properties of the fibers [32], epoxy-resin [47,48], and homogenized lamina [49–51].

Material Property *	**Fibers (Carbon)**	**Matrix (Epoxy)** +	**Homogenized Outer Plies (V_f = 60%)**
Young's Moduli			
$E_{11}(\text{GPa})$	276	3.76	171.42
$E_{22}(\text{GPa})$	15	-	9.08
Poisson's Ratio			
ν_{12}	0.2	0.39	0.32
ν_{23}	0.07	-	-
Shear Moduli			
$G_{12}(\text{GPa})$	15	1.35	5.29
$G_{23}(\text{GPa})$	7	-	3.92
Thermal Expansion Coefficient ($°C^{-1}$)			
$\alpha_{11}(°\text{C}^{-1})$	-0.5×10^{-6}	58×10^{-6}	-5.5×10^{-6}
$\alpha_{22}(°\text{C}^{-1})$	15×10^{-6}	-	25.8×10^{-6}
Plastic Poisson's Ratio			
ν_p	-	0.3	-
Tensile Strength			
$\sigma_{11}^{UT}(\text{MPa})$	-	93	-
Compressive Strength			
$\sigma_{11}^{UC}(\text{MPa})$	-	350	-

* 1, 2, and 3 are the principal material coordinate system axes for a ply, denoting the fiber direction, in-plane transverse direction and out-of-plane transverse direction, respectively.
+ Note, the integer subscripts can be dropped for the isotropic matrix properties.

5.2.2 Representative volume element generation

The method developed for generating an RVE for unidirectional composites containing a periodically nonuniform fiber spatial dispersion in the 90^o ply (Fig. 30) is described by Li et al. [52] (see Chapter 4). The same study reported the results of two comprehensive RVE validation efforts. First, statistical analyses were conducted to compare the degree of nonuniformity of fiber distribution within the generated RVEs with the same analyses based on the observed microstructures of the same

unidirectional composite material. Also, volume averaged elastic constants for the generated RVEs with different fiber dispersions were calculated and verified with experimental data. Therefore, for brevity details will not be described here and the reader is referred to Ref. [52]. As noted in that work, the size of an RVE should generally be determined to properly capture the average local material response in terms of the damage modes, while also balancing the computational effort. Elnekhaily et al. [27] investigated the influence of RVE size on the local stress fields in a transversely loaded unidirectional composite with linear elastic fibers and matrix and found that the adequate minimum size in terms of the number of fibers was 200. In another investigation, Pathan et al. [53] calculated the elastic and damping properties of a unidirectional composite using different RVE sizes and found that the adequate minimum RVE size for the elastic case was given by $\delta = w/D_f = 24$, where w is the length of the square-shaped RVE and D_f is the fiber diameter. For the viscoelastic damping, a smaller RVE size, $\delta = 12$, was found to be adequate. In this study, the width of the RVE was chosen to be 200 μm ($\delta = 38.5$) which ensured that there were at least 420 fibers in the full-thickness 90° ply of all generated RVEs.

5.2.3 Finite element model

The local stress fields within the matrix of an RVE were calculated by a finite element (FE) model. For this purpose, using the commercial FE software Abaqus, CPEAR 4-node bilinear plane strain quadrilateral elements with reduced integration were used to mesh the homogenized 0° plies, while the constituents in the 90° layer of the RVE were meshed with a combination of CPE4R 4-node and CPE3 3-node plane strain elements (see Fig. 31). A plane strain analysis was used since the cross-ply laminate was subjected to uniaxial tensile loading and the fibers in the 90° ply were perfectly aligned. A uniform displacement with one-dimensional periodic boundary conditions (PBCs) along the x–direction were applied to the RVE (see Fig. 30) [54]. The effect of thermal cooldown was also studied by imposing temperature drops $\Delta T = -50$, -75 and -100°C before applying the displacement to the boundaries.

The local stress fields were calculated within four 10 μm square regions in the RVE to study the effects of different aspects of fiber arrangements on the stress fields. The regions, as illustrated in Fig. 32, were identified as “resin-rich”, “fiber cluster”, “interface” and “typical”, and henceforth denoted as the “specified zones”. Additionally, two separate scenarios were considered, one with a microvoid, and the other with a microcrack, as depicted in Fig. 32. In the first scenario, circular microvoids of different diameters were placed within the matrix with a minimum distance between the void and fiber surfaces (e.g., 10% of the fiber diameter) for resin-rich zones, as shown in Fig. 32 (b). It is worth noting that

since the focus of this study is to investigate the onset of local failure, and not the effective macroscopic response, only local voids were considered in the RVEs.

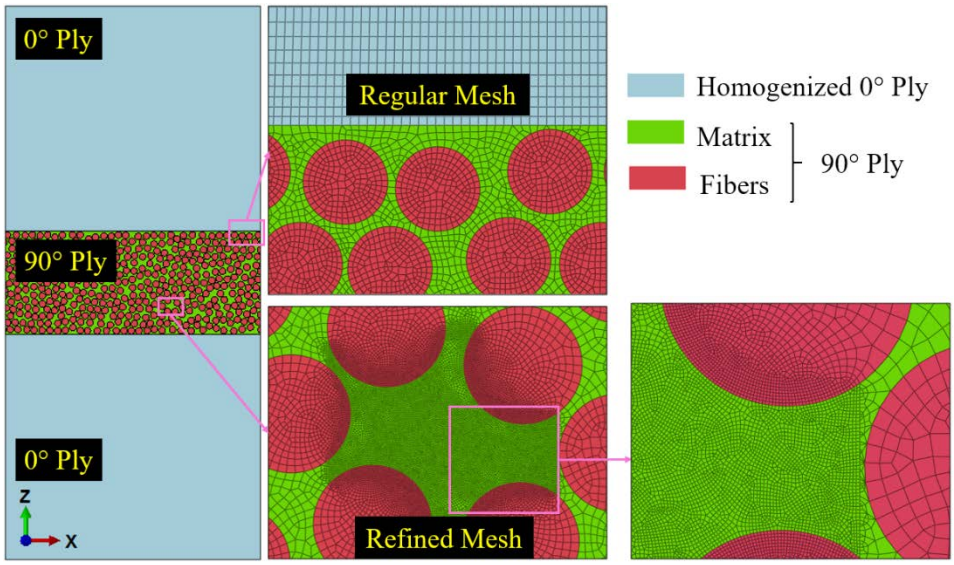

Figure 31. Representative FE model of the periodic RVE with 80 μm thick transverse layer.

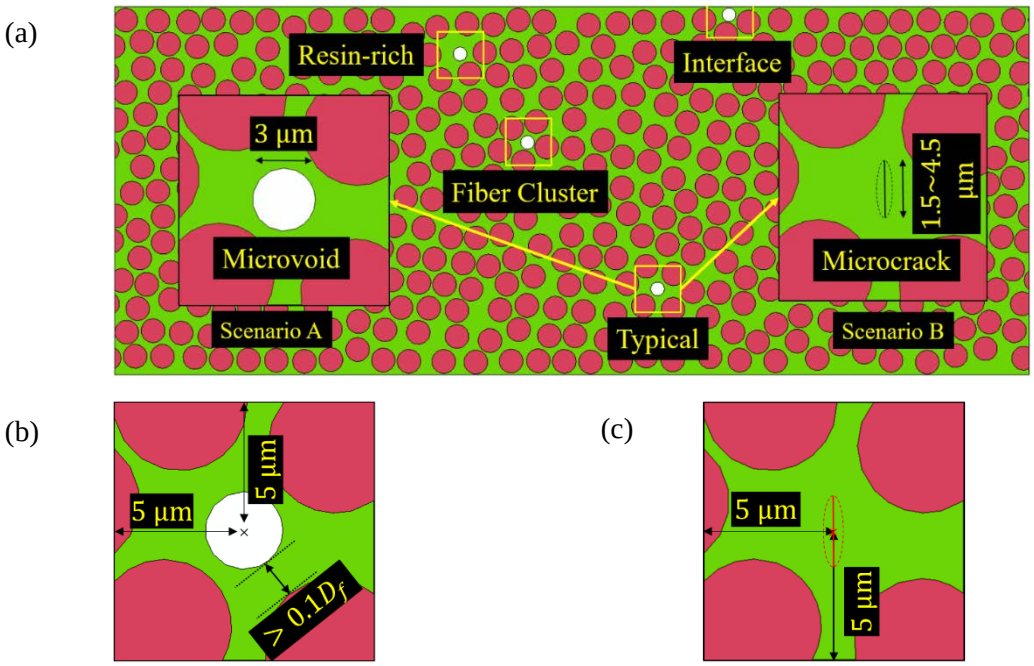

Figure 32. (a) Representation of the different specified zones, including microvoids (or microcrack), in the 90° layer of a representative FE model, (b) Location of a microvoid in a resin-rich zone, (c) Location of a microcrack in a resin-rich zone.

Microvoids have been observed in laminates at ply interfaces and various locations within the ply [55], and result directly from air entrapment during processing with various techniques (e.g., prepreg vacuum bagging/autoclave). In the second scenario, pre-existing microcracks were located in the different specified zones of the generated RVEs, and were oriented with surfaces perpendicular to the applied transverse load (see Fig. 32). Microcracks may stem directly from processing as a result of the cooldown step after curing. This size of microvoids is viewed as typical and sufficient to study their effect on failure initiation, while microcracks are expected to have more severe effect than the microvoids and this effect is expected to depend significantly on their length. Therefore, microcracks of different lengths in the range 1.5–4.5 μm in the resin-rich zone and 1.5–3.0 μm in other specified zones were introduced. A refined mesh for the matrix and fiber phases was used in the different specified zones, whereas a coarser mesh was used for the other "adjacent regions" in the RVE (see "regular mesh" in Fig. 31).

5.2.4 Stress and failure analysis

At the very beginning of the failure process in a cross-ply laminate subjected to axial tension, failure is expected to occur at points within the matrix of the 90° ply where critical conditions for failure initiation are reached. As described above, the intention of the current study was to investigate two possible failure events – brittle cavitation and yielding – as precursors to subsequent failure progression. For brittle cavitation in epoxy, the critical dilatation energy density criterion was used [21], and for yielding, the commonly used pressure-dependent yield criterion for polymers was employed. In stress terms, the yield criterion is expressed as a function of the second invariant of the deviatoric stress tensor (J_2) with the pressure sensitivity given by the first invariant of stress tensor (I_1). Equivalently, the corrected octahedral shear stress at yielding can be written as [59]:

$$\tau_0^* = \tau_0 - \mu\sigma_m \tag{5-1}$$

where $\tau_0 = \sqrt{2J_2/3}$ and the mean stress $\sigma_m = 1/3\ (\sigma_1 + \sigma_2 + \sigma_3)$. The coefficient of internal friction μ was set to 0.175, as was suggested for a similar epoxy by Elnekhaily and Talreja [28]. The corrected octahedral shear stress was used in the calculation of the distortional energy density.

When comparing the two failure events under the same conditions, the distortion energy density (U_d) and the dilatation energy density (U_v) were used for the occurrence of yielding and brittle cavitation, respectively. As known, total strain energy density (U) is given by:

$$U = U_v + U_d \tag{5-2}$$

where:

$$U_d = \frac{1}{2G} J_2 \tag{5-3}$$

$$U_v = \frac{1-2\nu}{6E} I_1^2 \tag{5-4}$$

where G, E, and ν are the shear modulus, Young modulus, and Poisson ratio, respectively. In the current study, inelastic behavior of the matrix was addressed by implementing the inner cone of Drucker-Prager where the yield surface is described as:

$$\Phi\left(\eta, \bar{c}\right) = \sqrt{J_2} + \eta\sigma_m - \bar{c} \tag{5-5}$$

where η and $\bar{c}$ are material constants. These material constants can be obtained by coinciding the Drucker-Prager surface at the inner edge of Mohr-Columb criteria as:

$$\eta = \frac{6\sin\phi}{\sqrt{3}\left(3+\sin\phi\right)}, \qquad \bar{c} = \frac{6c\cos\phi}{\sqrt{3}\left(3+\sin\phi\right)} \tag{5-6}$$

where φ and c are frictional angle and cohesion, respectively. Fitting the yield surface by the matrix uniaxial compressive (σ^{UC}) and tensile strength (σ^{UT}), frictional angle and cohesion are defined as:

$$\phi = \sin^{-1}\left(\frac{3\left(\sigma^{UC}-\sigma^{UT}\right)}{\sigma^{UC}+\sigma^{UT}}\right), \qquad c = \frac{\sigma^{UC}\sigma^{UT}}{3\left(\sigma^{UC}+\sigma^{UT}\right)}\left(\frac{3+\sin\phi}{\cos\phi}\right) \tag{5-7}$$

Utilizing reported data in Table 4, inputs for Abaqus FE code were prepared. In the conducted simulations, strain hardening and a non-associative flow rule were used while the dilatancy angle was set to zero.

5.3 Results and discussion

Before conducting the stress and failure analysis described above, the mesh sensitivity in the FE model was assessed. Due to the importance of inter-fiber spacing in determining the local stress fields, it was also necessary to assess if the distribution of inter-fiber spacing within the generated RVEs corresponds with what has been observed experimentally. The results of these assessments are presented in Section 5.3.1. This is followed by an in-depth assessment of ply constraining effects in Section 5.3.2. Here the influence of fiber clusters, resin-rich areas and ply interfaces, as well as microvoids and microcracks, are described using the specified zones illustrated in Fig. 32. The stress field results are expressed in

terms of the von Mises and hydrostatic stresses while the failure initiation criteria are in terms of the dilatation and distortion energy densities, as explained in Section 5.2.4. A discussion of all results is carried out in Section 5.3.3. Note that the parameters introduced in Section 5.2 are used for the FE models presented in Sections 5.3.1 and 5.3.2, unless stated otherwise.

5.3.1 Mesh sensitivity and fiber spatial dispersion assessment

A mesh sensitivity study was performed on the generated RVEs to determine the appropriate element size in both the specified zones and the other adjacent zones within the 90° ply, with a focus on the stresses in the specified zones (see Fig. 31). Figure 33 illustrates the variation of the normalized peak and the volume-averaged von Mises and hydrostatic stresses with the element size for the specified and adjacent zones. Results show that the proper element size d normalized by the fiber radius r_f, for the specified and adjacent zones is 0.03 μm and 0.18 μm, respectively, as indicated by vertical dashed lines in the figure. These normalized element sizes correspond to an element area of 0.028 μm^2 and 0.20 μm^2, respectively. The peak stresses within the elements were directly obtained from the Abaqus FE code while the volume-averaged stresses were calculated by using the following expression:

$$\sigma_{ij}^{avg} = \frac{\sum_{k=1}^{n} \sigma_{ij}^{k} A^{k}}{\sum_{k=1}^{n} A^{k}} \tag{5-8}$$

where n is the total number of elements, and A^k and σ_{ij}^k are the element area and stress components of the k^{th} element, respectively.

To thoroughly assess the nonuniformity of fiber spatial dispersions in the RVEs, a statistical analysis was also performed using the nearest neighbour distance distribution [56]. This distribution for one generated RVE was compared with the averaged distribution of ten additional RVEs with distinct nonuniform fiber spatial dispersions (respectively, blue and red histograms in Fig. 34). This verifies that the generated RVEs have a statistically equivalent fiber dispersion since the nearest neighbour distance distribution follows that obtained from fabricated unidirectional composite materials (see Ref. [56]).

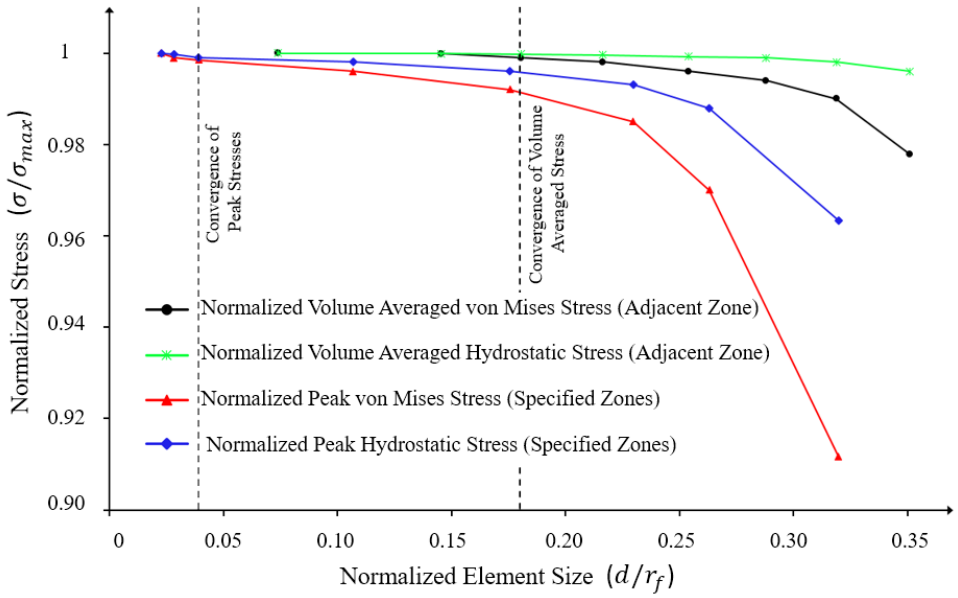

Figure 33. Normalized von Mises and hydrostatic stress variation with normalized element size for the matrix at the specified and adjacent zones of the 90° ply of the void contained in [0/90/0] laminate subjected to 0.6% transverse strain.

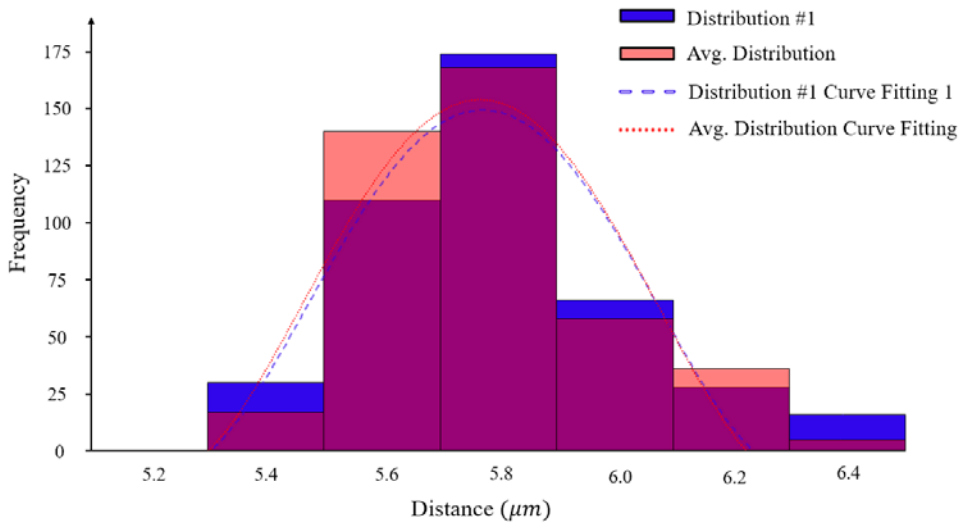

Figure 34. Nearest neighbour distance distribution of fibers in the transverse layer for one generated RVE (blue histogram and fit curve) and the averaged distribution from ten additional RVEs (red histogram and fit curve).

5.3.2 Assessment of ply constraining effects

To begin, the local stress fields were assessed to indicate the influence of the constraining effect of the 0^o plies onto the 90^o plies. To this end, FE models were developed to calculate the stress fields in the unconstrained 90° ply and the constrained 90^o ply in the [0/90/0] laminate. To provide a one-to-one comparison of the results, identical meshes were used in the unconstrained and the constrained plies. In both cases, the imposed transverse strain was 0.6%, which is expected to be high enough to initiate a first local failure event of yielding or brittle cavitation in the matrix.

Figure 35 illustrates the distortion and dilatation energy densities associated with elements having peak von Mises and hydrostatic stresses, respectively, where the element size was approximately $0.04r_f$. Values corresponding to the constrained and unconstrained 90° plies in different specified regions are compared (black and green bars) and, as indicated, there are insignificant differences in all cases. However, when a void of 3 μm diameter is introduced (Scenario A, Fig. 32a), the situation changes. Now measurable reductions in both energy densities are seen in all specified regions. Note that the energy densities shown in Fig. 35 are averages of ten realizations of each RVE and the standard deviation shows the range of variation of the values.

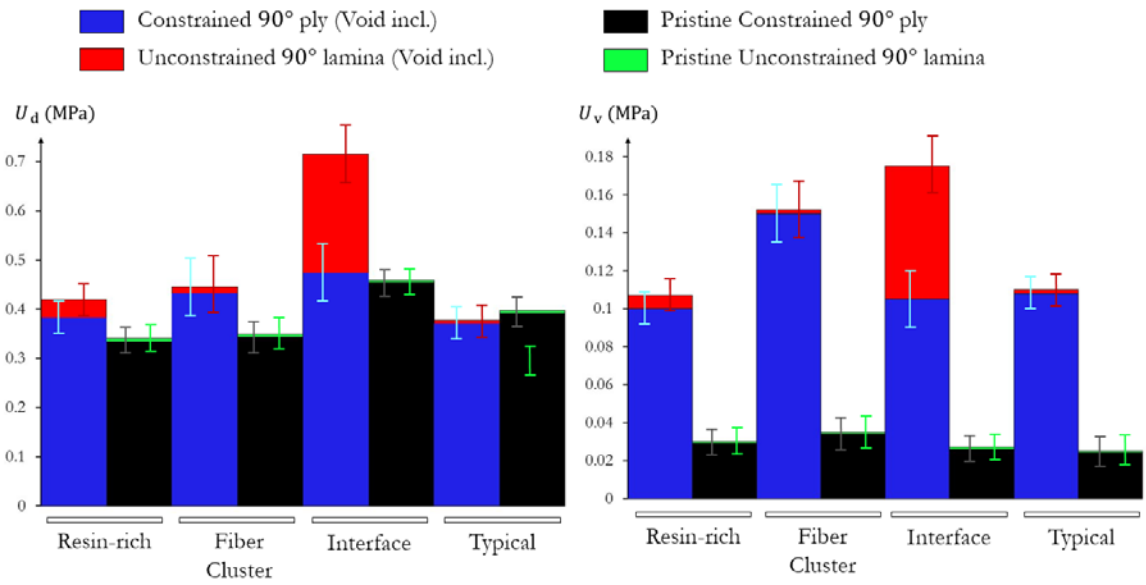

Figure 35. (a) Distortion energy densities in elements with peak von Mises stresses, and (b) dilatation energy densities in elements with peak hydrostatic stresses. Data corresponds to the specified regions of the constrained and unconstrained transverse plies with and without a microvoid. The bars indicate the average energy densities from ten generated RVE models with different nonuniform fiber spatial dispersions, while the standard deviation is represented by scatter bars.

As seen in Fig. 35, the constraining effect is most severe when a microvoid is placed close to the ply interface (see Fig. 35a), while in other cases it is less severe. However, it is likely that the constraining effect will be more significant if the microvoid size is increased. This was investigated by a parametric study where the microvoid size was varied from 0 to 4 μm in the resin–rich region while in the fiber cluster region it was limited to 3 μm. The results are shown in Fig. 36 where the dilatation and distortion energy densities normalized by their maximum values in the similar pristine (no microvoid) region are plotted. As can be seen, the dilatation energy density is affected significantly by the presence of microvoids in both the resin-rich and fiber cluster regions, while the distortion energy density remains practically unaffected by microvoids. The other two specified regions were also studied, and the results were found to be in between those of the resin-rich and fiber cluster results.

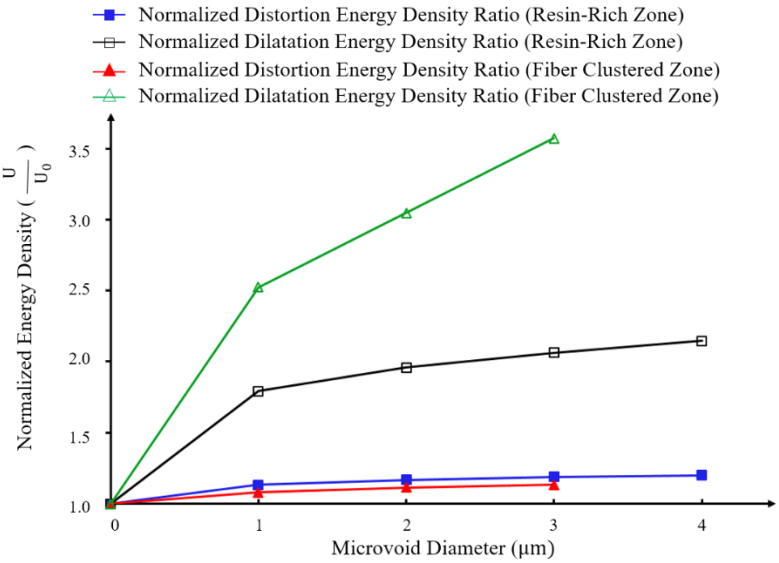

Figure 36. Effect of the microvoid size on the normalized peak energy density at the resin-rich and fiber cluster zones of constrained 90° ply.

Figure 37 illustrates the hydrostatic stress contours of an interface zone containing a void within the unconstrained and constrained 90° plies for one of the RVEs used to generate data in Fig. 35. As expected, the contours reveal the influence of ply constraining for the case when the 90° ply contains a void, while identical stress states were obtained for the case when pristine 90° plies were considered (not shown). This important observation further confirms that in the presence of local defects the magnitude of stresses (and energy density) within the constrained ply have reduced. It is worth noting that the stress perturbation resulting from the presence of microvoids in the specified zones dissipates beyond the 10 μm square regions investigated in this study.

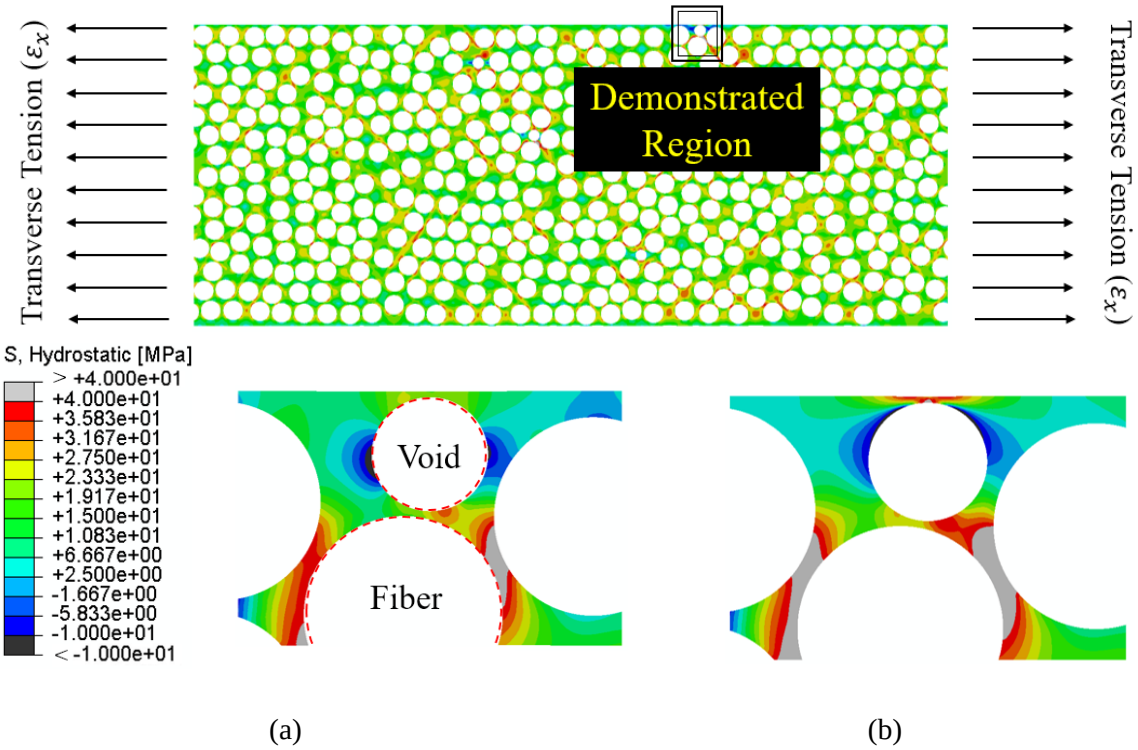

Figure 37. Hydrostatic stress contours of an interface region with a void for: (a) constrained 90° ply, and (b) unconstrained 90° ply.

It is known that for laminates comprised of unidirectional prepreg tapes and consolidated by hot pressing or in an autoclave a layer of resin forms between the plies, the thickness of which is notably influenced by the pressure applied during consolidation. As was mentioned earlier, the presence of this interlaminar resin layer is important in transferring the stress between plies [5]. To study the effect of this layer when a void is present near the layer in the 90° ply, a void was located near the top layer (i.e., interface zone) while the bottom layer is left without a void (see Fig. 38). The layer thickness is varied in the range 0-10 μm and the void had a 3 μm diameter as indicated in Fig. 35 (b). The dilatation and distortion energy densities are calculated under a transverse strain of 0.6% applied to the laminate.

Similar to what is shown in Fig. 36, Figure 39 shows the variation of the normalized distortion and dilatation energy densities, except here the void is of fixed diameter (3 μm), and the parameter varied is the resin layer thickness. The results shown are for two cases, when a void is present (top layer) and when it is not (bottom layer). Note, for this case U_0 is the distortion (dilatation) energy density associated with the element having peak von Mises (hydrostatic) stress value in the constrained 90°

ply, where the thickness of the pure resin layer was zero. The interesting result is that the distortion energy density increases with the layer thickness, and more so when a void is present. The opposite trend is seen for the dilatation energy density (i.e., a reduction as the layer thickness increases) and the presence of a void causes further reduction. It is also noteworthy that all energy density values tend to constant values at large resin layer thickness.

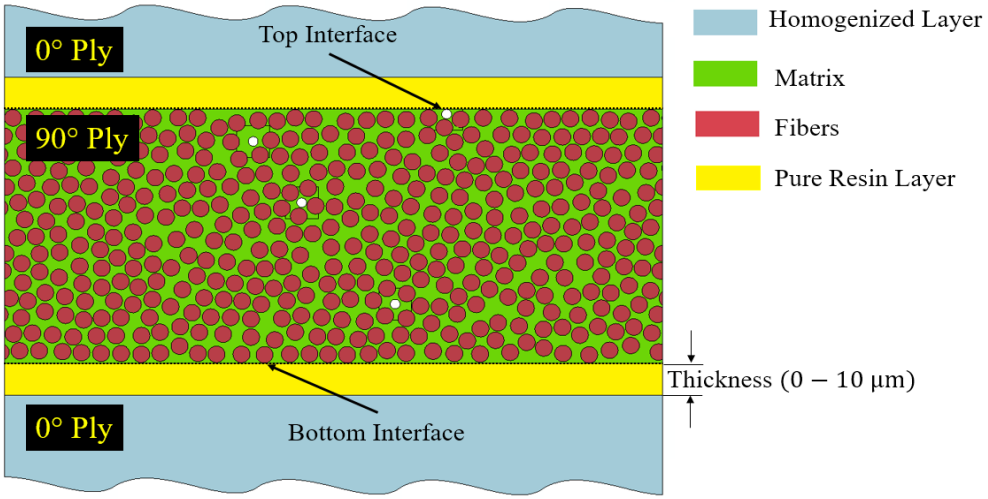

Figure 38. Representation of the RVE of the [0/90/0] laminate including a thin resin layer at the interface between laminate.

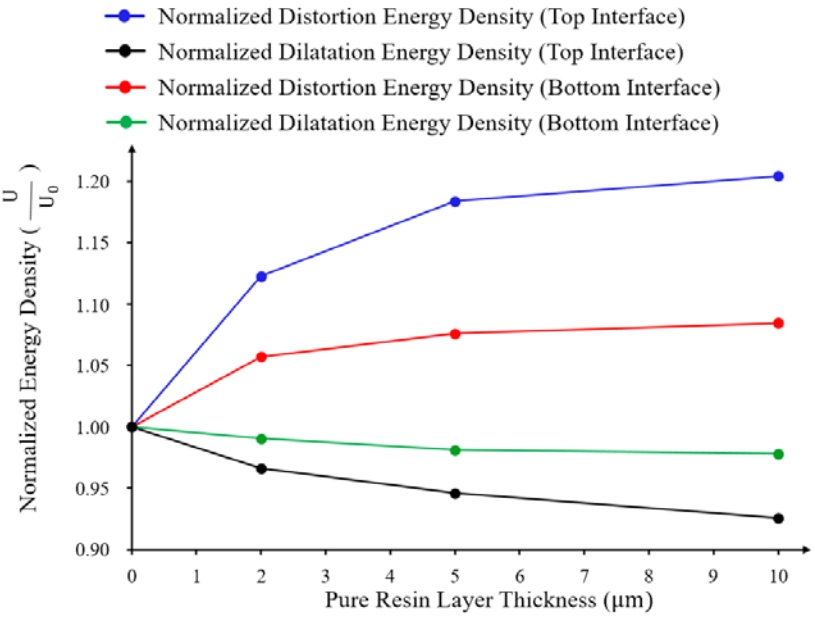

Figure 39. Variation of normalized peak energy density in the 90° ply with changing the thickness of the pure resin layer at the interface.

The results of Fig. 36 and Fig. 39 indicate that defects such as microvoids and resin layers at ply interfaces affect the dilatation and distortion energy densities differently. It must also be kept in mind that the critical values of the two energy densities are different. For epoxies, the critical dilatation energy density for initiating brittle cavitation is approximately 0.15 MPa while the critical distortion energy density for yielding is often reported as 0.7 MPa or higher depending on the epoxy [21]. Thus, which of the two failure events occurs first would depend on the fiber distribution nonuniformity (e.g., fiber clusters, resin-rich regions) combined with the presence of other defects such as microvoids and microcracks. Furthermore, the cooldown temperature in processing of a laminate will affect the dilatation and distortion energy densities differently. In the following, therefore, a systematic study of the occurrence of the two failure events was conducted while keeping the constraining effect of the 0^o plies onto the 90^o ply in focus.

First, the variation of two energy densities in a resin-rich zone containing a 3 μm diameter void (Fig. 32b) with increasing transverse strain up to 0.6% is investigated. The results are plotted in Fig. 40a where each energy density is calculated in elements with maximum von Mises stress or maximum hydrostatic stress. As expected, the dilatation energy density is higher in the element with maximum hydrostatic stress than in the element with maximum von Mises stress. Similarly, the distortion energy density is higher corresponding to the maximum von Mises stress. The critical value of the dilatation energy density for brittle cavitation of 0.15 MPa is also indicated in the figure. As can be seen, the dilatation energy density in the element with maximum hydrostatic stress reaches the critical value at approximately 0.47% strain. Clearly, the distortion energy density in the element with maximum von Mises stress reaches its critical value of 0.7 MPa (not shown in the figure) at a much higher strain, while occurrence of cavitation prior to yielding in this element remains possible. This situation is in compliance with what has been found for unconstrained plies (i.e., unidirectional composites) under transverse tension [27,29].

In a separate investigation, a post-cure temperature cooldown of $\Delta T = -100°C$ was applied to the same RVE prior to applying an increasing transverse strain of 0.6%. Distortion and dilatation energy densities for elements with maximum von Mises and hydrostatic stresses within a resin-rich zone are illustrated in Fig. 40b. The overall trend for the case with thermal cooldown is similar, where dilatation energy density is higher in the element with maximum hydrostatic stress and failure caused by brittle cavitation is likely to occur. One important observation is that the initial distortion and dilatation energy density values prior to applying a transverse strain are notable. Due to the mismatch in the coefficient of thermal expansion along the x–direction for the 0° and 90° plies, tensile stresses are imposed on the

90° ply during thermal cooldown. Thus, the strain at which the dilatation energy density in the element with maximum hydrostatic stress reaches the critical value (0.25%) has decreased. Also, the rate of increase for both the distortion and dilatation energy density values are distinct from the case without thermal cooldown (compare Fig. 40a and Fig. 40b).

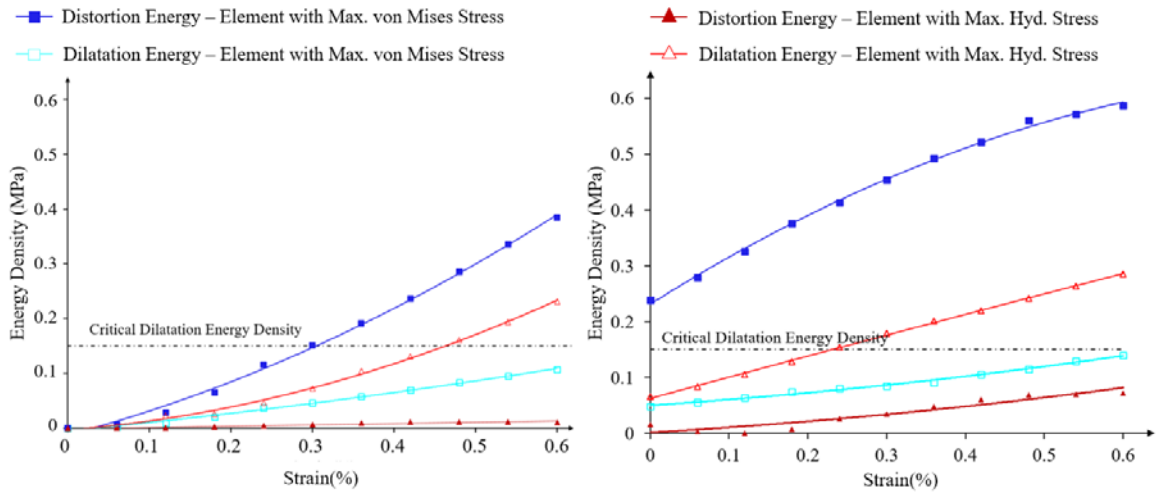

Figure 40. Variation of peak distortion and dilatation energy densities within the constrained 90° ply at the resin-rich zone containing a 3 μm microvoid: (a) no post-cure cooldown, and (b) cooldown of ΔT = –100°C.

The thermal residual stress in the matrix resulting from the cooldown from the cured state of the laminate was calculated for different cooling temperature ranges, ΔT, for both cases of the constrained and unconstrained 90° plies containing a 3 μm void. Figure 41 shows the calculated volume-averaged energy density in the resin-rich and fiber cluster zones due to the initial thermal cooldown (i.e., prior to applying the strain). The matrix phase of the unconstrained 90° plies in both selected zones experienced an increase in the volume-averaged distortional energy density with increase in the magnitude of ΔT, while the change in dilatation energy density was less pronounced. In contrast, the constrained 90° ply exhibited a considerable rise in the volume averaged dilatation energy density due to the mismatch in thermal expansion coefficient for the 0° and 90° plies. A comparison between Fig. 41a,b reveals that the change of the dilatation energy density caused by the adjacent 0° plies is relatively higher in the resin-rich zone, while the distortional energy density is not greatly affected by the constraining 0° plies in either zone. The residual stresses due to thermal cooldown imparted in the constrained 90° ply have resulted in notable local dilatation energy density values, in both the resin-rich and fiber cluster zones,

revealing that the conditions for brittle cavitation will occur at lower applied strains as was shown in Figure 40b. Furthermore, the results indicate that there is a higher probability for the occurrence of microcracks in epoxies on cooldown from higher curing temperatures.

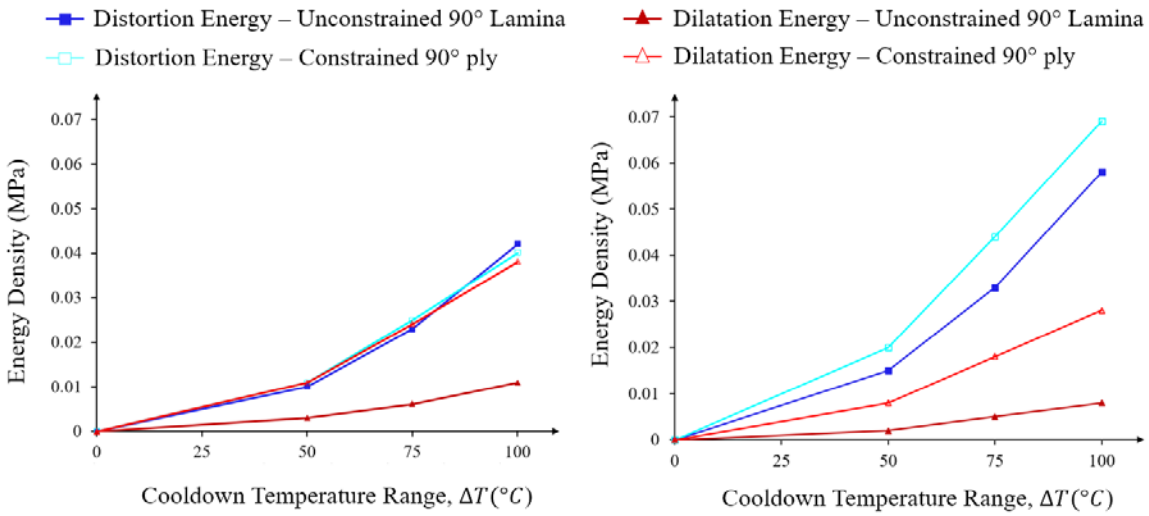

Figure 41. Variation of volume-averaged residual distortion and dilatation energy densities for constrained and unconstrained 90° plies with voids after the cooldown stage in: (a) resin-rich and (b) fiber cluster zones.

Next, the RVEs subjected to a thermal cooldown were subsequently mechanically loaded (ε_x = 0.6%). Figure 42 presents the variation of distortion and dilatation energy densities, which are respectively associated with elements having peak von Mises and hydrostatic stresses, for the constrained and unconstrained 90° ply in the resin-rich and fiber cluster zones, without and with thermal cooldown (ΔT = –100°C). An increase in the magnitude of distortion and dilatation energy densities was observed in both regions of the 90° ply due to the thermal cooldown, with a larger increase for the constrained case compared to the unconstrained case. In other words, as was indicated previously for the constrained 90° ply, due to the mismatch in thermal expansion coefficient between the 0° and 90° plies along the direction of mechanical loading the thermal cooldown resulted in higher magnitude distortion and dilatation energy density values. This increase was observed in both the resin-rich and fiber cluster zones (see Fig. 42), with the highest increase for distortion energy density in the fiber cluster zone. It is clear that the constraining plies result in higher magnitude energy density values when thermal cooldown is considered, which is an important finding. Moreover, the results also reveal that the presence of thermal residual stresses increases the possibility of cavitation in the resin-rich and fiber

cluster regions of the constrained 90° ply, while there is a lower possibility for yielding prior to cavitation.

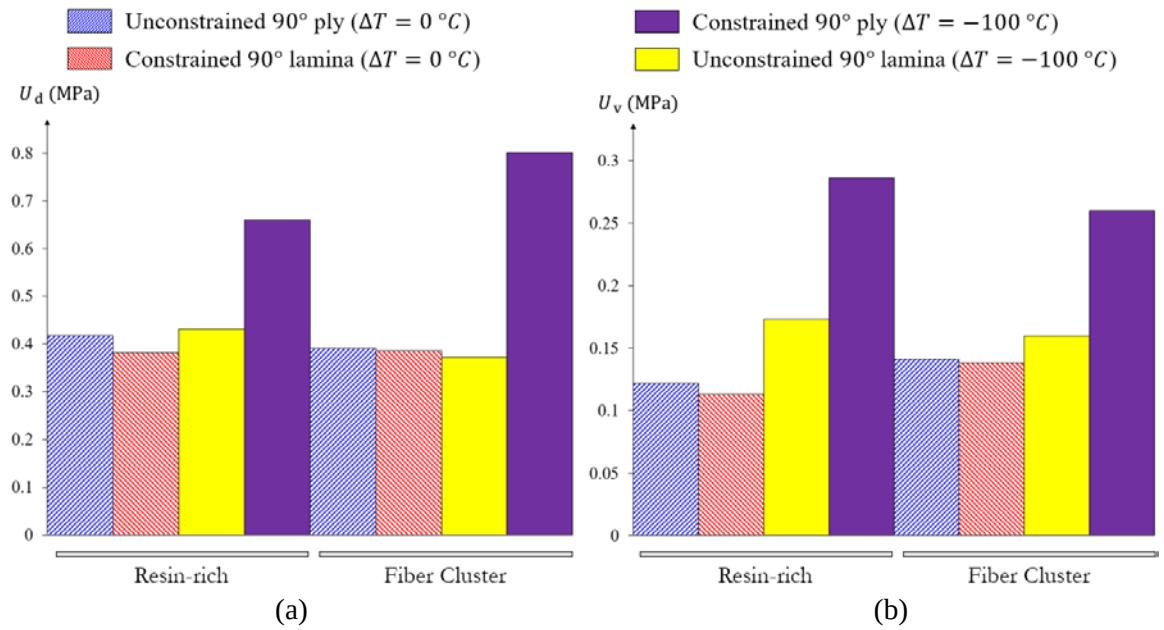

Figure 42. (a) Distortion energy densities in elements with peak von Mises stresses, and (b) dilatation energy densities in elements with peak hydrostatic stresses. Data corresponds to the specified regions of the constrained and unconstrained 90° plies with a 3μm microvoid, for the cases with and without a 100°C thermal cooldown and an applied transverse strain of 0.6%.

An additional study was performed to investigate the influence of a microcrack within the specified zones of the generated RVEs under a tensile strain of 0.6% (see Scenario B in Fig. 32a). Figure 43a,b illustrate the variation of distortion and dilatation energy densities, which are respectively associated with elements having peak von Mises and hydrostatic stresses in the indicated zones, for the constrained and unconstrained 90° ply. In these plots, solid lines represent the magnitude of energy densities while the dashed lines show the degree of ply constraining in terms of the energy ratio (i.e., $U^{\text{Constrained}}/U^{\text{Unconstrained}}$). For both the unconstrained and constrained 90° ply an increase in the distortional and dilatational energy densities was predicted with increasing microcrack length in all specified zones. As was discussed previously, the energy densities at the ply interface region are more greatly influenced by the constraining plies when compared to the other zones considered. This is expected and in part due to the shear-lag effect between the adjacent plies. The energy densities in the resin-rich zone are notably influenced by the constraining plies, particularly distortional energy density. In contrast, the constraining plies do not greatly affect the energy densities in the fiber cluster zone.

Figure 43c illustrates the maximum crack opening displacement of the pre-existing microcrack with different lengths for each indicated region. These results also reveal the notable influence of the constraining plies on the local deformation field at the ply interface and the resin-rich zones, while fiber cluster zones were less influenced.

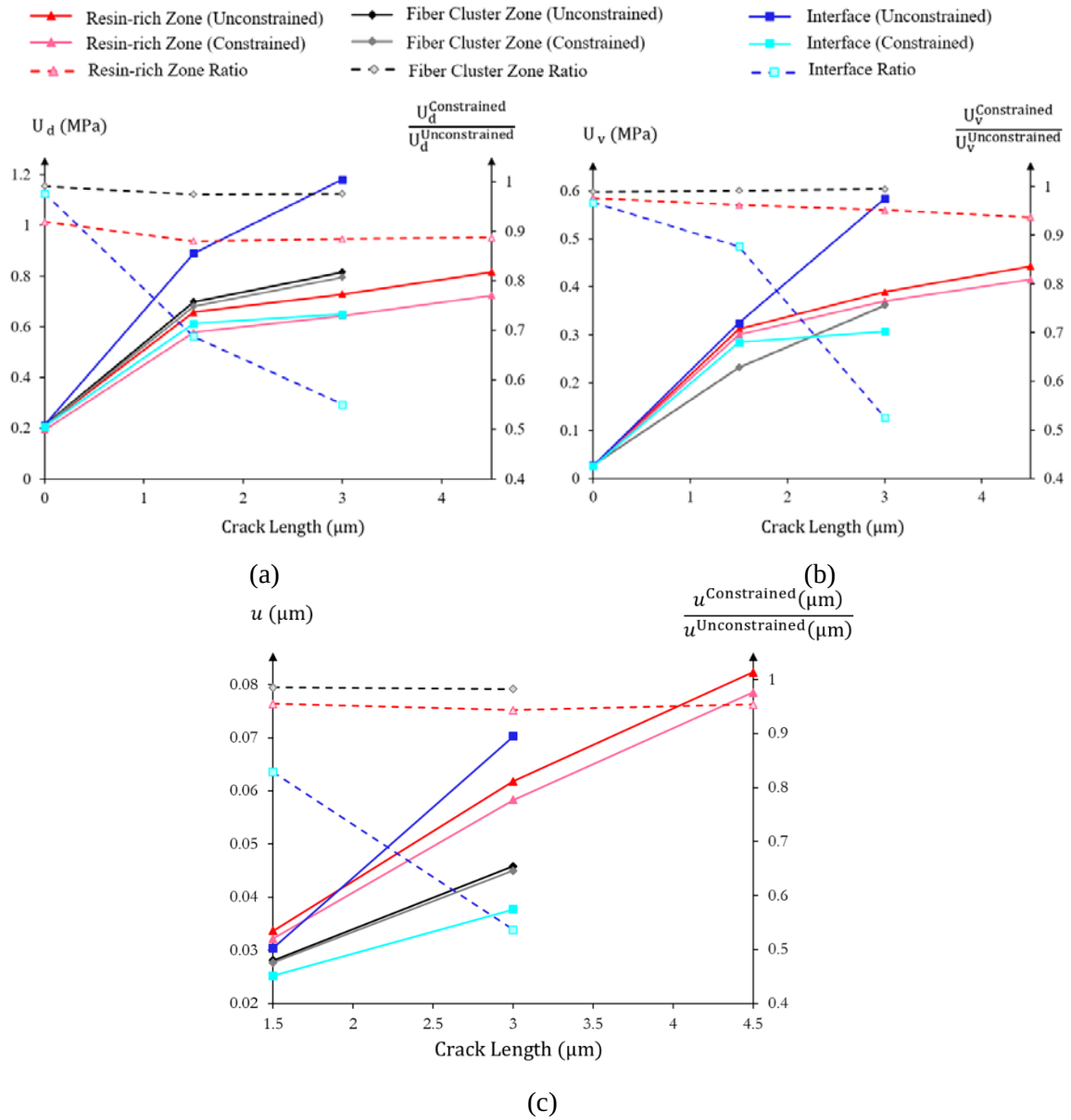

Figure 43. (a) Distortion energy densities in elements with peak von Mises stresses, (b) dilatation energy densities in elements with peak hydrostatic stresses, and (c) crack opening displacements. Data corresponds to the specified regions of the constrained and unconstrained 90° ply with preexisting microcracks of varying lengths.

5.3.3 General discussion

It was demonstrated that for a [0/90/0] cross-ply laminate subjected to a tensile strain the constraining effect imparted on the 90° ply from the adjacent 0° plies can significantly influence the local stress and deformation fields of the matrix. However, the emergence of this effect was not observed in pristine laminates for the case when thermal cooldown was not considered, and instead depends on the presence and size of pre-existing manufacturing induced defects in the 90° ply (e.g., microvoids or microcracks) which is a notable finding. The predicted distortional and dilatational energy densities were both found to generally decrease for constrained 90° plies containing pre-existing defects. Also, despite this decrease in the predicted dilatational energy density, the conditions to initiate the first local failure event in the matrix were consistently associated with brittle cavitation. Thus, if one were to consider subsequent crack propagation it is expected that local matrix cracks would be restrained since the associated energy available for crack propagation would be lower for a constrained ply. Notwithstanding, it was shown that the thermal residual stresses due to cooldown following cure in laminates were tensile, which is a result of the mismatch in thermal expansion coefficient between the 90° and 0° plies along the laminate *x*–direction. This revealed that the strain associated with the conditions to cause brittle cavitation in the matrix decreased once thermal cooldown was considered as a result of the increased dilatation energy density (see Fig. 40). Nevertheless, the rate of increase of dilatation energy density during increase in applied strain was distinct when thermal cooldown was considered for the constrained 90° ply. This would influence subsequent local crack growth.

Furthermore, the constraining plies had a varying degree of influence on the local matrix distortion and dilatation energy densities in the different regions assessed within the 90° ply containing a microvoid or microcrack. A remarkable reduction of both distortion and dilatation energy was observed at the ply interface region, which is expected since the constraining plies would tend to cause stress perturbations in the 90° ply near the ply interface. The resin-rich regions also showed a decrease in both distortion and dilatation energy levels, demonstrating that both local yielding and brittle cavitation can be hindered. On the other hand, regions containing fiber clusters were less impacted by the constraining plies even though it is well known that ply cracks typically cavitate in these regions. The significance of these observations is that the local deformation in these specified zones can either directly or indirectly influence the growth of a ply crack after brittle cavitation occurs in one of these zones. In other words, the restraining effect on a cavitated crack that is on the verge of growing within a resin-rich zone is high due to the corresponding reduction in available energy. For cracks set to propagate in fiber cluster regions, the rate of propagation may be the same regardless of the degree of constraining

from the 0° plies. However, if these cracks do propagate their growth rate will be influenced by the "constrained deformation" in the adjacent resin-rich regions and their propagation may be postponed once the crack reaches a resin-rich region. Thus, it can be perceived that the local position of a microcrack or pre-existing defect within the ply, and consequently the ply constraining effect, can influence crack growth. Therefore, it is necessary to consider both brittle cavitation and yielding as local matrix failure mechanisms.

Moreover, the influence of different parameters on the degree of ply constraining and early-stage crack formation for 90° plies with local defects was assessed. An increase in the thickness of the pure resin layer at the ply interface was found to notably increase the local distortional energy density at this zone, while decreasing the dilatation energy density. This increases the likelihood of local matrix yielding at the ply interface for case when thicker resin layers exists, however, brittle cavitation remains possible since the corresponding critical distortional energy density value of 0.15 MPa is notably less than the critical distortional energy density of epoxies (>0.7 MPa). The high magnitude of distortion at the ply interfaces may also influence the local deformation fields at regions away from the interface. In another assessment, different magnitudes of thermal cooldown temperatures after laminate cure were considered to determine the variation in the thermal residual stresses within the constrained 90° ply. With increasing temperature range, the dilatational and distortional energy densities in different zones of the 90° ply notably increased. The constraining plies had a greater influence on the dilatational energy density in the resin-rich and fiber cluster zones of the 90° ply, which reveals that brittle cavitation remains favourable.

5.4 Conclusions

A computational micromechanical model was developed to study the influence of ply constraints on the early stages of local matrix failure in the 90° ply of a [0/90/0] cross-ply laminate under tensile loading. Representative microstructural models explicitly accounted for manufacturing induced defects, including nonuniform fiber spatial distribution, microvoids and microcracks, while residual stresses due to post-cure thermal cooldown of the laminate were considered. Distortion and dilatation energy densities were used to define local matrix failure associated with yielding and brittle cavitation, respectively. It was observed that the emergence of the constraining effect highly depends on the presence and size of pre-existing local defects (e.g., microvoids or microcracks) while different zones (e.g., resin-rich and fiber cluster) in the 90° ply exhibit varying degrees of constraining. For the cases investigated in this study, the conditions for brittle cavitation of the matrix preceded yielding. However,

the variation in the effect of ply constraining on the local deformation field at different ply zones can influence crack growth subsequent to brittle cavitation, where local yielding of the matrix in adjacent zones may influence crack propagation. Furthermore, the thermal cooldown for a constrained 90° ply imposed higher dilatational energy density values in the matrix, thus leading to brittle cavitation at lower applied strain levels when compared to the unconstrained case. Overall, the results of this study provide important insight on the mechanisms that influence the early stages of ply crack formation in a constrained ply with manufacturing induced defects, which are important for improving the understanding of the sub-critical ply crack growth process and for using the lowest damage thresholds for safe designs. Ultimately, the local failure criteria presented in this study may be integrated within a multiscale modeling framework for predicting the accumulation of ply cracks in laminates. In particular, the micromechanical assessments can provide estimates of effective critical energy release rates associated with the formation of ply cracks.

References

[1] A. S. Kaddour, M. J. Hinton, P. A. Smith, and S. Li, A comparison between the predictive capability of matrix cracking, damage and failure criteria for fibre reinforced composite laminates: Part A of the third world-wide failure exercise, Journal of Composite Materials 47 (2013) 2749-2779.

[2] J. Montesano, C.V. Singh, Predicting evolution of ply cracks in composite laminates subjected to biaxial loading, Composites Part B: Engineering 75 (2015) 264–273.

[3] R. Talreja, C.V. Singh, Damage and Failure of Composite Materials, Cambridge University Press, 2012.

[4] J. Aveston, G.A. Cooper, A. Kelly, Single and multiple fracture: The properties of fiber composites. Conference Proceedings, National Physical Laboratory, Guildford, U.K., 1971: pp. 15–26. IPC Science and Technology Press, Ltd. Teddington, U.K.

[5] K. W. Garrett and J. E. Bailey, Multiple transverse fracture in 90° cross-ply laminates of a glass fibre-reinforced polyester, Journal of Materials Science 12 (1977) 157–168.

[6] P. W. Manders, T. W. Chou, F. R. Jones, and J. W. Rock, Statistical analysis of multiple fracture in 0°/90°/0° glass fibre/epoxy resin laminates, Journal of Materials Science 18 (1983) 2876–2889.

[7] Z. Hashin, Analysis of cracked laminates: a variational approach, Mechanics of Materials 4 (1985) 121–136.

[8] L. N. McCartney, Theory of stress transfer in a 0°-90°-0° cross-ply laminate containing a parallel array of transverse cracks, Journal of the Mechanics and Physics of Solids 40 (1992) 27–68.

[9] P. Gudmundson and S. Östlund, First order analysis of stiffness reduction due to matrix

cracking, Journal of Composite Materials 26 (1992) 1009–1030.

[10] J. Varna, R. Joffe, N. V Akshantala, and R. Talreja, Damage in composite laminates with off-axis plies, Composites Science and Technology 59 (1999) 2139–2147.

[11] C. V. Singh and R. Talreja, Evolution of ply cracks in multidirectional composite laminates, International Journal of Solids and Structures, 47 (2010) 1338–1349.

[12] R. Talreja, A continuum-mechanics characterization of damage in composite materials, Proceedings of the Royal Society A: Mathematical, Physical and Engineering Sciences 399 (1985) 195–216.

[13] C. V. Singh and R. Talreja, Analysis of multiple off-axis ply cracks in composite laminates, International Journal of Solids and Structures, 45 (2008) 4574–4589.

[14] J. Montesano and C. V. Singh, A synergistic damage mechanics based multiscale model for composite laminates subjected to multiaxial strains, Mechanics of Materials, 83 (2015) 72–89.

[15] J. Montesano and C. V. Singh, Critical stiffness damage envelopes for multidirectional laminated structures under multiaxial loading conditions, Materials and Design 97 (2016) 218–229, 2016.

[16] J.A. Nairn, S. Hu, Micromechanics of damage: A case study of matrix micro cracking, in: R. Talreja (Ed.), Damage Mechanics of Composite Materials, Elsevier Ltd, Amesterdam, 1994: pp. 187–243.

[17] P.P. Camanho, C.G. Dávila, S.T. Pinho, L. Iannucci, P. Robinson, Prediction of in situ strengths and matrix cracking in composites under transverse tension and in-plane shear, Composites Part A: Applied Science and Manufacturing 37 (2006) 165–176.

[18] S. T. Pinho, C. G. Dávila, P. P. Camanho, L. Iannucci, and P. Robinson, Failure models and criteria for FRP under in-plane or three-dimensional stress states including shear non-linearity, NASA/TM-2005-213530 (Langley Research Center Hampton), 2005.

[19] G. Catalanotti, P.P. Camanho, A.T. Marques, Three-dimensional failure criteria for fiber-reinforced laminates, Composite Structures 95 (2013) 63–79.

[20] C.G. Dávila, P.P. Camanho, C.A. Rose, Failure Criteria for FRP Laminates, Journal of Composite Materials 39 (2005) 323–345.

[21] L.E. Asp, L.A. Berglund, R. Talreja, A criterion for crack initiation in glassy polymers subjected to a composite-like stress state, Composites Science and Technology 56 (1996) 1291–1301.

[22] L.E. Asp, L.A. Berglund, P. Gudmundson, Effects of a composite-like stress state on the fracture of epoxies, Composites Science and Technology 53 (1995) 27–37.

[23] L.E. Asp, L.A. Berglund, R. Talreja, Prediction of matrix-initiated transverse failure in polymer composites, Composites Science and Technology 56 (1996) 1089–1097.

[24] L.E. Asp, L.A. Berglund, R. Talreja, Effects of fibre and interphase on matrix initiated transverse failure in polymer composites, Composites Science and Technology 56 (1996) 657–665.

[25] T. Okabe, H. Imamura, Y. Sato, R. Higuchi, J. Koyanagi, R. Talreja, Experimental and numerical studies of initial cracking in CFRP cross-ply laminates, Composites Part A: Applied Science and Manufacturing 68 (2015) 81–89.

[26] Y. Kumagai, S. Onodera, M. Salviato, T. Okabe, Multiscale analysis and experimental validation of crack initiation in quasi-isotropic laminates, International Journal of Solids and Structures 193–194 (2020) 172–191.

[27] S.A. Elnekhaily, R. Talreja, Damage initiation in unidirectional fiber composites with different degrees of nonuniform fiber distribution, Composites Science and Technology 155 (2018) 22–32.

[28] S.A. Elnekhaily, R. Talreja, Effect of axial shear and transverse tension on early failure events in unidirectional polymer matrix composites, Composites Part A: Applied Science and Manufacturing 119 (2019) 275–282.

[29] A. Sudhir, R. Talreja, Simulation of manufacturing induced fiber clustering and matrix voids and their effect on transverse crack formation in unidirectional composites, Composites Part A: Applied Science and Manufacturing 127 (2019) 105620.

[30] E. Marklund, L.E. Asp, R. Olsson, Transverse strength of unidirectional non-crimp fabric composites: Multiscale modelling, Composites Part B: Engineering 65 (2014) 47–56.

[31] A.R. Melro, P.P. Camanho, F.M.A. Pires, S.T. Pinho, Micromechanical analysis of polymer composites reinforced by unidirectional fibres : Part I – Constitutive modelling, International Journal of Solids and Structures 50 (2013) 1897–1905.

[32] A. Arteiro, Structural mechanics of thin-ply laminated composites, University of Porto – FEUP, 2016.

[33] A. Arteiro, G. Catalanotti, A.R. Melro, P. Linde, P.P. Camanho, Micro-mechanical analysis of the in situ effect in polymer composite laminates, Composite Structures 116 (2014) 827–840.

[34] H. Saito, H. Takeuchi, I. Kimpara, A study of crack suppression mechanism of thin-ply carbon-fiber-reinforced polymer laminate with mesoscopic numerical simulation, Journal of Composite Materials 48 (2014) 2085–2096.

[35] L. Zhuang, R. Talreja, J. Varna, Transverse crack formation in unidirectional composites by linking of fibre/matrix debond cracks, Composites Part A: Applied Science and Manufacturing 107 (2018) 294–303.

[36] H. Ghayoor, C.C. Marsden, S. V Hoa, A.R. Melro, Numerical analysis of resin-rich areas and their effects on failure initiation of composites, Composites Part A: Applied Science and Manufacturing 117 (2019) 125–133.

[37] Y.K. Hamidi, L. Aktas, M.C. Altan, Formation of microscopic voids in resin transfer molded composites, Journal of Engineering Materials and Technology 126 (2004) 420.

[38] D. Zhang, D. Heider, J.W. Gillespie, Determination of void statistics and statistical representative volume elements in carbon fiber-reinforced thermoplastic prepregs, Journal of Thermoplastic Composite Materials 30 (2017) 1103–1119.

[39] K.A. Chowdhury, R. Talreja, A.A. Benzerga, Effects of Manufacturing-Induced Voids on Local Failure in Polymer-Based Composites, Journal of Engineering Materials and Technology 130 (2008) 021010-1-021010–9.

[40] E.K. Gamstedt, B.A. Sjögren, Micromechanisms in tension compression fatigue of composite laminates containing transverse plies, Composites Science and Technology 59 (1999) 167–178.

[41] S. Zhandarov, E. Mäder, Characterization of fiber/matrix interface strength: Applicability of

different tests, approaches and parameters, Composites Science and Technology 65 (2005) 149–160.

[42] P.A. Carraro, M. Quaresimin, Modelling fibre-matrix debonding under biaxial loading, Composites Part A: Applied Science and Manufacturing 61 (2014) 33–42.

[43] S. Ghosh, Y. Ling, B. Majumdar, R. Kim, Interfacial debonding analysis in multiple fiber reinforced composites, Mechanics of Materials 32 (2000) 561–591.

[44] A.R. Melro, P.P. Camanho, F.M.A. Pires, S.T. Pinho, Micromechanical analysis of polymer composites reinforced by unidirectional fibres : Part II – Micromechanical analyses, International Journal of Solids and Structures 50 (2013) 1906–1915.

[45] ABAQUS, "ABAQUS 6.14 Analysis User's Manual." Dassault Systemes Simulia Corporation, 2014.

[46] T. Yu, J.G. Teng, Y.L. Wong, S.L. Dong, Finite element modeling of confined concrete-I: Drucker-Prager type plasticity model, Engineering Structures 32 (2010) 665–679.

[47] B. Fiedler, M. Hojo, S. Ochiai, K. Schulte, M. Ando, Failure behavior of an epoxy matrix under different kinds of static loading, Composites Science and Technology 61 (2001) 1615–1624.

[48] F.J. Guild, K.D. Potter, J. Heinrich, R.D. Adams, M.R. Winsom, Understanding and control of adhesive crack propagation in bonded joints between carbon fibre composite adherends II. Finite element analysis, International Journal of Adhesion and Adhesives 21 (2001) 445–453.

[49] P.P. Camanho, M. Lambert, A design methodology for mechanically fastened joints in laminated composite materials, Composites Science and Technology 66 (2006) 3004–3020.

[50] M.R. Wisnom, B. Khan, S.R. Hallett, Size effects in unnotched tensile strength of unidirectional and quasi-isotropic carbon/epoxy composites, Composite Structures 84 (2008) 21–28.

[51] H. Koerber, J. Xavier, P.P. Camanho, Y.E. Essa, F. Martín de la Escalera, High strain rate behaviour of 5-harness-satin weave fabric carbonepoxy composite under compression and combined compressionshear loading, International Journal of Solids and Structures 54 (2015) 172–182.

[52] G. Li, F. Sharifpour, A. Bahmani, J. Montesano, A new approach to rapidly generate random periodic representative volume elements for microstructural assessment of high volume fraction composites, Materials and Design 150 (2018) 124–138.

[53] M. V. Pathan, V.L. Tagarielli, S. Patsias, Numerical predictions of the anisotropic viscoelastic response of uni-directional fibre composites, Composites Part A: Applied Science and Manufacturing 93 (2017) 18–32.

[54] S. Lejeunes and S. Bourgeois, Une Toolbox Abaqus pour le calcul de propriétés effectives de milieux hétérogènes, in 10e colloque national en calcul des structures At: Giens, 2011.

[55] R. Talreja, Defect damage mechanics: broader strategy for performance evaluation of composites, Plastics Rubber and Composites 38 (2009) 49–54.

[56] T.J. Vaughan, C.T. Mccarthy, A combined experimental – numerical approach for generating statistically equivalent fibre distributions for high strength laminated composite materials, Composites Science and Technology 70 (2010) 291–297.

Chapter 6

Micromechanical assessment of local failure mechanisms and early-stage ply crack formation in cross-ply laminates

(Accepted manuscript, Composites Science & Technology, January 2022)

6.1 Introduction

The integration of high-performance fiber-reinforced plastic (FRP) composites into primary load-bearing structures has further increased interest to investigate the complex failure processes of laminates and damage thresholds of corresponding structures. Typically, the evolution of damage in FRP laminates subjected to mechanical loading begins with the formation of ply cracks in transverse or off-axis plies (i.e., so-called sub-critical ply cracking). During this stage, laminates may endure a significant degradation of stiffness without loss of material integrity, which can cause the rigidity of a structure to reach a critical threshold. In general, sub-critical ply cracking is followed by the formation and evolution of critical damage mechanisms such as delamination and fiber breakage/micro-buckling, and can subsequently lead to the catastrophic failure of a structure [1,2].

Although an improved understanding of damage evolution in FRP laminated composites has been achieved, predicting this behaviour remains challenging due to the complex multiscale nature of the damage mechanisms [3] and the variabilities in the material brought on by the manufacturing process [4,5]. Several models have been developed to predict the overall degradation of FRP laminates stemming from ply-level (mesoscale) and macroscopic damage accumulation. Typically, such models are phenomenological and formulated at the macroscale where the microscale damage formation and the influence of manufacturing-induced defects on the failure process, as described in Refs. [2–6], are not incorporated. Therefore, a need exists for assessing the local deformation fields of laminates to treat the mechanisms that influence the formation, growth, and accumulation of ply cracks. Furthermore, it is only through reliable predictions of the ply crack formation and evolution that a multiscale modelling framework for laminate damage will be possible [3,7,8].

The formation and evolution of ply cracks within a transverse ply of a laminate is further influenced by the constraint imposed by the adjacent plies (i.e., so-called ply constraining effect). The effect of ply constraints on the formation and evolution of ply cracks is often neglected in structural analyses, causing a conservative prediction of the performance. Previous studies [7,9,10] have reported the effect

of ply constraints on the accumulation of ply cracks once cracks were fully formed. However, this effect also impacts local deformation fields during the early stages of formation of new cracks, which can be captured through a microscale assessment [6].

The formation of ply cracks in laminates begins with the onset of local or point-failure mechanisms in the matrix and the subsequent development of a microcrack from a cluster of these mechanisms at or near the fiber/matrix interfaces (i.e., debonds) [11–13]. Several of these microcracks can grow and eventually link to form a full ply crack [14–16]. Point-failure mechanisms may include ductile failure and brittle cavitation of the matrix [16–28]. It has been well-documented that ductile failure occurs due to the pressure-dependent inelastic deformation of the matrix [16–19], while the latter case occurs once the dilatational energy density of the matrix reaches a critical value under equitriaxial stress state [20–28]. Adopting the concept of cavitation, the formation of fiber/matrix debonding under tensile loading during the early stages of ply crack formation has been predicted as the dominating mode of damage [21–23]. However, in the absence of brittle cavitation, local inelastic deformation can lead to ply crack formation induced by ductile failure. To capture the effect of inelastic deformation on the failure of polymers, Melro et al. [17] proposed a new model that did not consider brittle cavitation of the matrix. The proposed model has been used to predict the formation and propagation of ply cracks in micromechanical finite element (FE) models [9,18,29]. Other micromechanical models have been developed for capturing ply cracking, where brittle failure of epoxy is simulated via cohesive zone models [30–33]. Two-dimensional plane strain FE models have also been utilized by Saito et al. [16] and Herráez et al. [33], where the concept of local damage was limited to simplified plasticity and cohesive zone models. Although several researchers have outlined the necessity of capturing both inelastic deformations and brittle cavitation for predicting the formation of ply cracks, combinations of both processes in a single-ply have been rarely discussed [24–26]. Thus, an approach inclusive of both brittle and ductile failure has not been presented for damage in laminates.

Several forms of defects can manifest during the processing of FRP laminates, which directly influence ply crack formation. Fiber spatial nonuniformity and void formation are common manufacturing-induced defects, and their effect on ply crack formation has been the focus of several reported investigations [6,19,26–28,34]. Elnekhaily and Talreja [26,27] used an energy-based approach to investigate the influence of fiber spatial nonuniformity on the onset of local damage, where the inter-fiber spacing was found to greatly influence brittle cavitation. Additionally, the inter-fiber distance was reported by Zhuang et al. [28] to be a decisive parameter during the coalescence of local damage. The presence of resin pockets and fiber clusters and their influence on the initiation and progression of local

damage was also investigated by Sudhir and Talreja [34], Ghayoor et al. [19], and Sepasdar and Shakiba [31]. Sudhir and Talreja [34] also analyzed the impact of void presence triggering the local damage initiation in a ply. Applying the same perspective on a cross-ply laminate, Sharifpour et al. [6] discussed the interdependency of inter-fiber distance and void formation on damage initiation and ply constraining effect (see Chapter 5).

Although several important studies have provided an improved insight into the early stages of ply crack formation, there are still unexplained questions regarding the interactive contribution of inelastic deformations and brittle cavitation. Similarly, there is an opportunity to better understand the role of manufacturing-induced defects on the initiation of damage in laminates, where constraining plies will further influence local deformations in damaged plies. In the study described in Chapter 5, the effects of ply constraints and manufacturing-induced defects on the local stress and deformation fields in the 90° ply of cross-ply laminates were investigated using a 2D FE micromechanical model. In this chapter, a 3D FE model was developed to predict local failure preceding the formation of local cracking in the 90° ply of a carbon fiber/epoxy [0/90/0] cross-ply laminate under tensile loading, which enabled capturing of the local triaxial stress state in the matrix. A new user-defined material subroutine was developed to accurately capture both the pressure-dependent inelastic deformation of the epoxy and brittle cavitation. Solution-dependent variables were defined in the subroutine to identify the onset of local failure and its corresponding damage mode in the 90° ply. The capability of the subroutine was verified with the available experimental data for an epoxy. Nonuniform fiber spatial dispersions within the constrained 90° ply were explicitly represented and local failure was predicted. The role of ply constraints, inelastic deformations of the matrix, and manufacturing-induced defects on local failure prior to the formation of ply cracks was evaluated. Associated dilatational and distortional energy densities were calculated to highlight the influence of corresponding parameters on the local energy state of the epoxy. The 3D micromechanical FE model developed in the current study is the first that employs a local failure criterion for cavitation along with a comprehensive pressure-dependent yield criterion and material model for the inelastic deformation of the matrix, thus capturing the interaction between these local failure mechanisms.

6.2 Computational model

6.2.1 Micromechanical representation

A carbon fiber/epoxy [0/90/0] cross-ply laminate comprising unidirectional (UD) plies was simulated. In the corresponding representative volume element (RVE), carbon fibers and epoxy matrix in the 90°

ply were explicitly modelled, where the 90° ply was constrained by two homogenized 0° plies (see Fig. 44). A constant diameter D_f = 5.2 μm was assigned to fibers within the 90° ply. Furthermore, a constant fiber volume fraction V_f = 55% and thickness h = 80 μm thickness were assigned to all plies. Note, the ply thickness is representative of a laminate manufactured using thin UD prepregs. The fibers and matrix in the 90° ply were perfectly bonded to represent a strong interfacial bond, while the interfaces between plies were also perfectly bonded since delamination was not a focus of this study.

A periodic nonuniform fiber spatial dispersion within the 90° ply was generated using the method developed by Li et al. [35] (see Chapter 4). The statistical assessment of fiber spatial dispersion and resultant energy (stress) states in generated RVEs were reported in Refs. [35] and [6], respectively, and are not included here for brevity. The length of the RVEs along the global x–direction (see Fig. 44) was set to 200 μm to ensure that the local strain and stress fields were adequately captured as described in [6], resulting in at least 420 fibers within the full-thickness 90° ply and a minimum aspect ratio of $\delta = l/D_f$ = 24. The width of the RVEs along the global y-direction (see Fig. 44) was set to $0.1D_f$ since it was previously reported to be adequate when periodic boundary conditions were used [9].

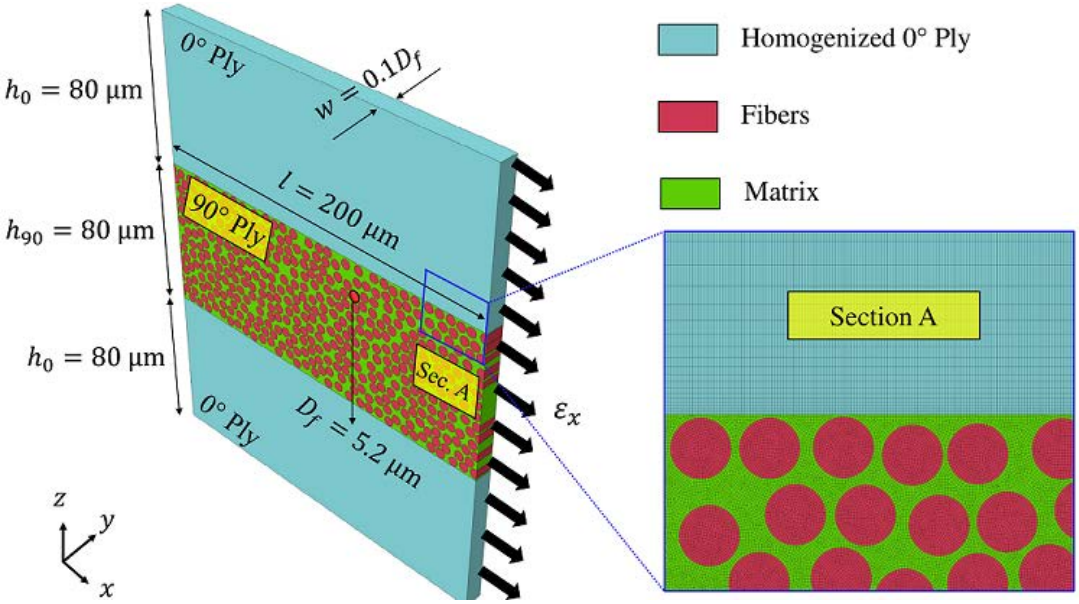

Figure 44. Geometrical attributes of the 3D RVE for the [0/90/0] cross-ply laminate with 2D periodicity along the global x– and y–directions.

The homogenized 0° plies were treated as linear-elastic and transversely isotropic, where the assigned effective properties were determined by the rule of mixtures [36], Halpin-Tsai [37], and Chamis [38] models using the properties of the fiber and matrix constituents (see Table 5). Carbon

fibers were also modelled as linear-elastic and transversely isotropic. An explicit user-defined material subroutine (VUMAT) was developed for the isotropic epoxy matrix to model pressure-dependent inelastic behaviour in the commercial FE software Abaqus [39]. The developed constitutive model for the epoxy is discussed in Section 6.2.2. It should be noted that the experimental data reported in [20,40] were used for the epoxy, and the properties of fibers were taken from Arteiro et al. [9] (see Table 5).

Table 5. Properties of the fibers [9], epoxy resin [20,40], and homogenized plies.

Material Property *	**Fibers (Carbon)**	**Matrix (Epoxy)** +	**Homogenized Plies (V_f = 55%)**
Young's Moduli			
E_{11}(GPa)	276	3.76	153.49
E_{22}(GPa)	15	-	8.03
Poisson's Ratio			
ν_{12}	0.2	0.39	0.28
ν_{23}	0.07	-	0.19
Shear Moduli			
G_{12}(GPa)	15	1.35	3.65
G_{23}(GPa)	7	-	3.37
Thermal Expansion Coefficients			
$\alpha_{11}(°C^{-1})$	-0.5×10^{-6}	58×10^{-6}	0.14×10^{-6}
$\alpha_{22}(°C^{-1})$	15×10^{-6}	-	35.9×10^{-6}
Plastic Poisson's Ratio			
ν_p	-	0.3	-
Density			
ρ (kg/m^3)	1780	1300	1560
Tensile Strength			
X_T(MPa)	-	93	-
Compressive Strength			
X_C(MPa)	-	124	-
Critical Dilatation Energy Density			
U_{dil}^c(MPa)	-	0.15	-

* 1, 2, and 3 are the principal material coordinate system axes for a ply, denoting the fiber direction, in-plane transverse direction and out-of-plane transverse direction, respectively.
+ Note, the integer subscripts can be dropped for the isotropic matrix properties.

6.2.2 Epoxy resin constitutive model

An explicit VUMAT subroutine was developed to capture both the inelastic pressure-dependent deformation and brittle cavitation of the epoxy according to the model described by Melro et al. [17] and concepts presented by Asp et al. [20], respectively. Further details and equations of the plasticity model used in this study are found in Appendix A. A paraboloidal yield criterion [41] and non-associative flow rule were utilized to account for the influence of volumetric deformation in the inelastic regime. Although a variety of yield surfaces have been proposed for polymers (e.g., see Ref. [42]), yield functions with several parameters are often overly complex and do not provide improved accuracy for low or mid-strain plastic materials. On the other hand, simplified yield functions, such as the modified Drucker-Prager model that was initially developed for understanding deformations of geological materials [43], might restrict the validity of a study. Thus, it is necessary to find a balance between the simplicity and computational cost of the yield surface employed. It should be noted that the paraboloidal yield surface used in this study can be solely calibrated by the epoxy tensile (X_T) and compressive (X_C) strength and their corresponding (uniaxial) strain hardening curves (see Appendix A). Piecewise exponential hardening functions of the equivalent plastic strain were used to ensure convergence. As a result of symmetricity of the fully differentiable yield surface and the flow potential, a return mapping algorithm was used in an explicit (i.e., forward Euler) framework (see Appendix B).

A solution-dependent variable (SDV) was defined within the VUMAT subroutine, denoted as SDV3, to indicate the occurrence of local failure mechanisms in the elements during the simulations. The SDV was capable of indicating yielding, cavitation after yielding, and brittle cavitation. Although the subroutine is also capable of capturing ductile failure after inelastic deformation, this was not considered for the current study. It is worth noting that the absence of any damage (i.e., pristine condition) was considered as the baseline state. The onset of ductile failure follows a paraboloidal yield criterion at the tensile and compressive strength using the effective stress concept in continuum damage mechanics [2]. Accordingly, the following relation identifies an occurrence of ductile failure:

$$F_{dis} = \frac{3\tilde{J}_2}{X_C X_T} + \frac{\tilde{I}_1 (X_C - X_T)}{X_C X_T} - 1 \geq 0 \tag{6-1}$$

Here, $\tilde{J}_2$ and $\tilde{I}_1$ are the second deviatoric invariant and the first invariant of effective stress tensors, respectively. Based on the continuum mechanics concept, the effective stress tensor defined as:

$$\tilde{\boldsymbol{\sigma}} = \tilde{\mathbf{C}} : \boldsymbol{\varepsilon} \tag{6-2}$$

where $\boldsymbol{\varepsilon}$ is the current strain and $\tilde{\boldsymbol{C}}$, the effective stiffness tensor, is determined by:

$$\tilde{\boldsymbol{C}} = \begin{bmatrix} \zeta & \lambda & \lambda & 0 & 0 & 0 \\ \lambda & \zeta & \lambda & 0 & 0 & 0 \\ \lambda & \lambda & \zeta & 0 & 0 & 0 \\ 0 & 0 & 0 & G & 0 & 0 \\ 0 & 0 & 0 & 0 & G & 0 \\ 0 & 0 & 0 & 0 & 0 & G \end{bmatrix} \tag{6-3}$$

with

$$\zeta = \frac{E(1-\nu)}{(1+\nu)(1-2\nu)} \tag{6-4}$$

$$\lambda = \frac{E\nu}{(1+\nu)(1-2\nu)} \tag{6-5}$$

Here E, G, and ν denote Young's modulus, shear modulus, and Poisson's ratio, respectively.

The concept of critical dilatation energy density was used to capture cavitation of the epoxy matrix [20]. Although cavitation is understood to occur in the elastic regime, when the matrix exhibits an equitriaxial tensile stress state, this local failure mode can also occur after yielding. Cavitation depends on the critical dilatation energy density, U_{dil}^{c}, where the dilatation energy density is defined as:

$$U_{dil} = \frac{I_1^2(1-2\nu)}{6E} \tag{6-6}$$

Combining the introduced criterion for cavitation by Asp et al. [20] and the continuum mechanics approach, the cavitation damage activation function is introduced as:

$$F_{dil} = \frac{U_{dil}}{U_{dil}^{c}} - 1 \geq 0 \tag{6-7}$$

Figure 45 demonstrates the overall procedure of the VUMAT model with further details found in Appendix B. The subroutine follows conventional explicit integration plasticity algorithms while different branches have been added to capture ductile failure and cavitation of the epoxy. The code begins with an elastic trial and continues by monitoring the requirement for an inelastic deformation (i.e., yield function $\Phi \geq 0$). If inequality has not been satisfied, the subroutine checks for the activation of brittle cavitation; otherwise, the code repeats the inelastic convergence loop. In the loop, the related parameters, including Φ, hardening variables, derivatives, plastic strain, and stress tensor are updated

using the Newton-Raphson root-finding method within the return mapping algorithm. Then, failure in the inelastically deformed epoxy is checked. Accordingly, the damage indicator variable (i.e., SDV3) is updated for all increments. Meanwhile, dilatation and distortion energy densities have been defined as different SDVs where the former can be measured using Eq. (6), and the latter is defined as:

$$U_{dis} = \frac{3}{4G}\left(\sqrt{\frac{2}{3}J_2} - \frac{\mu I_1}{3}\right)^2 \tag{6-8}$$

Here, μ is the internal friction parameter that is set to 0.175 [26]. It should be noted that the invariants at this step were calculated from the updated stress tensor. Loading is also distinguished within the subroutine by measuring the first invariant where $I_1 > 0$, $I_1 < 0$, $I_1 = 0$ indicates tensile, compressive, shear loading cases, respectively.

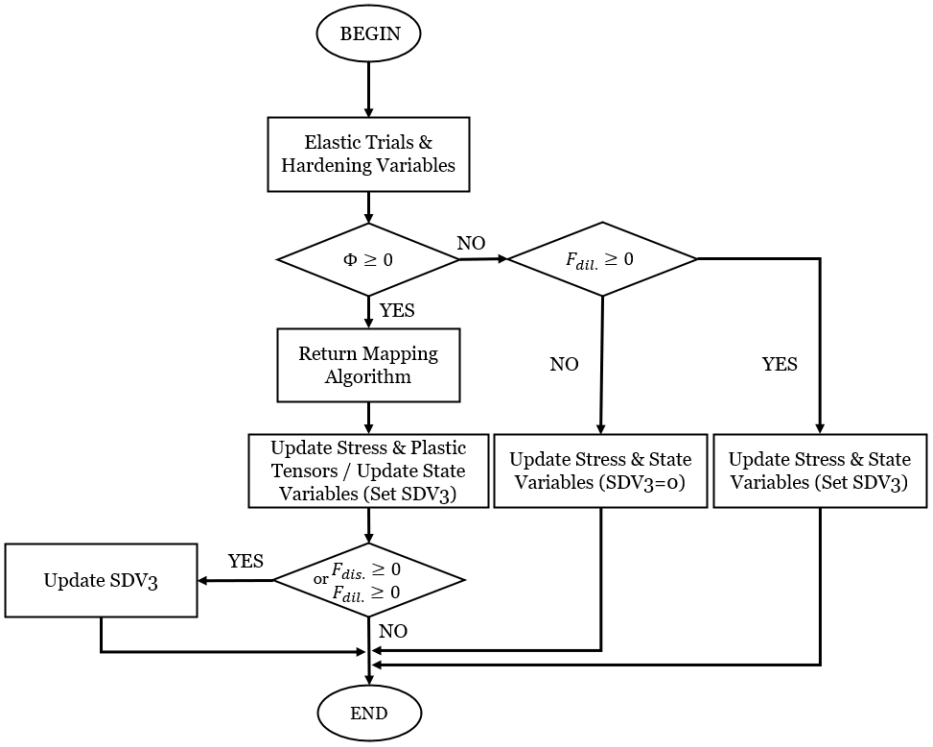

Figure 45. General procedure of the developed user-defined material subroutine for capturing inelastic deformations and failure of epoxies.

6.2.3 Finite element model

A combination of 6-node linear triangular prism elements (C3D6) and 8-node linear brick elements with reduced integration (C3D8R) were utilized to mesh the fibers and matrix within the 90° plies,

whilst only the latter element type was used for the homogenized 0° plies (see Fig. 44). Two-dimensional periodic boundary conditions (PBCs) were applied to the RVEs along the global *x*– and *y*–directions (see Fig. 44). The cross-ply laminate was subjected to an initial thermal cooldown $\Delta T = -100$°C to represent cooldown after curing during fabrication, which was followed by a uniaxial tensile strain along the *x*–direction, ε_x. Also, the described FE models were compared with the case of an unconstrained 90° ply to investigate the influence of ply constraints on the local failure and energy states of the epoxy. In addition to the baseline case (see Fig. 46a), two cases were considered to investigate the consequences of the presence of a resin pocket in the 90° ply (see Fig. 46b,c). It should be noted that the number of fibers in all FE models was kept constant to maintain the fiber volume fraction of the 90° ply.

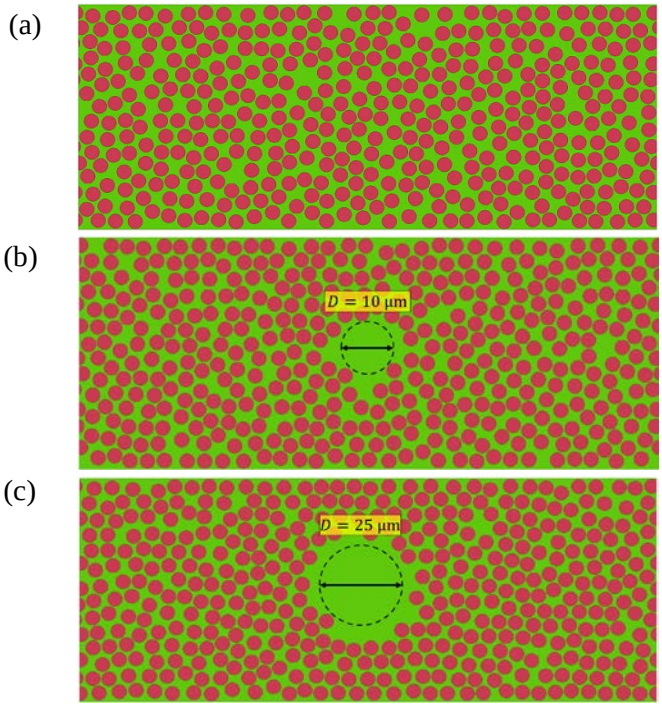

Figure 46. Representation of the nonuniform fiber spatial dispersion in the 90° ply within the laminate with: (a) no resin pocket (i.e., baseline case), (b) 10 μm resin pocket, (c) 25 μm resin pocket.

6.3 Results and discussion

Prior to conducting an assessment using the generated RVEs, the capability of the subroutine to predict inelastic deformation and local failure of the epoxy is examined in Section 6.3.1, followed by a mesh sensitivity analysis in Section 6.3.2. The subsequent sections provide the results of several

investigations focused on the initiation of local damage. In Section 6.3.3, the effect of inelastic deformations is assessed, while an in-depth investigation on the initiation of local damage for the [0/90/0] cross-ply laminate is conducted in Section 6.3.4. The influence of ply constraints on the local energy states and failure is demonstrated in Section 6.3.5. Consequences of manufacturing-induced defects on the early stage of ply cracking are presented in Section 6.3.6. Finally, a general discussion of the results is provided in Section 6.3.7.

6.3.1 Single element verification

A single element was subjected to different loading cases, including uniaxial tension, uniaxial compression, and simple shear, to verify the capability of the developed VUMAT subroutine to predict the inelastic deformation of the epoxy. The predicted stress-strain response of the single element for the different loading scenarios compared well with the experimental data [40] (see Fig. 47a). Note, compression and shear loading results were confined to 15% strain since in CFRP laminates subjected to tensile loads, the epoxy does not experience high strains due to the constraint imparted by the fibers.

The capability of the subroutine in predicting the formation of local failure (i.e., brittle cavitation and ductile failure) is shown in Fig. 47b. At the damage onset point, the subroutine updates the related SDV parameter. When the epoxy experiences an equitriaxial stress state, the result is brittle cavitation, and the graph represents the hydrostatic stress-volumetric strain [21].

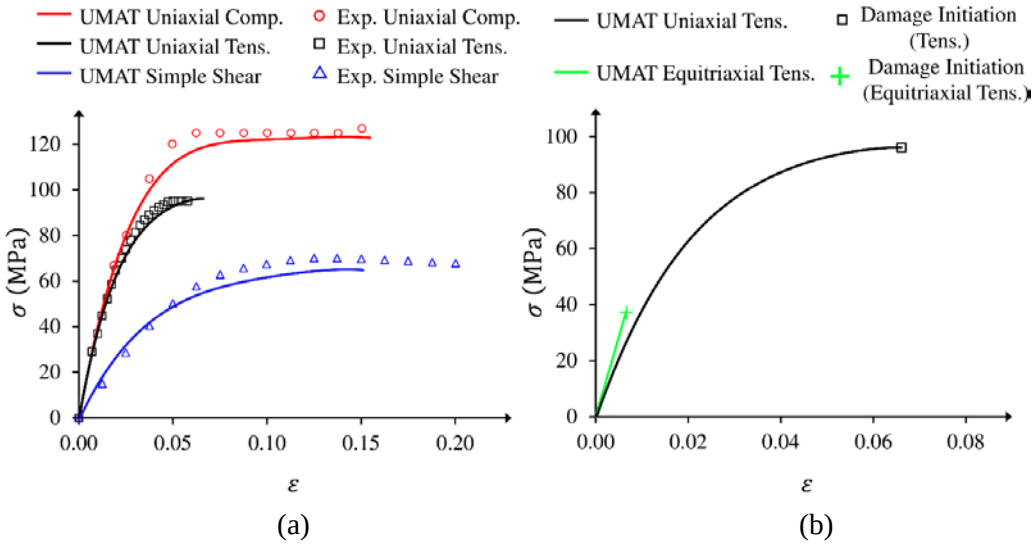

Figure 47. (a) True stress-strain response for the epoxy under different loading cases, (b) True stress-strain response and local failure of the epoxy under uniaxial tensile and equitriaxial loading. The experimental data was taken from [40].

6.3.2 Assessment of the element size

Since local failure of the epoxy within the 90° ply is governed by the energy (stress) states, the dilatation and distortion energy density associated with elements having corresponding peak values during loading was considered for the mesh sensitivity study. The variation of the normalized energy densities with element size for an RVE subjected to a tensile strain along the x–direction reveals that the values converge below a normalized element size of $l_e/r_f = 0.1$, which corresponds to an average element area of 0.068 μm^2 (Fig. 48). RVEs with elements corresponding to this size were used for all simulations reported in this study.

A time efficiency graph (i.e., the inverse of total run time) was added to Fig. 48 to give an approximation for the simulation time, where the overall time step was set to 10^{-7}. The loading rate was set such that the kinetic energy of the RVE was minimized to ensure that quasi-static loading conditions were maintained during the explicit analysis. The overall run-time for analyzing a single RVE comprising 650,000 elements, including thermal and displacement loading, with the chosen element size and the developed VUMAT model was close to 18 hours. The simulation was conducted on an Intel Core i7-6700T with 8 GB RAM to obtain the reported results in the current study.

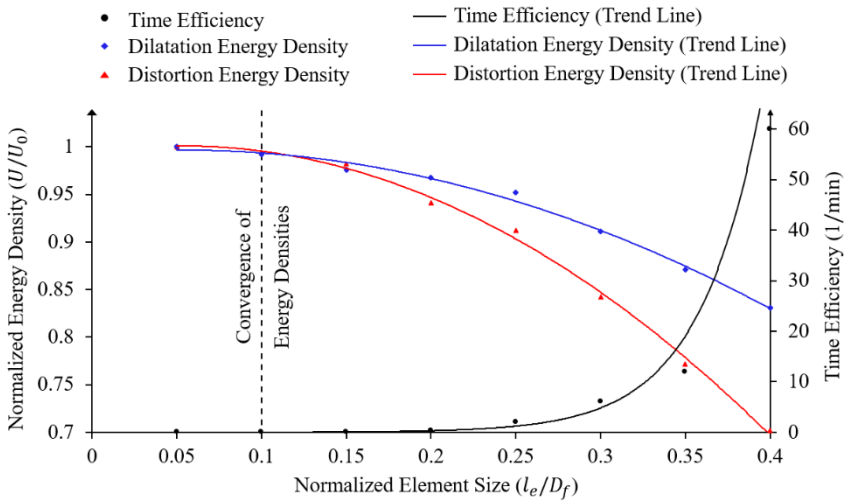

Figure 48. Variation of normalized energy density and the overall simulation time with normalized element size of the matrix for elements with peak energy densities.

6.3.3 Effect of inelastic matrix deformation

Two FE models for the generated RVEs were analyzed to assess the significance of the inelastic matrix deformation in the cross-ply laminate, one with the matrix assumed to undergo elasto-plastic

deformations (i.e., using the developed VUMAT model), the other with linear-elastic matrix deformations. A point-failure contour was obtained according to the defined solution-dependent variable (SDV3) to elucidate the occurrence of cavitation and yielding of the matrix within the 90° ply.

Figure 49 illustrates a one-to-one comparison between the two above-mentioned models after a thermal cooldown of 100°C and a tensile strain of 0.1% along the *x*-direction, which corresponds to a region in the 90° ply where there was negligible interaction between local failure mechanisms. The distortion energy densities of both cases at the same loading are compared in Fig. 50. Based on the described relations in Section 6.3.2, the distortion energy density of elements subjected to tensile and compressive loading was distinguished by a positive and negative sign, respectively. The same definition was used for the dilatation energy density in further subsections, where under compressive stresses cavitation cannot be activated.

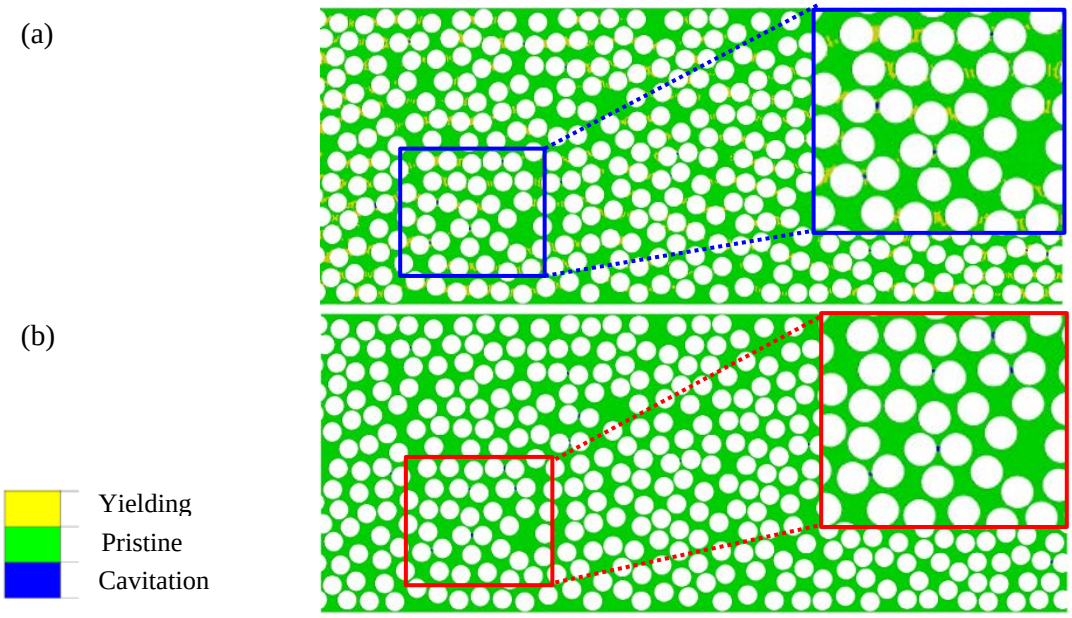

Figure 49. Point-failure (SDV3) contours of the matrix within the 90° ply of the [0/90/0] laminate after 0.1% transverse strain and the initial cooldown for the case when the matrix deformation is: (a) elasto-plastic, and (b) linear-elastic.

When the epoxy was treated as an elastic material the number and location of predicted cavitation sites deviated from those predicted when inelastic matrix deformation was considered (Fig. 49). The indirect influence of local inelastic deformation on brittle cavitation is further demonstrated from the distinct distortion energy density contours for both cases (Fig. 50a,b). Linear elastic representation of

the epoxy in the simulation failed to capture a realistic local distortion energy distribution. For the case where inelastic matrix deformation was considered, a higher degree of distortion formed in the oblique direction between adjacent fibers (Fig. 50c), where the effective stress is greater [24]. As expected, the brittle cavitation sites were located between adjacent fibers with limited inter-fiber spacing where equitriaxial tension, and therefore a critical dilatation energy density (Fig. 50d), was achieved due to the constraint imposed by the fibers on the matrix [27].

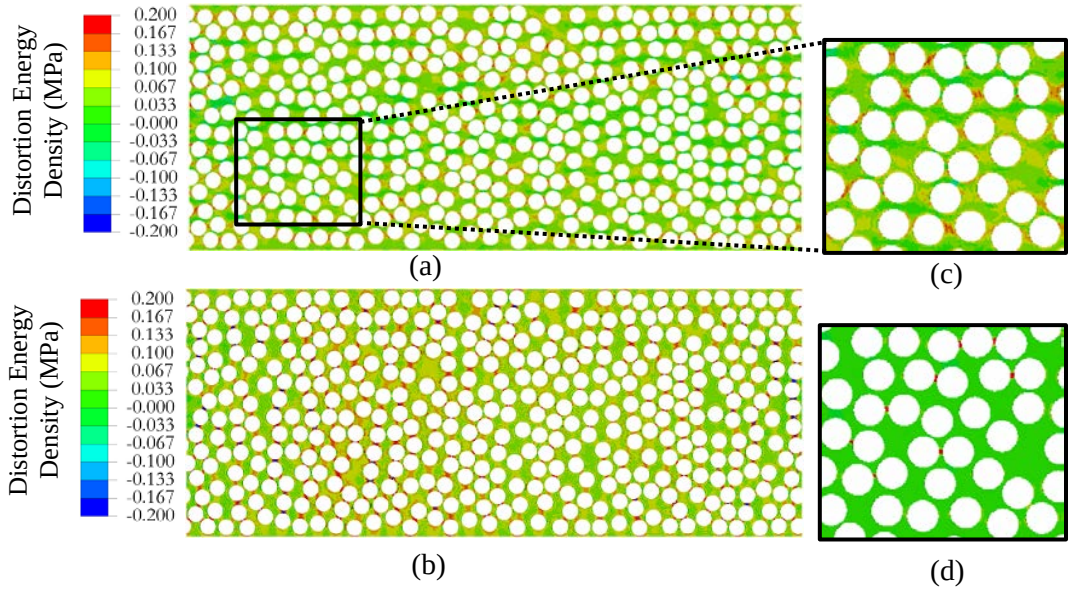

Figure 50. Energy contours of the matrix within the [0/90/0] laminate after 0.1% transverse strain and the initial cooldown: (a) distortion energy density of the elasto-plastic model; (b) distortion energy density of the linear-elastic model; (c) magnified distortion energy density contour of the elasto-plastic model; (d) magnified dilatation energy density of the elasto-plastic model (same region as in (c)).

6.3.4 Local failure in laminates

Here, the progression of local failure in the [0/90/0] laminate under a thermal cooldown followed by an applied tensile strain is assessed. Cavitation was predicted in some locations after the laminate was subjected to the thermal cooldown and prior to the application of strain (Fig. 51a). In addition to the mismatch in the thermal expansion coefficients for the fibers and the matrix, the onset of cavitation during thermal cooldown was also influenced by the mismatch in the effective thermal expansion coefficients of the 90° and 0° plies along the global *x*-direction which caused tensile stresses in the 90° ply. Cavitation induced during thermal cooldown can explain experimentally observed debonding crack after processing [43]. Even though cavitation occurred during and after thermal cooldown, the number

of cavitation sites gradually increased up to an applied tensile strain of 0.1% (Fig. 51b), revealing that cavitation was somewhat suppressed. After 0.15% strain, the number of cavitation sites began to increase with a higher rate (Fig. 51c). Predicted inelastic deformations of the matrix increased continually with increasing applied tensile strain; however, this did not cause any local ductile failure. Note that compressive-driven inelastic deformations of the matrix were predicted to occur at the top and bottom of fibers and resulted from different thermal and mechanical properties of fiber and matrix.

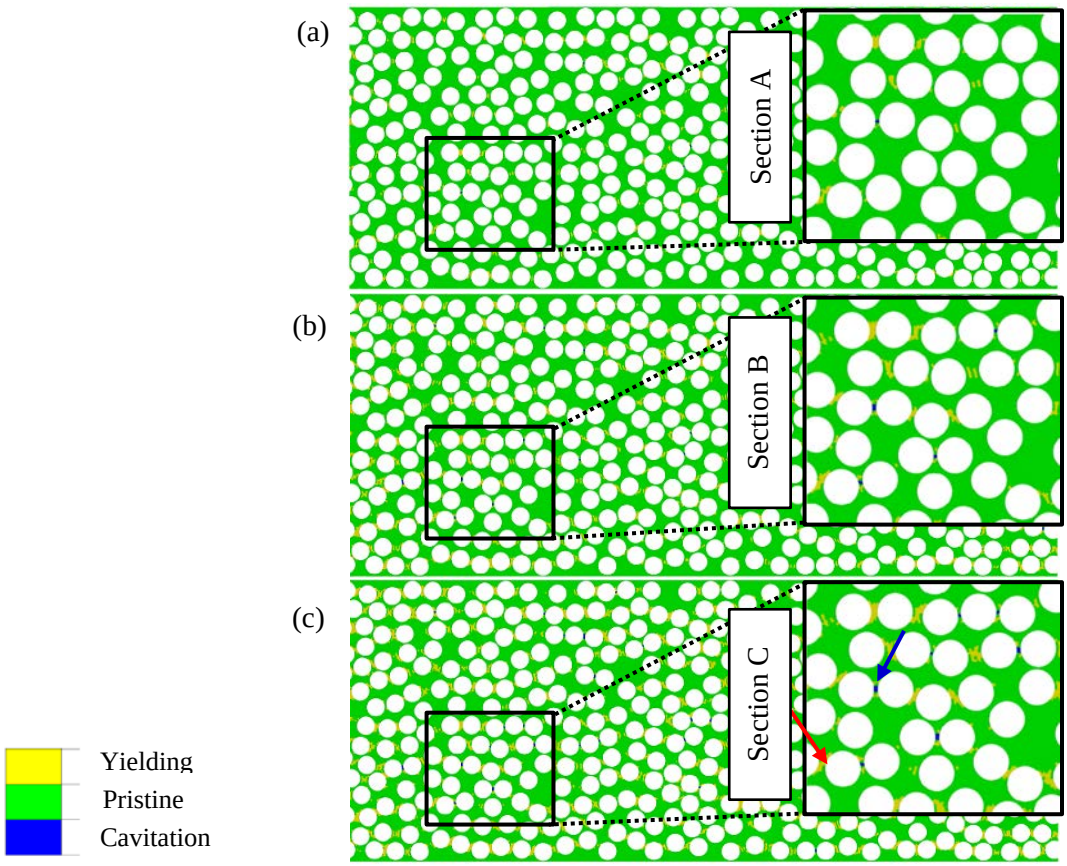

Figure 51. Point-failure contours of the inelastic matrix within the [0/90/0] laminate after the initial cooldown and: (a) no transverse strain, (b) 0.1% transverse strain, and (c) 0.15% transverse strain.

The location of critical distortion and dilatation energy density in the 90° ply (Fig. 52, Sections A and B) confirms the location of ductile failure and cavitation reported in previous studies, where stress concentrations in the vicinity of fibers along the *x*- and *y*-axes were defined as favourable locations [24]. Nevertheless, the presence of a nonuniform fiber spatial distribution competes against the

conventional presumption (Fig. 52, Section C), which, consequently, causes a nonuniform stress concentration and stress redistribution in the matrix during thermal and strain loading.

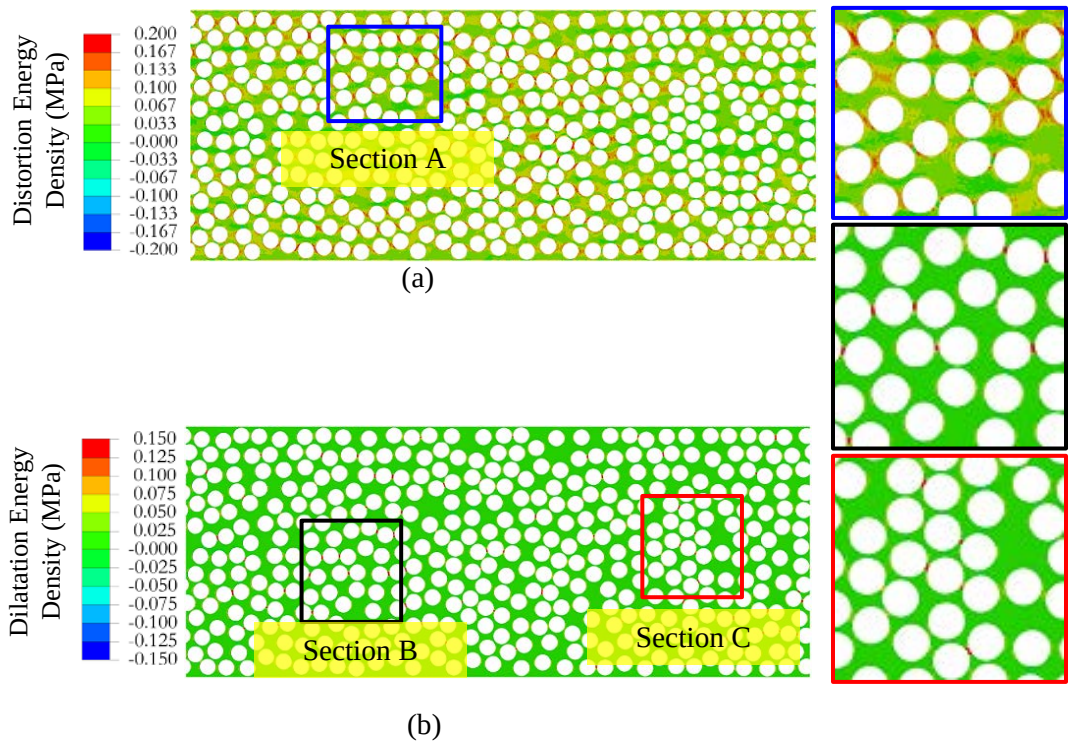

Figure 52. (a) Distortion, and (b) dilatation energy density contours of the matrix within the [0/90/0] laminate after 0.2% transverse strain and the initial cooldown.

The principal stresses (σ_1, σ_2, σ_3) and the hydrostatic stress (σ_{hyd}) of a single matrix element within the RVE that experiences cavitation during and after thermal cooldown was tracked (Fig. 53). The σ_1/σ_{hyd} ratio is a representative of the triaxial stress state where a value of 1 indicates an equitriaxial stress state. It is worth noting that elements were selected far from other cavitation sites to minimize stress interaction effect. The cavitated element initially inclined toward an equitriaxial stress state during the thermal cooldown stage. Notwithstanding, the degree of hydrostatic stress later declined in the element, which was followed by a subsequent tendency toward the equitriaxial stress state. The change of stress ratios suggests the presence of a transition stage where the initial triaxial type loading (i.e., thermal loading) in the epoxy gradually transforms to a combined stress state. This observation can explain a delay in the formation of cavitation in the laminate.

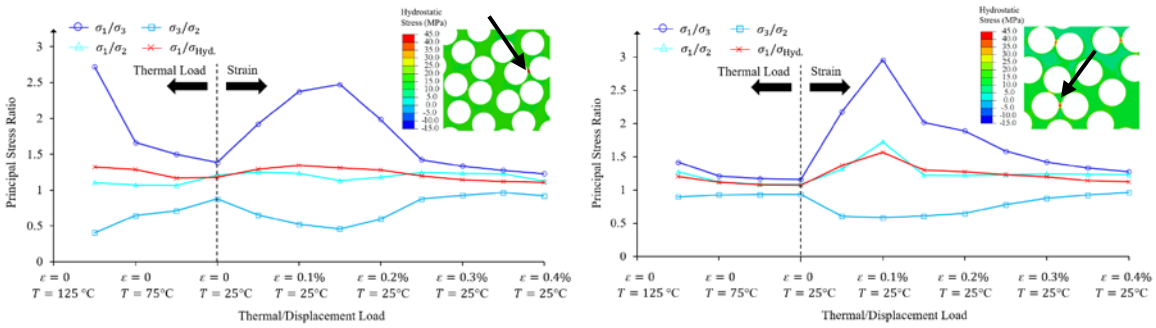

(a) (b)

Figure 53. Variation of principal stress ratios for an element that cavitated (a) during and (b) after thermal cooldown in the matrix of 90° ply within the [0/90/0] laminate.

6.3.5 Effects of Ply Constraints

The subsequent investigation aimed at understanding the effect of ply constraints on the local failure mechanisms in the 90° ply of the [0/90/0] laminate, where corresponding point-failure contours for the unconstrained 90° ply (Fig. 54) were compared with that of the constrained 90° ply (Fig. 51). The same fiber spatial dispersion, mesh pattern and loading sequence were maintained in the 90° ply for both cases to enable a one-to-one comparison. As in Section 6.3.4, point-failure contour results were confined to strains up to 0.15%. The onset of cavitation and yielding were delayed for the unconstrained 90° ply when compared to the constrained case. For instance, no evidence of local failure was observed after thermal cooldown for the unconstrained 90° ply, while several elements experienced cavitation and inelastic deformations in the [0/90/0] laminate. Inelastic deformation was also more widespread in the constrained 90° ply (compare Fig. 51c and Fig. 54c). Furthermore, the location of local failure in some regions of the unconstrained 90° ply is distinct from that of the laminate. Previously, the authors have reported that the ply constraining effect was not observed before local damage formation [6] (see Chapter 5).

The dilatation and distortion energy density of identical elements in the RVEs of the constrained and unconstrained 90° plies (see indicators in Fig. 51c and Fig. 54c) were tracked for elements corresponding to sites of cavitation and inelastic deformation (Fig. 55). The element susceptible to cavitation is evidently affected by the ply constraints, while the element that underwent inelastic deformation follows an ascending trend. Notwithstanding, the parallel increase of the hydrostatic stress in the constrained ply confronts the amplification of distortion energy density in higher strains. Hence, it can be inferred that the cross-ply laminate undergoes a higher degree of so-called equitriaxial loading

than the unconstrained 90° ply before applying a mechanical strain. This difference originates from the thermal expansion coefficient of constituents (i.e., fiber, matrix, adjacent plies) and the Poisson effect during loading. In fact, adjacent layers impose greater tensile stress than the fibers and matrix along the *x*–axis during the thermal cooldown, which cause tensile stress in the constrained ply. Furthermore, the constraining effect of adjacent layers in restricting the deformation of the 90° ply along the global *z*–direction while applying strain enforces extra tensile stress to the constrained ply. Thus, the ply constraining effect caused by the adjacent plies expedites the local failure events in the laminate, while a lesser increase rate of energy densities is observed in the unconstrained 90° ply after the transition stage.

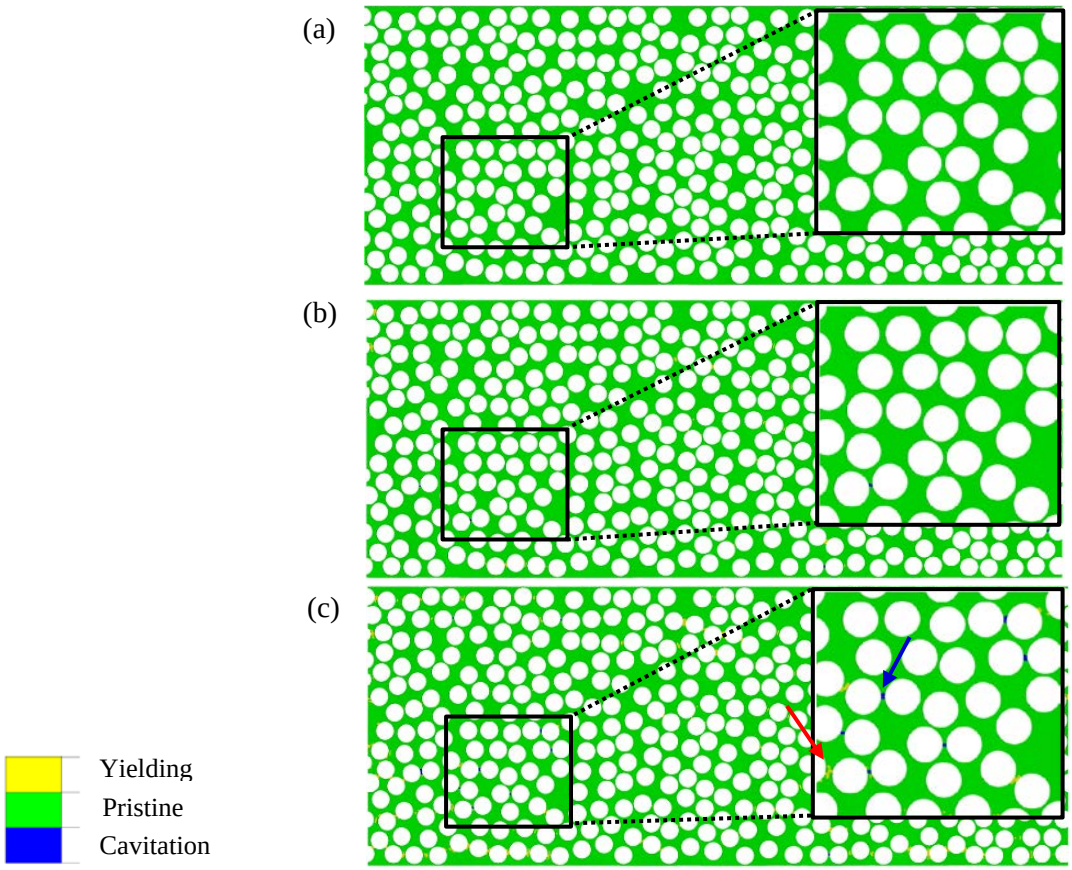

Figure 54. Point-failure contours of the inelastic matrix in the unconstrained 90° ply after the initial cooldown and (a) no transverse strain, (b) 0.1% transverse strain, (c) 0.15% transverse strain.

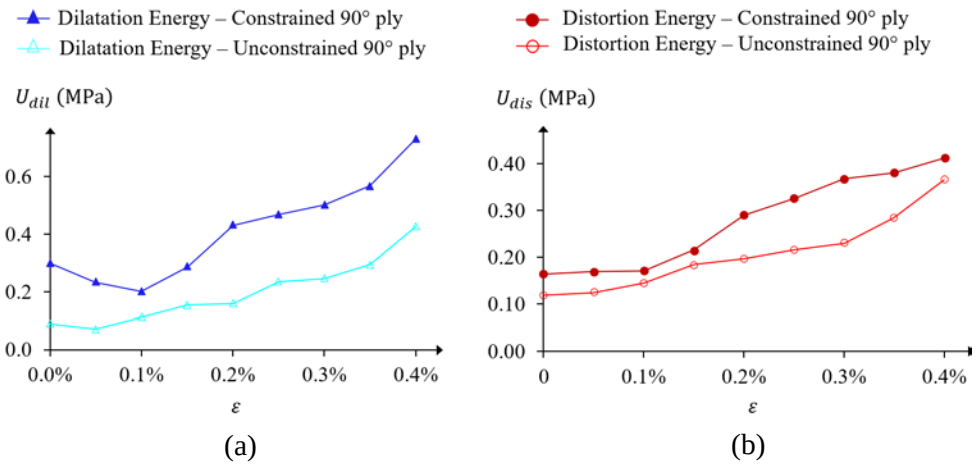

Figure 55. (a) Variation of dilatation energy density for a cavitated element in the constrained and unconstrained 90° ply, (b) variation of distortion energy density for an inelastically damaged element in the constrained and unconstrained 90° ply.

6.3.6 Effect of a resin-rich pocket on local failure

To better understand the influence of a resin-rich pocket within the 90° ply of the [0/90/0] laminate on the onset of local failure, the RVEs depicted in Fig. 46 were analyzed. Figure 56 depicts the number of brittle cavitation sites as a function of the applied strain after the initial thermal cooldown. Results show that the number of cavitation sites is always higher in the RVEs with larger resin pockets. A similar conclusion was gained after applying the initial thermal cooldown. This understanding is intuitive since a larger resin pocket leads to lower inter-fiber spacing in the adjacent regions. Thus, a higher degree of stress concentration, which was highlighted as the controlling parameter for local failure, increases the number of cavitation incidents.

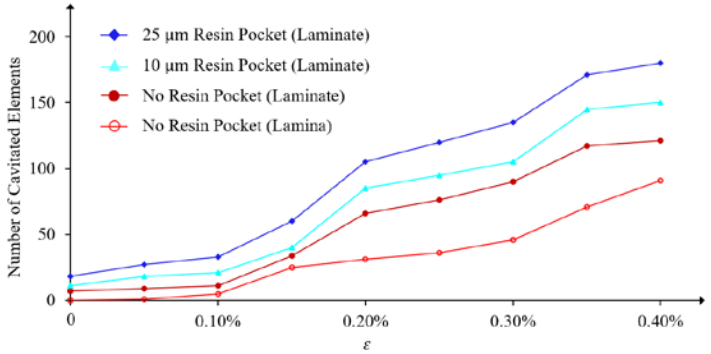

Figure 56. Number of cavitation incidents versus the strain influenced by the manufacturing-induced resin pocket presence and ply constraining effect.

6.3.7 General discussion

The physical reason behind local failure events in laminates subjected to tensile loading has been partially understood, while almost all the forerunners of the topic agree on the brittle nature of the local failure. The governing presence of cavitation in the current study (see Fig. 51) endorses the acquired comprehension and discards the possibility of ductile failure. It is unlikely that neglecting inelastic deformation of the epoxy can lead to accurate prediction of microcrack formation and propagation. Inelastic deformations indirectly influence the cavitation as well as the local energy (stress) states as was demonstrated in the present study. Although it was shown that the constrained 90° ply exhibited more cavitation sites than the unconstrained 90° ply, it cannot be concluded that the formation of microcracks occurs sooner in the laminate. In fact, local inelastic deformations, ply constraints in the presence of voids [6], and resisting effects after thermal cooldown (Fig. 53) can contribute to causing a delay in the formation and propagation of microcracks. Furthermore, cavitation and microcrack formation typically occurs close to the fiber/matrix interfaces, which can be misrepresented as decohesion. Thus, decohesion shall be regarded as the consequence of local brittle damage (not vice versa) as was reported in previous work [44]. Concurrent contributions of several factors, such as thermal residual stress, manufacturing-induced defects, and ply constraints, indicate the complexity of crack formation, while the outcome can be different for other material systems. The transition stage between thermal and mechanical loading is an example of confrontation of these factors in the studied laminate. The results confirm the previous investigation in Ref. [6] that ply constraints do not equally influence the distortion and dilatation energy density within the 90° ply. The presence of resin pocket was found to be a provocative factor in the formation of cavitation. This conclusion contradicts the previous observation in [19], where the cavitation in RVEs with a larger resin pocket was delayed. This may be because brittle damage (i.e., cavitation) was not considered in the cited study. Since it was predicted that local inelastic deformation was less influential on the formation of cavitation sites in the presence of resin pockets, it is expected that microcracks follow a path close to the fibers and not within the resin-rich zone.

6.4 Conclusions

A three-dimensional computational micromechanical model was developed to assess the onset of local failure mechanisms preceding the formation of a ply crack in [0/90/0] cross-ply laminates comprising carbon fiber/epoxy unidirectional (UD) plies. The representative volume elements (RVEs) included the constraining 0° plies and manufacturing-induced defects within the 90° ply and was subjected to a

thermal cooldown and tensile loading. A new user-defined material subroutine was developed to capture the influence of inelastic matrix deformations and to predict different modes of local failure (i.e., yielding and cavitation). The following points are the main conclusions of the study:

- Brittle cavitation was predicted as the first and governing local failure mechanism before inelastic deformation, which was followed by the interaction of cavitation sites. Nevertheless, local inelastic deformation was observed after cavitation occurred.
- It was shown that a thermal cooldown may provoke cavitation due to the occurrence of equitriaxial stress states that resulted from the presence of ply constraints and differences in the thermal expansion coefficients of the constituents. A transition stage from local equitriaxial stress state to a combined stress state was observed when a tensile load was subsequently applied.
- Comparing the case of a 90° ply within the laminate with an unconstrained 90° ply revealed that the local failure (cavitation) was more prominent in the constrained case, while local inelastic deformation was also more pronounced.
- Capturing the cavitation incidents of RVEs containing manufacturing-induced defects indicated that formation of a larger resin pocket causes more local failure sites due to reduced inter-fiber spacing in the adjacent regions.

This study provided a fundamental understanding of the onset of local failure mechanisms in constrained UD plies, which aids in improving the comprehension of ply crack formation. Particularly, micromechanical modelling can provide an estimation of the effective critical energy release rates associated with the formation of ply cracks and facilitate the establishment of a multiscale modelling framework.

References

[1] A.S. Kaddour, M.J. Hinton, P.A. Smith, S. Li, A comparison between the predictive capability of matrix cracking, damage and failure criteria for fibre reinforced composite laminates: Part A of the third world-wide failure exercise, Journal of Composite Materials 47 (2013) 2749–2779.

[2] R. Talreja, C.V. Singh, Damage and Failure of Composite Materials, Cambridge University Press, 2012.

[3] J. Montesano, F. Sharifpour, Modelling damage evolution in multidirectional laminates: micro to macro, in: W. Van Paepegem (Ed.), Multi-Scale Continuum Mechanics Modelling of Fibre-Reinforced Polymer Composites, Woodhead Publishing Series in Composites Science and Engineering, 2021: pp. 463–507.

[4] R. Talreja, Modelling defect severity for failure analysis of composites, in: W. Van Paepegem (Ed.), Multi-Scale Continuum Mechanics Modelling of Fibre-Reinforced Polymer Composites, Woodhead Publishing Series in Composites Science and Engineering, 2021: pp. 275–306.

[5] B. El Said, S.R. Hallett, Multiscale modelling of laminated composite structures with defects and features, in: W. Van Paepegem (Ed.), Multi-Scale Continuum Mechanics Modelling of Fibre-Reinforced Polymer Composites, Woodhead Publishing Series in Composites Science and Engineering, 2021: pp. 637–668.

[6] F. Sharifpour, J. Montesano, R. Talreja, Assessing the effects of ply constraints on local stress states in cross-ply laminates containing manufacturing induced defects, Composites Part B: Engineering 199 (2020) 1–13.

[7] J. Montesano, C.V. Singh, A synergistic damage mechanics based multiscale model for composite laminates subjected to multiaxial strains, Mechanics of Materials 83 (2015) 72–89.

[8] J. Montesano, C.V. Singh, Predicting evolution of ply cracks in composite laminates subjected to biaxial loading, Composites Part B: Engineering 75 (2015) 264–273.

[9] A. Arteiro, G. Catalanotti, A.R. Melro, P. Linde, P.P. Camanho, Micro-mechanical analysis of the in situ effect in polymer composite laminates, Composite Structures 116 (2014) 827–840.

[10] J. Tong, F.J. Guild, S.L. Ogin, P.A. Smith, On matrix crack growth in quasi-isotropic laminates-I. Experimental investigation, Composites Science and Technology 57 (1997) 1527–1535.

[11] C.A. Wood, W.L. Bradley, Determination of the effect of seawater on the interfacial strength of an interlayer E-glass/ graphite/epoxy composite by in situ observation of transverse cracking in an environmental SEM, Composites Science and Technology 57 (1997) 1033–1043.

[12] B.A. Sjögren, L.A. Berglund, The effects of matrix and interface on damage in GRP cross-ply laminates, Composites Science and Technology 60 (2000) 9–21.

[13] E.K. Gamstedt, B.A. Sjögren, Micromechanisms in tension compression fatigue of composite laminates containing transverse plies, Composites Science and Technology 59 (1999) 167–178.

[14] H. Saito, H. Takeuchi, I. Kimpara, Experimental evaluation of the damage growth restraining in 90° layer of thin-ply CFRP cross-ply laminates, Advanced Composite Materials 21 (2012) 57–66.

[15] J.E. Bailey, P.T. Curtis, A. Parvizi, On the transverse cracking and longitudinal splitting behavior of glass and carbon-fiber reinforced epoxy cross-ply laminates and the effect of Poisson and thermally generated strain, Proceedings of the Royal Society A: Mathematical, Physical and Engineering Sciences 366 (1979) 599–623.

[16] H. Saito, H. Takeuchi, I. Kimpara, A study of crack suppression mechanism of thin-ply carbon-fiber-reinforced polymer laminate with mesoscopic numerical simulation, Journal of Composite Materials. 48 (2014) 2085–2096.

[17] A.R. Melro, P.P. Camanho, F.M.A. Pires, S.T. Pinho, Micromechanical analysis of polymer composites reinforced by unidirectional fibres : Part I – Constitutive modelling, International Journal of Solids and Structures 50 (2013) 1897–1905.

[18] A.R. Melro, P.P. Camanho, F.M.A. Pires, S.T. Pinho, Micromechanical analysis of polymer composites reinforced by unidirectional fibres : Part II – Micromechanical analyses, International Journal of Solids and Structures 50 (2013) 1906–1915.

[19] H. Ghayoor, C.C. Marsden, S. V Hoa, A.R. Melro, Numerical analysis of resin-rich areas and their effects on failure initiation of composites, Composites Part A: Applied Science and Manufacturing 117 (2019) 125–133.

[20] L.E. Asp, L.A. Berglund, R. Talreja, A criterion for crack initiation in glassy polymers subjected to a composite-like stress state, Composites Science and Technology. 56 (1996) 1291–1301.

[21] L.E. Asp, L.A. Berglund, P. Gudmundson, Effects of a composite-like stress state on the fracture of epoxies, Composites Science and Technology. 53 (1995) 27–37.

[22] L. Maragoni, R. Talreja, Transverse crack formation in unidirectional plies predicted by means of a percolation concept, Composites Part A: Applied Science and Manufacturing 117 (2019) 317–323.

[23] Y. Kumagai, S. Onodera, M. Salviato, T. Okabe, Multiscale analysis and experimental validation of crack initiation in quasi-isotropic laminates, International Journal of Solids and Structures 193–194 (2020) 172–191.

[24] L.E. Asp, L.A. Berglund, R. Talreja, Prediction of matrix-initiated transverse failure in polymer composites, Composites Science and Technology. 56 (1996) 1089–1097.

[25] T. Okabe, H. Imamura, Y. Sato, R. Higuchi, J. Koyanagi, R. Talreja, Experimental and numerical studies of initial cracking in CFRP cross-ply laminates, Composites Part A: Applied Science and Manufacturing 68 (2015) 81–89.

[26] S.A. Elnekhaily, R. Talreja, Effect of axial shear and transverse tension on early failure events in unidirectional polymer matrix composites, Composites Part A: Applied Science and Manufacturing 119 (2019) 275–282.

[27] S.A. Elnekhaily, R. Talreja, Damage initiation in unidirectional fiber composites with different degrees of nonuniform fiber distribution, Composites Science and Technology. 155 (2018) 22–32.

[28] L. Zhuang, A. Pupurs, J. Varna, R. Talreja, Z. Ayadi, Effects of inter-fiber spacing on fiber-matrix debond crack growth in unidirectional composites under transverse loading, Composites Part A: Applied Science and Manufacturing 109 (2018) 463–471.

[29] M. Mehdikhani, N.A. Petrov, I. Straumit, A.R. Melro, S. V. Lomov, L. Gorbatikh, The effect of voids on matrix cracking in composite laminates as revealed by combined computations at the micro- and meso-scales, Compos. Part A Appl. Sci. Manuf. 117 (2019) 180–192.

[30] M. Naderi, N. Iyyer, Micromechanical analysis of damage mechanisms under tension of 0°–90° thin-ply composite laminates, Compos. Struct. 234 (2020) 111659.

[31] R. Sepasdar, M. Shakiba, Micromechanical study of multiple transverse cracking in cross-ply fiber-reinforced composite laminates, Compos. Struct. (2021) 114986.

[32] A. Farrokhabadi, H. Madadi, M. Naghdinasab, A. Rafie, S.A. Taghizadeh, M. Herráez, Micromechanical investigation of cross-ply carbon composite laminates with glass microtubes using CZM and XFEM, Mech. Adv. Mater. Struct. (2021).

[33] M. Herráez, D. Mora, F. Naya, C.S. Lopes, C. González, J. Llorca, Transverse cracking of cross-ply laminates: A computational micromechanics perspective, Compos. Sci. Technol. 110 (2015) 196–204.

[34] A. Sudhir, R. Talreja, Simulation of manufacturing induced fiber clustering and matrix voids and their effect on transverse crack formation in unidirectional composites, Composites Part A: Applied Science and Manufacturing 127 (2019) 105620.

[35] G. Li, F. Sharifpour, A. Bahmani, J. Montesano, A new approach to rapidly generate random periodic representative volume elements for microstructural assessment of high volume fraction composites, Materials & Design 150 (2018) 124–138.

[36] K.K. Chawla, Composite Materials, Third Ed., Springer, 2012.

[37] J.C. Halpin, J.L. Kardos, Halpin–Tsai equations – review, Polymer Engineering & Science 16 (1976) 344–352.

[38] C.C. Chamis, Mechanics of Composite Materials: Past, Present, and Future, Journal of Composites, Technology and Research ASTM. 11 (1989) 3–14.

[39] ABAQUS, ABAQUS 6.14 Analysis User's Manual, (2014).

[40] B. Fiedler, M. Hojo, S. Ochiai, K. Schulte, M. Ando, Failure behavior of an epoxy matrix under different kinds of static loading, Composites Science and Technology. 61 (2001) 1615–1624.

[41] N.W. Tschoegl, Failure surfaces in principal stress space, Journal of Polymer Science: Polymer Symposia 32 (1971) 239–267.

[42] X. Bai, M.A. Bessa, A.R. Melro, P.P. Camanho, L. Guo, W.K. Liu, High-fidelity micro-scale modeling of the thermo-visco-plastic behavior of carbon fiber polymer matrix composites, Composite Structures. 134 (2015) 132–141.

[43] D.L. Hiemstra, N.R. Sottos, Thermally Induced Interfacial Microcracking in Polymer Matrix Composites, Journal of Composite Materials. 27 (1993) 1030–1051.

[44] F. París, M.L. Velasco, E. Correa, Modelling fibre–matrix interface debonding and matrix cracking in composite laminates, in: Multi-Scale Continuum Mechanics Modelling of Fibre-Reinforced Polymer Composites, Woodhead Publishing Series in Composites Science and Engineering, 2021, pp. 243–274.

Chapter 7

Micromechanical simulation of ply crack formation in cross-ply laminates under quasi-static tensile loading

(Manuscript to be submitted January 2022, Composites Part A: Applied Science and Manufacturing)

7.1 Introduction

Increased usage of laminated composites in load-bearing structures within different industrial sectors has prompted the need to further assess their failure characteristics and long-term durability in order to optimize structural performance. However, the complex multiscale nature of failure in these materials challenges the current understanding of damage evolution processes and the ability to accurately predict failure. The unavoidable presence of processing-induced defects (e.g., voids) and variability of the microstructure of composite materials have further complicated prediction of their mechanical performance [1–2]. Specifically, the microstructure of laminates comprising unidirectional (UD) plies is influenced by factors such as the processing method, constituent type, fiber architecture, and structural geometry. Multiscale modelling approaches have been proposed as a remedy to capture and link damage evolution processes at different length scales, in particular for ply cracking [3]. A comprehensive valuation of damage progression in laminated composites requires an improved understanding of the response of the constituents at the microscale.

Damage evolution processes in laminates have been well-established at the coupon level [4–6]. The formation of ply cracks in laminates subjected to tensile loading has been reported as the first failure event, which is often followed by a sub-critical crack multiplication stage that is responsible for degradation of the laminate properties. It should be noted that ply cracks that form under quasi-static loading quickly span the width of laminates [4,5], while during cyclic loading ply cracks tunnel with increasing loading cycles [6]. Conservative methods that ignore the damage evolution process, such as the so-called ply discount method, or those that overly simplify the damage evolution process continue to be used by designers since these approaches are available in commercial finite element codes. Consequently, the failure threshold in laminates is underestimated and the damage tolerance characteristics are ignored which are otherwise enabled by the constraint from adjacent plies. [3,7].

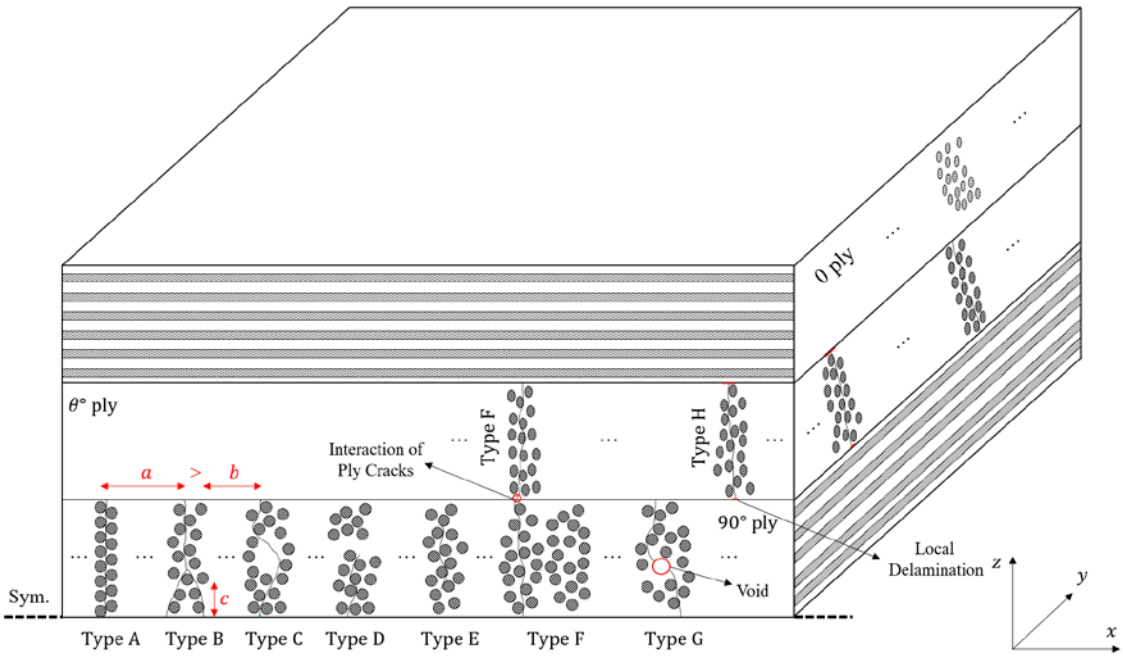

Figure 57. Schematic illustration of crack types in a $[0/\theta/90]_s$ laminate; Type A: ideal ply crack; Type B: branched crack; Type C: oblique crack; Type D: partial crack at the ply surface; Type E: partial crack at center; Type F: ply crack interaction of cracks in different plies; Type G: void; Type H: interaction of damage modes (local delamination).

Mesoscale modelling is generally regarded as a suitable approach to capture the degradation of laminate stiffness during the sub-critical cracking stage [3,8]. Despite the fact that mesoscale models are capable of accounting for the effect of ply constraints on ply cracking [8], they fail to account for microscale phenomena during ply cracking. Ply constraints influence the local deformation response of the epoxy, which can be stimulated by the presence of voids, non-uniform fiber spatial dispersion, and thermal residual stress caused during cooldown after curing [7] (see Chapter 5, 6). To clarify the difference in the presumptions of mesoscale modelling, a schematic representation of different forms of ply cracking at the microscale is illustrated in Fig 57. Type A is the only case that is considered in mesoscale modelling, while the other cases shown have been observed [5,9] and would result in distinct energy dissipation when compared to the ideal case. Thus, an ideal crack cannot represent the damage behaviour of plies. A microscale model is required to predict the ply crack formation process (i.e., local point failures and microcrack coalescence), which would capture the realistic shape of ply cracks, the interaction of damage modes, and the influence of manufacturing-induced defects on the response of laminates.

Conducting experiments to characterize damage in composite laminates at the microscale are costly and technically challenging. In recent years, virtual testing techniques utilizing representative volume elements (RVEs) have been proposed to study microscale phenomena in UD composites [10,11]. Although the concept is convenient for predicting the local phenomena, defining an RVE that captures all the internal features of composite materials is challenging and the constituent properties assigned to an RVE must be available [3]. Nevertheless, RVEs can capture most of the physical features of composites at the microscale and the ply crack formation process can be assessed.

Within the context of microscale mechanics of ply cracking in composites, the onset of local failure in epoxies occurs due to cavitation-induced or pressure-dependent ductile failure [12,13], while fiber/matrix interface debonding is often regarded as a distinct failure mode [14,15] (Fig. 58). However, Paris et al. [15] demonstrated the required energy release rate (ERR) to cause debonding is relatively higher than that of local matrix failure incidents. In other words, debonding originates from cavitation-induced or ductile failure in the vicinity of the fiber/matrix interface. Notwithstanding, the ERR associated with debonding may vary with inter-fiber distance, which is often neglected in micromechanical modelling [15,16]. Ply crack formation in laminates has been investigated within a micromechanical framework [14,17–21]; however, the developed models often disregarded at least one of the physical aspects of damage. Ductile failure in epoxy was captured in [14,17–19] using a pressure-dependent yield surface, while cavitation-induced cracking was neglected, and brittle fracture of the epoxy was captured via cohesive zone modelling [14,17–21]. Herraez et al. [20] and Farrokhabadi et al. [21] developed 2D plane strain models to study ply cracking in laminate, where the former utilized extended finite element method (XFEM) to simulate crack propagation in the epoxy. Nevertheless, a plane strain model fails to predict local 3D stress state of an element, which is necessary for capturing cavitation-induced failure, and in-plane behaviour of ply cracking in a laminate (i.e., tunnelling).

In the current study, a computational micromechanical model was developed to simulate the formation of ply cracks in carbon fiber/epoxy [0/90/0] cross-ply laminates subjected to quasi-static tensile loading. For this purpose, an explicit user-defined material (VUMAT) model within a finite element framework was developed to predict the onset of cavitation-induced and pressure-dependent ductile failure in the epoxy matrix (see Chapter 6), while an isotropic damage model was defined to capture the evolution of ply cracks. The developed material model was first used to predict ply crack formation in laminates where associated experimental observations were available from previous studies [4,22]. Additional predictions were made to investigate the effect of different parameters such as ply thickness, fiber volume fraction, and fiber spatial dispersion on the formation of first full-ply

crack. Unlike models reported in previous studies, the comprehensive three-dimensional micromechanical model developed in the current study considers both local cavitation and ductile failure of the matrix, residual thermal stresses due to post-cure thermal cooldown, and ply constraints imparted by adjacent plies.

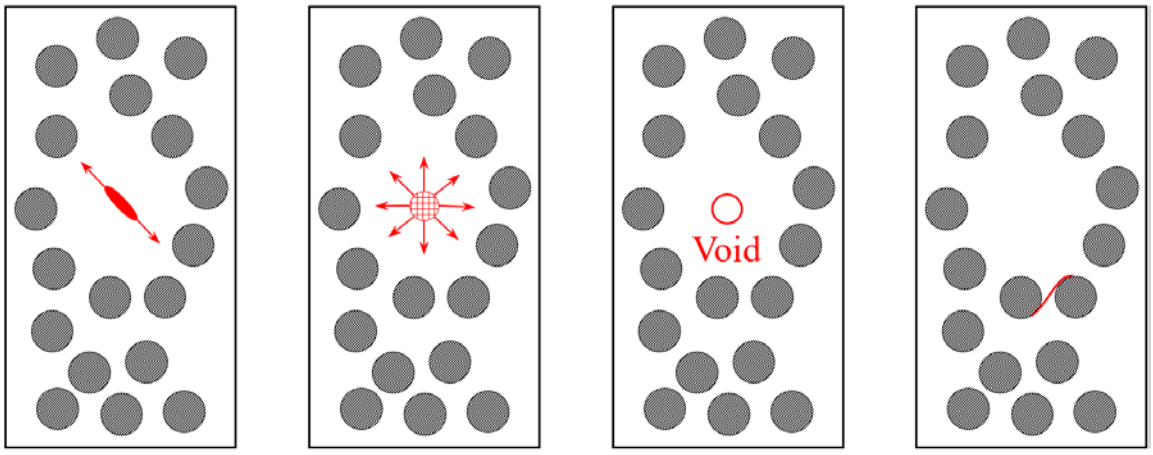

Figure 58. Local failure mechanisms in an epoxy: (a) ductile failure; (b) cavitation; (c) processing-induced defect; (d) debonding.

7.2 Computational model

7.2.1 Micromechanical representation

Three-dimensional representative volume elements (RVEs) were generated to simulate ply crack formation in carbon fiber/epoxy [0/90/0] cross-ply laminates. In all RVEs, the outer 0° plies were treated as homogeneous, while fibers and epoxy in the 90° ply were explicitly modelled. RVEs pertaining to two scenarios were considered in the study. For scenario I, RVEs were generated using images of the fiber spatial dispersion of a 90° ply from a previously study [22], where the focus was to conduct a one-to-one comparison of the predicted ply crack formation with experimental observations. The fiber diameter (3.8 μm $\leq D_f \leq$ 5.4 μm), fiber volume fraction ($V_f \cong$ 60%), 90° ply thickness (h_{90} = 40, 80 μm), and 0° ply thickness (h_0 = 480 μm) were assigned according to Ref. [22] (Fig. 59a). Additionally, a portion of the 90° plies in the RVE were treated as homogeneous since the fiber spatial dispersion of these regions was unavailable from the source.

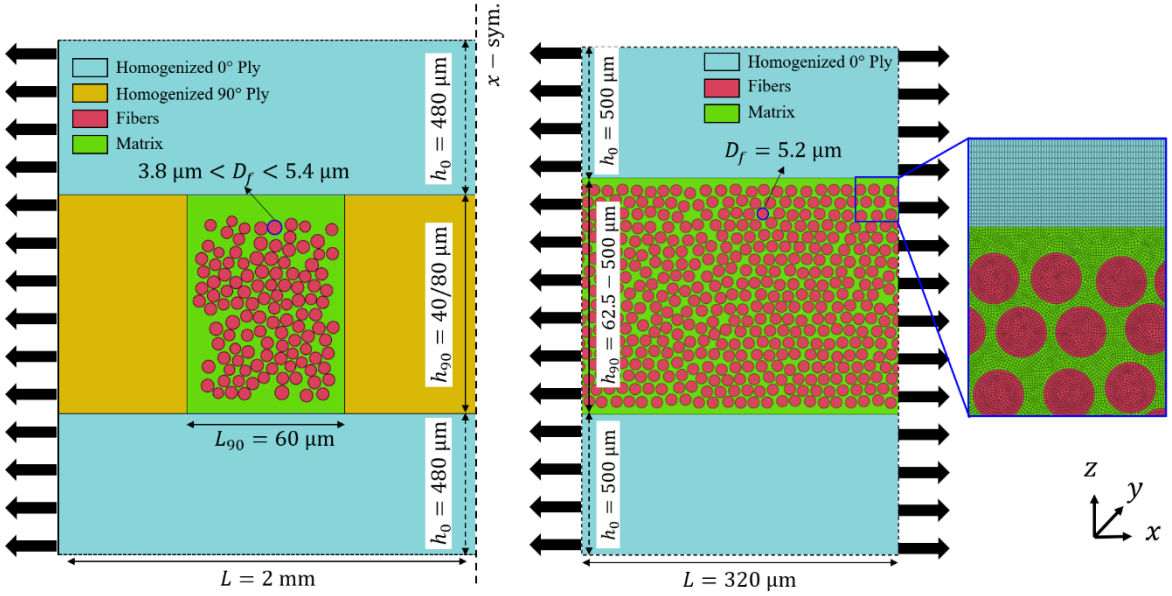

Figure 59. Geometrical attributes of the generated 3D RVE for the [0/90/0] cross-ply laminates: (a) scenario I; (b) scenario II.

The focus of scenario II was to conduct a broader parametric study on the formation of ply cracks. The developed method by Li et al. [10] (Chapter 4) was used to model the nonuniform fiber spatial dispersion within the 90° ply. The statistical assessment of local energy (stress) states of the generated RVEs was conducted in [7,10] (see Chapter 5). Geometrical attributes were defined according to Baily et al. [4] (Fig. 59b). Therein, the thickness of the 0° ply is set to 500 µm, while the thickness of the 90° ply varied for the different cases considered (62.5 µm ≤ h_{90} ≤ 500 µm). A constant fiber diameter D_f = 5.2 µm was assigned to the fibers within the 90° ply. The fiber volume fraction of the baseline model was set to V_f = 62% and assigned to all plies. To conduct further studies, additional RVEs with V_f = 55% and V_f = 50% were generated and the properties of 0° plies were updated accordingly.

For all RVEs generated, a strong interfacial bond was assumed for the fiber-matrix interfaces in the 90° ply, while the interface between plies was also treated as perfectly bonded. The full thickness of the 0° and 90° plies were represented in all RVEs, while the width of the RVE along global *y*–direction was set to $0.1D_f$ as it was deemed satisfactory when periodic boundary conditions were applied [14]. For scenario II, an RVE length of 320 µm along the global *x*–direction was assigned to all plies. The chosen length ensures a sufficient spacing between cracks in the 90° ply to avoid the interaction of stress fields between cracks (i.e., crack shielding). Additionally, the length respects the aspect ratio of

$\delta = l / D_f = 25$ suggested in previous studies [23,24]. The length of the RVE was set to 2 mm for scenario I.

For scenario I, the effective properties of the homogenized 0° plies (e.g., G_{23}) were calculated by using the experimental data reported for the T700SC/2592 material provided in Ref. [25]. The rule of mixtures [26] and Chamis [27] micromechanical models were used to determine the thermomechanical properties of the homogenized regions of the 90° ply using the reported properties of the fibers and epoxy matrix properties (IMS60-24k Toho Tenax®) [12,14,28]. The same properties were used for modelling linear-elastic fibers [14]. To capture pressure-dependent inelastic behaviour of the epoxy in the 90° ply, a user-defined material (VUMAT) model was developed in the commercial finite element software Abaqus. Details of the developed constitutive model for the epoxy are discussed in Section 7.2.2. The corresponding properties are indicated in Table 6. For scenario II, thermomechanical properties of the homogenized 0° plies were determined from experimental data by Bailey et al. [4]. The rule of mixture and Chamis models [26,27] were utilized to calibrate the fiber properties where the properties of the matrix were assumed to be constant [14]. Out-of-plane shear modulus (Poisson's ratio) of the fibers was approximated based on the overall behaviour of the 90° ply and according to experimental observations [28] as the limiting upper/lower bound. The fibers in the 90° ply were treated as a linear-elastic material, while the developed VUMAT model was used for modelling the matrix behaviour. Properties used for scenario II are presented in Table 7.

Table 6. Properties of the fibers [14], epoxy resin [12,28], and homogenized plies [25] (scenario I).

Material Property *	**Fibers (Carbon)**	**Matrix (Epoxy)** +	**Homogenized 90° Sections (V_f = 60 %) IMS60-24k Toho Tenax®**	**Homogenized 0° Plies (V_f = 60 %) T700SC/2592**
Young's Moduli				
E_{11}(GPa)	276	3.76	167.1	123
E_{22}(GPa)	15	-	8.96	8.07
Poisson's Ratio				
ν_{12}	0.2	0.39	0.28	0.33
ν_{23}	0.07	-	0.24	0.33
Shear Moduli				
G_{12}(GPa)	15	1.35	4.58	3.92
G_{23}(GPa)	7	-	3.61	3.25
Thermal Expansion Coefficients				
$\alpha_{11}(°C^{-1})$	-0.5×10^{-6}	58×10^{-6}	0.026×10^{-6}	0.12×10^{-6}
$\alpha_{22}(°C^{-1})$	15×10^{-6}	-	31.8×10^{-6}	31.8×10^{-6}
Plastic Poisson's Ratio				
ν_p	-	0.3	-	-
Density				
ρ (kg/m^3)	1780	1300	1590	1600
Tensile Strength				
X_T(MPa)	-	93	-	-
Compressive Strength				
X_C(MPa)	-	124	-	-
Critical Dilatation Energy Density				
U_{dil}^c(MPa)	-	0.175	-	-

* 1, 2, and 3 are the principal material coordinate system axes for a ply, denoting the fiber direction, in-plane transverse direction and out-of-plane transverse direction, respectively.
+ Note, the integer subscripts can be dropped for the isotropic matrix properties.

Table 7. Properties of the fibers, epoxy resin [12,28], and homogenized plies [4] (scenario II).

Material Property *	**Fibers (Carbon)**	**Matrix (Epoxy)** +	**Homogenized 0° Plies (V_f = 62 %)**
Young's Moduli			
E_{11}(GPa)	202.5	3.76	127
E_{22}(GPa)	12.3	-	8.3
Poisson's Ratio			
ν_{12}	0.23	0.39	0.29
ν_{23}	0.10	-	0.23
Shear Moduli			
G_{12}(GPa)	20.25	1.35	5.1
G_{23}(GPa)	5.61	-	3.36
Thermal Expansion Coefficients			
$\alpha_{11}(°C^{-1})$	-0.4×10^{-6}	58×10^{-6}	0.26×10^{-6}
$\alpha_{22}(°C^{-1})$	10×10^{-6}	-	30.2×10^{-6}
Plastic Poisson's Ratio			
ν_p	-	0.3	-
Density			
ρ (kg/m^3)	1750	1300	1580
Tensile Strength			
X_T(MPa)	-	93	-
Compressive Strength			
X_C(MPa)	-	124	-
Critical Dilatation Energy Density			
U_{dil}^c(MPa)	-	0.175	-

* 1, 2, and 3 are the principal material coordinate system axes for a ply, denoting the fiber direction, in-plane transverse direction and out-of-plane transverse direction, respectively.
+ Note, the integer subscripts can be dropped for the isotropic matrix properties.

7.2.2 Epoxy resin constitutive model

The pressure-dependent inelastic deformations and failure (i.e., cavitation-induced and ductile failure) of the epoxy were captured via an explicit VUMAT model that has been described in Chapter 6. The model was further modified to predict the post-peak behaviour of the epoxy (i.e., stress/stiffness reduction) based on an isotropic damage model, which was able to capture the localization of stress at

the crack tip. An explicit damage model was deemed appropriate to account for the stress perturbation after activation of damage. The developed damage model for capturing cavitation-induced and ductile failure is described in Appendix C. The overall procedure of the VUMAT subroutine is illustrated in Fig. 60.

The code begins with an elastic trial stress and check for inelastic deformation based on the defined yield function, $\Phi \geq 0$. If the conditions are satisfied, the return mapping algorithm is applied to find the plastic strain by a Newton-Raphson root-finding method. Accordingly, other related parameters including stress tensor, hardening variables, and other solution-dependent variables (SDVs) are calculated. The failure of the material under all the conditions (i.e., ductile failure, cavitation after yielding, brittle cavitation) is checked within the loop. After activation of damage conditions, damage variables and compliance damage tensor, which are required for updating the stress tensor and SDVs, are calculated by finding the damage parameter. Note that unique damage parameters (i.e., A_m^{dis}, A_m^{dil}) are functions of energy release rate and characteristic length of an element. These constants are always positive and need to be calculated once (see Appendix C). If the damage mode is activated, the code directly follows the damage model at the beginning of the next step.

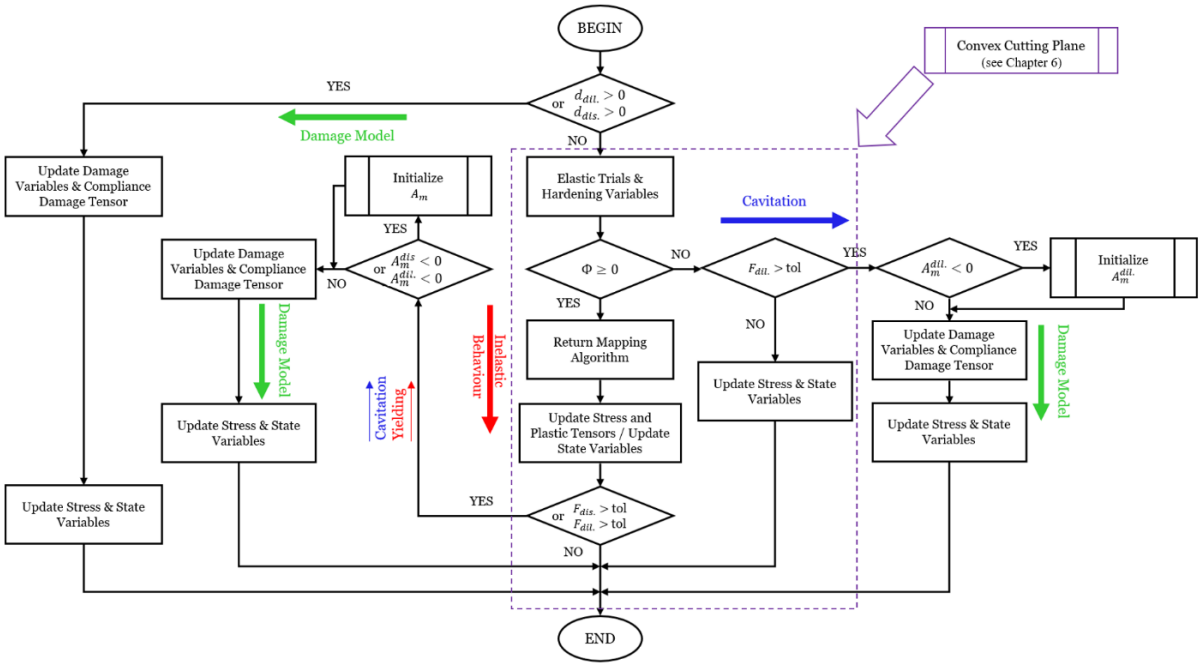

Figure 60. Overall procedure of the developed user-defined material subroutine for capturing pressure-dependent inelastic deformations and failure of epoxies.

7.2.3 Finite element model

Linear brick elements with reduced integration (C3D8R) were used to mesh the homogenized 0° plies and 90° sections in the RVE for scenario I using the commercial finite element (FE) software Abaqus. Moreover, a combination of C3D8R and triangular prism elements (C3D6) were utilized to mesh the fibers and matrix in the 90° ply (see Fig. 59b). For scenario I, the laminate was initially subjected to $\Delta T = -105°C$ to simulate thermal cooldown during processing [22]. An increasing uniaxial strain ε_x was applied subsequent to the initial thermal loading, where a symmetric boundary condition was applied along the x–direction and periodic boundary condition (PBC) were applied to the corresponding faces of the RVE (see Fig. 59a). For scenario II, 2D PBCs were applied along the global x– and y–directions (see Fig. 59b). An initial thermal cooldown $\Delta T = -145°C$ was applied to the RVE and followed by an increasing uniaxial tensile strain [4]. It should be noted that the RVEs with $V_f = 55\%$ and $V_f = 50\%$ were also subjected to the same loading conditions. For both scenarios, the predictions using generated RVEs for the [0/90/0] laminates were compared with prediction for the unconstrained 90° ply to study the influence of the ply constraining effect.

7.3 Results

7.3.1 Single element verification

The capability of the developed subroutine to predict the deformation response and post-peak behaviour of epoxy was investigated by subjecting single elements to four different loading conditions, including uniaxial tension, uniaxial compression, simple shear, and equitriaxial tension (Fig. 61a). A steady post-peak softening response was predicted for the epoxy and was expected due to the damage model used, while the initiation of failure was comparable with experimental data (Fig. 61a). Since the post-peak response of the material is a function of the characteristic length of the element (see Appendix C), the influence of this parameter on the stress-strain response for a single element under tensile loading was investigated (Fig. 61b). The results indicate that the length dependency of the epoxy is minimized for elements smaller than 10 μm. It should be noted that an approximate element size of 0.25 μm was used for all RVEs developed in this study.

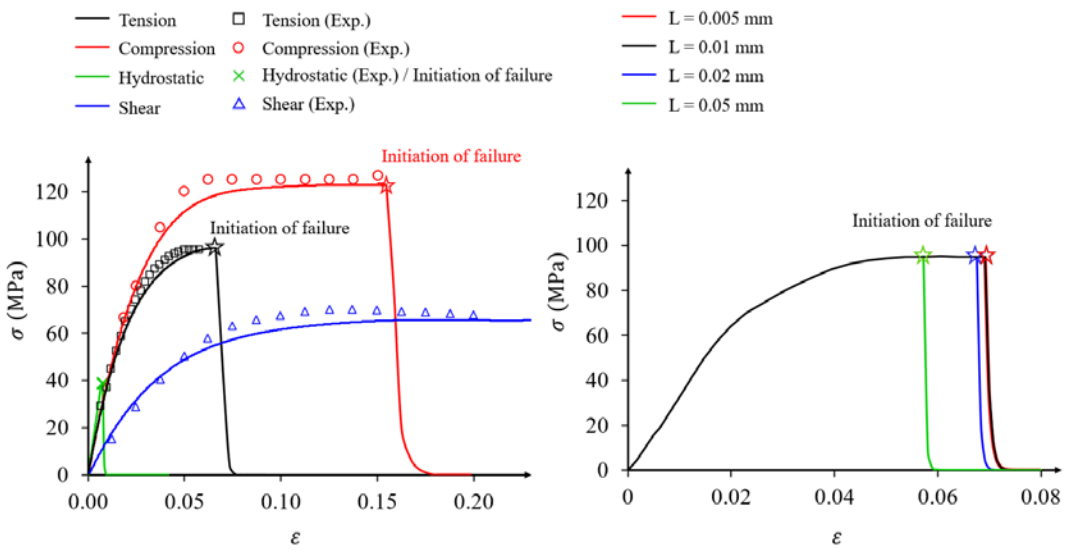

(a) (b)

Figure 61. (a) True strain-stress and post-peak behaviour of the epoxy under uniaxial tensile, uniaxial compressive, equitriaxial tensile, and simple shear loading; (b) Element size dependency of the epoxy under tensile loading.

7.3.2 Ply crack formation – RVEs generated using microscopic images

The formation of ply cracks was predicted for FE micromechanical models pertaining to scenario I (Fig. 59a), where RVEs were generated using experimental observations of fiber spatial dispersion [22]. The predicted results were compared to the observed crack evolution images to validate the FE micromechanical models. The predicted crack path for the laminate with a 40 μm thick 90° ply was remarkably similar to the experimental results (Fig. 62), while for the laminate with a 80 μm thick 90° ply there were minor discrepancies (Fig. 63). These discrepancies may be due to the assumed fiber diameter, slight variation in the location of fibers, the approximated fiber volume fraction, and the properties of the epoxy used in the FE models. For both thicknesses, local cavitation-induced failure initiated at the central region of the 90° ply as was observed in the experiment, albeit it is not clear from the experiments if cavitation or interfacial debonding initiated the ply crack formation process. Nevertheless, the result emphasizes that the stress concentration around the fiber is the controlling factor for local failure onset. Subsequently, the propagation of microcracks is related to the local conditions at the tip of the microcrack, while the stress concentrations in the vicinity of the fibers ahead of the crack tip remains a decisive factor in the crack formation pattern. Formation of oblique cracks indicates the ductile nature of crack propagation when there is enough space around the crack tip and relatively low stress concentration caused by the presence of fibers (see Fig. 62).

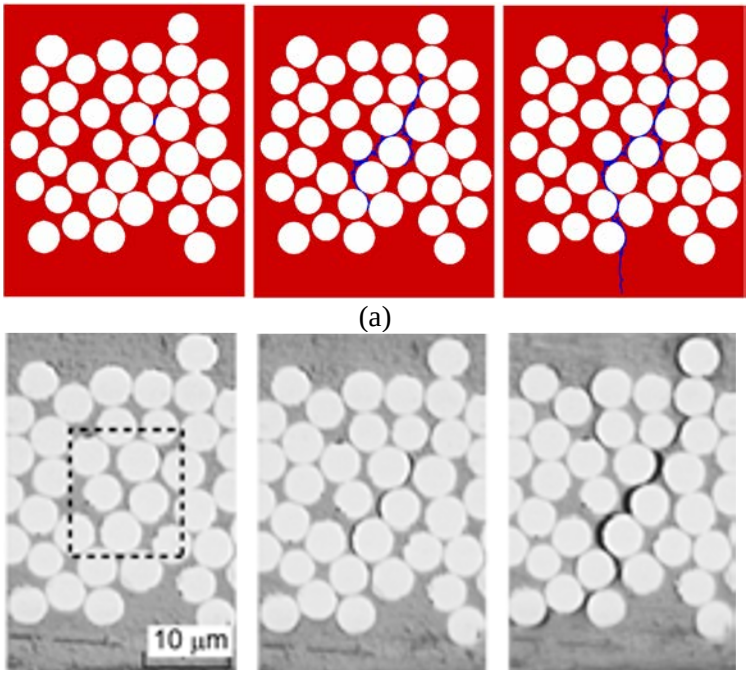

(a)

(b)

Figure 62. The process of ply crack formation in a [0/90/0] cross-ply laminate with h_{90} = 40 μm: (a) FE model; (b) experimental observation [22] (courtesy of H. Saito et al. 2012, Taylor & Francis, UK).

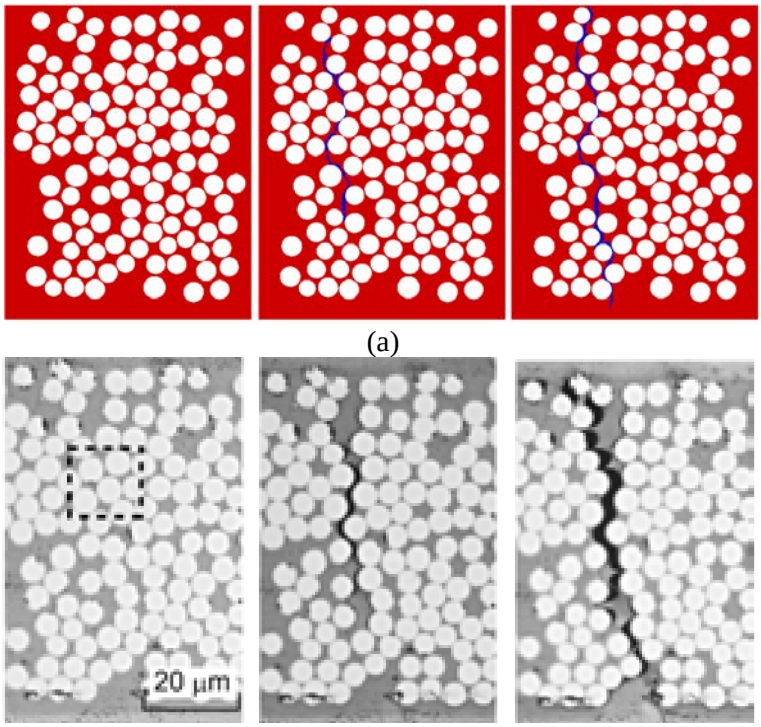

(a)

(b)

Figure 63. The process of ply crack formation in a [0/90/0] cross-ply laminate with h_{90} = 80 μm: (a) FE model; (b) experimental observation [22] (courtesy of H. Saito et al. 2012, Taylor & Francis, UK).

7.3.3 Ply crack formation – randomly generated RVEs

The goal of the next study was to simulate ply crack formation for cross-ply laminates with different 90° ply thicknesses and fiber volume fractions. FE micromechanical models pertaining to scenario II (Fig. 59b) were used, where RVEs were randomly generated as described in Section 7.2.1. The magnitude of strain corresponding to the formation of the first full ply crack (i.e., a crack spanning the entire ply thickness) for the laminates was compared to available experimental data [4] (Fig. 64). The predicted strains correlate well with the experimental data for the baseline model (V_f = 0.62%), demonstrating the ability of the micromechanical model to capture the decrease in strain with increasing ply thickness (i.e., the effect of ply constraints). In a different set of simulations, RVEs of unconstrained 90° plies were generated and underwent a similar thermomechanical loading. A consistent range was seen in the failure strain of lamina (i.e., formation of full ply crack); however, thicker unconstrained laminae were slightly influenced by the thermal residual stress caused by the difference in thermal expansion of the constituents (Fig. 64).

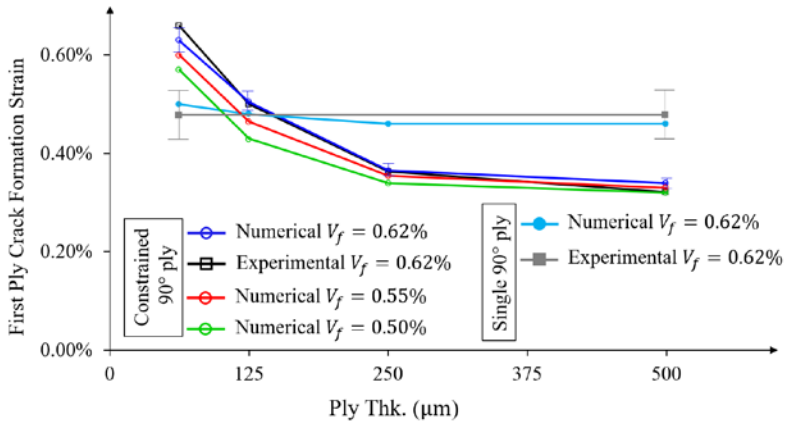

Figure 64. First ply crack formation strain for constrained and unconstrained 90° plies with different thickness. Experimental data taken from Ref. [4].

The process of ply crack formation in the 90° ply of the RVE with 125 μm thickness is illustrated in Fig. 65. Initially, cavitation-induced local failure between fibers led to the formation of a microcrack at the central region of the ply (Fig. 65a). A high stress concentration at the tip of the crack and around the fibers controls the propagation of formed microcracks in the direction perpendicular to the applied load (Fig. 65c). In other words, ply crack formation is driven by Mode I (i.e., crack opening displacement). Notwithstanding, oblique microcrack branches are formed locally where there is sufficient space at the tip of the crack for ductile failure to occur and there is minimum interaction with the triaxial stress fields at the fibers (Fig. 65d).

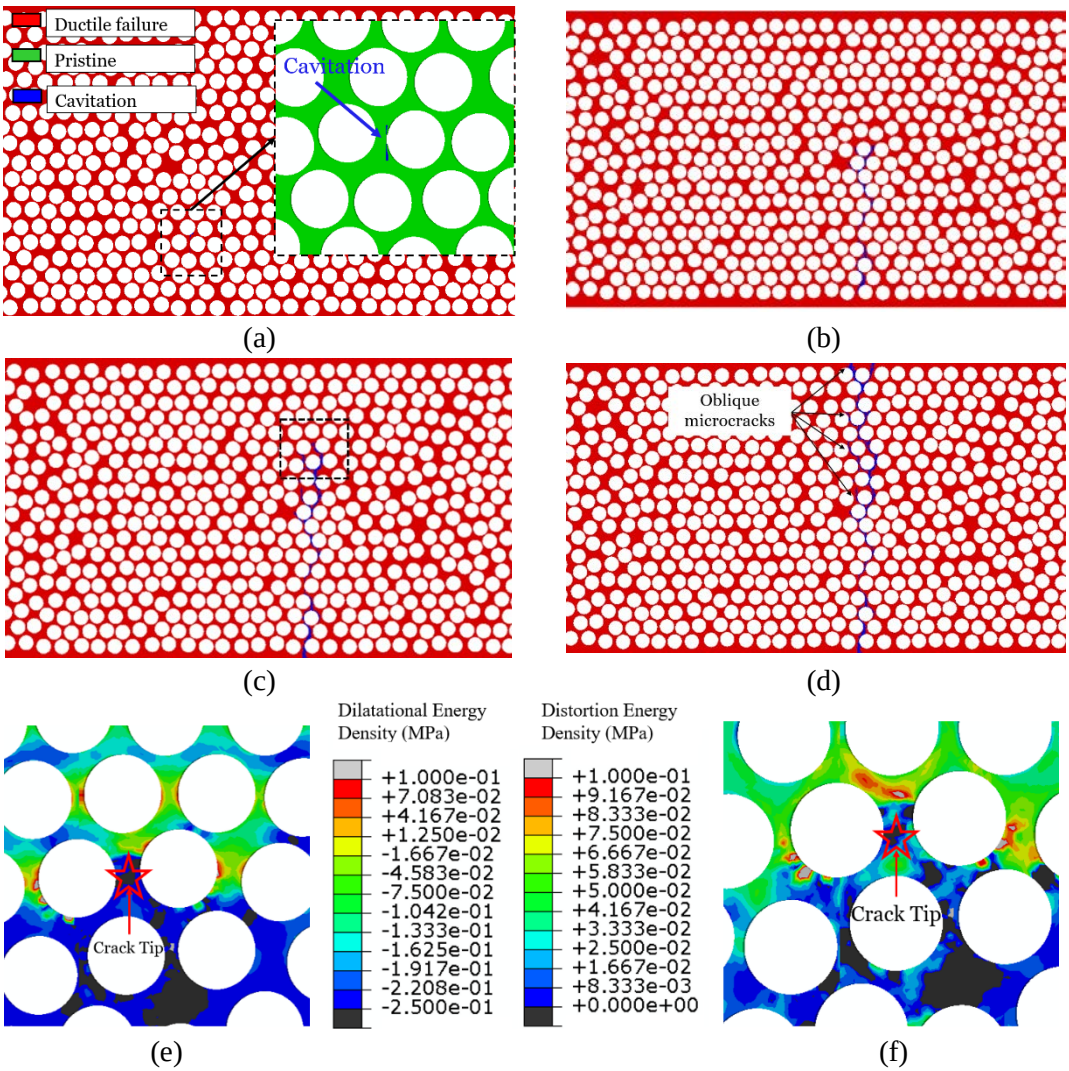

Figure 65. Crack propagation in the 90° ply (125 μm thickness) of a [0/90/0] laminate at an applied strain of: (a) ε_x = 0.20% (local failure initiation mechanisms also shown); (b) ε_x = 0.28%; (c) ε_x = 0.36%; (d) ε_x = 0.48%; (e) dilatational energy density contour of the highlighted section in (c); and (f) distortion energy density contour of the highlighted section in (c).

The first full ply crack that formed and the corresponding damage mode during formation of the ply crack is shown in Fig. 66 for the thinnest constrained and unconstrained 90° ply (i.e., h_{90} = 62.5 μm). It should be noted that only a portion of the width of the 90° ply in the RVE is shown in Fig. 66a and 66d. For the laminate, the relative deformation between 0° and 90° plies experienced during the initial thermal cooldown, which was caused by the mismatch in the effective coefficient of thermal expansion for the 0° and 90° plies along the loading direction, and the subsequently applied strain resulted in a higher degree of shear stress on the 90° ply that eventually led to the formation of local oblique microcracks (Fig. 66a,b). The energy density contours indicate that local ductile failure governs the

formation of oblique microcracks (Fig. 66c). This interpretation is confirmed by analyzing the ply crack formation of the unconstrained 90° ply (Fig. 66d). Here, formation of obliqued microcracks was limited, where crack initiation was driven by cavitation-induced local failure (Fig. 66e) and linkage of microcracks was related to both cavitation and ductile failure (see Fig. 66f). It was also found that the formation of the full ply crack in the constrained 90° ply was delayed, demonstrating the effect of ply constraints. It is noteworthy that the local shear stress in the 90° ply caused by the thermal cooldown delayed cavitation-induced failure in the laminate, and in some cases changed the local failure mode to ductile failure, which was not observed for thicker 90° plies.

The influence of the thickness change on the volume averaged stress of the transverse ply was also investigated (Fig. 67). Here, the volume average stress is defined as:

$$\sigma_{ij}^{avg} = \frac{\sum_{k=1}^{n} \sigma_{ij}^{n} V^{n}}{V} \tag{7-1}$$

where σ_{ij}^{n} and V^{n} are stress component and volume of n^{th} element, respectively, and V is the overall volume of the 90° ply. A gradual stiffness reduction occurred in the 90° plies with 62.5 μm thickness due to formation of multiple partial ply cracks; however, other cases experienced a sharper drop in the average stress-strain behaviour since a single ply crack caused the stiffness reduction. The material degradation in different thicknesses indicates a higher resistance in thinner laminates that can be related to the supportive effect of the ply constraints. This effect was minimized in higher thicknesses, while a similar response was captured for the 90° plies with 250 μm and 500 μm thicknesses.

The normalized crack length of the constrained 90° plies was tracked for different ply thicknesses (Fig. 68). Therein, the average behaviour of five different fiber spatial distributions is shown for each ply thickness. Note that the vertical distance between the top and bottom of a crack was defined as the crack length (i.e., the length of the projected crack on a vertical surface) as shown in Fig. 68. The results indicate a slower rate in the formation of the full ply crack for a thinner ply. Furthermore, the full ply crack forms at a lower strain and with a higher rate in thicker plies. Results also reveal that the constraining effect of the adjacent layers diminishes after the ply thickness increases beyond a certain value.

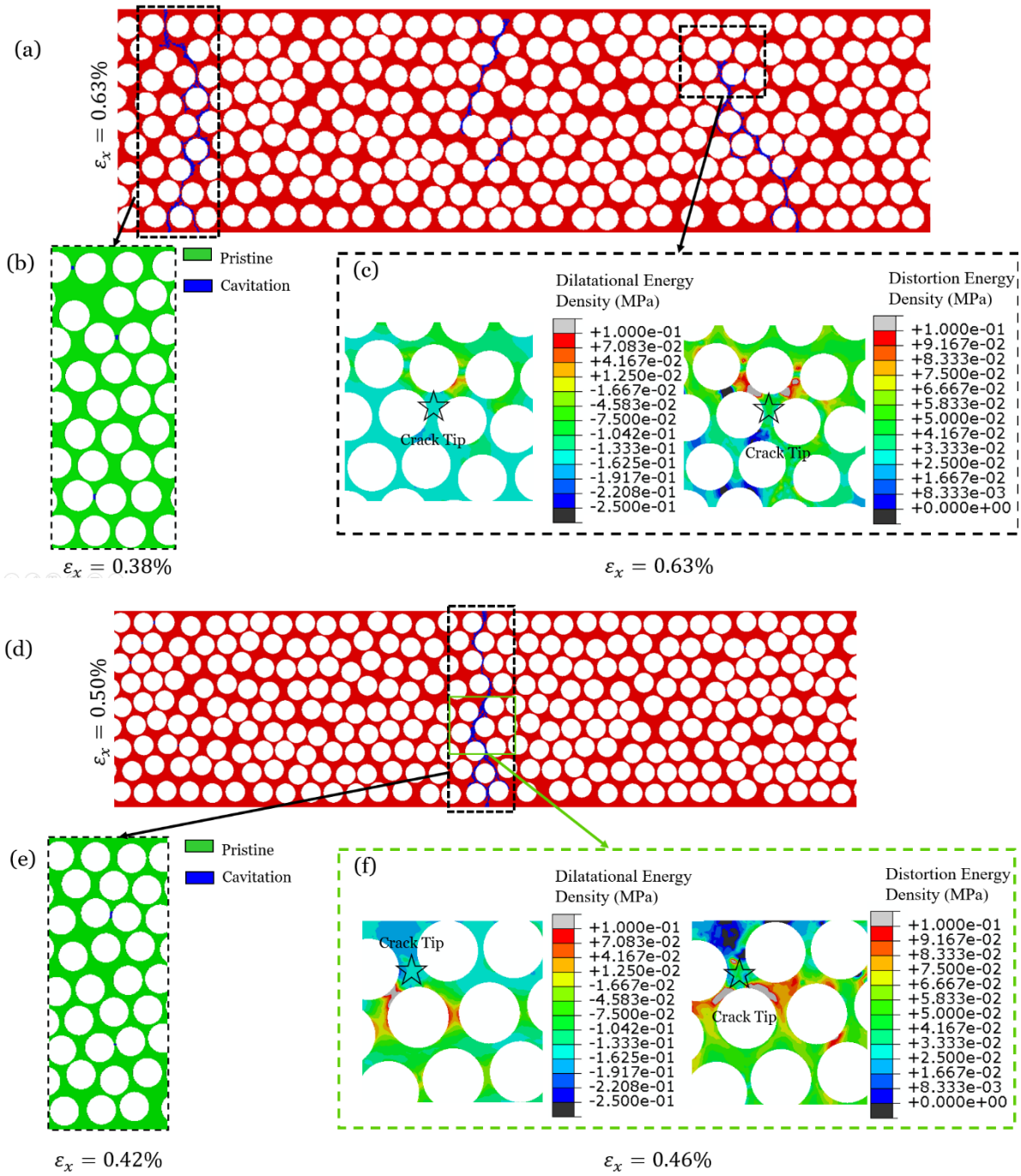

Figure 66. (a) Formation of the first full ply crack in the laminate with a 62.5 μm thick 90° ply (ε_x = 0.63%), along with corresponding (b) local failure initiation mechanisms (ε_x = 0.42%) and (c) dilatational and distortion energy contours (ε_x = 0.63%). (d) Formation of the full ply crack in a 62.5 μm thick lamina (ε_x = 0.50%), along with corresponding (e) local failure initiation mechanisms (ε_x = 0.42%) and (f) dilatational and distortion energy contours (ε_x = 0.46%).

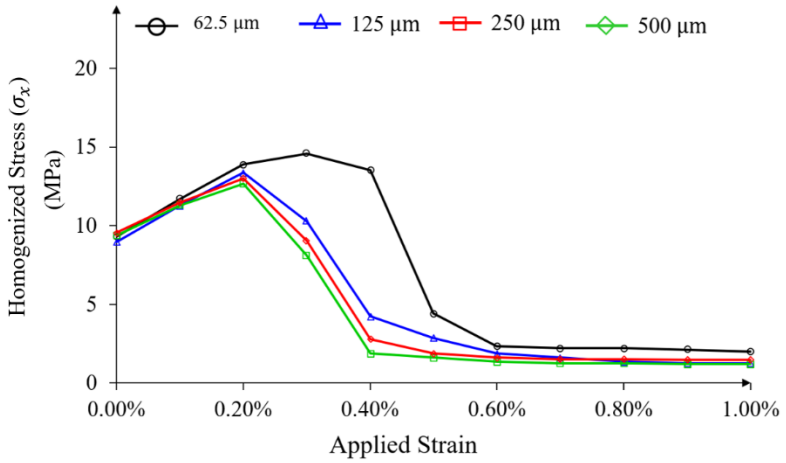

Figure 67. Volume averaged stress of constrained 90° plies during the crack formation.

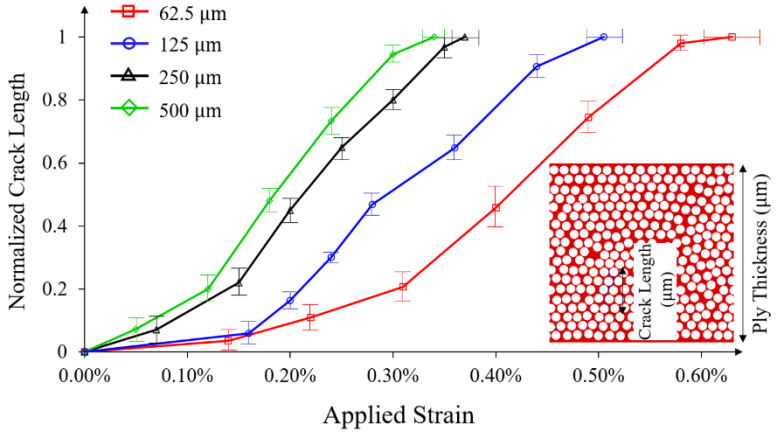

Figure 68. Normalized crack length within the 90° ply of laminates subjected to tensile loading, with 90° ply thickness indicated.

The influence of the fiber volume fraction on the formation of ply cracks was also investigated. The strains at full ply crack formation for laminates with V_f = 0.55% and V_f =0.50% were obtained and compared with the baseline model (see Fig. 64). A reduction of the strain was predicted for lower fiber volume fractions when the 90° ply was ≤ 250 µm, while for thicker laminates the influence of fiber volume fraction was less pronounced due to reduced constraint from the adjacent plies. Figure 69 demonstrates the propagation of ply cracks in constrained 90° plies with 125 µm thickness for different fiber volume fractions, which reveals that a laminate with a lower fiber volume fraction has more tendency to form oblique microcracks and undergo more extensive local inelastic deformation. This finding can be related to the relatively large space around a crack when the inter-fiber spacing is higher

or the influence of the constraining plies. Although the pattern of the formed ply crack is generally transverse to the loading direction, a portion of the dissipated energy drove the formation of oblique microcracks. In other words, there is a higher probability to observe inelastic behaviour in the epoxy at a lower fiber volume fraction, which consumes a higher amount of energy compared to local cavitation-induced failure.

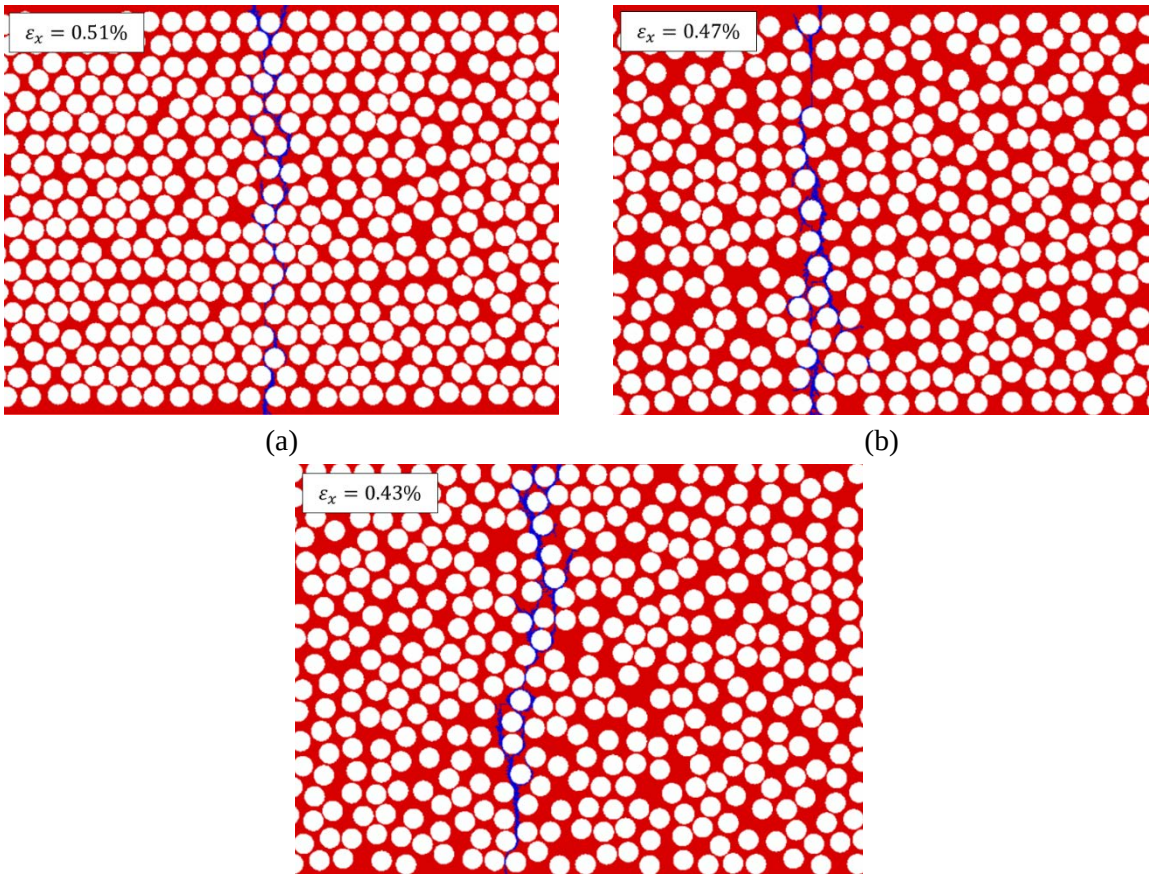

Figure 69. Crack propagation in the 90° ply of the laminate with 125 μm thickness: (a) V_f = 62%; (b) V_f =55%; (c) V_f =50%.

The effect of thermal cooldown was previously studied on the local failure initiation in a [0/90/0] cross-ply laminate (see Chapter 6). The current study confirms the previous remarks, where modelling the thermal cooldown not only affects the occurrence of local failure but may also change the failure mode (Fig. 70). The results indicate that the cavitation-induced failure initiate the ply cracking in the presence of thermal residual stress (Fig. 70a), while an oblique crack forms in the absence of thermal stress (Fig. 70b). Note that the same fiber distribution was assigned to both cases. In the absence of

thermal cooldown there were a limited number of cavitation sites, where the critical value of dilatational energy density of the epoxy was rarely attained (Fig. 70c). Thus, an oblique formation of a crack in 90° ply is related to the high distortional energy density in the epoxy, and ultimately local ductile failure (Fig. 70d).

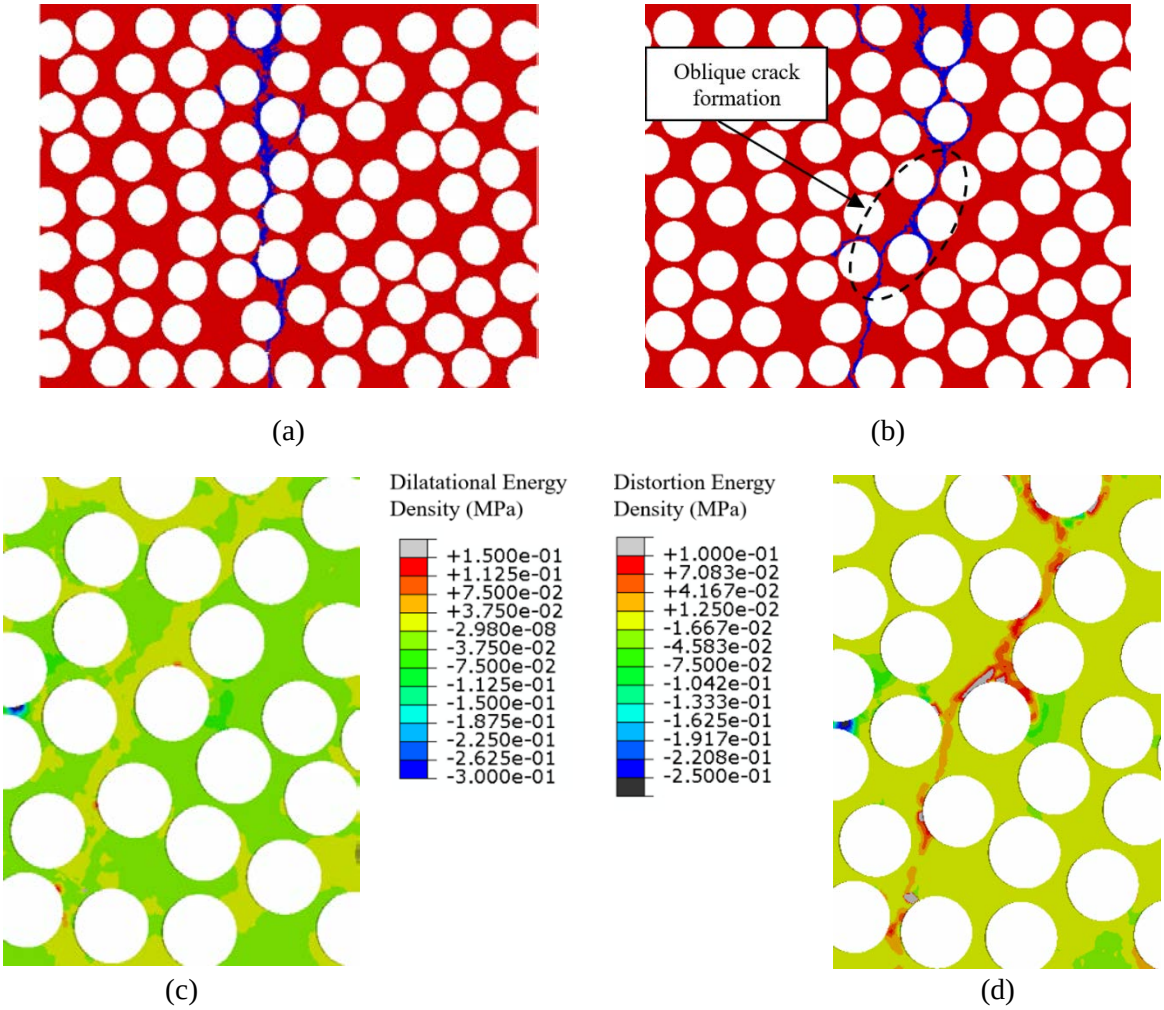

Figure 70. Evolution of a ply crack in the 90° ply of the laminate with 125 μm thickness: (a) after initial thermal cooldown; and (b) without initial thermal cooldown. (c) The dilatational energy density contour of the region shown in (b) without initial thermal cooldown. (d) The distortion energy density contour of the region shown in (b) without initial thermal cooldown.

7.3.4 Energy release rate

Employing the thermodynamics framework and decoupling between elasticity-damage and plastic hardening, the free energy of the body is defined as [30]:

$$\psi = \psi^{ed} + \psi^{p} \tag{7-2}$$

where ψ^{ed} represent elastic-damage potential and ψ^{p} is the plastic contribution to the free energy density. The elastic-damage potential is postulated as:

$$\rho\psi^{ed} = \frac{1}{2}\boldsymbol{\varepsilon}^{e} : \boldsymbol{\sigma} \tag{7-3}$$

where $\boldsymbol{\varepsilon}^{e}$ is the elastic strain tensor (see Appendix B), $\boldsymbol{\sigma}$ is the current stress tensor, ρ is material's density (i.e., epoxy). Note that stress is updated within an isotropic damage model as described in Appendix C.

Despite the fact that plastic contribution to the free energy ψ^{p} can be explicitly found [30], an indirect approach was used to determine this value for numerical purposes as:

$$\psi^{p} = \psi - \psi^{ed} \tag{7-4}$$

where the complementary energy density ψ is defined as the incremental summation of energy (see Appendix B) as:

$$\rho\psi = \int \boldsymbol{\sigma} : \dot{\boldsymbol{\varepsilon}}\ dt \tag{7-5}$$

Thus, the strain energy density of an element that contributed to the ply crack formation can be related to effective energy released rate of the ply, when the geometrical attributes of the element and ply crack are available. Thus, the total energy dissipation associated with ply cracking, due to the inelastic response and micro-cracking of the epoxy, can be captured by monitoring the stress-strain response of the corresponding elements. For the duration of the simulations the local energy was calculated for all the elements as an SDV. Accordingly, the effective energy release rate was estimated by the summation of local energy of the failed elements divided by the crack surface area. Here, the ply thickness is assumed as the crack length, and the overall energy contribution is related to crack opening (i.e., Mode I). Furthermore, the length of the element along global *x*– and *y*–direction was assumed to be constant and equal to the averaged characterized length of elements and elements width, respectively. The calculated effective energy release rate for ply crack formation of the carbon fiber/epoxy 90° plies with different thicknesses are presented in Table 8. The reduction of the computed ERRs with decreasing 90° ply thickness is further evidence that the effect of ply constraints was captured by the model, where ERR is a function of thickness ratio (t_0/t_{90}) for a cross-ply laminate. The obtained values of ERRs are similar to the assumed values reported by Montesano and Singh [31] for the 90° ply of a similar carbon fiber/epoxy cross-ply laminate, where a similar ERR vs ply thickness trend was also reported.

Table 8. Measured energy release rate of ply cracking for a carbon/fiber epoxy laminate.

Description	90° Ply Thickness (μm)	Energy Release Rate (J/m^2)
90° lamina	-	153.19
[0/90/0]	500	139.51
[0/90/0]	250	126.03
[0/90/0]	125	112.54
[0/90/0]	62.5	105.08

7.3.5 General discussion

It was shown that the onset of local failure and crack formation in epoxy is caused by triaxial stress states (i.e., brittle cavitation), while formed microcracks propagate due to high stress concentrations around the fibers ahead of the crack tip or ductile failure at the tip of the crack. Oblique microcracks tend to propagate along the direction of maximum distortion energy, which is more likely in a low fiber volume fraction laminate. Notwithstanding, oblique microcracks also form as a result of shear stress imparted on the 90° ply of a cross-ply laminate from the constraining 0° plies. Changes in the direction of a propagated crack, even at the microscale, contradicts the initial presumption of mesoscale models, where the initial shape of a ply crack is always perpendicular to the loading direction. Furthermore, the ply crack formation process is not necessarily binary and simultaneous formation of debonding or ply cracks is possible. Thus, the sources of energy dissipation, crack interaction, and irregular damage behaviour relatively increase. The formation of full ply crack was delayed in the constrained 90° ply with a 62.5 μm thickness when compared to the unconstrained 90° ply of the same thickness. Thus, despite that fact that the local failure initiation is expedited in the constrained ply (see Chapter 6), the constraining effect became evident during the crack formation process for laminates with thinner plies. Finally, the proposed approach for measuring ERRs within a micromechanical framework opens a path to connect micro-, meso-, and macro-scales through multiscale modelling, while the epoxy and fiber material properties were the only inputs in this model. Notwithstanding, it is important to decouple the influence of Mode I and II driving factors during the formation of ply cracks at different thickness, which can be achieved using computational models.

7.4 Conclusions

A 3D computational model was developed to predict local point failure in the matrix and a damage model to capture ply crack formation in laminated composites. Mechanical behaviour of the epoxy was

captured using a user-defined material (VUMAT) model within explicit finite element (FE) framework, where an isotropic damage model was developed to predict post-peak response of the epoxy. Two sets of representative volume elements (RVEs) were generated to simulate ply crack formation of carbon fiber/epoxy [0/90/0] cross-ply laminates. Comparing the available experimental data, the results verified the capability of the model in capturing crack propagation at the microscale and predicting the failure strain corresponding to the formation of the first full ply crack. It was observed that the local cavitated sites linked by ductile failure due to a high stress concentration around the fibers and at the tip of the crack. This understanding was confirmed in analyzing the formation of ply cracks in laminates with a low fiber volume fraction, where oblique cracks were formed under the same loading conditions. The same conclusion was obtained for a thin ply laminate, where the shear stress was applied to the 90° as a result of neighbouring to relatively thicker 0° plies. It should be noted that a nearly ideal ply crack was formed in the 90° ply in the absence of 0° neighbouring plies. Verifying the experimental observations, the strain at full ply crack formation in the 90° ply of thinner laminates was delayed compared to an unconstrained 90° ply. However, the ply constraining effect expedited formation of ply cracks in thicker laminates. It was seen that a portion of energy dissipates to form mix mode cracks (i.e., oblique crack, microcrack branches, scattered debonds). These types of cracks originate from the local behaviour of the epoxy which depends on numerous factors including, but not limited to, nonuniform fiber spatial dispersions, manufacturing-induced defects, the constraining plies. The computational micromechanical model was used to adequately measure the strain energy release rates for ply cracking in the studied laminates, thus providing an opportunity for integrating the results into a multiscale modeling framework in the future. The fidelity of predictions using this approach may be improved by enhancing the epoxy material model. In conclusion, complex ply crack patterns driven by microscopic phenomena revealed the limitation of mesoscale or macroscale models in accurately capturing the ply cracking response.

References

[1] Talreja, Modelling defect severity for failure analysis of composites, in: W. Van Paepegem (Ed.), Multi-Scale Continuum Mechanics Modelling of Fibre-Reinforced Polymer Composites, Woodhead Publishing Series in Composites Science and Engineering, 2021: pp. 275–306.

[2] B. El Said, S.R. Hallett, Multiscale modelling of laminated composite structures with defects and features, in: W. Van Paepegem (Ed.), Multi-Scale Continuum Mechanics Modelling of Fibre-Reinforced Polymer Composites, Woodhead Publishing Series in Composites Science and Engineering, 2021: pp. 637–668.

[3] J. Montesano, F. Sharifpour, Modelling damage evolution in multidirectional laminates: micro

to macro, in: W. Van Paepegem (Ed.), Multi-Scale Continuum Mechanics Modelling of Fibre-Reinforced Polymer Composites, Woodhead Publishing Series in Composites Science and Engineering, 2021: pp. 463–507.

[4] J.E. Bailey, P.T. Curtis, A. Parvizi, On the transverse cracking and longitudinal splitting behavior of glass and carbon-fiber reinforced epoxy cross-ply laminates and the effect of Poisson and thermally generated strain, Proceedings of the Royal Society A: Mathematical, Physical and Engineering Sciences 366 (1979) 599–623.

[5] J. Tong, F.J. Guild, S.L. Ogin, P.A. Smith, On matrix crack growth in quasi-isotropic laminates-I. Experimental investigation, Composites Science and Technology 57 (1997) 1527–1535.

[6] M. Quaresimin, P.A. Carraro, L.P. Mikkelsen, N. Lucato, L. Vivian, P. Brøndsted, B.F. Sørensen, J. Varna, R. Talreja, Damage evolution under cyclic multiaxial stress state: A comparative analysis between glass/epoxy laminates and tubes, Composites Part B: Engineering 61 (2014) 282–290.

[7] F. Sharifpour, J. Montesano, R. Talreja, Assessing the effects of ply constraints on local stress states in cross-ply laminates containing manufacturing induced defects, Composites Part B: Engineering 199 (2020) 1–13.

[8] R. Talreja, C.V. Singh, Damage and Failure of Composite Materials, Cambridge University Press, 2012.

[9] T. Okabe, H. Imamura, Y. Sato, R. Higuchi, J. Koyanagi, R. Talreja, Experimental and numerical studies of initial cracking in CFRP cross-ply laminates, Composites Part A: Applied Science and Manufacturing 68 (2015) 81–89.

[10] G. Li, F. Sharifpour, A. Bahmani, J. Montesano, A new approach to rapidly generate random periodic representative volume elements for microstructural assessment of high volume fraction composites, Materials and Design 150 (2018) 124–138.

[11] S.A. Elnekhaily, R. Talreja, Damage initiation in unidirectional fiber composites with different degrees of nonuniform fiber distribution, Composites Science and Technology 155 (2018) 22–32.

[12] L.E. Asp, L.A. Berglund, P. Gudmundson, Effects of a composite-like stress state on the fracture of epoxies, Composites Science and Technology 53 (1995) 27–37.

[13] A.R. Melro, P.P. Camanho, F.M.A. Pires, S.T. Pinho, Micromechanical analysis of polymer composites reinforced by unidirectional fibres : Part I – Constitutive modelling, International Journal of Solids and Structures 50 (2013) 1897–1905.

[14] A. Arteiro, G. Catalanotti, A.R. Melro, P. Linde, P.P. Camanho, Micro-mechanical analysis of the in situ effect in polymer composite laminates, Composite Structures 116 (2014) 827–840.

[15] F. París, M.L. Velasco, E. Correa, Modelling fibre–matrix interface debonding and matrix cracking in composite laminates, in: Multi-Scale Continuum Mechanics Modelling of Fibre-Reinforced Polymer Composites, Woodhead Publishing Series in Composites Science and Engineering, 2021: pp. 243–274.

[16] L. Zhuang, A. Pupurs, J. Varna, R. Talreja, Z. Ayadi, Effects of inter-fiber spacing on fiber-matrix debond crack growth in unidirectional composites under transverse loading, Composites Part A: Applied Science and Manufacturing 109 (2018) 463–471.

[17] M. Mehdikhani, N.A. Petrov, I. Straumit, A.R. Melro, S. V. Lomov, L. Gorbatikh, The effect of voids on matrix cracking in composite laminates as revealed by combined computations at the micro- and meso-scales, Compos. Part A Appl. Sci. Manuf. 117 (2019) 180–192.

[18] M. Naderi, N. Iyyer, Micromechanical analysis of damage mechanisms under tension of 0°–90° thin-ply composite laminates, Compos. Struct. 234 (2020) 111659.

[19] R. Sepasdar, M. Shakiba, Micromechanical study of multiple transverse cracking in cross-ply fiber-reinforced composite laminates, Compos. Struct. (2021) 114986.

[20] M. Herráez, D. Mora, F. Naya, C.S. Lopes, C. González, J. Llorca, Transverse cracking of cross-ply laminates: A computational micromechanics perspective, Compos. Sci. Technol. 110 (2015) 196–204.

[21] A. Farrokhabadi, H. Madadi, M. Naghdinasab, A. Rafie, S.A. Taghizadeh, M. Herráez, Micromechanical investigation of cross-ply carbon composite laminates with glass microtubes using CZM and XFEM, Mech. Adv. Mater. Struct. (2021).

[22] H. Saito, H. Takeuchi, I. Kimpara, Experimental evaluation of the damage growth restraining in 90° layer of thin-ply CFRP cross-ply laminates, Advanced Composite Materials 21 (2012) 57–66.

[23] T.J. Vaughan, C.T. Mccarthy, A combined experimental – numerical approach for generating statistically equivalent fibre distributions for high strength laminated composite materials, Composites Science and Technology 70 (2010) 291–297.

[24] A.R. Melro, P.P. Camanho, S.T. Pinho, Generation of random distribution of fibres in long-fibre reinforced composites, Composites Science and Technology 68 (2008) 2092–2102.

[25] M.J.M. Fikry, S. Ogihara, V. Vinogradov, The effect of matrix cracking on mechanical properties in FRP laminates, Mechanics of Advanced Materials and Modern Processes, 4 (2018) 1-16.

[26] K.K. Chawla, Composite Materials, Third Ed., Springer, 2012.

[27] C.C. Chamis, Mechanics of Composite Materials: Past, Present, and Future, Journal of Composites, Technology and Research ASTM 11 (1989) 3–14.

[28] B. Fiedler, M. Hojo, S. Ochiai, K. Schulte, M. Ando, Failure behavior of an epoxy matrix under different kinds of static loading, Composites Science and Technology 61 (2001) 1615–1624.

[29] S. Kohler, Multiscale Characterisation and Modelling of Transverse Cracking in Thin-Ply Composites, École Polytechnique Fédérale de Lausanne (EPFL), 2018.

[30] E.A. de Souza Neto, D. Peric, D.R.J. Owen, Computational Methods for Plasticity, John Wiley & Sons, 2008.

[31] J. Montesano, C.V. Singh, Predicting evolution of ply cracks in composite laminates subjected to biaxial loading, Composites Part B: Engineering 75 (2015) 264–273.

[32] P. Maimí, P.P. Camanho, J.A. Mayugo, C.G. Dávila, A Thermodynamically Consistent Damage Model for Advanced Composites, 2006.

[33] Z.P. Bažant, B.H. Oh, Crack band theory for fracture of concrete, Matériaux Constr. 16 (1983) 155–177.

Chapter 8
Conclusions & Future Directions

8.1 Conclusions

Characterizing the local damage behaviour of laminated fiber-reinforced composites through experimental tests is challenging, particularly if microscopic tests must be performed. Alternatively, virtual testing may be a cost-effective approach that reduces physical testing requirements. However, the complex nature of progressive damage and failure in laminates occurs over several material length scales which must be captured to ensure high-fidelity predictions. Hierarchical multiscale modelling has been proposed to simulate damage evolution in laminated composites. In the current study, the developed numerical microscale model was implemented as a tool to characterize local failure and predict the formation of ply cracks in the constrained ply of carbon fiber/epoxy [0/90/0] cross-ply laminates. An experimentally calibrated user-defined material subroutine was developed to capture the local response of the epoxy, including pressure-dependent inelastic deformation, onset of local failure (i.e., brittle cavitation and ductile failure), and the post-peak response through an isotropic damage model. Representative volume elements (RVEs) comprising the fibers and matrix phases of the constrained 90° ply and the homogenized 0° plies were generated and used to create 3D finite element (FE) models that were subjected to a thermal cooldown followed by a uniaxial tensile load. The energy dissipated during ply crack formation was captured and the associated effective energy release rate was estimated, which will ultimately enable the integration of the developed microscale model within a multiscale modelling framework. The main conclusions of this thesis are as follows:

- The developed micromechanical FE model effectively captured ply crack formation for a set of cross-ply laminates, with reasonable correlation to available experimental data for a subset of laminates. The model predicted a well-known characteristic of ply cracking in laminates where the strain at formation of the first ply crack decreases with increasing ply thickness.
- Cavitation-induced local failure was observed as the dominant local failure mechanism, while ductile failure was found to be the driving force for the propagation of microcracks. The developed micromechanical FE model is the first that accounts for the interaction between these two local failure mechanisms during the ply crack formation process.

- The onset of local failure in constrained 90° plies was expedited by the residual stresses that formed during thermal cooldown, which were caused by the mismatch in the thermal expansion coefficients between the fibers and matrix and between the 0° and 90° plies. Thus, after thermal cooldown the effect of ply constraints on the onset of local failure was negative. The regions susceptible to local cavitation transitioned from an equi-triaxial stress state after the thermal cooldown to a combined stress state during the application of the tensile load, revealing the confrontation between thermal residual stresses and mechanical stresses in the constrained plies (particularly for thin plies). During application of the tensile load, the constraining 0° plies suppressed ply crack formation in the 90° ply leading to higher strains at full ply crack formation compared to unconstrained plies or the thicker constrained plies.
- Manufacturing-induced defects (e.g., nonuniform fiber spatial dispersion, resin-rich pockets, micro-voids) caused a perturbation of the local stress fields in the epoxy, which may expedite the onset of local failure or alter the local failure mechanism. Defects also influence the crack formation process and the strain at first ply crack formation.
- During the ply crack formation process a portion of energy may dissipate to form mix mode crack segments (i.e., oblique cracks or microcrack branches), which depends on numerous factors such as nonuniform fiber distribution, manufacturing-induced defects, ply constraints effect.
- The collective energy dissipative mechanisms during ply crack formation were captured by the estimated effective energy release rates, which were in good agreement with values reported in previous studies for similar cross-ply laminates.

8.2 Future Directions

In closing, the following suggestions are provided for further development of the numerical model and next steps towards assessing damage for laminated composite materials.

- To invoke the developed numerical microscale model for other material systems, the corresponding resin properties must be known. It is recommended that microscale tests are used to characterize the inelastic response of commonly used resins, while poker-chip tests also performed to determine the critical dilatation energy density.
- The developed user-defined material subroutine can be extended to capture anisotropic damage for an improved prediction of local stress field around the crack tip. Also, interactions between other damage modes (e.g., inter- and intra-laminar cracking) and corresponding energy dissipation (i.e.,

G_{IC}/G_{IIC}) can be predicted in a more sophisticated FE model. Furthermore, the time-efficiency of the computational micromechanical model can be improved by changing the boundary conditions (e.g., uniform displacement boundary conditions instead of periodic), modifying the meshing strategy. Additionally, enhancing the computational efficiency of the VUMAT code may lead to a reduction in the required number of iterations for each solution increment.

- The role of different manufacturing-induced defects (e.g., voids, fiber misalignment, decohesion) on the formation of ply cracks can be further investigated. Qualitative and quantitative information about defects in a manufactured laminate can be used as input for representing these defects in the micromechanical model. Results from these studies will provide insight on optimizing manufacturing processes to produce higher quality materials.
- Capturing cure-induced shrinkage of the resin may lead to improved estimates of the thermal residual stresses in the RVE, while capturing the variation of the degree of resin cure (i.e., material properties) throughout a ply may better represent a manufactured laminate.
- Delamination and ply crack-induced delamination can be captured using the current material code, while it is necessary to model the fibers in the vicinity of the ply interface. Simulating the breakage of linear-elastic fibers using the corresponding damage model further extends applications of a 3D computational model; however, larger RVEs will be required to consider the crack propagation along the global width of the laminate.
- The same numerical modelling strategy developed in this thesis can be used for simulating local failure and ply crack formation under dynamic loads, which was one of the main motivations for invoking explicit FE analysis in the study instead of an implicit analysis. Note, the strain rate-dependent behaviour of the epoxy must be characterized, and the material model updated to account for this behaviour.
- The computational model can be extended and used for predicting damage evolution in laminates under quasi-static or dynamic compressive, in-plane shear, biaxial, and bending loads. Extending the computational model may require modifications to capture fiber failure and fiber-matrix interfacial behaviour. Also, damage evolution under cyclic loads can be predicted.
- The developed modelling approach can also be used to predict the behaviour of multidirectional laminates subjected to complex loading conditions that are consistent with practical applications.

Appendix A

Inelastic Modelling

Here, preliminary steps of an incremental inelastic modelling approach for employment in an explicit framework are provided. Note, the references cited below are found in Chapter 6. A linear elastic stress/strain relationship for an epoxy is expressed as:

$$\boldsymbol{\sigma} = \boldsymbol{C} : \boldsymbol{\varepsilon} \tag{A-1}$$

where $\boldsymbol{\sigma}$, $\boldsymbol{\varepsilon}$, and $\boldsymbol{C}$ are Cauchy stress, strain, and fourth-order stiffness tensors. The second-order stress tensor can be divided to isochoric, so-called deviatoric, and volumetric stress tensors as:

$$\boldsymbol{\sigma} = \boldsymbol{S} + \boldsymbol{P} \tag{A-2}$$

where $\boldsymbol{S}$ and $\boldsymbol{P} = \frac{tr(\boldsymbol{\sigma})}{3}\boldsymbol{I}$ are the deviatoric and hydrostatic stress tensors. It should be noted that $\boldsymbol{I}$ is the second-order identity tensor. Similarly, the second-order strain tensor can be divided to deviatoric and volumetric strain tensors as:

$$\boldsymbol{\varepsilon} = \boldsymbol{\varepsilon}_d + \boldsymbol{\varepsilon}_v \tag{A-3}$$

Corresponding stress/strain tensors can also be related by the following relations as:

$$\boldsymbol{S} = \frac{E}{1+\nu}\boldsymbol{\varepsilon}_d, \quad \boldsymbol{P} = \frac{E}{3(1-2\nu)}\boldsymbol{\varepsilon}_v \tag{A-4}$$

where E and ν are the elastic constants.

A paraboloidal pressure-dependent yield surface was used in the paper to capture the behaviour of the epoxy. The corresponding yield function is defined as [36]:

$$\Phi\left(\boldsymbol{\sigma}, \sigma_C, \sigma_T\right) = 6J_2 + 2I_1 - 2\sigma_C\sigma_T \tag{A-5}$$

where $J_2 = \frac{1}{2}\boldsymbol{S}:\boldsymbol{S}$ and $I_1 = tr(\boldsymbol{\sigma})$ are the second invariant of deviatoric and first invariant of Cauchy stress tensors, respectively. Furthermore, σ_c and σ_T are the compressive and tensile stresses on the defined hardening curves that express as functions of the equivalent plastic strain ε_{eq}^{p} as:

$$\sigma_C = \sigma_C\left(\varepsilon_{eq}^{p}\right), \quad \sigma_T = \sigma_T\left(\varepsilon_{eq}^{p}\right) \tag{A-6}$$

where the equivalent plastic strain rate $\dot{\varepsilon}_{eq}^{p}$ is defined as [17]:

$$\dot{\varepsilon}_{eq}^{p} = \sqrt{\frac{1}{1+2\nu_p^2}\dot{\boldsymbol{\varepsilon}}^{p} : \dot{\boldsymbol{\varepsilon}}^{p}} \tag{A-7}$$

and $\dot{\boldsymbol{\varepsilon}}^p$ and ν_p are the plastic strain rate tensor and plastic Poisson ratio. ε_{eq}^p is calculated according to $\dot{\varepsilon}_{eq}^p$ via time integration within the subroutine. Below, the plastic strain rate tensor is expressed in Eq. (A-10) while the plastic Poisson ratio is reported in Table 5.

A non-associative flow rule was used to consider the volumetric deformations of the epoxy where the flow potential is defined as [17]:

$$\Psi = 3J_2 + \beta I_1^2 \tag{A-8}$$

and β is calibrated from comparing the plastic strains in uniaxial loading case and stated as:

$$\beta = \frac{1-2\nu_p}{2\left(1+\nu_p\right)} \tag{A-9}$$

Here, the plastic strain tensor can be expressed as a function the flow tensor and the time derivative of plastic multiplier ($\dot{\gamma}$) as:

$$\dot{\boldsymbol{\varepsilon}}^p = \dot{\gamma}\frac{\partial\Psi}{\partial\boldsymbol{\sigma}} = \dot{\gamma}\left(3\boldsymbol{S} + 6\beta\boldsymbol{P}\right) \tag{A-10}$$

while the plastic multiplier and the consistency condition shall constantly obey the following conditions:

$$\dot{\gamma} \geq 0, \quad \Phi \leq 0, \quad \dot{\gamma}\cdot\Phi = 0 \tag{A-11}$$

Appendix B

Explicit Time Integration

An explicit time integration method was utilized in the study while return mapping algorithm was used for correcting the elastic predictor. Here, a straight-forward summary of the applicable relations for the subroutine is provided. The reader is referred to Ref. [30] of Chapter 7 for understanding the computational approaches in plasticity.

Defining an elastic trial stress between the time increments $[t_n, t_{n+1}]$, the updated trial stress is expressed as:

$$\boldsymbol{\sigma}_{n+1}^{Trial} = \boldsymbol{\sigma}_n + \boldsymbol{C} : \Delta\boldsymbol{\varepsilon} \tag{B-1}$$

where the $\boldsymbol{\sigma}_n$ is the resulting stress from the previous increment. Equation (B-1) can be split into two parts:

$$\boldsymbol{S}_{n+1}^{Trial} = \boldsymbol{S}_n + \frac{2E}{1+\nu}\Delta\boldsymbol{\varepsilon}_d, \quad \boldsymbol{P}_{n+1}^{Trial} = \boldsymbol{P}_n + \frac{E}{3(1-2\nu)}\Delta\boldsymbol{\varepsilon}_v \tag{B-2}$$

Therefore, the corrected stress at the current increment is defined as:

$$\boldsymbol{\sigma}_{n+1} = \boldsymbol{\sigma}_{n+1}^{Trial} - \boldsymbol{C} : \Delta\boldsymbol{\varepsilon}^p = \boldsymbol{C} : \left(\Delta\boldsymbol{\varepsilon} - \Delta\boldsymbol{\varepsilon}^p\right) \tag{B-3}$$

Using Eq. (B-1) and the deviatoric ($\boldsymbol{I}_d$) and volumetric ($\boldsymbol{I}_v$) projection tensors at n^{th} increment, the corresponding stress tensors components can be extracted. The definition helps reducing the overall computation time. Now, the plastic strain can be obtained using Eq. (A-10). Hence, using Eq. (B-2) and Eq. (B-3), the updated components of the stress tensor are determined by:

$$\boldsymbol{S}_{n+1} = \frac{\boldsymbol{S}_{n+1}^{Trial}}{\xi_d}, \quad \boldsymbol{P}_{n+1} = \frac{\boldsymbol{P}_{n+1}^{Trial}}{\xi_v} \tag{B-4}$$

where:

$$\xi_d = 1 + \frac{6E\Delta\gamma}{1+\nu}, \quad \xi_v = 1 + \frac{6E\beta\Delta\gamma}{1-2\nu} \tag{B-5}$$

Afterwards, equations are presented at the current (n^{th}) time increment and the subscript is dropped to facilitate reading the equations. Thereby, the consistency condition is rewritten as:

$$\Phi = \frac{6J_2^{Trial}}{\xi_d^2} + \frac{2\left(\sigma_C - \sigma_T\right)I_1^{Trial}}{\xi_v} - 2\sigma_C\sigma_T = 0 \tag{B-6}$$

Hence, employing Eq. (A-10) into the Eq. (A-7) and using Eq. (B-4), the equivalent plastic strain at the current increment is stated as:

$$\Delta\varepsilon_{eq}^{p}=\Delta\gamma\sqrt{\frac{1}{1+2\nu_{p}^{2}}\left(\frac{18J_{2}^{Trial}}{\xi_{d}^{2}}+\frac{12\beta^{2}\left(I_{1}^{Trial}\right)^{2}}{\xi_{v}^{2}}\right)} \tag{B-7}$$

For the sake of simplicity, the multiplier is divided into two terms as:

$$A=\sqrt{\frac{1}{1+2\nu_{p}^{2}}},\quad B=\sqrt{\frac{18J_{2}^{Trial}}{\xi_{d}^{2}}+\frac{12\beta^{2}\left(I_{1}^{Trial}\right)^{2}}{\xi_{v}^{2}}} \tag{B-8}$$

In this study, the Newton-Raphson root-finding method within the return mapping algorithm framework was used to solve nonlinear equations for finding the plastic multiplier. Thus, the derivatives of the consistency condition with respect to the plastic multiplier is defined as:

$$\begin{aligned}\frac{\partial\Phi}{\partial\Delta\gamma}&=\frac{2I_{1}^{Trial}}{\xi_{v}}\left(\frac{\partial\sigma_{C}}{\partial\Delta\gamma}-\frac{\partial\sigma_{T}}{\partial\Delta\gamma}\right)-\frac{12E\beta I_{1}^{Trial}\left(\sigma_{C}-\sigma_{T}\right)}{\left(1-2\nu\right)\xi_{v}^{2}}\\&-\frac{72EJ_{2}^{Trial}}{\left(1+\nu\right)\xi_{d}^{3}}-2\left(\sigma_{C}\frac{\partial\sigma_{T}}{\partial\Delta\gamma}+\sigma_{T}\frac{\partial\sigma_{C}}{\partial\Delta\gamma}\right)\end{aligned} \tag{B-9}$$

where the derivatives of the hardening functions by using the chain rule are expressed as:

$$\begin{aligned}\frac{\partial\sigma_{C}}{\partial\Delta\gamma}&=\frac{\partial\sigma_{C}}{\partial\Delta\varepsilon_{eq}^{p}}\frac{\partial\Delta\varepsilon_{eq}^{p}}{\partial\Delta\gamma}\\\frac{\partial\sigma_{T}}{\partial\Delta\gamma}&=\frac{\partial\sigma_{T}}{\partial\Delta\varepsilon_{eq}^{p}}\frac{\partial\Delta\varepsilon_{eq}^{p}}{\partial\Delta\gamma}\end{aligned} \tag{B-10}$$

The first term of Eq. (B-10) has been defined with regards to the selected compressive and tensile hardening curves while the second term is determined by using Eq. (B-5) as:

$$\frac{\partial\Delta\varepsilon_{eq}^{p}}{\partial\Delta\gamma}=A\left[B-\frac{\Delta\gamma}{2B}\left(\frac{216EJ_{2}^{Trial}}{\left(1+\nu\right)\xi_{d}^{3}}+\frac{144E\beta^{3}I_{1}^{Trial}}{\left(1-2\nu\right)\xi_{v}^{3}}\right)\right] \tag{B-11}$$

Thus, the numerical solution for Eq. (B-6) during iteration can be found by using Newton-Raphson root-finding method at each increment to measure the plastic multiplier, $\Delta\gamma$:

$$\Delta\gamma_{new}^{n+1}=\Delta\gamma_{old}^{n+1}-\frac{\Phi_{old}}{\left(\frac{\partial\Phi}{\partial\Delta\gamma}\right)_{old}} \tag{B-12}$$

It should be noted that stresses at the hardening curves, as functions of the plastic multiplier, are updated during the loop convergency, *i.e.* $\Phi\leq tol$. Accordingly, the stress tensor, plastic strain tensor, and equivalent plastic strain are determined at different increments.

Based on the experience in this study, consistent tangent operator for small strain materials, *e.g.* epoxy, enforces an extra computation time to the subroutine while fails to improve the overall prediction time. This is also valid for a damage analysis. Nevertheless, one can utilize the approach by replacing the elastic stiffness tensor in Eq. (B-1) by the consistent tangent operator to improve the trial stress at each increment. This approach is not covered here.

The pseudo-code for the employed algorithm is demonstrated in Table B-1.

Table B-1. Pseudo-code for implementation of the inelastic modelling for an epoxy.

(i)	Elastic predictor	
	Find $\boldsymbol{\sigma}_{n+1}^{Trial}$	$\boldsymbol{\sigma}_{n+1}^{Trial} = \boldsymbol{\sigma}_n + \boldsymbol{C} : \Delta\boldsymbol{\varepsilon}$
	Find $\boldsymbol{S}_{n+1}^{Trial}$	$\boldsymbol{S}_{n+1}^{Trial} = \boldsymbol{I}_d : \boldsymbol{\sigma}_{n+1}^{Trial}$
	Find $\boldsymbol{P}_{n+1}^{Trial}$	$\boldsymbol{P}_{n+1}^{Trial} = \boldsymbol{\sigma}_{n+1}^{Trial} - \boldsymbol{S}_{n+1}^{Trial}$
	Find I_1^{Trial} and J_2^{Trial}	See Appendix A
	Update equivalent plastic strain	$\left(\Delta\varepsilon_{eq}^{p}\right)^{Trial} = \left(\Delta\varepsilon_{eq}^{p}\right)^{Old}$
	Find σ_C^{Trial} and σ_T^{Trial} according to the defined strain hardening curve in the model	
(ii)	Check for inelastic deformations (Φ)	Eq. (A-5)
	if $\Phi < 0$ then	Elastic response
	$\boldsymbol{\sigma}_{n+1} = \boldsymbol{\sigma}_{n+1}^{Trial}$, Update other variables accordingly	
	Check for cavitation, Update solution-dependent variables*	Eq. (6-7)
	elseif $\Phi \geq 0$ then "iterate over the following subparts"	Inelastic response
(ii-1)	Set an initial value for plastic multiplier, *e.g.* $\Delta\gamma = 10^{-8}$	
(ii-2)	Find ξ_d and ξ_v	Eq. (B-5)
	Find $\Delta\varepsilon_{eq}^{p}$	Eq. (B-7)
	Find σ_C^{Trial} and σ_T^{Trial} according to the hardening curve	
	Find Φ	Eq. (B-6)
	Find derivatives	Eqs. (A-9), (B-8), (B-9), (B-10), (B-11)
	Find the new plastic multiplier $\Delta\gamma$	Eq. (B-12)
(ii-3)	Check for convergence	

	if $\Phi \leq$ tol then	
	Update $\boldsymbol{\sigma}_{n+1}$, $\Delta\varepsilon_{eq}^{p}$, $\boldsymbol{\varepsilon}^{p}$, and other related variables	
	Inelastic deformation, Update solution-dependent variables*	
	"end the loop"	
(iii)	Check for cavitation and inelastic damage, Update solution-dependent variables*	Eqs. (6-1) and (6-7)

* Solution-dependent variables do not influence the stress/strain definition.

Appendix C

Isotropic Damage Model

An isotropic damage model (i.e., single variable) was used to predict the post-peak response of the epoxy. In the following, a summary of the damage model is presented, while further details of deriving the equations are provided in Ref. [13,30,31] of Chapter 7. Assuming the elastic-damage response of the material is decoupled from the plastic contribution, the specific free energy relation in a thermodynamical framework is defined as:

$$\psi\left(\varepsilon^{e}, R, \boldsymbol{X}, d\right) = \psi^{ed}\left(\varepsilon^{e}, d\right) + \psi^{p}\left(R, \boldsymbol{X}\right) \tag{C-1}$$

where ψ^{ed} and ψ^{p} are elastic-damage and plastic contribution to the specific free energy. Here, ε^{e} and d are elastic strain and isotropic damage variables. Also, R and $\boldsymbol{X}$ are internal variables related to isotropic and kinematic hardening. In an explicit framework, the complementary energy density ψ is determined by:

$$\rho\psi = \int \boldsymbol{\sigma} : \dot{\boldsymbol{\varepsilon}}\ dt \tag{C-2}$$

Here, $\boldsymbol{\sigma}$ and $\dot{\boldsymbol{\varepsilon}}$ are Cauchy's stress tensor and strain rate. Also, ρ is the material density. In the scalar format, the elastic-damage specific energy is defined as:

$$\psi^{ed} = \frac{\sigma_{11}^{2} + \sigma_{22}^{2} + \sigma_{33}^{2}}{2E\left(1-d\right)} - \frac{\nu}{E}\left(\sigma_{11}\sigma_{22} + \sigma_{11}\sigma_{33} + \sigma_{22}\sigma_{33}\right) + \frac{1+\nu}{E\left(1-d\right)}\left(\sigma_{12}^{2} + \sigma_{13}^{2} + \sigma_{23}^{2}\right) \tag{C-3}$$

where E and ν denote Young's modulus and Poisson's ratio, respectively. Although finding an explicit answer for calculating ψ^{p} is possible, an indirect method facilitates numerical calculation of the corresponding energy as:

$$\psi^{p} = \psi - \psi^{ed} \tag{C-4}$$

The irreversible nature of damage process ensures a positive dissipation of energy. Based on this presumption, the stress-strain relation for an isotropic damage model is expressed as:

$$\boldsymbol{\sigma} = \boldsymbol{C}\left(d\right) : \boldsymbol{\varepsilon} \tag{C-5}$$

Here, $\boldsymbol{C}(d)$ is the stiffness tensor as a function of damage parameter (d) and defines as:

$$\boldsymbol{C}(d)=\begin{bmatrix} \zeta_d & \lambda_d & \lambda_d & 0 & 0 & 0 \\ \lambda_d & \zeta_d & \lambda_d & 0 & 0 & 0 \\ \lambda_d & \lambda_d & \zeta_d & 0 & 0 & 0 \\ 0 & 0 & 0 & G(1-d) & 0 & 0 \\ 0 & 0 & 0 & 0 & G(1-d) & 0 \\ 0 & 0 & 0 & 0 & 0 & G(1-d) \end{bmatrix} \tag{C-6}$$

where G is shear modulus and:

$$\zeta_d=\frac{E(1-d)\left(1-\nu(1-d)\right)}{\left(1+\nu(1-d)\right)\left(1-2\nu(1-d)\right)} \tag{C-7}$$

$$\lambda_d=\frac{E\nu(1-d)^2}{\left(1+\nu(1-d)\right)\left(1-2\nu(1-d)\right)} \tag{C-8}$$

Thus, the stress-strain state of the material depends on calculating the damage variable. In the following, the method for finding this parameter is presented.

Using the concept of effective stress, damage activation functions for cavitation-induced and ductile failure are proposed as:

$$F_{dis}=\frac{3\tilde{J}_2}{X_C X_T}+\frac{\tilde{I}_1(X_C-X_T)}{X_C X_T}-r_{dis}\le 0 \tag{C-9}$$

$$F_{dil}=\frac{U_{dil}}{U_{dil}^c}-r_{dil}\le 0 \tag{C-10}$$

and r_{dis} and r_{dil} are the internal variables and defines as:

$$r_{dis}=\max\left[1,\ \left(\frac{3\tilde{J}_2}{X_C X_T}+\frac{\tilde{I}_1(X_C-X_T)}{X_C X_T}\right)\right] \tag{C-11}$$

$$r_{dil}=\max\left[1,\ \frac{U_{dil}}{U_{dil}^c}\right] \tag{C-12}$$

Based on the Bazant's crack band model [32], the energy dissipation per unit volume is expressed as:

$$\Psi=\int_1^{\infty}\frac{\partial\psi}{\partial d}\frac{\partial d}{\partial r}dr=\frac{G_f}{l^e} \tag{C-13}$$

where G_f and l_e are the energy release rate and characteristic length, that is defined based on the geometry of an elements in an FE software. The following expressions relate the damage variables and internal variables:

$$d_{dis} = 1 - \frac{e^{A_{dis}\left(3-\sqrt{7+2r_{dis}^2}\right)}}{\sqrt{7+2r_{dis}^2}-2} \tag{C-14}$$

$$d_{dil} = 1 - \frac{e^{A_{dil}\left(1-r_{dil}\right)}}{r_{dil}} \tag{C-15}$$

These damage evolution laws have been defined with respect to the two boundaries imposed by the damage variable (i.e., pristine and fully damaged) to ensure damage localization and strain softening of the material.

Using the uniaxial loading cases for cavitation-induced and ductile failure, the unique damage parameters A_{dis} and A_{dil} can be determined by the following equations:

$$\begin{aligned}&\int_1^{\infty} \frac{1}{2E}\left(\frac{X_T - X_C + \sqrt{\left(X_C - X_T\right)^2 + 4X_C X_T r_{dis}}}{2}\right)^2 \\ &\times \frac{2\nu^2 d_{dis}^2 + \left[1-\nu\left(1-d_{dis}\right)\left(1+2\nu\right)\right]^2}{\left[1+\nu\left(1-d_{dis}\right)\right]^2\left[1-2\nu\left(1-d_{dis}\right)\right]^2} \\ &\times \frac{2r_{dis}e^{A_{dis}\left(3-\sqrt{7+2r_{dis}^2}\right)}}{\sqrt{7+2r_{dis}^2}\left(\sqrt{7+2r_{dis}^2}-2\right)}\left(A_{dis} + \frac{1}{\sqrt{7+2r_{dis}^2}-2}\right)dr_{dis} = \frac{G_f}{l^e}\end{aligned} \tag{C-16}$$

$$\begin{aligned}&\int_1^{\infty} \frac{3U_{dil}^c r_{dil}}{1-2\nu} \times \frac{2\nu^2 d_{dil}^2 + \left[1-\nu\left(1-d_{dil}\right)\left(1+2\nu\right)\right]^2}{\left[1+\nu\left(1-d_{dil}\right)\right]^2\left[1-2\nu\left(1-d_{dil}\right)\right]^2} \\ &\times \frac{e^{A_{dil}\left(1-r_{dil}\right)}}{r}\left(A_{dil} + \frac{1}{r_{dil}}\right)dr_{dil} = \frac{G_f}{l^e}\end{aligned} \tag{C-17}$$

To facilitate defining the following expressions, the left-hand side of Eqs. (C-16) and (C-17) are represented as:

$$g_{dis} = \int_1^{\infty} f_{dis}\left(A_{dis}, r_{dis}\right)dr_{dis} \tag{C-18}$$

$$g_{dil} = \int_{1}^{\infty} f_{dil}\left(A_{dil}, A_{dil}\right) dr_{dil} \tag{C-19}$$

To find the improper integral on the left-hand side, Simpson's 1/3 rule can be used as:

$$g_{dis/dil} \approx \frac{h}{3}\left(f_{dis/dil}\left(r_0\right) + 2\sum_{j=1}^{n/2-1} f_{dis/dil}\left(r_{2j}\right) + 4\sum_{j=1}^{n/2} f_{dis/dil}\left(r_{2j-1}\right) + f_{dis/dil}\left(r_n\right)\right) \tag{C-20}$$

Here n is the number of iterations, r_0 and r_n are the first and last value for r starting from 1. Also, the increment h was defined as:

$$h_{dis/dil} = nA_{dis/dil}^{Trial} \ln K_{dis/dil} \tag{C-21}$$

and A^{Trial} are constants within the loop. To limit the number of iterations for calculating the improper integral, the absolute value of the effective stress/energy is limited to X_t/K and $\sqrt{6EU_{dil}^c/1-2\nu}/K$ for ductile failure and cavitation-induced failure, respectively, while the remaining energy is negligible. The parameter K = 100 for both cases. The flowchart for calculating the improper integral is demonstrated in Fig. C-1b.

The secant method is used to find the unique damage variables by solving Eqs. (C-16) and (C-17). Accordingly, the expression for finding $A_{dis/dil}$ at the next step, based on the predictions in two previous steps, is defined as:

$$\begin{aligned} \ln\left(A_{dis/dil}^{i+1}\right) &= \ln\left(A_{dis/dil}^{i}\right) - \left[\ln\left(g_{dis/dil}\left(A_{dis/dil}^{i}\right)\right) - \ln\left(\frac{G_f}{l^e}\right)\right] \\ &\times \frac{\ln\left(A_{dis/dil}^{i}\right) - A_{dis/dil}^{i-1}}{\ln\left(g_{dis/dil}\left(A_{dis/dil}^{i}\right)\right) - \ln\left(g_{dis/dil}\left(A_{dis/dil}^{i-1}\right)\right)} \end{aligned} \tag{C-22}$$

and the following values are suggested for initializing the root-finding iterations [32]:

$$A_{dis/dil}^{1} = \frac{2l^e X_T^2}{2EG_f - l^e X_T^2}, \qquad A_{dis/dil}^{0} = 0.5A_{dis/dil}^{1} \tag{C-23}$$

Worth noting that the damage variable, *d*, in the code cannot be equal to 1 which enforces unrealistic deformations to an element; however, failed elements carry an insignificant amount of stress, while they are not removed in the FE model.

The flowchart for the secant root-finding method is illustrated in Fig. C-1a. Additionally, the pseudo-code for developing the subroutine is provided in Table C-1.

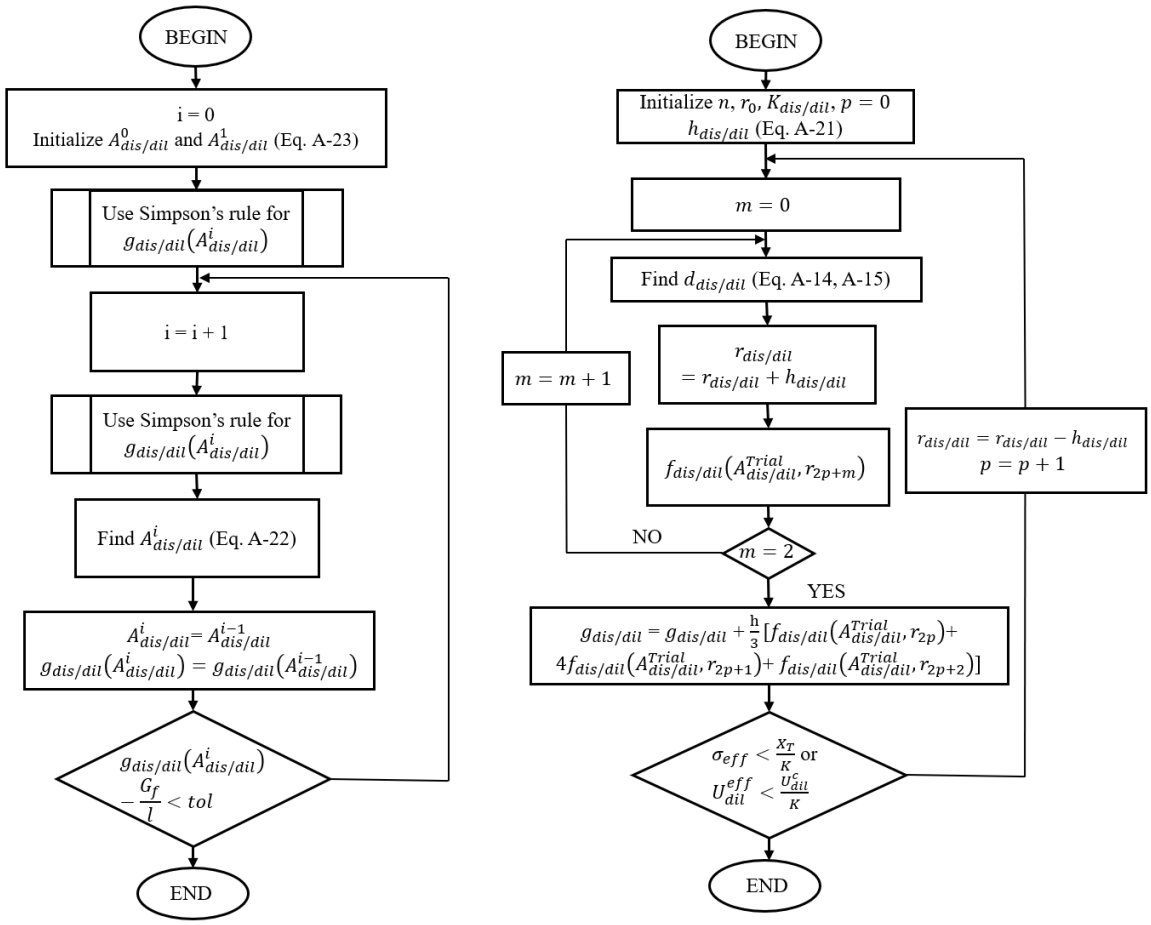

(a) (b)

Figure C-1. Flowcharts for: (a) secant root-finding method; (b) Simpson's improper integral estimation.

Table C-1. Pseudo-code for implementation of the plasticity and damage modelling.

(I)	if $d_{dis/dil} \leq 0$ then	
(i)	Elastic predictor	
		$\boldsymbol{\sigma}_{n+1}^{Trial} = \boldsymbol{\sigma}_n + \boldsymbol{C} : \Delta\boldsymbol{\varepsilon}$
		$\boldsymbol{S}_{n+1}^{Trial} = \boldsymbol{I}_d : \boldsymbol{\sigma}_{n+1}^{Trial}$
	Find $\boldsymbol{\sigma}_{n+1}^{Trial}$/ $\boldsymbol{S}_{n+1}^{Trial}$/ $\boldsymbol{P}_{n+1}^{Trial}$/ I_1^{Trial}/ J_2^{Trial}	$\boldsymbol{P}_{n+1}^{Trial} = \boldsymbol{\sigma}_{n+1}^{Trial} - \boldsymbol{S}_{n+1}^{Trial}$
		$\boldsymbol{I}_1^{Trial} = tr\left(\boldsymbol{\sigma}_{n+1}^{Trial}\right)$
		$J_2^{Trial} = \frac{1}{2}\boldsymbol{S}_{n+1}^{Trial} : \boldsymbol{S}_{n+1}^{Trial}$
	Update equivalent plastic strain	$\left(\Delta\varepsilon_{eq}^{p}\right)^{Trial} = \left(\Delta\varepsilon_{eq}^{p}\right)^{Old}$
	Find σ_C^{Trial} and σ_T^{Trial} (Hardening curves)	
(ii)	Check for inelastic deformations (Φ)	Appendix A Eq. (A-5)
(a)	if $\Phi < 0$ then	Elastic response
	$\boldsymbol{\sigma}_{n+1} = \boldsymbol{\sigma}_{n+1}^{Trial}$, Update other parameters and solution dependent variables (SDV)	
	Check for cavitation	Eq. (A-10)
(a-1)	if $F_{dil} = U_{dil} / U_{dil}^{c} - 1 \leq 0$ then	
	Go to the next increment	
(a-2)	elseif $F_{dil} = U_{dil} / U_{dil}^{c} - 1 \geq 0$ then	
	Find A_{dil}	Follow Fig. C-1
	Find r_{dil}	Eq. (C-12)
	Find d_{dil}	Eq. (C-15)
	Update effective stiffness tensor	Eqs. (C-6) - (C-8)
	Update stress tensor, update other parameters and SDVs	
(b)	elseif $\Phi \geq 0$ then	Inelastic response
	Set an initial value for plastic multiplier, *e.g.* $\Delta\gamma = 10^{-8}$	
	Iterate over (b-1)	
(b-1)	Find ξ_d and ξ_v	Appendix B Eq. (B-5)

		Find $\Delta\varepsilon_{eq}^{p}$	Appendix B Eq. (B-7)
		Find σ_C^{Trial} and σ_T^{Trial} (Hardening curves)	
		Find Φ	Appendix B Eq. (B-6)
		Find derivatives	Appendix A & B Eqs. (A-9) & (B-8) - (B-11)
		Find the new plastic multiplier $\Delta\gamma$	Appendix B Eq. (B-12)
	(b-2)	Check for convergence, if $\Phi \leq$ tol then	
		Update $\boldsymbol{\sigma}_{n+1}$, $\Delta\varepsilon_{eq}^{p}$, $\boldsymbol{\varepsilon}^{p}$, update other parameters and SDVs	
	(b-3)	Check for cavitation and ductile failure	Eq. (C-10) & (C-11)
	(b-3-1)	if $F_{dis} = \frac{3\tilde{J}_2}{X_C X_T} + \frac{\tilde{I}_1(X_C - X_T)}{X_C X_T} - 1 \geq 0$ then	
		Find A_{dis}	Follow Fig. C-1
		Find r_{dis}	Eq. (C-11)
		Find d_{dis}	Eq. (C-14)
		Update effective stiffness tensor	Eqs. (C-6) - (C-8)
		Update stress tensor, update other parameters and SDVs	
	(b-3-2)	elseif $F_{dil} = U_{dil} / U_{dil}^{c} - 1 \geq 0$ then	
		Find A_{dil}	Follow Fig. C-1
		Find r_{dil}	Eq. (C-12)
		Find d_{dil}	Eq. (C-15)
		Update effective stiffness tensor	Eqs. (C-6) - (C-8)
		Update stress tensor, update other parameters and SDVs	
	(b-3-3)	else	
		Go to the next increment	
(II)	elseif $d_{dis/dil} > 0$ then		Eq. (C-14) / (C-15)

		* A_{dis}/A_{dil} have been already calculated in the previous increment
	Find r_{dis} / r_{dil}	Eq. (C-11)
	Find d_{dis} / d_{dil}	Eq. (C-14)
	Update effective stiffness tensor	Eqs. (C-6) - (C-8)
	Update stress tensor, update other parameters and SDVs	

Appendix D

Letter of Copyrights Permission

According to Elsevier's author rights policy, one retains the right to include their article in a thesis/dissertation without prior formal request. The following journals/book chapter have been referred as the original source in entire or parts of Chapters 2, 4, 5, 6, and 7.

J. Montesano, **F. Sharifpour**, Modelling damage evolution in multidirectional laminates: micro to macro, in: W. Van Paepegem (Ed.), Multi-Scale Continuum Mechanics Modelling of Fibre-Reinforced Polymer Composites, Woodhead Publishing Series in Composites Science and Engineering, 2021: pp. 463–507.

G. Li, **F. Sharifpour**, A. Bahmani, J. Montesano, A new approach to rapidly generate random periodic representative volume elements for microstructural assessment of high volume fraction composites, Materials & Design 150 (2018) 124–138.

F. Sharifpour, J. Montesano, R. Talreja, Assessing the effects of ply constraints on local stress states in cross-ply laminates containing manufacturing induced defects, Composites Part B: Engineering 199 (2020) 1–13.

F. Sharifpour, J. Montesano, R. Talreja, Micromechanical assessment of local failure mechanisms and early-stage ply crack formation in cross-ply laminates, Composite Science and Technology (Under Review).

F. Sharifpour, J. Montesano, Micromechanical simulation of ply crack formation in cross-ply laminates under quasi-static tensile loading, Composite Part A: Applied Science and Manufacturing (To be submitted in January 2022)

The necessary copyright permission has been granted for the following materials and corresponding right holder. The agreements are between University of Waterloo (Farzad Sharifpour) and the right holder with the following license numbers:

Material	Right Holder	Reference	License Number	License Date
Figure 1	Dr. Gareth D. Padfield	G.D. Padfield, So You Want to Be an Engineer?: A Guide to a Wonderful,Mysterious Profession, Second Ed., Gareth D Padfield, 2015.	Sent via email	09/19/2021
Figure 2	Elsevier	J. Tong, F.J. Guild, S.L. Ogin, P.A. Smith, On matrix crack growth in quasi-isotropic laminates-I. Experimental investigation, Composite Science & Technology 57 (1997) 1527–1535.	5173170324340	10/20/2021
Figure 3a	Elsevier	C.A. Wood, W.L. Bradley, Determination of the effect of seawater on the interfacial strength of an interlayer E-glass/ graphite/epoxy composite by in situ observation of transverse cracking in an environmental SEM, Composite Science & Technology 57 (1997) 1033–1043.	5173170592428	10/20/2021

Figure 3a	Elsevier	V.S. Romanov, S. V. Lomov, I. Verpoest, L. Gorbatikh, Modelling evidence of stress concentration mitigation at the micro-scale in polymer composites by the addition of carbon nanotubes, Carbon N. Y. 82 (2015) 184–194.	5173170781497	10/20/2021
Figure 3a	Elsevier	D.T.G. Katerelos, J. Varna, C. Galiotis, Energy criterion for modelling damage evolution in cross-ply composite laminates, Composite Science & Technology 68 (2008) 2318–2324.	5173170895710	10/20/2021
Figure 3a	Elsevier	P.P. Camanho, P. Maimí, C.G. Dávila, Prediction of size effects in notched laminates using continuum damage mechanics, Composite Science & Technology 67 (2007) 2715–2727.	5173171023440	10/20/2021
Figure 3b	Elsevier	J. Montesano, C.V. Singh, A synergistic damage mechanics based multiscale model for composite laminates subjected to multiaxial strains, Mechanics of Materials 83 (2015) 72–89.	5173171296601	10/20/2021
Figure 3b	Elsevier	A. Arteiro, G. Catalanotti, A.R. Melro, P. Linde, P.P. Camanho, Micro-mechanical analysis of the in situ effect in polymer composite laminates, Composite Structures 116 (2014) 827–840.	5173171181210	10/20/2021
Figure 4	Cambridge University Press	R. Talreja, C.V. Singh, Damage and Failure of Composite Materials, Cambridge University Press, 2012.	57195	10/20/2021
Figure 5	Cambridge University Press	R. Talreja, C.V. Singh, Damage and Failure of Composite Materials, Cambridge University Press, 2012.	57195	10/20/2021
Figure 6	Dr. John Montesano	J. Montesano, Fatigue Damage Characterization of Braided and Woven Fiber Reinforced Polymer Matrix Composites at Room and Elevated Temperatures, Ryerson University, 2012.	Sent via email	Contact John
Figure 7	Elsevier	Q. Sun, G. Zhou, H. Guo, Z. Meng, Z. Chen, H. Liu, H. Kang, X. Su, Failure mechanisms of cross-ply carbon fiber reinforced polymer laminates under longitudinal compression with experimental and computational analyses, Compos. Part B Eng. 167 (2019) 147–160.	5173171405852	10/20/2021
Figure 8	Elsevier	C.A. Wood, W.L. Bradley, Determination of the effect of seawater on the interfacial strength of an interlayer E-glass/ graphite/epoxy composite by in situ observation of transverse cracking in an environmental SEM, Composite Science & Technology 57 (1997) 1033–1043.	5173170592428	10/20/2021
Figure 9a	Elsevier	E.K. Gamstedt, B.A. Sjögren, Micromechanisms in tension compression fatigue of composite laminates containing transverse plies, Compos. Sci. Technol. 59 (1999) 167–178.	5173180003467	10/20/2021
Figure 9b	Elsevier	D.T.G. Katerelos, J. Varna, C. Galiotis, Energy criterion for modelling damage evolution in cross-ply composite laminates, Composite Science & Technology 68 (2008) 2318–2324.	5173170895710	10/20/2021
Figure 10d	Cambridge University Press	R. Talreja, C.V. Singh, Damage and Failure of Composite Materials, Cambridge University Press, 2012.	57195	10/20/2021
Figure 11	Cambridge University Press	R. Talreja, C.V. Singh, Damage and Failure of Composite Materials, Cambridge University Press, 2012.	57195	10/20/2021
Figure 12	Cambridge University Press	R. Talreja, C.V. Singh, Damage and Failure of Composite Materials, Cambridge University Press, 2012.	57195	10/20/2021
Figure 13	Cambridge University Press	R. Talreja, C.V. Singh, Damage and Failure of Composite Materials, Cambridge University Press, 2012.	57195	10/20/2021

Figure 14	Cambridge University Press	R. Talreja, C.V. Singh, Damage and Failure of Composite Materials, Cambridge University Press, 2012.	57195	10/20/2021
Figure 15	Cambridge University Press	R. Talreja, C.V. Singh, Damage and Failure of Composite Materials, Cambridge University Press, 2012.	57195	10/20/2021
Figure 16	Cambridge University Press	R. Talreja, C.V. Singh, Damage and Failure of Composite Materials, Cambridge University Press, 2012.	57195	10/20/2021
Figure 18	Elsevier	T. Yokozeki, T. Aoki, T. Ishikawa, Consecutive matrix cracking in contiguous plies of composite laminates, Int. J. Solids Struct. 42 (2005) 2785–2802.	5173180099873	10/20/2021
Figure 20	SAGE Publishing	S.T. Pinho, R. Darvizeh, P. Robinson, C. Schuecker, P.P. Camanho, Material and structural response of polymer-matrix fibre-reinforced composites, 46 (2012) 2313–2341.	Permission is granted for doctoral dissertations	10/20/2021
Figure 22	Cambridge University Press	R. Talreja, C.V. Singh, Damage and Failure of Composite Materials, Cambridge University Press, 2012.	57195	10/20/2021
Figure 62 & 63	Taylor & Francis	H. Saito, H. Takeuchi, I. Kimpara, Experimental evaluation of the damage growth restraining in 90° layer of thin-ply CFRP cross-ply laminates, Adv. Compos. Mater. 21 (2012) 57–66.	5172010603641	10/18/2021